PhD-FSTM-2021-93
The Faculty of Sciences, Technology and Medicine

DISSERTATION

Defence held on 23/11/2021 in Esch-sur-Alzette
to obtain the degree of

DOCTEUR DE L'UNIVERSITÉ DU LUXEMBOURG

EN PHYSIQUE

by

Antoine DUHAIN

Born on 22 November 1991 in Charleroi, (Belgium)

COPPER-CARBON NANOTUBE COMPOSITES FOR LIGHTING STRIKE PROTECTION

Dissertation defence committee

Dr Damien Lenoble, dissertation supervisor
Luxembourg Institute of Science and Technology (LIST)

Dr Guillaume Lamblin
Luxembourg Institute of Science and Technology (LIST)

Dr Jens Kreisel, Chairman
Professor, Université du Luxembourg

Dr Philippe Lalande
Office National d'Etudes et de Recherches Aérospatiales (ONERA)

Dr Manuel Dossot, Vice Chairman
Professor, Université de Lorraine

Copper-Carbon Nanotube Composites for Lightning Strike Protection

Antoine Duhain, Materials Research and Technology department,
Luxembourg Institute of Science and Technology (LIST),
Rue du Brill 41, L-4422 Belvaux, Luxembourg.

Thesis supervisor: Dr. Damien Lenoble
Tutor: Dr. Guillaume Lamblin

Abstract

Copper-carbon nanotube composites (Cu-CNT composites) were recently identified as promising materials to withstand large electrical current densities, with their use being considered in a variety of domains where materials progressively hit their current-carrying capacity limits (ampacity). In this thesis, we aim to integrate Cu-CNT composites into the lightning strike protection used in aircrafts. The expected outstanding properties of this material result from a synergy between copper, which is among the best electrical and thermal conductors, and CNT, which can have a high ampacity, a low temperature coefficient of resistance, a high conductivity, and a very low density. As a result, pure copper could be replaced in lightning strike protection by a significantly lighter material that has a better resistance to lightning strikes.

However, many challenges remain before we can obtain a composite with the ideal features. First, its fabrication is not trivial and has only been achieved, up to now, via an electroplating of copper into a pre-deposited CNT layer that requires the use of an organic plating solution. Secondly, CNT have versatile transport properties that depend on numerous parameters (type, dimensions, level of defects, ...), and that are hardly predictable and measurable. Thirdly, the interface bonding between copper and CNT is weak and generally leads to a very poor electronic transport synergy between the two materials. Finally, the state of the art reports Cu-CNT composite electrical properties that are controversial and only few papers have reported encouraging electrical properties of Cu-CNT composites used as an interconnect/wire, providing several potential guidelines to reproduce the high ampacity material. In addition, the experimental measurement conditions that are commonly used in laboratory are hardly comparable to the harsh electrical fields and temperatures induced by lightning strikes.

In this work, we report a novel fabrication method for the composite that outperforms the state of the art, requiring only the use of a standard electroplating solution thanks to Cu-doped polydopamine coating of the CNT. Then, we prospect several types of CNT and investigate their contribution to the composite electrical properties. Several paths are also explored for the tuning of the interface between the coated CNT and the copper. In particular, we investigate the use of nickel to boost the electronic transport between the metal matrix and the CNT. Finally, we report on the promising efficiency of our composites when used as lightning strike protection.

Acknowledgments

The Luxembourgish National Research Fund (FNR) is acknowledged for funding this thesis work under project CUCFOILS4LSP (C-PPP16/MS/11515319).

The PhD thesis that I undertook at the Luxembourg Institute of Science and Technology (LIST) during four years and four months was one of the most enriching experiences of my life. Here, I would like to acknowledge the people that helped me and made this journey a unique adventure.

First of all, I want to thank both my supervisor, Dr. Damien Lenoble, and my tutor, Dr. Guillaume Lamblin, who gave me their trust to carry out this research work. With our weekly meetings to review my results and Guillaume's support on a daily basis, I received very consistent scientific guidance that led me to thrive throughout this PhD thesis. Their excellent human qualities brightened my time at LIST. I have no doubt that their examples will become a source of inspiration in my future career.

Of course, I am also grateful to the members of the supervisory committee, Prof. Jens Kreisel and Prof. Manuel Dossot, who took the time to follow my work during these four years. I also give thanks to the external members of the jury, Dr. Philippe Lalande and Mr. Michel Streel, for the time they dedicated to the assessment of my manuscript.

Moreover, I want to acknowledge all the colleagues who contributed to the scientific results in this manuscript. In particular, I would like to thank Jérôme Guillot for the various XPS analyses, Mathieu Gérard for his help with the setup to measure ampacity and the 3D-printed grid of the system of compression during electroplating, Marc Michel for introducing me to the magical world of polydopamine and for the spraying of carbon nanotubes, Brahime El Adib for the Raman spectroscopy, Benoit Marcolini and Régis Vaudemont for the DSC analyses, Jérôme Polesel for his help with the fabrication of my substrates, Didier Arl for the STEM analyses, Kevin Menguelti for his support and advice, and Lindsey Auguin for the proof-reading of my papers. I would also like to acknowledge our colleagues of the French Aerospace Lab (ONERA) who performed the lightning strike tests.

More generally, I am thankful to all my colleagues of the MRT department who supported me one way or another but also for all the good memories I keep from the moments we shared together. LIST is full of friendly and fascinating people.

I want to thank especially my former colleagues, Nicolas G. and Aymen with whom I spent most of my time at LIST. Thanks to you, this experience was amazing in so many ways and I am glad to count you, now and for a long time to come, amongst my closest friends. I also thank Nicolas B., Laurianne, Kevin, Stéphanie, Philipp, Raoul, and Poorani for their good company during our numerous parties, skiing sessions, and munstiflette tastings... Last but not least, I tip my hat to the Hon. Chevreuilz for keeping me distracted during (from) the writing of my manuscript.

Finally, I thank my dear Estelle who supported me unwaveringly during all this time and I thank my family without whom I would not be who I am today.

List of abbreviations and symbols

A	Area
C	Specific heat
$\overrightarrow{C_h}$	Chiral vector
D	Diameter
DA	Dopamine
DLS	Dynamic light scattering
DOS	Density of states
DSC	Differential scanning calorimetry
CNT	Carbon nanotube
CNT@Pda	Carbon nanotube coated with polydopamine
CNT@PdaCu	Carbon nanotube coated with Cu-doped polydopamine
CNT@PdaFe	Carbon nanotube coated with Fe-doped polydopamine
CNT@PdaNi	Carbon nanotube coated with Ni-doped polydopamine
CNT@TACu	Carbon nanotube coated with Cu-doped tannic acid
CVD	Chemical vapour deposition
e	Electrical charge of an electron
E	Electrical field
E_A	Activation energy
E_F	Fermi Level
E_g	Band-gap energy
E_v	Energy gap between Van Hove singularities
EDTA	Ethylenediaminetetraacetic acid
EDX	Energy-dispersive X-ray spectroscopy
F	Force
G	Conductance
G_0	Quantum conductance

h	Volumetric enthalpy of sublimation or Planck constant
H	Specific enthalpy of sublimation
HIM-SIMS	Helium ion microscopy-secondary ion mass spectroscopy
I	Current intensity, intensity
J	Current density
l, L	Length
m	Mass
MFT	Mean free time to failure
MWCNT	Multi-walled carbon nanotube
N_{chan}	Number of conduction channels
P	Power or pressure
PEG	Polyethylene glycol
Pda	Polydopamine
PdaCu	Cu-doped polydopamine
PdaFe	Fe-doped polydopamine
PdaNi	Ni-doped polydopamine
PTFE	Polytetrafluoroethylene
q	Electrical charge
v_d	Drift velocity
v_e	Electron velocity
V	Volume
V_p	Particle Volume fraction
r	Radius
R	Resistance
R_s	Sheet resistance
S	Surface of vaporization
SCE	Standard calomel electrode
SEM	Scanning electron microscopy
SPS	Bis(3-sulfopropyl)-disulfide
STEM	Scanning transmission electron microscopy
SWCNT	Single-walled carbon nanotube
t	Thickness
T	Temperature
$\overrightarrow{T}$	Translational vector
TA	Tannic acid
TACu	Cu-doped tannic acid

T_n	Transmission coefficient
TCR	Temperature coefficient of resistance
TRL	Technology readiness level
LSP	Lightning strike protection
XPS	X-ray photoelectron spectroscopy
α	Temperature coefficient of resistance
β	Volume percentage
γ	Density
γ_{LV}	Liquid-vapor surface tension
δ	Graphene inter-layer distance
ϵ	Energy
θ	Contact angle or porosity parameter
κ	Thermal conductivity
λ	Area density
λ_0	Mean free path
μ	Electron mobility
ν	Sound velocity
ρ	Resistivity
ρ_R	Residual resistivity
ρ_T	Temperature dependent resistivity
σ	Conductivity
τ	Time or scattering time
Ω	Frequency

Contents

Introduction

In their early times, aircrafts were mostly composed of metals with good conductivity/density ratio (such as aluminum and titanium). These aircrafts were rarely prone to accidents due to lightning strikes because the current could flow through the airplane without hazardous damaging. In fact, the first accident caused by lightning happened in 1954 when a Boeing 707 crashed (Pan Am flight 214), killing its 81 occupants. After 11 years of investigation, it was concluded that lightning had ignited the fuel vapors, causing an explosion in the left wing. This raised much attention and triggered the improvement of the fuel tank features and, more generally, the development of lightning strike protections (LSP) in aircrafts.[a] Today, the Airbus A350 and the Boeing 787 are composed of about 50% of composite materials, saving a significant amount of fuel but raising the need for effective LSP.

As LSP, foils or meshes of metals (Al, Cu, ...) are strategically integrated in the outer-skin of the aircraft. The metallic meshes are usually a compromise between the mass and the conductance. In this regard, aluminum performs better than copper as its resistivity/density ratio is 7.23 Ω.g.cm^{-2} (vs 15.14 Ω.g.cm^{-2} for copper). Yet, aluminum is more easily corroded than copper, leading to a faster degradation of the aluminum based LSP. In this case, copper can be used preferably.[1] Always aiming to reduce the mass of the airplanes, alternatives to the use of pure metals in LSP are researched.

With the emergence of carbon nanotubes (CNT) in 1991,[2] metal-CNT composites began to be investigated and, in particular, the Cu-CNT composite was identified in 2013 as a promising candidate for LSP. Indeed, taking advantage of the outstanding properties of CNT, the composite has a conductivity that is similar to copper at room temperature and can withstand great current density (10^6 and 10^8 A.cm^{-2} for Cu and Cu-CNT composite, respectively), enabling a significant reduction of material to carry the same amount of current. Combined to its low density in comparison to pure copper (8.96 and 5.2 g.cm^{-3} for Cu and Cu-CNT composite, respectively),[3] the composite could greatly reduce the mass of the LSP.

However, the understanding of CNT is not mature and the research on Cu-CNT composites is still juvenile, demanding extensive efforts to grasp the physical mechanisms enabling such synergy between CNT and copper. In addition, great challenges remain for the fabrication of Cu-CNT composites. This thesis addresses several of these challenges, bringing more insight to the under-

---

[a] "Lessons Learned from Civil Aviation Accidents: Pan Am Flight 214 at Elkton, Maryland–Resulting Safety Initiatives". FAA Lessons Learned. Federal Aviation Administration. Retrieved in August 2021.

standing of Cu-CNT materials. In particular, we investigate for the first time (to the best of our knowledge) the resistance of Cu-CNT composites to lightning strikes. After a first background section explaining the main theoretical concepts, this work will be organized as follows:

- **Chapter 1** will address the challenges associated to the fabrication of Cu-CNT composites. We show a novel method that outperforms the state of the art, opening routes to further studies with higher TRL and potential industrial applications (this thesis being made in collaboration with Circuit Foil). In particular, we highlight the benefits of using a copper-doped dopamine coating on the CNT for the fabrication of the composite by electroplating.

- **Chapter 2** focuses on the characterization of CNT that are integrated into the composite. The properties of CNT are versatile and their baseline characterization is necessary prior to their integration into the composite. We investigated the effect of the CNT coating on the CNT electrical properties. The electrical properties of the CNT are tuned by reducing the coating of CNT and by using a CNT annealing post-treatment.

- In **chapter 3**, we characterize the electrical properties of Cu-CNT composites with different features. In particular, we measure their resistivity, temperature coefficient of resistivity, and the maximum current density that they can withstand (ampacity). Also characterizing Ni-CNT composites, we propose the use of nickel as a functional interface between the copper matrix and the CNT network to enhance the electrical properties of the composites.

- In **chapter 4**, we investigate the performances of Cu-CNT composites when used as lightning strike protection. Lightning strikes on Cu-CNT composites were mimicked in collaboration with the French Aerospace Research Center (ONERA). Our composites seem to respond better to the extreme conditions generated by lightning strike than when characterized by standard electrical means in our lab. In particular, we show that several Cu-CNT composites with specific features are particularly resistant to lightning strikes.

Background

RESISTIVITY

Here, we remind the basic principles of the resistivity as it is an important concept for this work. An electrical current is a stream of charge carrier q, moving through space, and is measured in ampere (coulomb per second). When an electric field E is applied to the charge carrier q, it generates a force $F = qE$ which imposes a drift motion to the carrier. A general definition of the current density (A.m^{-2}) is given by

$$J = nqv_d \tag{1}$$

where n is the carrier density, q is the carrier charge, and v_d is the drift velocity. The resistivity can be defined as

$$\rho = \frac{E}{J} \tag{2}$$

which reflects the ease for an electric field to induces a current density J. Considering electrons as charge carriers, we have

$$\frac{1}{\rho} = \sigma = ne\frac{v_d}{E} = ne\mu \tag{3}$$

The conductivity σ of a material depends on the density of electrons and their mobility μ. The mobility describes the ease for an electric field to trigger the electron drift motion. It is linked to the electron scattering time (τ) and to the electron mean free path (λ_0) by

$$\mu = \frac{e\tau}{m_e} \qquad\qquad \tau = \frac{\lambda_0}{\nu_e} \tag{4}$$

where m_e is the effective mass of electrons and ν_e is the velocity of electrons. To understand how vary the conductivity in different materials, we need to understand what affects the density of carrier n and the mobility μ in equation 3. The material band schemes are useful to understand how vary the carrier density n. The valence band is defined as the last band occupied by electrons while the conduction band is the first energy band which is not fully occupied by electrons. Completely filled bands or completely emptied bands do not contribute to the current conduction. In order to contribute to the current, electrons must feature an energy level located in the conduction band. In insulators, the valence band and the conduction band are separated by a band gap that is so large (e.g E_g= 5.4 eV for diamond)[4] that electrons have a very low probability to move from the valence band to the conduction band. This probability is given by the Fermi-Dirac distribution

$$f(\epsilon) = \frac{1}{e^{(\epsilon - E_F)/k_B T} + 1} \tag{5}$$

Where ϵ is the energy, E_F is the Fermi level, k_B is the Boltzmann constant, and T is the temperature. In insulators, E_F is situated at the center of the band gap so $(\epsilon - E_F) = \frac{E_g}{2}$. Thus for an insulator as diamond, the probability for an electron to be excited in the conduction band would be 10^{-47} at room temperature ($k_B T \approx$ 0.025 eV). The density of electron that can contribute to the current is thus very low, leading to a high resistivity (10^{16} Ω.cm).[5]

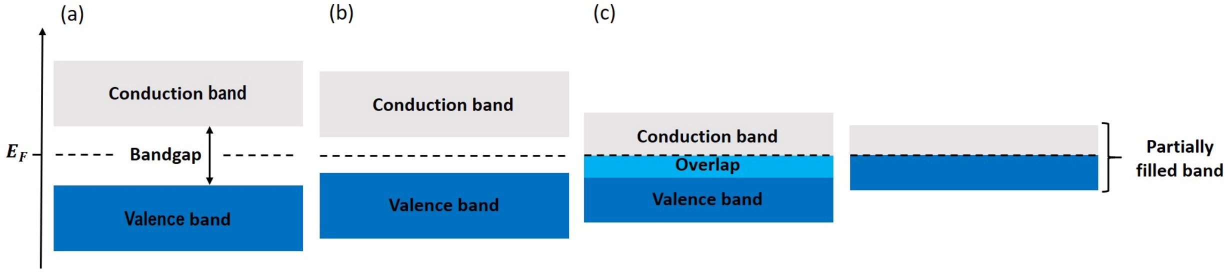

Figure 1. Example of energy-band diagrams of (a) an insulator, (b) an intrinsic semiconductor, and (c) metal with overlapping bands (left) or a partially filled band (right).

In intrinsic semiconductors (as pure Si), the forbidden band gap is narrower than in insulators (E_g = 1.17 eV),[4] and the probability to excite an electron is higher (ρ = 2.3 × 10^5 Ω.cm).[6] The conductivity of semi-conductors usually increases with the temperature as more electrons can be excited in the conduction band. Metals are good conductors (resistivity around 10^{-8} Ω.m) because either the valence band overlaps the conduction band or the Fermi level is directly situated in the conduction band. In both cases, a large density of electrons, near the Fermi level, contributes to the electric current.

The resistance to movement of electrons comes mainly from their scattering by static defects (impurities, vacancies, grain boundaries,...) and by dynamic perturbations (lattice vibrations). The total mobility of electrons is then given by the sum of the respective contributions that are related to scattering mechanisms.

$$\mu = \sum_i \mu_i \tag{6}$$

where μ_i represent contribution of one scattering mechanism. The resistivity is usually described by the Matthiessen's rule[7]

$$\rho = \rho_R + \rho_T \tag{7}$$

Where ρ_R is the residual resistivity which is related to the static defects (nearly temperature independent), and ρ_T represents the contribution of the lattice vibration (temperature dependent). In most metals (except at very low temperature), the phonon concentration increases with T leading to $\mu \propto \tau \propto T^{-1}$. n being nearly independent of T in metals, we have $\rho \propto T$ and the variation of resistivity with temperature can be approximated by a linear relation[7]

$$\rho(T) = \rho_0(1 + \alpha(T - T_0)) \tag{8}$$

where α is the temperature coefficient of resistance (TCR) and ρ_0 is the resistivity at T_0. The TCR is an important constant that will be extensively investigated in the context of this PhD work.

AMPACITY

The term ampacity (also called current carrying capacity) comes from the combination of "ampere" and "capacity". It is the maximum amount of current density that a conductor can withstand without failure. Ampacity calculation is an old but still challenging problem.[8] In 1957, Neher and McGrath[9] provided a model to evaluate the ampacity of electrical systems which is still used nowadays in the National Electric Codes (NFPA 70) in United States.[10] This model can be summarized by the Neher and McGrath equation[9]

$$I_{max} = \sqrt{\frac{T_c - (T_a + \Delta T_i)}{R(1 + Y_c)R'_{ca}}} \tag{9}$$

where I_{max} is the maximum current, T_a is the ambient temperature (where the heat is dissipated), T_c is the maximum allowed temperature of the conductor (operating temperature), ΔT_i represents all external heat source interferences, R is the resistance of the conductor (Ω), R'_{ca} is the effective thermal resistance between the conductor and its environment (K.W^{-1}), and Y_c is a factor to take in account in case of an alternating current. This equation is no more than the development (in its abbreviated form) of the following equation

$$T_c - T_a = \Delta T_c + \Delta T_i \tag{10}$$

where ΔT_c is the temperature change (of the conductor) due to the Joule heating

$$\Delta T_c = RI^2(1 + Y_c)R'_{ca} \tag{11}$$

The ampacity of a conductor can thus be described practically as the maximum current that a conductor can withstand so that the heat generated by Joule heating (ΔT_C) and by any interference (ΔT_i) does not increase its temperature beyond its operating temperature T_c. The maximum operating temperature has to be defined considering the application. For example, temperature affects the micro-structure of metals, and hence their mechanical properties. For electrical lines submitted to high mechanical stress, the maximum operating temperature could be defined in accordance

	Copper	Nickel	Ni-Cu(55%)	CNT
Resistivity ($\times$ 10^{-8} Ω.m)	1.69[12]	6.9[12]	49-52[12]	Fig. 13a
TCR ($\times 10^{-3}$ K^{-1})	3.69-4.09[13]	6.8[12]	$\pm$0.02[12]	Fig. 13b
Melting point (K)	1356[12]	1728[12]	$\approx$ 1422[14]	2600-4800[15]
Thermal Conductivity (W.[m.K]$^{-1}$)	397[12]	88.5[12]	19.5[12]	20-6000[16,17]
Specific heat (J.[kg.K]$^{-1}$)	386[12]	452[12]	421[12]	$\approx$400[16]
Density (g.cm^{-3})	8.96[12]	8.9[12]	8.88[12]	0.37-4.3[18,19]

Table 1. Material constants of interest for Cu, Ni, Ni-Cu alloy, and carbon nanotubes.

to this parameter. Alternatively, one could take only into account the melting temperature of the conductor. For micro-electronic applications, the operating temperature could be determined by the failure of the conducting lines by electromigration (migration of the conductor atoms in the same direction than the electron flow), which is drastically impacted by the temperature of the conductor.[11] Therefore, ampacity must not be treated like a material constant, like it is sometimes the case in the literature, but like a complex problem which requires to clearly identify the failure mechanism in order to determine the corresponding operating temperature. A striking example is the material chart (Fig. 2a) in the work of Subramaniam et al.[3] where the ampacity of various materials are summarized as material constants all along with their resistivity. As we will discuss in chapter 3, the ampacity values referenced in this chart are obviously obtained via different methodologies (presence of a heat sink or not, specific atmosphere, ...), and as a consequence, make impossible a quantitative comparison between the ampacity of the different materials.

As we saw, the ampacity of a material is proportional to its resistance (and thus also its resistivity) according to the Joule heating relation.

$$P = RI^2 = \rho I^2 \frac{L}{A} \tag{12}$$

where P is the dissipated power, L is the conductor length and A is its cross-sectional area. Considering that the resistivity varies with temperature, it is important to take into account the TCR of the material. In addition, the temperature reached in the conductor depends on other constants as its thermal conductivity and specific heat. Considering a failure by melting, we can also consider the melting point of the material as its physical limit of ampacity. Thus, a material can have its ampacity intrinsically increased by high electrical conductivity, thermal conductivity, specific heat, and melting point. For several applications where the mass of the conductor is the parameter of interest, as it is in our case, the specific ampacity should be taken into account (ampacity divided by the density). Constants of interest for this work are reported in Table 1. Copper has the highest ampacity among the metals in Fig. 2a considering its high electrical conductivity, thermal conductivity, and low TCR. CNT can even have a higher ampacity, electrical and thermal conductivity, with a low density and a TCR that can be negative. Therefore, it should be possible to engineer a Cu-CNT composite with a significantly higher specific ampacity than copper, in particular at the high temperatures induced by a lightning strike.

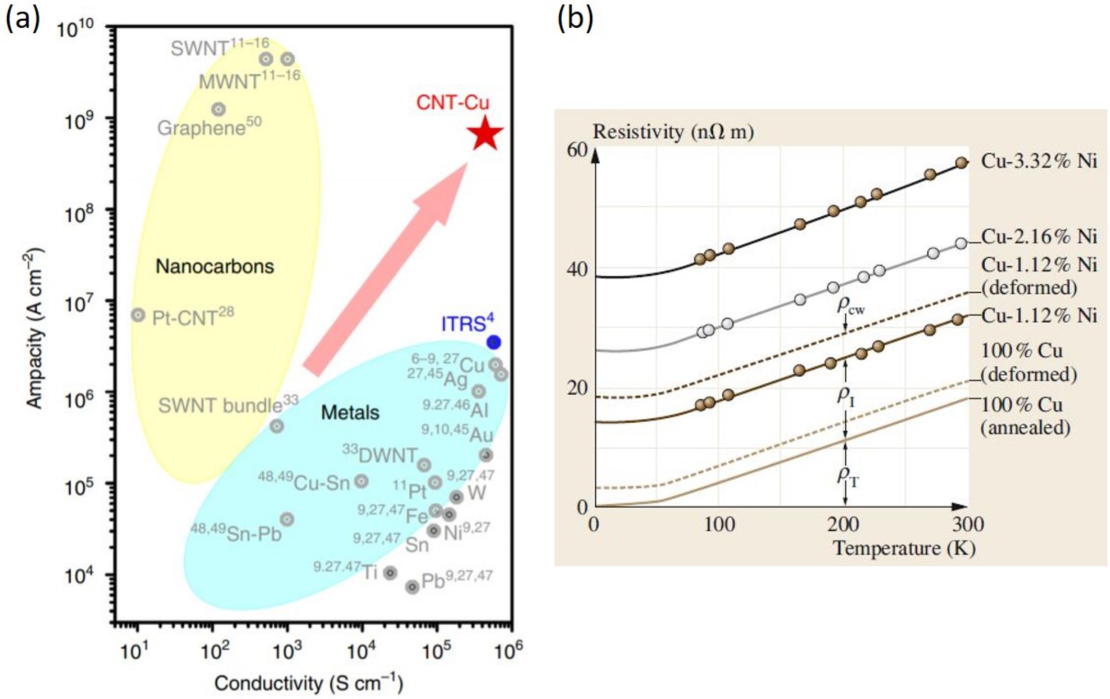

Figure 2. (a) Materials chart of ampacity and conductivity.[3] (b) Resistivity against temperature of cold worked and annealed copper with various amount of contained Ni. ρ_T represent the contribution of lattice vibration, ρ_I represents the residual resistivity due to impurities, and ρ_{cw} represents the residual resistivity due to scattering with mechanically created lattice defects (dislocations, ...).[7]

Alloying Cu with Ni has a devastating effect on the transport properties (Table 1 and Fig. 2b). This is the illustration of the electron scattering by impurities resulting in an increased residual resistivity. Hence, a special care should also be given when attempting to fabricate efficient composites based on Cu-Ni-CNT systems (discussed in chapter 3). In addition, the TCR of such alloy is surprisingly low in comparison to pure Cu and Ni, which is something to keep in mind while measuring the TCR of Cu-Ni-CNT systems.

Increased energy of activation of electromigration is believed to be one possible explanation for the high ampacity of Cu-CNT composites.[3] Electromigration[11] can be described as the diffusion of the conductor atoms due to the force generated by the transfer of momentum from the electron "wind" to the lattice atoms. The electromigration occurs in the same direction than the electron flow until the formation of a depleted region that ultimately leads to the failure of the interconnect. In order to start the diffusion, the electron wind must transfer a threshold energy to lattice atoms that is higher than the activation energy E_A associated to one of the migration mechanisms. There are mainly three diffusion mechanisms: diffusion along the grain boundaries, along the surface, and through the crystal lattice. E_A differs from material to material as seen in Fig. 3.2, leading to a preferential migration along the path with the lowest E_A. E.g. a mechanism of diffusion along grain boundaries is based on Frenkel pair creation (an atom of the lattice move into an interstice leaving a vacancy site). In this case, E_A is low and results from the sum of the energy of the Frenkel pair formation (Fig. 3.4) and the energy of migration of atoms, moving via interstitial sites or vacancy sites (the migration via both types of sites having a similar energy).[20] To reduce the electromigration, it is possible to play on certain parameters (material micro-structure, coating of the conductor, doping, ...). E.g. a bamboo like micro-structure would mitigate the electromigration along the grain boundaries (Fig. 3.3, second image).

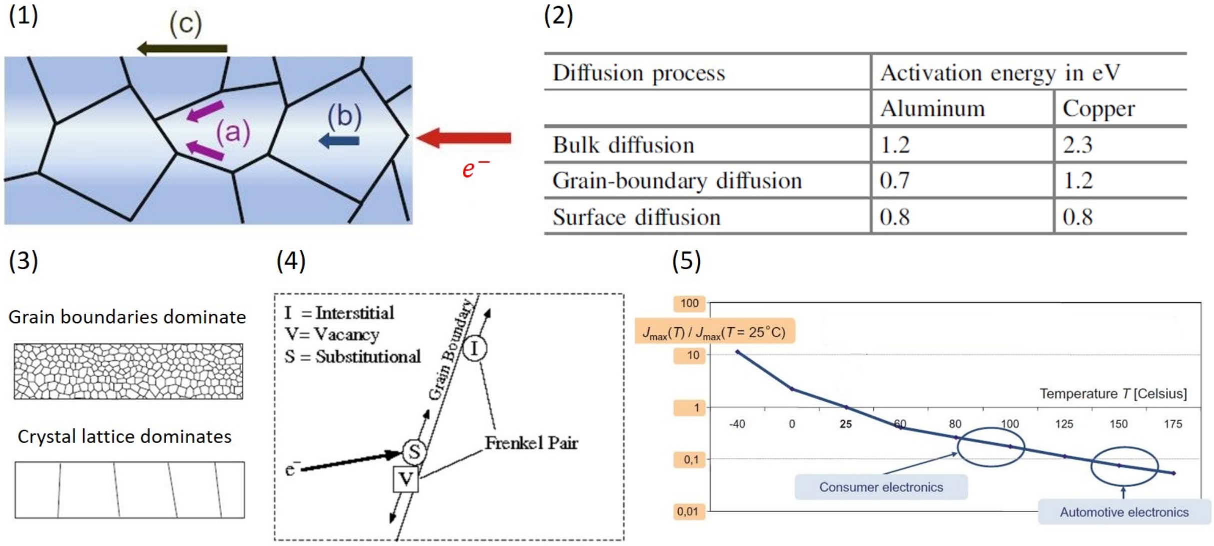

Diffusion process	Activation energy in eV	
	Aluminum	Copper
Bulk diffusion	1.2	2.3
Grain-boundary diffusion	0.7	1.2
Surface diffusion	0.8	0.8

Figure 3. (1) Illustration of the different electromigration diffusion processes (a) by grain boundary diffusion, (b) by bulk diffusion, and (c) by surface diffusion. (2) Table of the energies of activation for copper and aluminum. (3) Grain boundaries dominated and lattice crystal dominated (bamboo like structure) electromigration. (4) Illustration of the mass transport mechanism along grain boundary. (5) Illustration of the effect of temperature on J in equation 13 in comparison to its value at 25 °C. Example for an aluminum interconnect.[11,20]

The electromigration can be quantified by the mean free time to failure (MFT) using the Black equation[11,21]

$$MFT = \frac{a}{J^n} \exp \frac{E_A}{k_B T} \tag{13}$$

where a is a constant dependent on the cross-section and n depends on the mechanism of failure. The temperature largely affects the MFT because it brings a thermal energy that is added to the energy of the electron wind. Furthermore, the temperature increases the mobility of atoms. Copper is particularly sensitive to temperature as, for a 10 K increase, J has to be halved to maintain the same MFT. This temperature dependence is illustrated for aluminum in Fig. 3.4. Hence, one have to be very careful when investigating the resistance to electromigration of a material as it depends on various parameters, but also on temperature which can be tricky to control due to the joule heating induced by the measurement itself. As we will see later, a critical look should be taken when reviewing the Cu-CNT composite ampacity reported in the literature, which sometimes attribute too easily their results to an electromigration resistance (e.g.[22,23]) without giving enough importance to their measurement conditions, and specifically to the heat exchanges with the sample environment.

CARBON NANOTUBES

A carbon nanotube (CNT) is a hexagonal network, of sp^2 bonded carbon atoms (graphene), rolled into a cylinder of a nanoscaled diameter, micrometer length, and with capped ends. CNT is a generic term that includes single-walled carbon nanotubes (SWCNT, Fig. 4a) and multi-walled carbon nanotubes (MWCNT, Fig. 4b). A MWCNT is coaxial arrangement of SWCNT having an inter-layer distance of 0.34 nm. The history of CNT begins in 1991, with S. Iijima, who first reported the observation of MWCNT,[2] and, two years later, of SWCNT.[24] Just like SWCNT can have different diameters, MWCNT can have different inner and outer diameters, leading to a large variation of density between different CNT (from 0.37 to 4.3 $g.cm^{-3}$).[18,19]

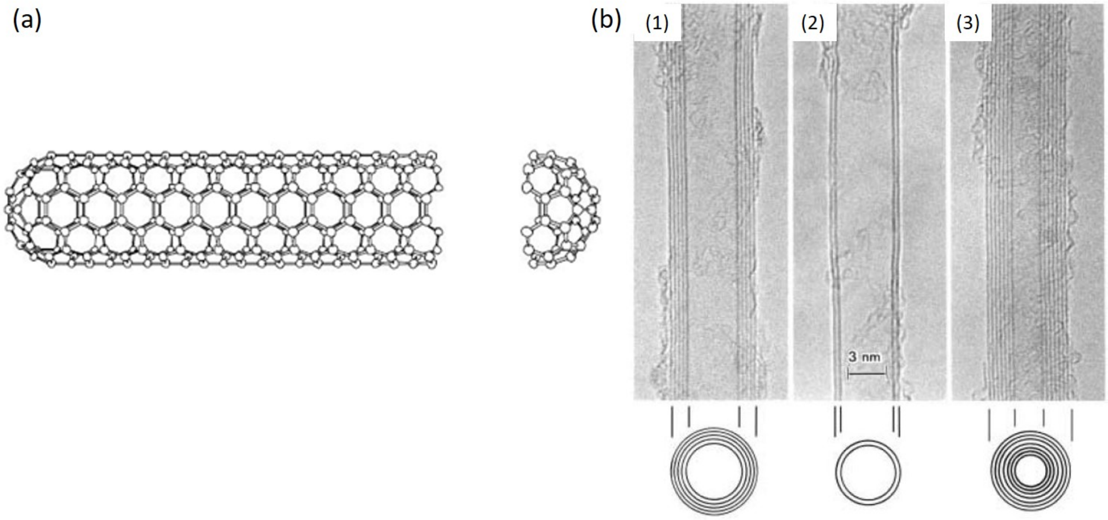

Figure 4. (a) Structure of a single-walled carbon nanotube. (b) TEM pictures of multi-walled carbon nanotubes with different outer/inner tube diameters and different number of walls (1) N=5, (2) N=2, and (3) N=7.[2,25]

Techniques of fabrication

The fabrication methods of CNT can produce very different CNT (CNT type, dimensions, purity, level of defects, ...). In the framework of an enlightened choice of the CNT used to fabricate a high quality Cu-CNT composite, the methods are briefly introduced here. There are mainly three fabrication techniques: arc discharge, laser ablation and chemical vapor deposition (Fig. 5).[26–28] Arc discharge and laser ablation methods involve the sublimation of carbon atoms by a very high temperature plasma (3000-4000 °C)[27] from a carbon solid source followed by their condensation onto the cathod (usually a graphite rod) to form either SWCNT or MWCNT. Typically, MWCNT with a length of few tens of microns and a diameter ranging from 5 to 30 nm can be obtained with few by-products (graphitic particles, ...). The obtained SWCNT are less pure than MWCNT because the process requires few atomic % of metal catalysts in the carbon source (e.g Ni and Co). Among other advantages, laser ablation generally yields to CNT with a higher quality than arc discharge. These methods allow to produce CNT at a rate of 2-6 $g.h^{-1}$,[28] and are used to obtain highly crystalline CNT with a low amount of structural defects because of the high process temperatures.

The chemical vapor deposition principle is based on the dissociation of a flowing hydrocarbon gas by heated metal catalyst particles. The dissociated carbon atoms dissolve into the catalyst, saturate and finally precipitate into tubules. The tubular form is favored over other carbon forms with higher energy (e.g graphitic sheet with open edges) as the tubules have no dangling bond. The main drawback of this method is the lesser crystallinity of the CNT because of the lower temperatures used in CVD ($600 < T < 1200$ °C). Still, this method is improving on this aspect and well crystallized CNT are also obtainable. On the other side, CVD is considered as a very interesting mass production method (up to 16 kg.h^{-1}) of high purity CNT while controlling their structure (CNT type, dimensions, ...) and architecture (growth of CNT forest, CNT patterned growth, ...). Both SWCNT and MWCNT of very large dimensions can be obtained by this method: up to 14 cm[29] in length and, in the case of MWCNT, with a diameter of about 100 nm. The CNT characteristics depend on parameters like the choice of the hydrocarbon, metal catalyst or operating temperature.[26,30]

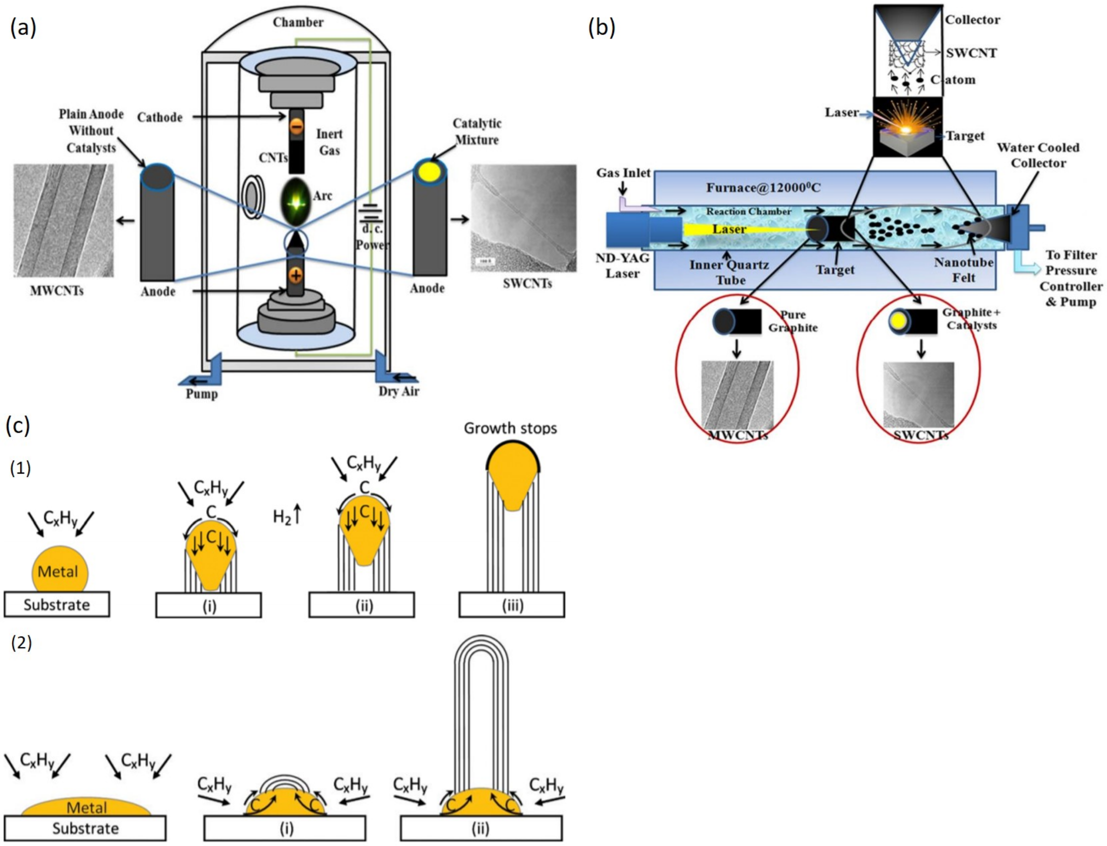

Figure 5. Schematic of the experimental setups used for CNT growth (a) arc discharge, (b) laser ablation, and (c) chemical vapor deposition with a (1) tip growth model (when the substrate-catalyst interaction is weak), (2) base growth model (when the substrate-catalyst interaction is strong).[28,30]

Electronic properties

Single-walled carbon nanotubes

The SWCNT electronic structure depends essentially on its chiral vector $\overrightarrow{C_h}$. It is used to describe how to the carbon hexagonal network is warped on itself (Fig. 6) and is given by

$$\overrightarrow{C_h} = n\overrightarrow{a_1} + m\overrightarrow{a_2} \tag{14}$$

where $\overrightarrow{a_1}$ and $\overrightarrow{a_2}$ are the unit vectors of the carbon network and (n,m) is a pair of integers. More precisely, $\overrightarrow{C_h}$ defines the relative position of two carbon atoms of the network which, when rolled onto themselves, defines the circumferential periodicity of the tube. The diameter D of the tube can be calculated from $\overrightarrow{C_h}$ by[31]

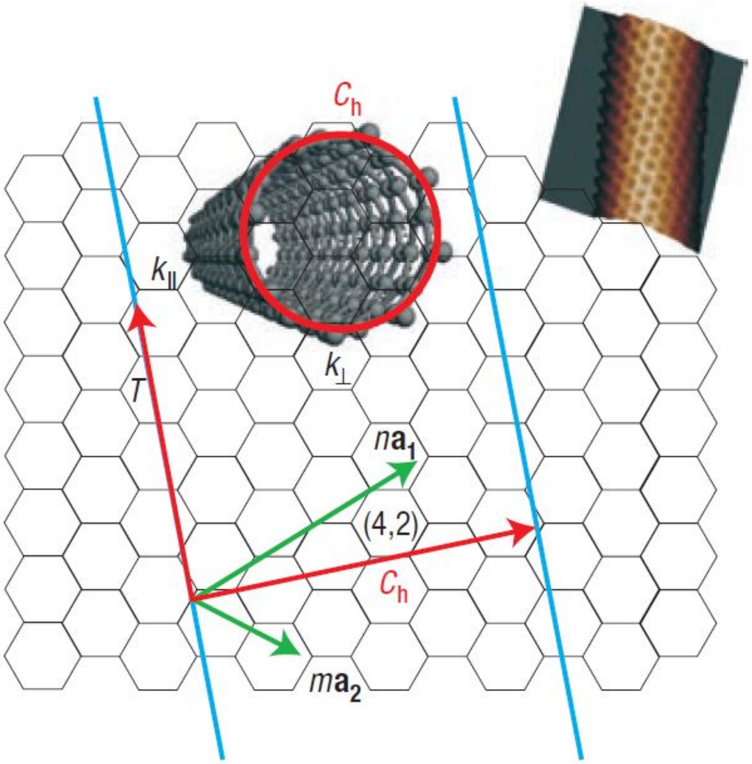

Figure 6. Chiral vector $\overrightarrow{C_h}$ and translational vector T of a (4,2) SWCNT. A scanning tunneling microscopy image of a SWCNT is also provided.[32]

$$D = L/\pi, \ L = |\overrightarrow{C_h}| = a\sqrt{n^2 + m^2 + nm} \tag{15}$$

where L is the circumference of the tube. The translational vector $\overrightarrow{T}$ is perpendicular to the chiral vector (along the main axis of the nanotube) and corresponds to the position of the first lattice point encountered (Fig. 6). The unit cell is thus defined by the chiral vector together with the translational vector and can be seen as a slice of the tube having a thickness $|\overrightarrow{T}|$. SWCNT can be either semi-conducting or semi-metallic as a function of $\overrightarrow{C_h}$. The condition for a SWCNT to be semi-metallic is that (2n+m), or equivalently (n-m), should be a multiple of 3. Specifically, armchair SWCNT (n,n) are always semi-metallic and zigzag SWCNT (n,0) are semi-metallic when n is multiple of 3 (Fig. 7a). Fig. 7b shows the different (n,m) combinations; 2/3 of the combinations lead to semi-conducting tubes while 1/3 lead to semi-metallic tubes.

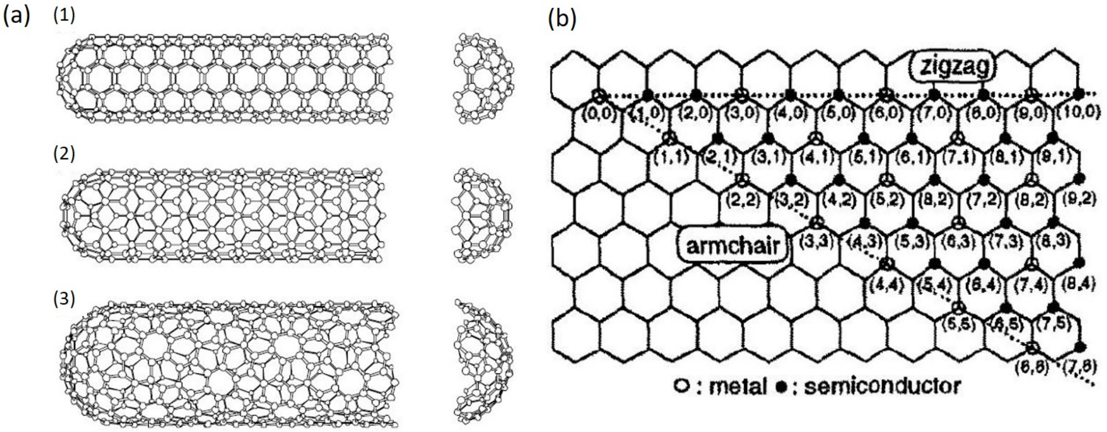

Figure 7. (a) Schematics of (1) a (5,5) armchair tube, (2) (9,0) zigzag tube, and (3) (10,5) chiral tube. (b) Conductivity map of a SWCNT as a function of its chiral vector (n,m).[25,31]

It follows that the probability for a SWCNT to be semi-metallic is 1/3. During its fabrication, it may be possible to "control" the chirality of the SWCNT by playing on many parameters (e.g. the size of the catalyst particle because it influences the CNT diameter and thus $\overrightarrow{C_h}$). However, it is a very challenging topic and extensive efforts are still required.[33] When the CNT is semi-metallic, the energy dispersion relation displays a zero band gap between the first band of conduction (π-anti bonding character) and the first valence band (π-bonding character) (Fig. 8a). Because only two energy sub-bands are available, the density of states (DOS) is constant near the Fermi level and leads to the so-called quantization of the conductance of the CNT. In contrast, semi-conducting SWCNT have a zero DOS near the Fermi level (Fig. 8b). We should point out that semi-metallic CNT are sometimes inaccurately called "metallic" in literature.

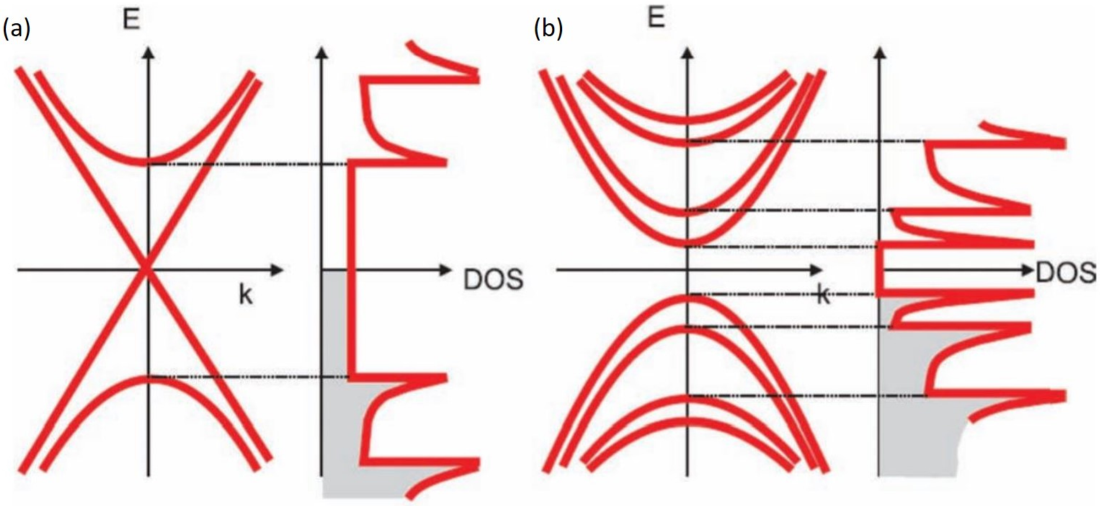

Figure 8. Schematics of the electronic energy dispersion relation and the density of state of: (a) semi-metallic (n=m) and (b) semi-conducting SWCNT ((n-m) mod 3 = ± 1).[34]

As reminded previously, the conductance of a system depends on the number of electrons able to contribute to the charge transport. Hence, it depends on the DOS of the system near the Fermi level (at low bias and temperature). In semi-metallic SWCNT, two energy sub-bands (channels of conduction) are available near the Fermi level. In a ballistic regime (electrons do not experience any scattering event), the maximum conductance of an electron in a channel of conduction is quantized by G_0, the quantum conductance.[35] The total conductance of a system with n channels of conduction is given by the Landauer-Buttiker formula[36,37]

$$G = G_0 \sum_n T_n = (2e^2/h) \sum_n T_n \tag{16}$$

where G_0 is the quantum conductance and T_n are the transmission coefficients of electrons in the conduction channels.[38] The factor 2 in the quantum conductance G_0 results from the spin degeneracy (one up, one down). In a ballistic regime, T = 1 and, in semi-metallic SWCNT, the conductance is then quantized by

$$G = 2G_0 = \frac{4e^2}{h} \approx 3.1 \times 10^{-4} S \tag{17}$$

In the case of a semi-conducting SWCNT (Fig. 8b), the DOS, and thus the conductance, is null near the Fermi level. The band gap in semi-conducting SWCNT is given by[31]

$$E_g = \frac{t a_{C-C}}{D} \tag{18}$$

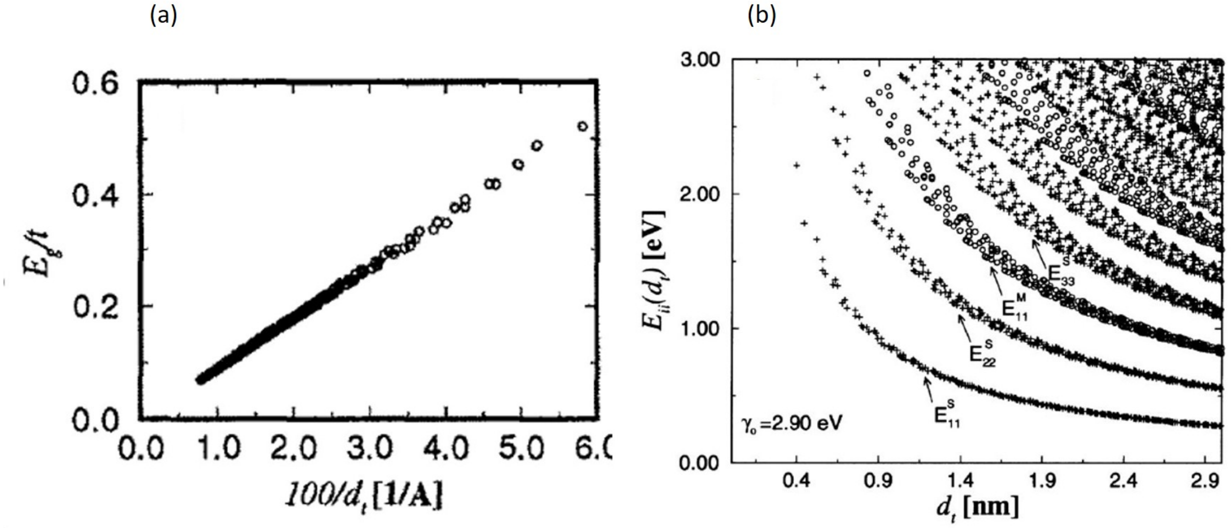

Figure 9. (1) E_g/t as function of $100/d_t$, where d_t is the semi-conducting SWCNT diameter (in Å) and t = 2.5 eV.[31] (2) Energy separations E_{ii} between the Van Hove singularities i in the 1D DOS for all the possible (n,m) values vs. the nanotube diameter in the range $0.4 < d_t < 3$ nm. Calculated using t = 2.9 eV. Semiconducting (S) and metallic (M) tubes are indicated by crosses and open circles, respectively.[39]

where t is the nearest neighbor C-C tight binding overlap energy, a_{C-C} is the nearest neighbor C-C distance on a graphene sheet (0.142 nm), and D is the diameter of the CNT. As seen on Fig. 9a, the band gap E_g exceeds the thermal energy (at room temperature) for semi-conducting SWCNT with $D \leq 14$ nm.[31] As consequence, even tubes whose $\overrightarrow{C_h}$ leads to semi-conducting feature will have available channel of conduction near the Fermi level (at room temperature) for sufficiently large diameter. However, the diameter of SWCNT does not usually exceed 6 nm[40] and this consideration will become important for MWCNT whose outer tubes can attain significantly larger dimensions. SWCNT have a DOS displaying Van Hove singularities typically observed in 1D materials. In metallic SWCNT, the energy gap between the Fermi level and those singularities is typically of the order of 1 eV.[41] This energy being larger than the thermal energy at room temperature k_BT = 0.025 eV, the conductance remains independent of the temperature (in ballistic regime) because the probability for electrons to be thermally excited in higher energy sub-bands is low.

The energy gap between the Van Hove singularities of a zigzag CNT (m,0) can be written as[42,43]

$$E_v = \pm \frac{3ta_{C-C}}{D} \mid v - \frac{2m}{3} \mid \tag{19}$$

where the plus and minus signs denote Van Hove singularities in the conduction and valence bands, respectively, and v is an integer smaller than m. For m being a multiple of 3, it exists a v for which E_v = 0 and the tube is semi-metallic. Therefore, the energy gap between the first Van Hove singularities in a semi-metallic zigzag tube is given by

$$E_v = \frac{3ta_{C-C}}{D} \tag{20}$$

which is 3 times larger than the band gap of a semiconducting tube. The energy gap between the Van Hove singularities of semi-metallic and semi-conducting tubes decreases linearly with the diameter (Fig. 9b). Using equation 20 (with t = 2.5 eV), E_v would become comparable to k_BT (at room temperature) for $D \geq$ 42.6 nm. The conductance of a semi-metallic tube is then no longer quantized to $2G_0$ and electrons are able to jump readily into higher energy sub-bands. As previously stated, the diameter of SWCNT does not usually exceeds 6 nm so, in general, the conductance of semi-metallic SWCNT is always quantized to $2G_0$ at room temperature.

Multi-walled carbon nanotubes

In this section, MWCNT electronic properties will be introduced. The measured properties that CNT display usually depend on the measurement method. Therefore, few key experiments will be described to put onto perspective several MWCNT features which are still generally debated, but also because the measurement method gives a piece of information on the best strategy to exploit the CNT exceptional properties.

As previously stated, multi-walled carbon nanotubes can be seen as set of concentric SWCNT whose the inter-layer distance is 0.34 nm. As 2/3 of SWCNT are statistically semi-conducting, a MWCNT will be statistically composed of 2/3 of semi-conducting walls and 1/3 of semi-metallic walls.[31,44] Formerly, there was no indication that MWCNT would behave like an 1D conductor, featuring ballistic transport at room temperature.[44,45] In fact, first experiments rather reported MWCNT as 2D/3D conductors[46] with quasi ballistic transport at low temperature[47] or even diffusive transport.[48] In 1998, Frank et al. evidenced for the first time a quantized conductance G_0 per MWCNT (around 14 nm diameter) and ballistic conduction over macroscopic distance ($\sim$2 μm) at room temperature (experiment described in Fig. 10a).[49] They also evidenced a reduction of the CNT conductance by the presence of localized defects. Two important pieces of information came out:

- First, a current density higher than 10^7 A.cm^{-2} was measured without any damaging of the CNT, dissipating 3 mW. If dissipated by the CNT, it would have led to a temperature of 20 000 K in the CNT. Thus, it was postulated that the power was mainly dissipated in the CNT-metal contacts; confirming the ballistic transport in the MWCNT and its importance to potentially achieve high ampacity in CNT. Still, we will see later that the power dissipation at the conductor/lead contact does not reach a consensus nowadays (see p. 22).
- Secondly, the quantization to G_0 showed that the conductance did not scale with the number of walls, featuring a current being carried principally by the last outer wall (in despite on the contact taken on the CNT ends and sides). This led to the belief that the current was mainly carried through the outer-wall in MWCNT.

A later experiment showed ballistic conduction on a larger distance in MWCNT, featuring an electron mean free path over 65 μm (in comparison to 40 nm in copper at room temperature).[50]

Compared to the perfect 2 G_0 conductance, they attributed its reduced value to the metal-CNT contact resistance (instead of the local defects).[45]

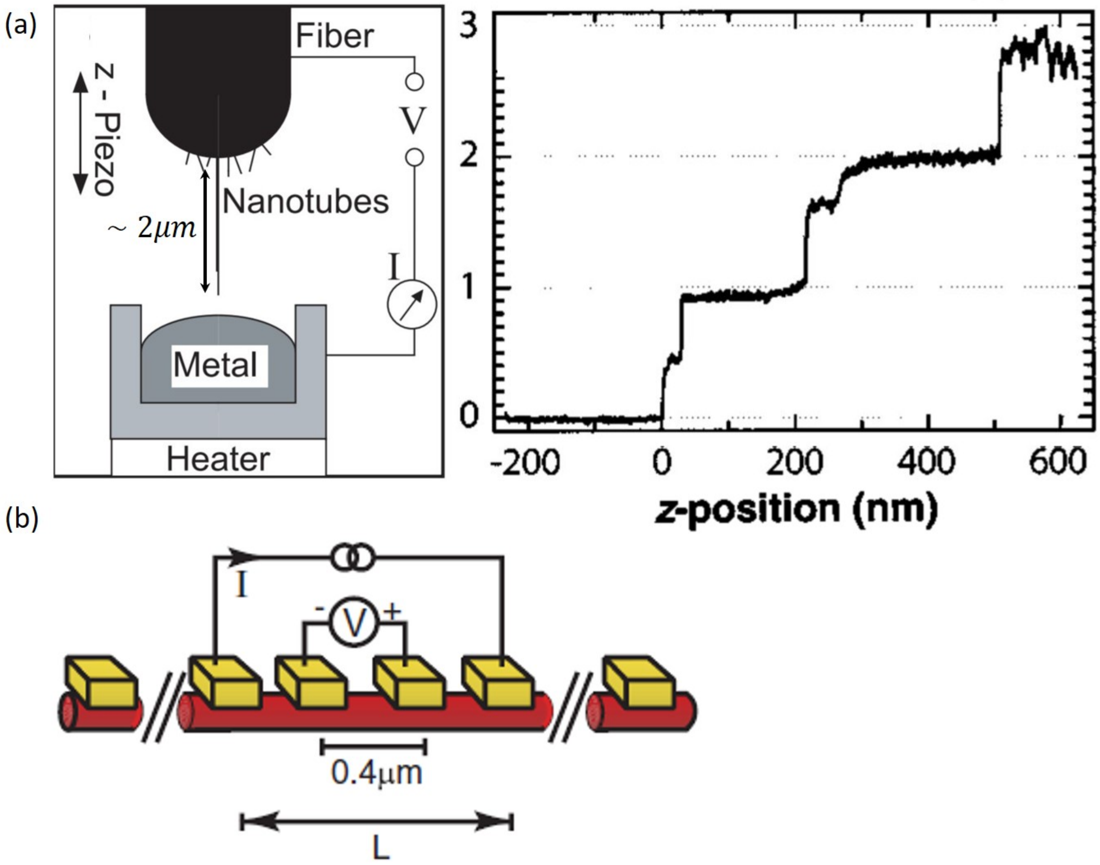

Figure 10. (a) Schematic of the setup used by Frank et al.[49] (left) Conductance of the CNT is measured by contacting the CNT with liquid metal. The tip of a CNT fiber is moved into liquid metal. (right) The conductance is measured as a function of the position of the fiber tip. Each step is attributed to the contribution of an additional MWCNT and the small sub-steps are attributed to the presence of localized defects being pushed below the metal surface. (b) Schematic of the measurement performed by Bourlon et al.[51]

Bachtold et al.[52] suggested that at most two outer-shells could conduct when a MWCNT is electrically contacted on the its sides (at $T \leq 70$ K and $D \approx 8$ nm). A similar result was reported by Bourlon et al.[51] (Fig. 10b) who observed a dependence between the inter-electrode distance and the current injection into inner shells (for arc discharged CNT, $D \approx 17$ nm). Their result suggests that the more important is the distance between the current bias electrodes, the more current is injected into the inner shells. For distance < 5 μm, the contribution of the third inner shell was calculated to be at most 10% of the total current and the radial resistivity was calculated to be ~ 1 Ω.m, which is in good agreement with an inter-shell conduction model based on electron tunneling between nearby π orbitals of the CNT shells.

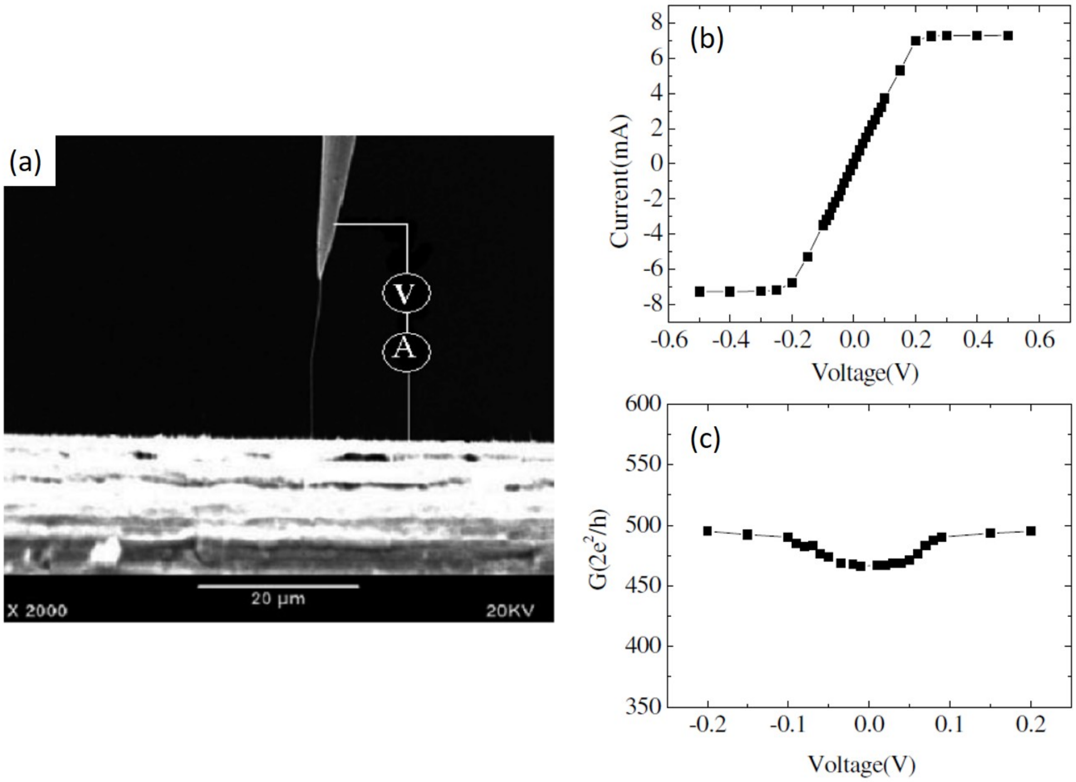

Figure 11. (a) Picture of the electrical measurement made on a single MWCNT, connected by its ends, in a SEM equipped with a movable tip, (b) Resulting I-V curve showing a current saturation around 0.2 V, and (c) the calculated conductance at room temperature.[53]

In contrast, Lee et al.[54] showed that MWCNT ($D \approx 55$ nm) whose ends are encapsulated into sputtered Nb electrodes features a good electrical contact with all the shells. One of the most exciting results was reported in 2005 by Li et al.[53] who measured the conductance of a large diameter CVD grown MWCNT (100 nm diameter, Fig. 11a). Indeed, a single MWCNT withstood a maximum density of current of 10^8 A.cm^{-2} (at 0.25 V bias, Fig. 11b), dissipating 1.82 mW. Considering a thermal conductivity of 25 W.[m.K]$^{-1}$ for a CVD grown CNT,[16] they postulated that the power was dissipated in the CNT lead contacts (CNT length $\approx$ 25 μm). Even more interestingly, they measured a conductance of 460 G_0 at zero bias and at room temperature (Fig. 11c). It showed that the MWCNT conductance is not quantized to $2G_0$ and it can conduct electrons through numerous walls in a ballistic regime. It also showed that CVD grown CNT can be more efficient than arc-discharged CNT in despite of their more defective nature. At this point, it is interesting to discuss one hypothesis usually given to explain the confinement in the outer walls of MWCNT. This hypothesis is that the second outer-wall could be semi-conducting,[49] and hence a rather insulating barrier for an electron injection into deeper walls. As we saw previously (equation 18), a semi-conducting wall stay rather insulating for $D < 14$ nm at room temperature. It conveniently fit with the low diameter of the CNT used in the experiments reporting this kind of confinement.[49,51,52] In contrast, the experiments of Lee et al.[54] and Li et al.[53] used MWCNT with $D = 55$ nm and $D = 100$ nm, respectively. We could thus deduce that the use of low diameter (thus arc discharge CNT) may have more chance to limit the conduction of the electron to the outer-walls while using large MWCNT (thus CVD grown CNT) may enable a conduction through numerous walls.

Li et al. remarked a last major feature: considering the number of walls in their MWCNT and a maximum allowed conductance of 2 G_0 per wall, the MWCNT was expected to display a maximum conductance of 148 G_0 instead of the measured 460 G_0. The conclusion was that, in large diameter MWCNT, the conductance is no longer limited to 2 G_0 per wall.

To explain this result, the joint contribution of the CNT diameter and length to the CNT conductance was further theorized by Naemi et al.[42,55] and Chiarellio et al.[56] between 2006 and 2012. The number of conduction channels in one CNT wall can be estimated using the Fermi-Dirac distribution probability as a weight for each energy sub-band to be occupied:[42,53]

$$N_{chan/shell} = \sum_{subbands} \frac{1}{\exp\left(\mid E_v \mid / K_B T\right) + 1} \tag{21}$$

By looking at the expression of E_v in equations 20 and 18 (energy gap with each sub-band), we see that $N_{chan/shell}$ is a function of ta_{C-C}/Dk_BT where increasing the temperature has exactly the same effect that increasing the diameter. This function is plotted in Fig. 12a for T=300K.

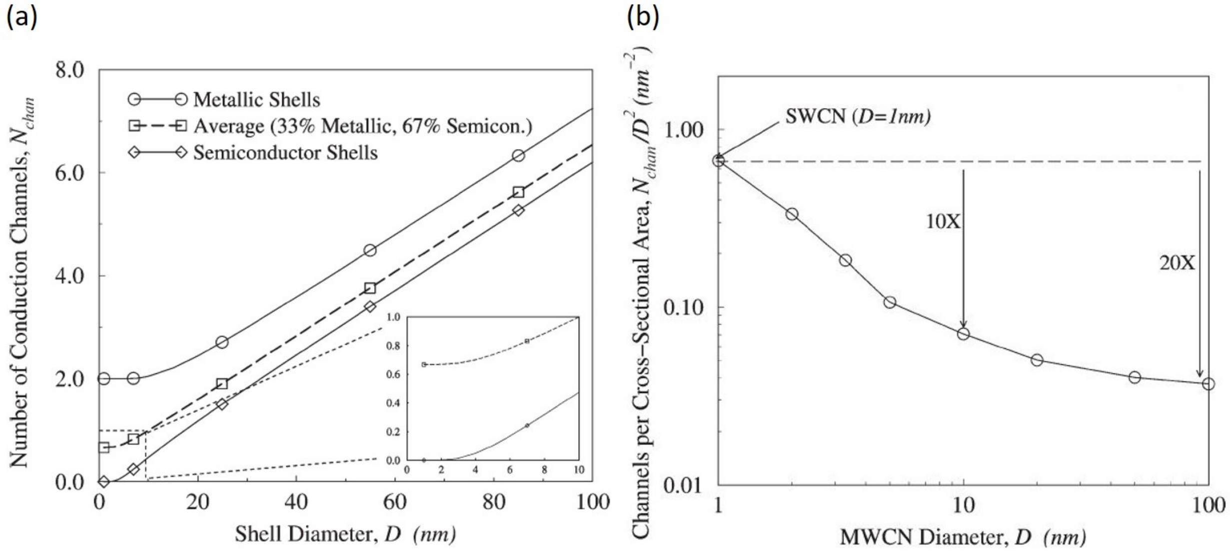

Figure 12. (a) Number of conduction channels per wall as a function of the shell diameter. The semi-conductive and semi-metallic cases are plotted as well as an average case for a wall in a MWCNT (33% metallic/66% semi-conductive). (b) Number of conduction channels normalized on the area of the wall cross-section.[42]

It can be seen that the number of channels in MWNCT can be approximated by a linear relation

$$\begin{aligned} N_{chan/shell}(D) &\approx aD + b && \text{for } D > 3\text{nm} \\ &\approx \frac{2}{3} && \text{for } D < 6\text{nm} \end{aligned} \tag{22}$$

with a = 0.0612 nm^{-1} and b = 0.425. As already discussed, each conduction channel has an ideal conductance of G_0 in a ballistic regime. To calculate the conductance of a MWCNT, the total N_{chan} of the system (sum of the contribution of all the walls) and the deviation from the ideal case (ballistic) due to diffusive conduction are accounted for. Indeed, if the CNT length (l) is larger than electron mean free path (λ_0), the conductance of a conduction channel decreases following

$$G = \frac{G_0}{1 + l/\lambda_0} \tag{23}$$

where λ_0 varies linearly with the diameter and is defined by

$$\lambda_0 = \frac{\sqrt{3}\pi t^2 D}{2var^2(\epsilon) + 9var^2(t)} \tag{24}$$

$var(t)$ and $var(\epsilon)$ being the variances of the C-C nearest neighbors binding energy t and the on-site energy ϵ.[57,58] It is possible to simplify this equation to

$$\lambda_0 = l_0 D \tag{25}$$

where $l_0 \approx 1000$ for a SWCNT having D= 1 nm (based on the measure of McEuen et al.).[38] Summing the conductance of each channel for the entire MWCNT we get

$$G_{total} = \sum_{shells} \frac{G_0 N_{chan/shell}(D)}{1 + l/l_0 D} \tag{26}$$

The conductivity of a MWCNT can then be calculated by normalizing the conductance over the cross-sectional area

$$\sigma = \frac{G_{total} l}{A} \tag{27}$$

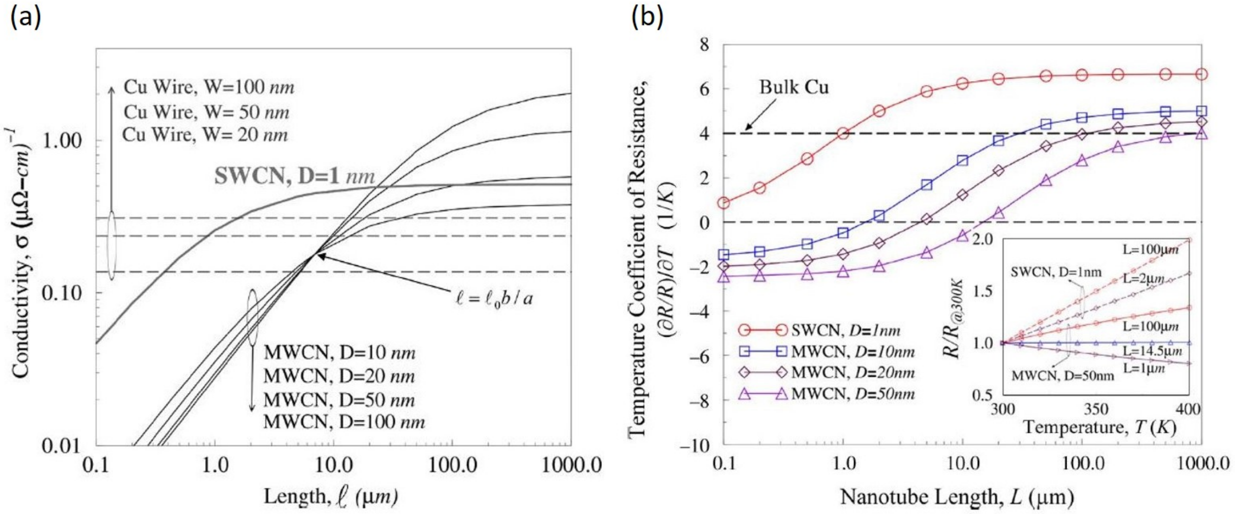

Figure 13. (a) Calculated conductivity, and (b) calculated temperature coefficient of resistance (at 350 K) of SWCNT and MWCNT of with different dimensions.[42,55]

Fig. 13a shows the calculated conductivity of MWCNT with different diameters as function of their lengths. First, lets discuss the dependence of the conductivity to the CNT length. For $l < \lambda_0$, the conductance of each conduction channel remains quantized to G_0 and the conductivity of each channel scales linearly with l (equation 27) until $l \geq \lambda_0$ where scattering mechanisms start. At this point, G is no longer quantized to G_0 (equation 23) and the conductivity reaches a plateau.

Considering the diameter of short CNT (typically less than 10 μm), the lower is the MWCNT diameter (culminating in the SWCNT case), the higher is its conductivity. It is counter-intuitive as equations 22 and 26 show (considering a ballistic regime) that the conductance of a MWCNT linearly increases with its diameter. To understand this, we need to consider the number of conduction channels normalized on the area of the CNT cross-section. By summing $N_{chan/shell}$ over all shells, equation 22 leads to

$$\begin{aligned} N_{chan}(D) &= \frac{2}{3}(1+\frac{D_{max}-D_{min}}{2\delta})(\frac{1}{2}a(D_{max}+D_{min})+b) && \text{for D>3nm} \\ &= \frac{2}{3}(1+\frac{D_{max}-D_{min}}{2\delta}) && \text{for D<6nm} \end{aligned} \tag{28}$$

where δ is the inter-layer distance and D_{min}/D_{max} is taken to 0.5 as several authors report ratio varying between 0.35 and 0.8.[44,53,59] $N_{chan}(D)/D^2$ represents the number of channels normalized over the cross-sectional area D^2 (Fig. 12b). In despite of the number of channels increasing with the diameter of the wall (Fig. 12a) (and hence its conductance), the normalized number of channels decreases, leading to a decrease of the conductivity of the wall (and hence of the MWCNT). In contrast, for MWCNT with $l > l_0 b/a$, Fig. 13a shows that MWCNT with larger diameters have a higher conductivity. This is because λ_0 scales with the shell diameter, extending the ballistic regime to higher CNT lengths (G remains quantized to G_0). In this case, the beneficial impact of σ

scaling with l (equation 27) overcomes the decrease of number of channel per cross-sectional area (scaling with D). For $l >> \lambda_0$ and $D_{min}/D_{max} = 0.5$, the conductivity can be approximated by

$$\sigma = \frac{G_0 l_0}{2\delta}(\frac{7}{24}aD + \frac{3}{8}b) \tag{29}$$

As a brief summary, the conductivity of a CNT depends highly on its dimensions which, if properly chosen, can lead to a higher conductivity than pure copper. The synthetic analysis also allows to identify the purposely targeted CNT dimensions depending on the application: e.g. long interconnects would require large diameter MWCNT and short interconnects would require SWCNT or very low diameter MWCNT. Similarly, long and large MWCNT may be required for a lightning strike application where the current is carried over long distances.

In contrast to metals that have a positive TCR, CNT have a TCR that is strongly affected by their dimensions (Fig. 13b). A large CNT diameter favors a low TCR because E_v becomes low enough to excite electrons in higher sub-bands, leading to an increase of N_{chan} with the temperature. For CNT with $l << \lambda_0$, it leads to negative TCR due to the absence of scattering event. In comparison, $l >> \lambda_0$ favors high TCR as electron/phonon scattering events multiply. Indeed, the conductivity is no longer independent of the number of thermally occupied phonons and the resistivity scales with temperature. Therefore, to maximize the CNT conductivity, its dimensions should be carefully chosen as a function of the temperature of interest and the length of the connector. The neutral CNT length L_N for which the TCR is 0 is given by

$$L_N = \frac{10^3 a T_0 D^2}{b + 2aT_0 D} \tag{30}$$

where $T_0 = 100$ K. Let us remind that models here are based on the hypothesis that CNT are perfect (neglecting defects scattering) and that all the shells are contributing to the CNT conductance. In the case of one or few outer shells contributing to the current (e.g. taking electrical contacts on the CNT sides), the conductivity would be drastically reduced while the apparent TCR would remain negative for larger length as the λ_0 in the outer shell would be higher than the average MWCNT mean free path.[42,55,60]

On the ballistic conduction in CNT

Ballistic conduction means that electrons have a very high mobility because they do not experience any scattering event generated by their interactions with static defects (impurities, vacancies, adsorbed molecules, ...) or with dynamic perturbations (like lattice vibrations). Ballistic transport in a CNT is dependent on the temperature, the magnitude of the electric field, and the number of defects in the CNT.[26,32,61] Evidences of ballistic conduction were observed in SWCNT at room temperature over a distance of about 300 nm.[62,63] Due to the 1 D feature of a CNT, small angle scattering are suppressed and only large momentum change scattering are allowed[7,32], resulting in a very low probability/absence of elastic scattering in CNT. Indeed, Ando et al.[64] reported that, due to the symmetry of the band-structure, backward scattering is forbidden in semi-metallic CNT.

Electrons scattering by static defects is generally considered as principally elastic.[65–67] For a CNT in general, and in presence of disorder, the conduction electrons would experience an effective disorder averaged on the CNT circumference so that the electron mobility would increase with the diameter of the CNT.[32,58,61,68,69] However, McEuen et al.[70] stressed that semi-conducting tubes would be far more sensitive to disorder than semi-metallic ones. Coming specifically to dynamic perturbations, ballistic transport at room temperature is only achieved thanks to the very weak electron/phonon scattering rate (at low bias). Indeed, due to their 1D feature, the carrier mobility of semi-conducting CNT exhibits a T^{-1} dependence[68,69] unlike typical semi-conductors which display a T^{-5} dependence.[71] In CNT, optical phonons have a high energy ($\hbar\Omega \approx$ 0.2 eV) and are not thermally populated at room temperature ($k_BT \approx$ 0.025 eV). Therefore electrons can only be scattered by acoustic phonons (low energy phonons). In CNT, the electron/acoustic phonon scattering rate is very small[63] because it would automatically means a large momentum change (Fig. 14a). At high bias, electrons can gain sufficient energy to emit an optical phonon (Fig. 14b) or a zone boundary phonon ($\hbar\Omega \approx$ 0.16 eV) (Fig. 14c). In this case, the electrons are scattered inelastically with a significantly lower mean free path (E.g, $\lambda_{acoustic} \approx$ 1.6 μm and $\lambda_{optical} \approx$ 10 nm in metallic SWCNT).[63] In this regime, the electrical current saturates in the CNT (e.g. Fig. 11).

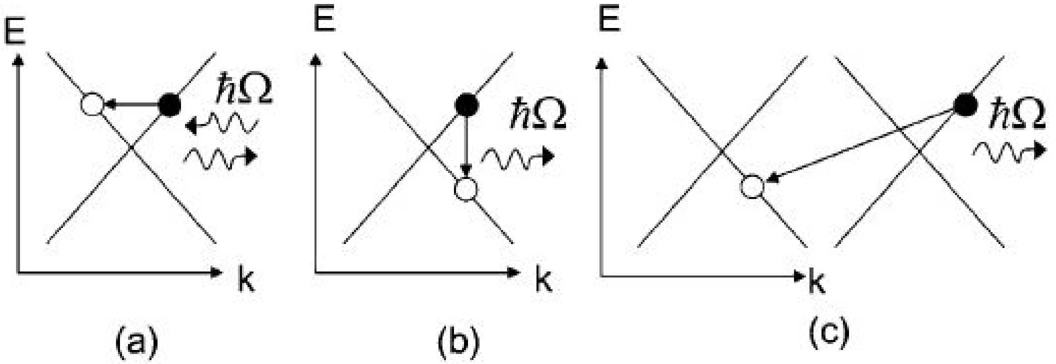

Figure 14. Schematic showing different electron-phonon scattering mechanisms (respecting both momentum and energy conservation conditions) in a metallic SWCNT. (a) Electron/acoustic phonon scattering (quasi-elastic[72]), with either absorption or emission of a phonon of small energy $\hbar\Omega$, (b) optical phonon emission with momentum conservation but energy loss, and (c) zone boundary phonon emission.[63]

Joule heating in carbon nanotubes ?

At this point, it is worth noticing that power dissipation will occur mainly through inelastic scattering with optical phonons at high bias. Inelastic scattering contributes to the joule heating, the energy being transferred from electrons to the lattice. In contrary, elastic scattering does to contribute to the joule heating as no energy exchange between the lattice and electrons occurs.[36,65,66] Finally, let us consider a semi-metallic SWCNT that is perfectly ballistic. In this case, CNT have a conductance $G = 2G_0$, so the power must be dissipated following the Joule heating law $P = GV^2$. But here is the problem: no scattering event occurs at all in a ballistic conductor. In 1987, Laudauer remarked "if energy is to be dissipated, e.g. through a conductance, where does it go ?"[73] In 1995, Datta asked the same question "where is the heat dissipated ?"[36] Most of theories propose that the energy would be dissipated in the contact resistance,[36,74] but this vision is not shared by everyone. In 2009, Das and Green state that the question remains unanswered[75] and propose an idea based on the fluctuation-dissipation theorem.[76] It seems that, to this day, a consensus on the question has not been reached.[77] Yet, as we saw in the background chapter (pp. 5-8), the ampacity of a conductor depends largely on how its internal heat is dissipated by its environment. Thus, the understanding of where and how a CNT dissipates its energy may be crucial to fabricate efficient ballistic electronic devices based on CNT.

Thermal conductivity

Thermal conductivity of CNT is briefly introduced here. The thermal transport in CNT is widely reported as dominated by phonons with values ranging from few tens[16,78] up to 6000 W.[K.m]$^{-1}$.[17] The scarcity of these values rests, as for the electronic transport, on the various possibilities of structure of CNT. More precisely, the thermal conductivity depends on the (MW)CNT chiral vector(s), its diameter, its length, and the number of defects and impurities. Indeed, thermal conductivity is dependent on the phonon mean free path λ_p following

$$\kappa \propto C_p \nu \lambda_p \tag{31}$$

where C_p is the specific heat, ν is the sound velocity in CNT ($\sim 10^4$ m.s^{-1} due to their strong C-C bonds).[16] High level of defects decreases λ_p, leading to a thermal conductivity that is lower than usually expected for CNT. For example, Yi et al.[16] (Fig. 15a) showed that CVD grown MWCNT (at 600 K) have a thermal conductivity around 25 W.[K.m]$^{-1}$ at room temperature while it raises to 2000 W.[K.m]$^{-1}$ after annealing at 3000°C (annealing at high temperature improves the crystallinity of CNT). Also, the CNT chirality has a large effect on its thermal conductivity (Fig. 15b).[79]

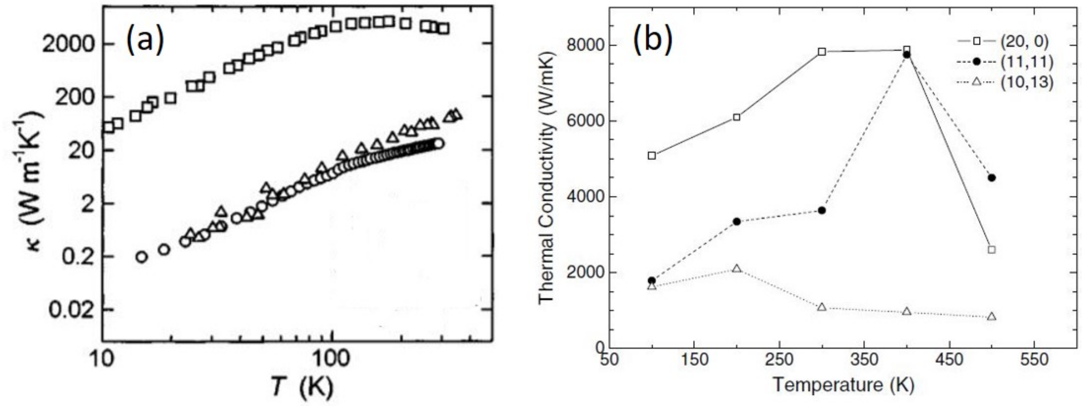

Figure 15. (a) (open circle) Thermal conductivity of a CVD grown CNT fiber (for comparison from[78]), (open triangle) fiber from as grown CNT and (open square) CNT annealed at 3000°C. (b) Thermal conductivity of CNT with three different chirality (and nearly same diameter): open triangle, open square, and filled circle correspond to (10,13), (20,0), and (11,11) CNT, respectively.[16,79]

The phonon mean-free path is expected to be around 500 nm in MWCNT (and even larger in SWCNT), and κ increases until $l \approx \lambda_p$ and reaches a plateau at larger CNT length.[17] In addition, the thermal conductivity is theoretically expected to decrease with the diameter.[80] Even if thermal conduction by electron is rarely reported for CNT (even for metallic one), Mensah et al.[81] reported theoretical value of electron thermal conductivity (in metallic CNT) as high as 11000 W.(K.m)$^{-1}$ at room temperature.

Carbon nanotubes for lightning strike protection ?

As we will see in chapter 4, LSP are mostly composed of metallic foils or meshes integrated in the outer skin of aircrafts. The lightning strikes generally at the tips/edges where the electric field is highly concentrated, propagating current as large as 200 kA and leading to high temperatures. In this context, it seems important to select the most suitable CNT to integrate into the Cu-CNT composite. Remembering that ampacity depends mostly on the balance between the Joule heating and evacuation of the heat outside the conductor (pp. 5-8), we draw the following conclusion from the previous sections. To decrease the Joule heating, we believe that MWCNT with a large diameter should be used to maximize the distance on which the electrons are carried in ballistic regime. Also, large diameter MWCNT seems more prone to promote a current conduction through numerous walls while thinner MWCNT could lead to a confinement of the current in the outer-walls. Furthermore, increasing the diameter decreases the TCR of the CNT, which may decrease drastically its resistivity at the high temperatures induced by the lightning. In this respect, the length of the MWCNT should be carefully selected to obtain a compromise between the TCR (becoming larger with the length) and the conductivity (increasing with the length). Theoretical models (Fig. 13b and equation 30) suggest that the length of a MWCNT having a diameter of 80-90 nm, as it is in our case, should not exceed 45 μm to keep a TCR ≤ 0. Beside the decrease of the joule heating, heat should be spread as quickly as possible on the LSP surface to reduce the temperature of the LSP at the impact location. Therefore, CNT with high thermal conductivity should be selected. However, we saw that, contrasting with the electrical conductivity, increasing the CNT diameter rather decreases its thermal conductivity, In addition, long and large diameter MWCNT are obtained via CVD process while CNT obtained via CVD are generally more defective than arc-discharged ones. As consequence, a special care should be given to ensure that such CNT have good thermal and electrical conductivity. However, the outstanding properties of the CNT are measured over a very small distance scale and it is difficult to extrapolate reliably their properties to a LSP system which has significantly larger dimensions.

CU-CNT COMPOSITES

Fabrication methods

A great number of routes exist for the fabrication of metal-CNT composites. Here, we give a rapid overview of few of the most common methods with a special focus on the state of the art related to the fabrication path that we selected in this thesis work.

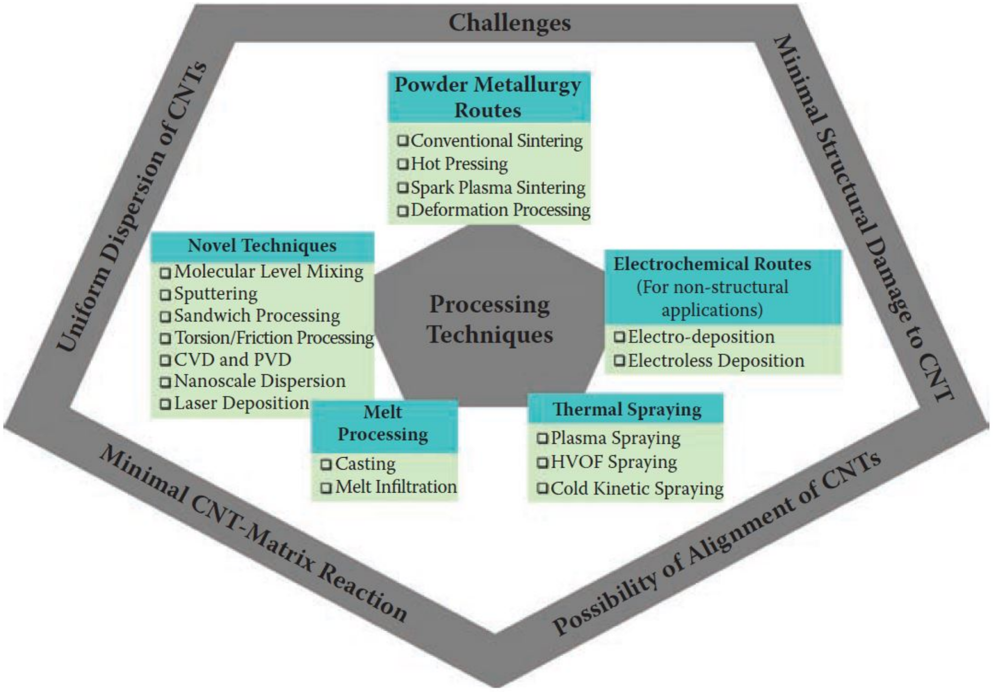

Figure 16. Diagram of the principal routes/challenges of fabrication of metal-CNT composites.[82]

The fabrication routes of metal-CNT composites are generally divided in five categories: powder metallurgy, melting and solidification, thermal spraying, electrochemical deposition (ECD), and "novel techniques" (Fig. 16).[82–85] Three features are principally researched for the fabrication of a metal-CNT composite:

- A uniform dispersion of CNT in metal to maximize the surface of interaction between CNT and metal.
- Considering the 1D feature of CNT, it is interesting to control the alignment of CNT.
- Minimization of the damage done to CNT by the fabrication process (e.g. mechanical deterioration of CNT or chemical reaction between metal and CNT). Indeed, we saw previously that the transport properties of CNT are very sensitive to the their structural integrity.

The "melting and solidification" route is based on the dispersion of CNT (or metal-CNT particles) in a molten metal. Its main advantage is the fabrication of bulk piece. However, the high temperatures needed to melt metals may lead to the degradation of CNT (reaction with oxygen, formation of metal carbide, reaction with impurities, ...), and this method is usually limited to metals having a low melting temperature (e.g. Mg, Al). In addition, CNT tend to aggregate in the molten metal due to the high surface tension between CNT and molten metal. An example of Al-CNT composite fabricated by pressure-less melt infiltration is shown in Fig. 17. Depending on several parameters (CNT wettability by the metal, ...), a threshold pressure should be applied to force the metal infiltration in the CNT preform. We give here the expression of this threshold pressure[86] as it is part of an interesting outlook of our work:

$$P_0 = \frac{6b}{D}\gamma_{LV}\cos\theta\frac{V_p}{1-V_p} \tag{32}$$

where b depends on the particle shape, D is the particle diameter, γ_{LV} is the liquid-vapor surface tension, θ is the contact angle between the CNT and the molten metal, and V_p is the particle volume fraction.

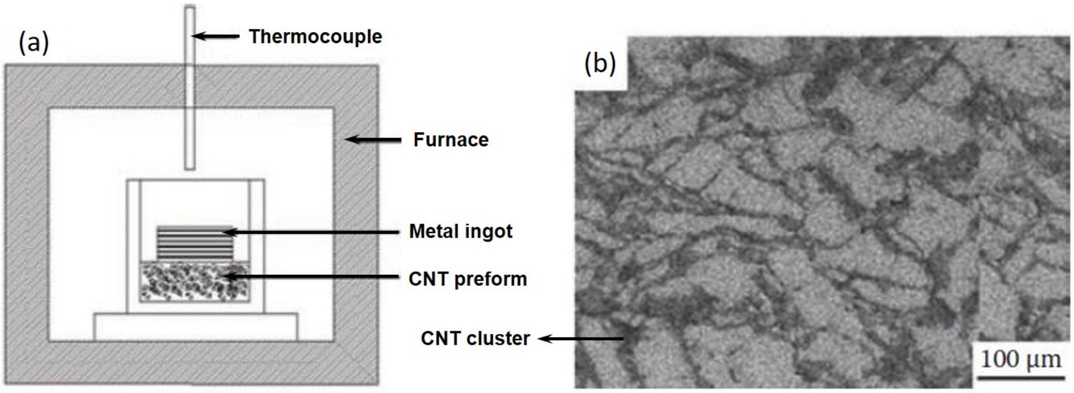

Figure 17. (a) Schematic of a pressure-less melt infiltration process: an Al ingot is melted on the top of a CNT pre-from. (b) Related micro-structure of the Al-10 vol. % CNT composite.[82].

Powder metallurgy is used for various metals (Mg, Ni, Ti, Al, Cu, ...) and is one of the most popular for the fabrication of Cu-CNT composites (Fig. 18). The method is based on the mixing of a CNT powder with a metal powder followed by a consolidation step (sintering, hot pressing, ...). Its main advantage is the fabrication of intricate shapes with virtually any composition (mix of different powder, alloys, ...). As there is no metal melting, the composite retains the main characteristics of the metal-CNT powder (e.g. the degree of dispersion of the CNT into the metal particles).

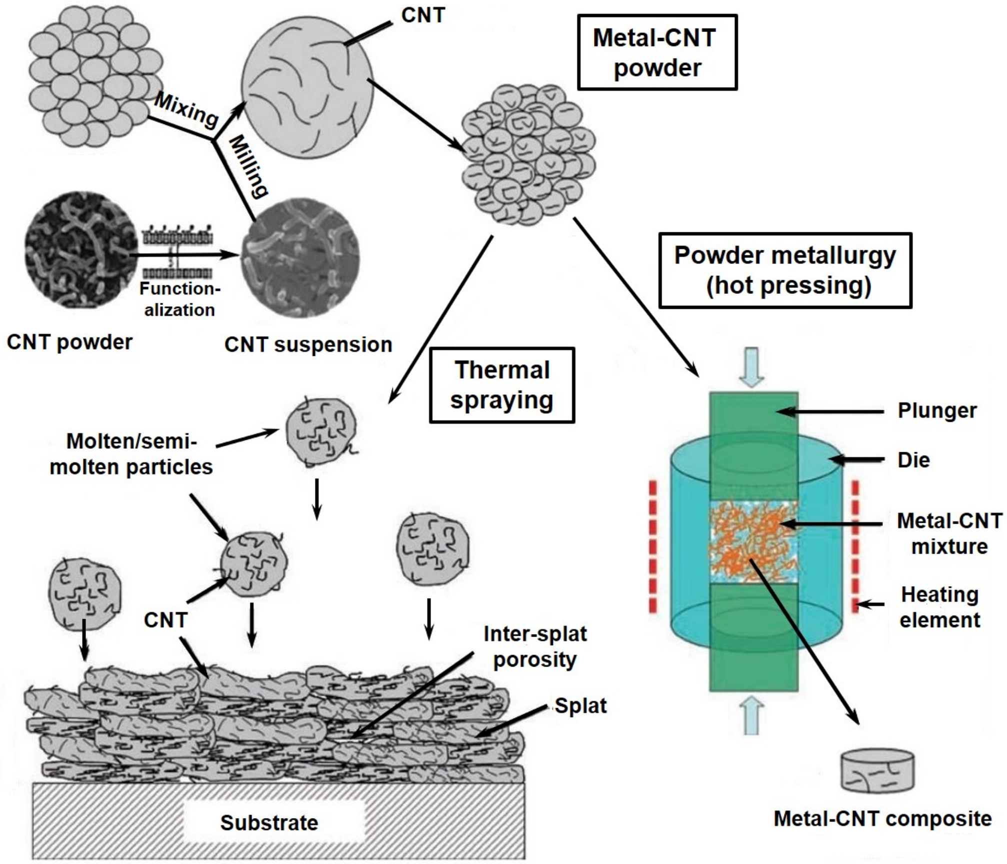

Figure 18. Schematic of the powder processing followed by powder metallurgy (hot pressing) or thermal spraying.[82,85]

The thermal spraying is based on the spraying of a molten/semi-molten CNT-metal powder using high temperature/velocity carrier gases (Ar, ...). An advantage is that the technique is already industrially scale-up for various applications (e.g. coatings or bulk materials). However, CNT can be damaged by the gases high velocity and temperature. Similarly to powder metallurgy, obtaining a good CNT dispersion in a metal matrix is based on the degree of dispersion of CNT in the sprayed powder (Fig. 18).

Metal-CNT powders are usually prepared by an extensive mechanical processing (e.g. ball milling) to obtain uniform distribution of CNT into the metal particles, but it also leads to the deformation/breaking of CNT. Here, CNT damaging minimization and CNT uniform distribution are conflicting objectives.

Electrochemical routes are used to produce thin films and coatings of metal-CNT composites (thickness < 200 μm).[82] They are non-destructive for CNT and can be sub-divided in three: electroplating on a CNT pre-form, electroless plating on CNT, and CNT/metal co-electrodeposition (Fig. 19).

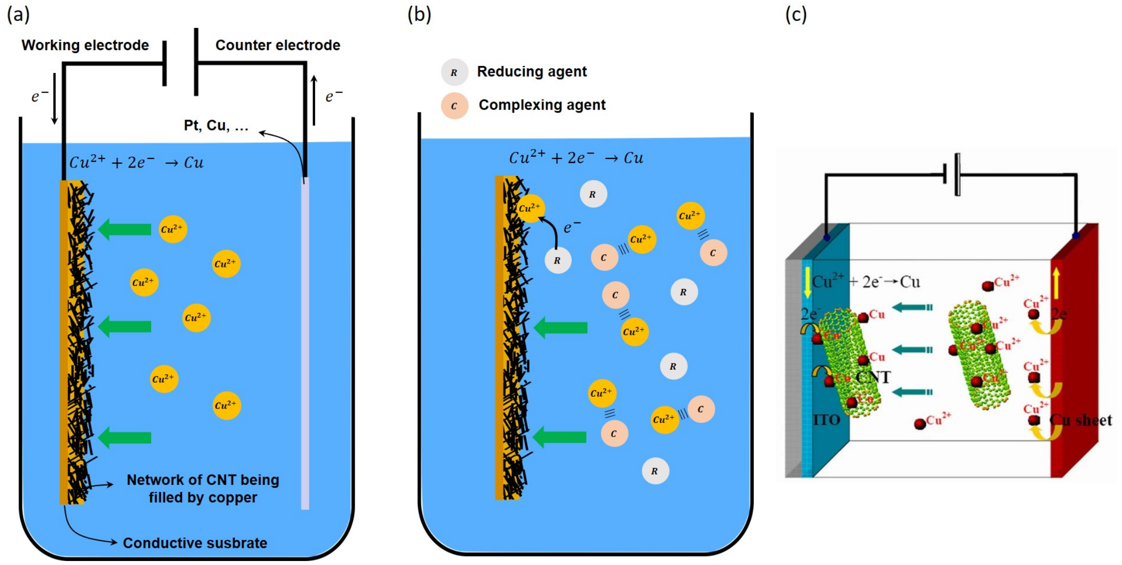

Figure 19. Schematics of (a) the electroplating of Cu in a CNT network pre-deposited on a susbtrate, (b) the electroless plating of copper in a CNT network pre-deposited on a substrate, and (c)[84] the Cu-CNT co-electrodeposition.

In the electroplating route, a CNT pre-form is immersed in the plating solution. Electrical contact is made on the CNT pre-form or on a conductive substrate to reduce the metal ions of the electrolyte solution in the CNT network. Classic aqueous plating solutions are usually constituted of copper sulphate, sulphuric acid and may contain organic additives (e.g. Bis(3-sulfopropyl)-disulfide, ethylene glycol, ...). It has several potential advantages:

- The CNT distribution in the composite depends on the CNT distribution in the CNT pre-deposit.
- A high vol. $\%$ of CNT ($> 40\%$) can be obtained while avoiding CNT clusters.
- Possibility to use CNT with large dimension.
- Possibility to control the CNT alignment (e.g. by plating directly on aligned CNT grown by CVD).

In electroless plating, CNT are dispersed in the electroless solution. The difference with electroplating is that electrons are provided by a reducing agent in the plating solution. Electroless plating is mostly used to coat CNT with metal for CNT-metal powder production and, up to now, mainly used to fabricate Ni and Co based metal-CNT composites. Compared to electroplating, electroless plating solutions contain harmful chemicals and are rather complex. For copper plating in particular: a reducing agent (e.g. dimethylamine borane) is required as electron source, a complexing agent (e.g. EDTA) is required to stabilize the metal ions at high pH (e.g. pH $\approx$ 12.5) and the temperature of the bath should be controlled (e.g. 60°C). In addition, the CNT surface should be activated to trigger the copper deposition (e.g. with Pd particles).[82–85,87,88]

In co-electrodeposition, and compared to electroplating, the CNT are dispersed in the plating solution and deposited at the same time than metal. The solutions used in co-electrodeposition are similar to the solutions used in electroplating. Most of the time, the method is based on electrostatic interactions between the deposited metal and CNT, favoring the absorption of CNT. Electrophoretic migration of CNT can also be used to increase the CNT concentration in the coating (e.g. adsorbed positive ions on the CNT surface will promote their migration towards the negatively charged working electrode, Fig. 19c). The CNT distribution in the deposit depends on the dispersion of CNT in solution. In this regard, this technique is more suited for short CNT (compared to long CNT) which are more easily dispersed in solution and absorbed in the deposit. Finally, the obtained CNT vol. % are usually lower than with electroplating.[89,90]

Electrochemical fabrication routes were mainly considered in this work. We give here the state of the art of the three routes with a special focus on electroplating which was extensively used in this thesis work.

Electroless plating remains relatively unexplored for the fabrication of Cu-CNT composites.[82–85] Cu-graphene and Cu-CNT composites are commonly obtained by electroless coating of the nanocarbons with copper followed by a sintering of the obtained powder.[91–93] A Cu-MWCNT composite was obtained via electroless plating by Arai et al. (Fig. 20 a).[94,95] The CNT were dispersed in the plating solution (using sodium dodecyl sulfate as surfactant) and the substrate (a copper plate) was activated with Pd nuclei. Because of the activation, the redox reaction occurs only on the substrate rather than on CNT. CNT are adsorbed on the substrate, and trapped in the growing copper coating. A significant increase of the amount of trapped CNT was observed (Fig. 20a) when CNT having a narrow diameter (⌀=15-20 nm) were used, in comparison to larger CNT (⌀=100-150 nm) having a similar length (L=10-15 μm). To the best of our knowledge, a successful electroless plating of copper on a CNT pre-deposit was not reported yet.

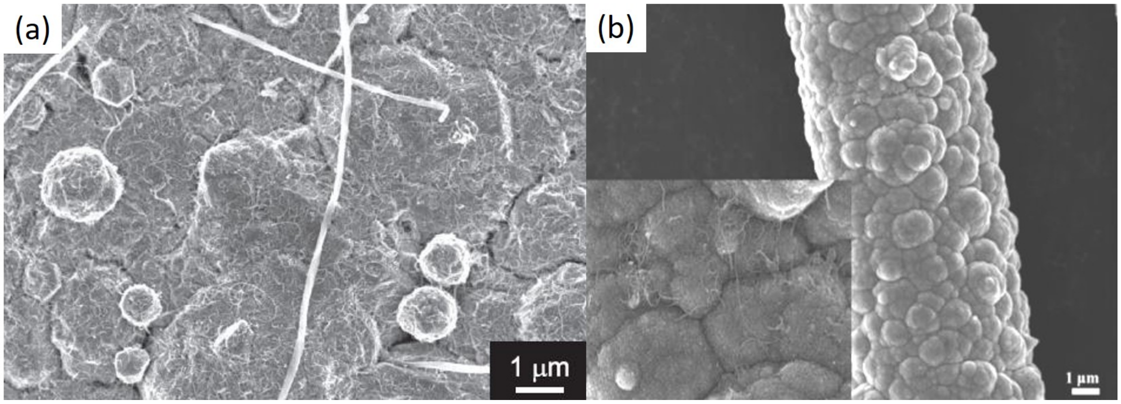

Figure 20. (a) Cu-CNT composite coating obtained by electroless plating,[95] (b) Cu-CNT composite obtained by co-deposition of Cu and CNT (functionalized with NH_2), using electrophoretic migration of CNT.[96]

Co-electrodeposition has been more often used than the electroless plating. Yang et al.[97] fabricated a Cu-CNT composite containing 0-10% vol. of SWCNT. To improve the CNT dispersion in the solution/composite, they oxidized the CNT (HNO_3 + H_2SO_4) to reduce their hydrophoby and applied ultra-sonication during 6 hours. However, long ultra-sonication is likely to damage CNT.[98] Feng et al.[99] claimed the fabrication of a Cu-CNT composite using a mix of oxidized

MWCNT and nano-diamonds in the plating solution (to improve the CNT dispersion in solution). However, it seems that CNT were very scarcely absorbed in the Cu deposit. In 2019, Yan et al.[96] used an electrophoretic migration of charged CNT (e.g. positively charged with NH_2 functional groups) towards the cathode to promote the absorption of the CNT (Fig. 20b). Alternatively, jet-electrodeposition of CNT-electrolyte having a high speed flow (1 $m.s^{-1}$), and directed onto the cathode, was used to increase the concentration of CNT around the cathode and increase their trapping.[100] Efficient absorption of a large amount of CNT in the copper deposit remains a huge challenge. Furthermore, to the best of our knowledge, no composite containing long CNT (e.g. $L \geq 200\ \mu m$) or featuring a CNT alignment was obtained via co-electrodeposition.

Electroplating is also challenging for the fabrication of Cu-CNT composite. Indeed, CNT are hydrophobic and the plating solution, which is usually aqueous, does not well penetrate inside the CNT pre-deposit (especially for dense CNT layer). In addition, CNT are intrinsically cuprophobic and the attachment of copper on CNT is not favored.[85] Therefore, it is not trivial to obtain a void-less composite. In general, electroplating rather leads to the deposition of a copper crust on the top of the CNT layer (Fig. 21a-c).[101–103]

Reducing the current density of deposition (thus the rate of deposition) can improve the degree of copper filling and increase the depth of deposition of the metal in the CNT layer. Indeed, Chen et al. reported that the CNT layer depth over which Cu is deposited was increased from 800 nm to 3.94 μm by reducing the current density from 20 to 1 $mA.cm^{-2}$.[101] However, low current density extends significantly the time of plating. In 2021, Bazbouz et al.[104] used a method of wet spinning to fabricate fibers of partially aligned MWCNT ($\varnothing \approx 8\ \mu m$). From this fiber, they managed to fabricate a highly filled metal-composite wire (40% vol. of CNT) by using periodic pulse reverse electroplating (Fig. 22a). This means that the depth of metal filling was at least 4 μm with this method.

CNT oxidization[101–103] promotes a better wetting of CNT and a higher degree of filling (Fig. 21c,d). In general, functional groups containing oxygen enhance adsorption and reduction of Cu ions onto the CNT surface.[103,105] Shuai et al.[106] by-passed this problem by plating copper on a very thin layer of aligned CNT ($\sim$ mono-layers) followed by a successive repetition of CNT layers and copper plating. In this way, they obtained a laminar composite (Fig. 22b) with a nice alignment of CNT, a high degree of copper filling, but with a low CNT vol. % (1%).

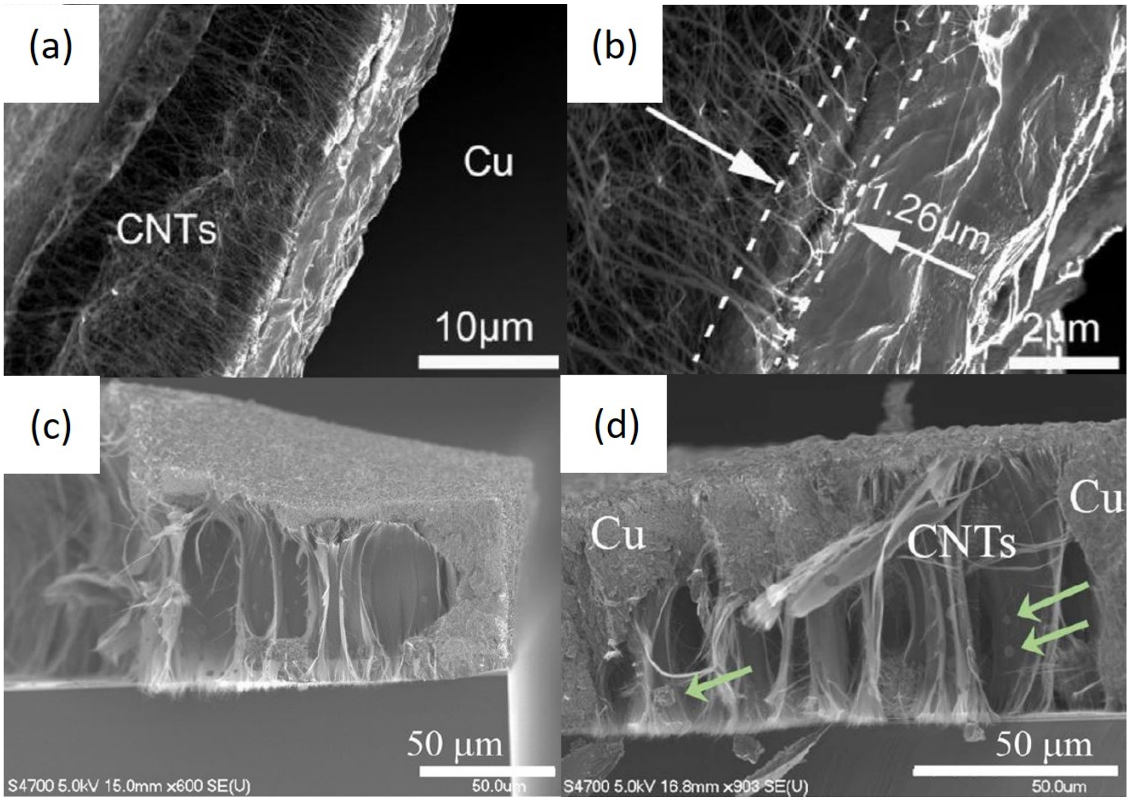

Figure 21. (a) Cu-CNT composite cross-section (from a pristine CNT buckypaper), and (b) enlarged image of the composite showing a depth of filling of 1.26 μm. Electroplating made with a DC current (10 mA.cm^{-2}) in a Cu sulphate based solution. (c) Copper capping of a vertically aligned CNT layer after electroplating (pulsed current: 2-10 mA.cm^{-2}) in a Cu sulphate solution, and (d) result obtained using the same electroplating parameters on oxidized CNT (ozone treatment - 30 min).[101,102]

The most remarkable result came from Subramaniam et al. in 2013.[3,107,108] They reported for the fist time the fabrication of a highly filled composite with 45 % of aligned SWCNT (Fig. 22d). The fabrication process is summarized in Fig. 22c. They used CVD to grow a vertically aligned SWCNT forest (500-700 μm long CNT) and, by applying a shear stress, aligned the forest horizontally. The CNT forest was densified by immersion in an organic electroplating solution (acetonitrile + copper acetate). Afterwards, a first electroplating was done to seed uniformly the CNT network with copper nuclei (DC current: 1-5 mA.cm^{-2}). A second electroplating was carried out in a copper sulphate based solution to finish the copper deposition. After each electroplating step, the composite was washed in acetonitrile and annealed at 250 °C in H_2 to remove the copper oxides. In the following years, several authors used the same method to fabricate Cu-CNT composites. Sun et al. produced Cu-CNT nano-pillar composites (vertically aligned CNT).[109] Using a dry-spun CNT fiber, Sundaram et al.[110,111] managed to fabricate a large diameter wire of Cu-CNT composite ($\varnothing$=100 μm) with a high CNT vol. % (45%), showing that this fabrication route enables the homogeneous filling of dense CNT layers over large depths (Fig. 22e) in comparison to methods using only aqueous plating solution.

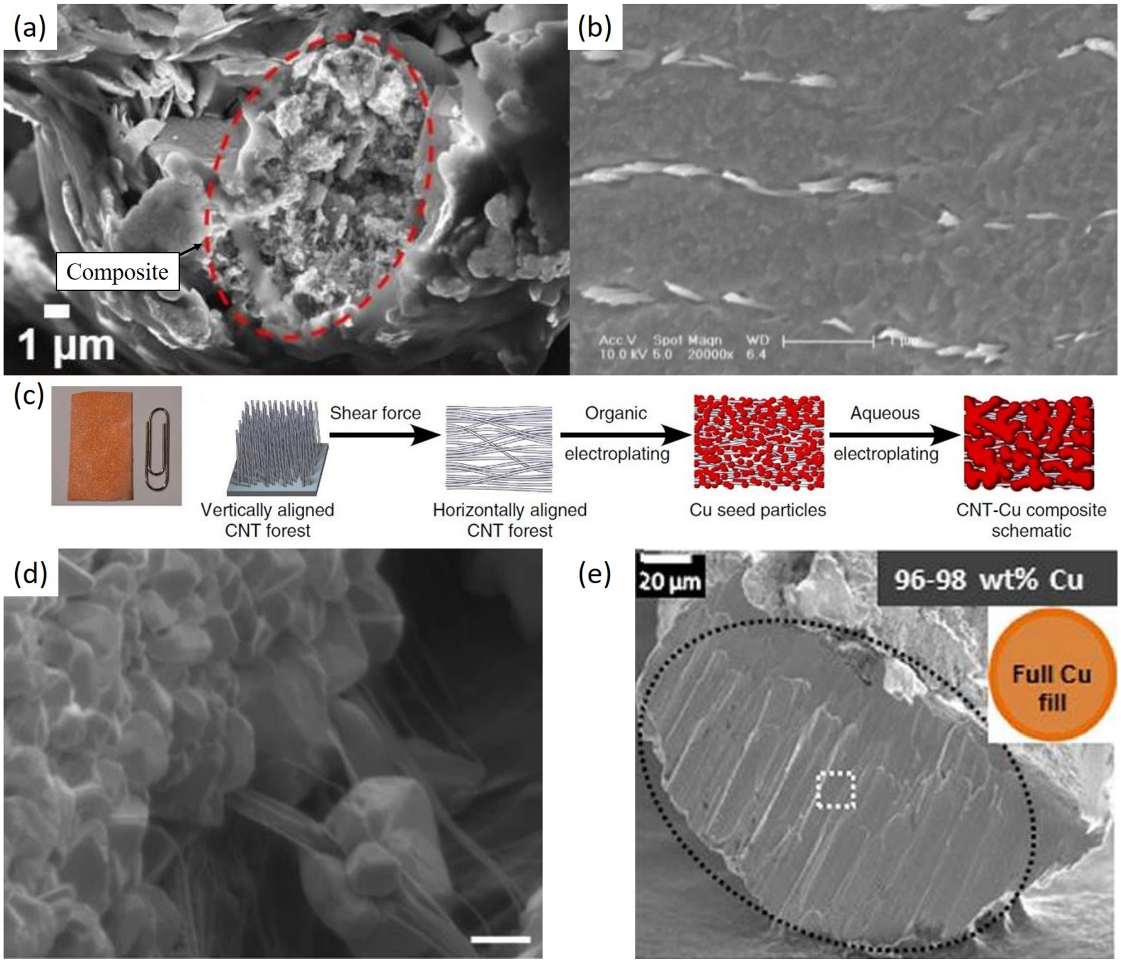

Figure 22. (a) Cu-CNT composite wire obtained via CNT wet-spinning followed by periodic pulse reverse plating,[104] (b) Cu-CNT composite with aligned mono-layers of CNT,[106] (c) composite photography and schematic of the fabrication protocol developed by Subramaniam et al., (d) cross section of the composite obtained by Subramaniam et al.[107,108], and (e) Cu-CNT composite wire ($\varnothing \approx 100$ μm) fabricated by Sundaram et al.[110]

Electrical properties

As we will see in Chapter 3, the state of the art on the electrical properties of Cu-CNT materials leads to results that are controversial. Therefore, we present only here a major result of the literature which, we believe, well represents the potential benefits of integrating CNT into copper. A more contradictory discussion on the state of the art will be given in chapter 3.

In 2013, Subramaniam et al. triggered the interest of the scientific community by reporting the most exceptional electrical properties (Fig. 23a) in a Cu-CNT composite.[3,85] Indeed their composite had an ampacity 100 × higher (6×10^{8} A.cm^{-2}) than that of pure copper ($\sim 10^{6}$ A.cm^{-2}, Fig. 23b). In addition, the resistivity of the composite (at room temperature) was only slightly higher (2.12×10^{-8} Ω.m) than that of pure copper (1.69×10^{-8} Ω.m). Combined to the low TCR of the composite (7.5×10^{-4} K^{-1}), in comparison to copper (3.69-4.09 $\times 10^{-3}$ K^{-1}),[13] the composite had a higher conductivity than that of copper at high temperature (Fig. 23c). Imposing high current densities ($\sim 10^{8}$ A.cm^{-2}) during a large amount of time (at 250 °C), they also highlighted the resistance to electromigration of the Cu-CNT composite compared to pure copper (Fig. 23d).[107]

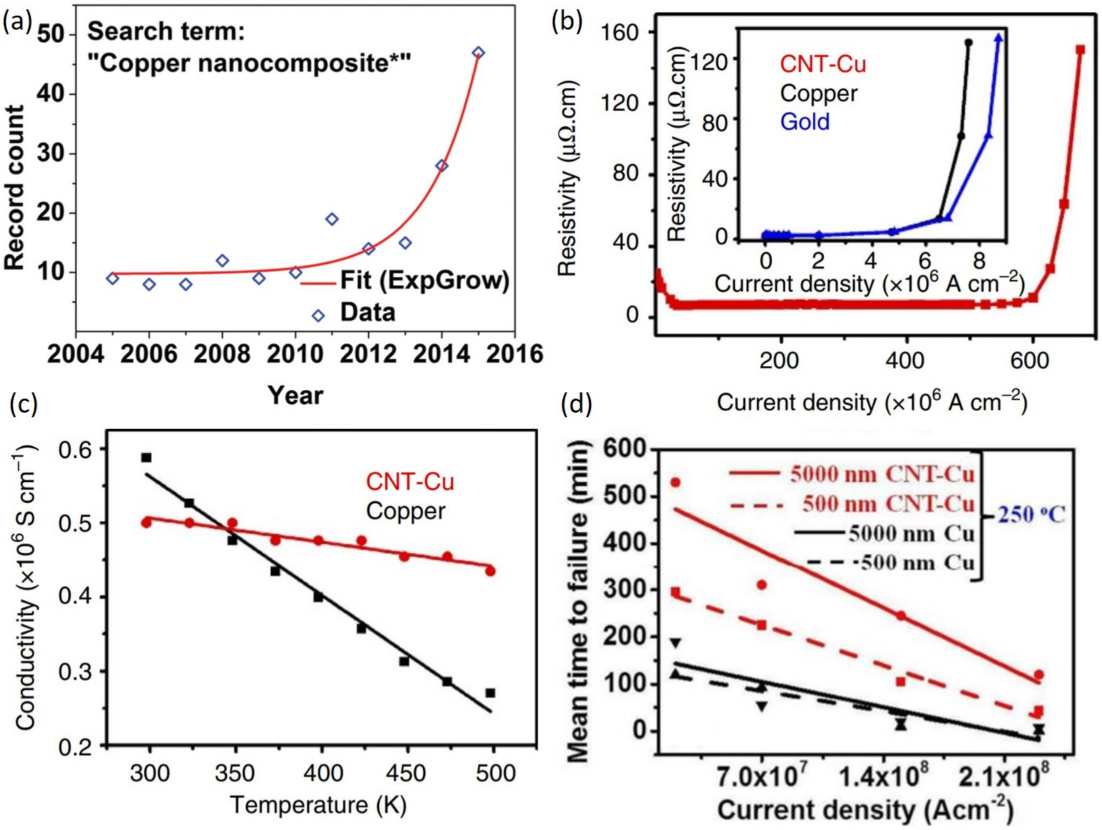

Figure 23. (a) Trends in copper nano-composites research represented by the number of journal publications between 2005 and 2015. (b) Measure of ampacity of the Cu-CNT composite compared to pure copper. (c) Conductivity vs temperature of the Cu-CNT composite compared to pure copper. (d) Mean free time to failure (by electromigration) measured for Cu and Cu-CNT composite at different current densities and for two line widths (500 and 5000 nm).[3,85,107]

The slope of resistivity of the composite provided a strong proof of the electron conduction by the CNT and showed the possibility to couple the high conductivity of copper with the low TCR of CNT. The high ampacity was attributed to the CNT being located at the copper grain boundaries, blocking of the electromigration of the Cu atoms. Compared to pure copper (Fig. 3.2), they calculated a high activation energy of electromigration in the composite ($E_A \approx 2$ eV),[3] and proposed that the electromigration could be limited by a dopant dragging effect (migration of Cu with C, increasing E_A) or a dopant blocking effect (occupancy of the interstitial sites by C, leading to a blockage of the Cu migration pathway).[20,107]

But considering that the temperature drastically affects electromigration (Fig. 3.5), calculation of the activation energy could be slightly biased (using equation 13) by a lack of accuracy in controlling the temperature. Indeed, calculations from Lee at al.[112] do not support the hypothesis of Subramaniam et al. and showed that the E_A of Cu atoms at the interface with CNT (E_A = 0.567 eV) is lower than the one of copper surface diffusion (E_A = 0.8 eV) or grain boundary diffusion (E_A = 1.2 eV). Instead, they propose a reduction of the self-heating in the composite because of a higher Lorentz number and conductivity. Specifically, they calculated that the conductivity and the Lorentz number of a composite interconnect increases with the length of the CNT.

In the work of Subramaniam et al., the Cu-CNT composite lines used for the ampacity measurement (patterned on a silicon substrate) had a length of 50 μm, which was significantly shorter than the length of their SWCNT (45$\%$ vol. of aligned CNT, D = 3 nm, L = 500-700 μm). The mean free path of a SWCNT being $\sim$ 1 μm (for D = 1 nm),[38] we cannot expect that the high ampacity was reached thanks to a ballistic transport over the 50 μm long interconnect (as previously seen in Fig. 11). The higher ampacity could not either be explained by a higher thermal conductivity which had a measured value similar to the one of pure copper. Lee at al. also mentioned that most of the self-heating occurs at the electrical contact between Cu and CNT. Therefore, we could postulate that most of the heat generated in the composite interconnect of Subramaniam et al. was dissipated at the interconnect pad contacts where the electrons may be injected.

The discussion above highlights the lack of understanding/proof of the mechanisms leading to high electrical performance in Cu-CNT composites. As already mentioned, Subramaniam et al. is virtually the only one to achieve such result and, at this time, we can only draw few guidelines from the previous discussion for the design of our future Cu-CNT composite:

- The low TCR of the composite in comparison to copper is a strong signature of the CNT contribution to the current transport.[3,107,108] Hence, CNT having a high conductivity and a low TCR should be used.
- The alignment of the CNT is expected to maximize their contribution to the current transport, decrease the electron scattering, and reduce the self-heating of the interconnect.[3,107,108]
- The Cu-CNT composite should feature a high copper filling with a high vol. $\%$ of CNT that have an uniform distribution in the composite.[3]
- A high CNT length is expected to favor high ampacity, high conductivity and Lorentz number.[107,108,112]
- We can expect that the dissipation of heat in the interconnect, being principally located in/next to the heat sink (substrate), is instrumental. The use of long CNT, in comparison to the interconnect length, may localize most of the heat dissipation in the lead contacts (outside the interconnect itself).
- CNT being located at grain boundaries may lead to an increase of E_A, which may be interesting in the case of a failure by electromigration.[3,107,108]

It is important to keep in mind that these guidelines are relevant for composite interconnects. To the best of our knowledge, there is no literature reporting on a Cu-CNT composite used as LSP and we can expect that a composite used as LSP demands rather different features, which are difficult to extrapolate from the current state of the art. Finally, as we will discuss in chapter 3, the result obtained by Subramaniam et al. stays by far unmatched and remains our principal point of reference to orient our research towards the fabrication of an efficient Cu-CNT composite.

Chapter 1

Fabrication of Cu-CNT composites

1.1 INTRODUCTION

Electroplating being suitable to produce thin layers of metal, it is one of the most meaningful choice to produce Cu-CNT composites for micro-electronic and lightning strike protection applications. Electroplating is also a very good method to reach the fabrication milestones that we identified just before. As previously discussed, the transport properties (thermal and electronic) of CNT are very sensitive to their surface chemistry and structural defects. Electroplating is a gentle process that can preserve the integrity of the CNT and its surface chemistry. Therefore, the length and surface functionalization of the CNT can be controlled. In addition, the distribution/orientation of the CNT can be tailored in the pre-deposited layer and transferred into the composite. Electroplating has proven to be successful, when using organic plating solution,[3] in achieving high vol. CNT $\%$ while keeping a high degree of copper filling. Still, this thesis was made in the framework of a partnership between LIST and Circuit Foil. Circuit Foil being an industrial specialized in the production of copper foils by electroplating, it was important to develop a new electroplating method only based on aqueous plating solution to reduce the hazard from the toxic and flammable organic solution.

Aiming for LSP, an isotropic orientation of the CNT in the composite was preferred as the current induced by lightning is expected to disperse radially. In addition, LSP imply the fabrication of large material pieces (e.g. compared to micro-electronic), therefore we selected a spraying method to deposit CNT. As an industrially oriented work demanding for large volume of production, this method was, a priori, suitable for up-scaling the deposition of CNT. Still, during the course of work, we encountered some difficulties to spray long CNT (L = 800 μm), and we developed a CNT filtration method to tackle this issue.

In order to widen our possibilities, we tried to develop a technology favorable to the three electrochemical fabrication routes. As it will be discussed in the next section, our method relies principally on the coating of CNT by polydopamine. The beauty of this coating is that it enables the efficient fabrication of the composite via electroplating and electroless plating, while potentially enabling an electrophoretic Cu-CNT co-electrodeposition. Briefly, our fabrication strategy consists in the functionalization of the CNT by Pda followed by their dispersion in a solution that is sprayed or filtrated to fabricate the CNT pre-deposit. Afterwards, the Cu-CNT composite is fabricated by using electroplating or electroless plating on the CNT layer (Fig. 1.1).

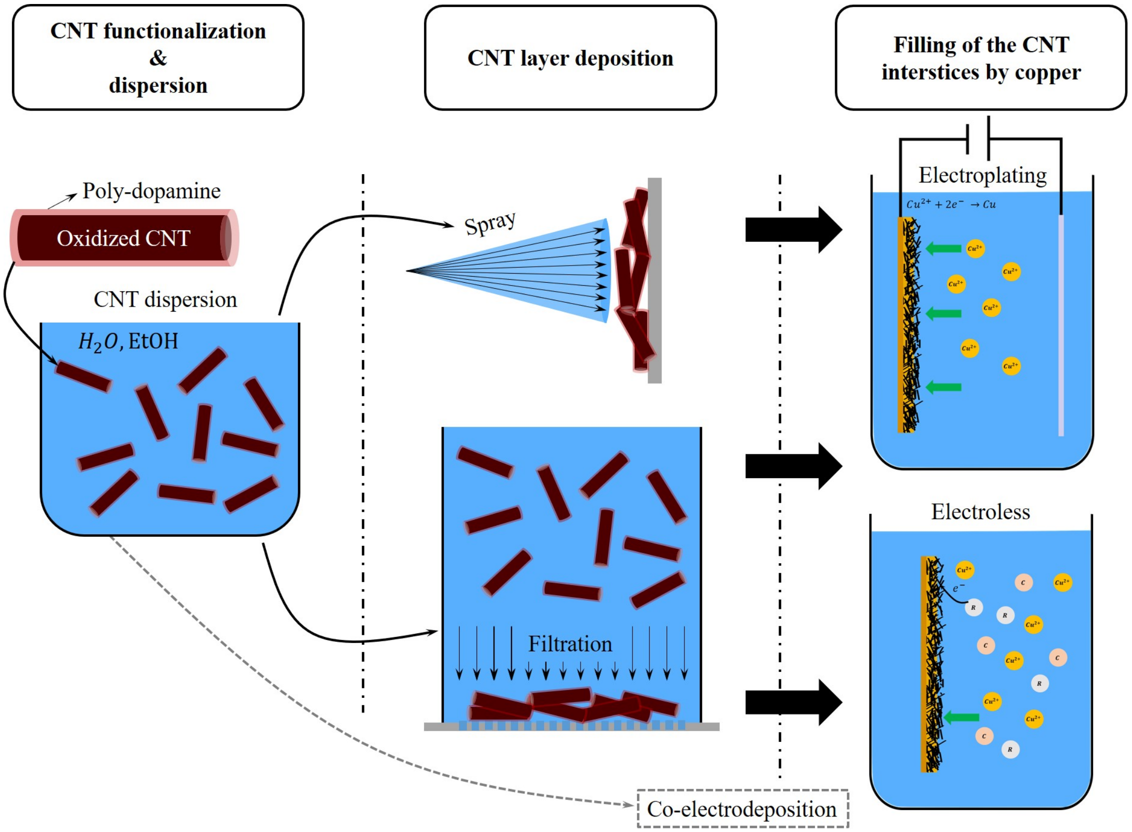

Figure 1.1. Summary of the Cu-CNT composite fabrications routes. The co-deposition is given here as a pending option.

1.2 CNT FUNCTIONALIZATION

1.2.1 Introduction

As already discussed, the CNT hydrophoby prevents the solution penetration inside any CNT network, leading to a weak depth of copper filling.[101–103] Subramaniam et al.[3] also showed that an uniform seeding of the CNT layer by copper nuclei is one of the key to achieve uniform copper filling using an aqueous plating solution. In particular, in the process of seeding (using the organic plating solution), he claimed that the good wetting of the CNT surface by the plating solution favored an efficient copper nucleation. It is known that metal ions attachment/immobilization onto the CNT surface can increase the rate of nucleation during electroplating[113] but the chemical interactions between CNT and copper are rather weak, even leading to metal debonding.[85]

Thus, the CNT surface should be tailored to increase the hydrophilicity of the CNT network while re-enforcing the Cu-CNT interface. As we saw before, the literature mostly reports on the functionalization of the CNT surface (e.g. by CNT oxidization) with oxygen containing chemical groups (COOH, OH, ...) to increase the CNT hydrophilicity while promoting chemical interactions between CNT and copper ions. Still, oxidation was not sufficient to enable a deep copper filling of the CNT layer (Fig. 21).[101,102]

The CNT dispersion (and uniformity) in the sprayed CNT deposit is dependent on the CNT dispersion in the sprayed solution. Thus, an hydrophilic CNT coating, which favors a good dispersion of the CNT in polar solution, should promote a good dispersion of CNT in the sprayed layer.

We identified polydopamine as a very promising candidate to tailor the CNT surface. In 2007, Lee et al.[114] reported that an adherent thin film of Pda could be deposited on a large range of organic and inorganic surfaces by a simple immersion into a dopamine (DA) solution under mild alkaline conditions (pH $\approx$ 8.5). Shi et al.[115] reported that, due to its high hydrophilicity, Pda could be used as CNT coating to efficiently disperse CNT in aqueous solution.

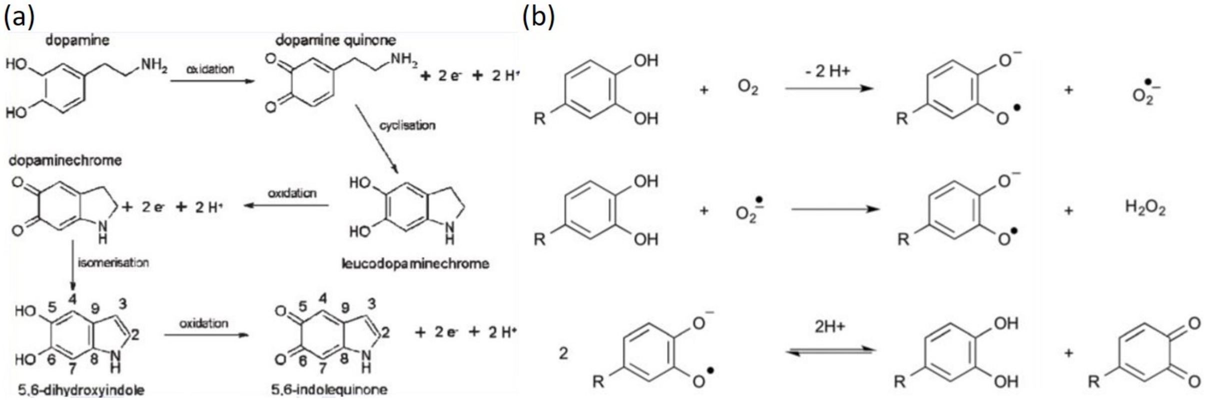

Figure 1.2. (a) Proposed pathway of dopamine oxidization, and (b) reaction schematic of the catechol to quinone oxidization.[116,117]

Pda standard polymerization (pH $\approx$ 8.5 with oxygen as oxidant) occurs by an oxidative route (Fig. 1.3a). The mechanism of dopamine oxidation is thus explained here. Dopamine is first oxidized to dopamine-quinone (Fig. 1.2a). The details of this oxidation step is shown in Fig. 1.2b: the dopamine is oxidized into semi-quinone radicals, then the two semi-quinone radicals react by disproportionation to form one dopamine-quinone and one dopamine unit. The semi-quinone radical formation is favored by the catechol deprotonation, which is more likely to happen at higher pH.[117] Once the dopamine-quinone is formed, it can undergo a cyclization by Michael addition reaction (Fig. 1.2a). Afterwards, two similar steps of oxidation lead to the formation of dopaminechrome and indolequinone units.[116]

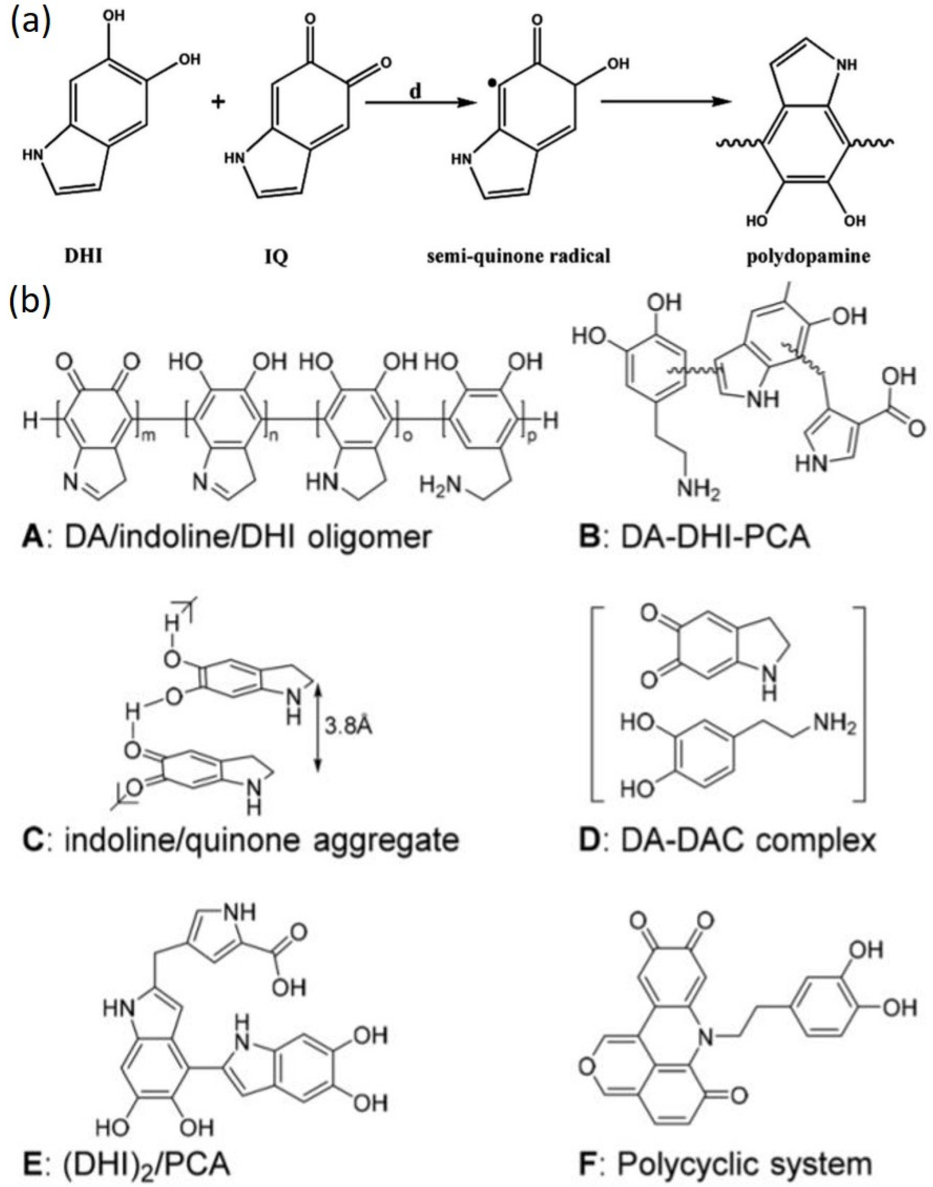

Figure 1.3. (a) Proposed pathway of dopamine polymerization by disproportionation reaction and (b) proposed Pda structure in literature.[118,119]

In fact, the polymerization of the dopamine units into polydopamine occurs via inverse disproportionation of the semi-quinone radicals (Fig. 1.3),[117,118] meaning that the polymerization is happening alongside with the monomer oxidation. Therefore, the Pda polymer is a mix of monomers having different states of oxidation (dopamine, dopamine-quinone, leucodopamine-chrome, ... - e.g. Fig. 1.3b.A). The Michael addition reaction does not necessarily lead to the cyclization of the monomer but can also lead to the attachment with another monomer. As a consequence, the Pda structure depends highly on the experimental conditions and is still widely debated in the literature (Fig. 1.3).[116,119,120] However, it is generally accepted that Pda is composed of small oligomers that form supra-molecular arrangements.[121,122]

Catechols, quinones and amino groups of Pda strongly chelate/interact with metal ions. When added during the polymerization step, metal ions promote the formation of a cross-linked polymer (Fig. 1.4). The formation of a mono, bis or tris-complex with the metal ion depends on the pH and the oxidation state of the dopamine. In alkaline conditions, the catechol groups tend to deprotonate, which enhances their interaction with the cations and their oxidization into quinones also promote oxygen-ions chelation. The electrostatic force of interaction vary with the type of ions and grows in the following order: $K^+ < Na^+ < Ca^{2+} < Mn^{2+} < Fe^{2+} < Co^{2+} \approx Ni^{2+} \approx Cu^{2+} < Zn^{2+}$.[123]

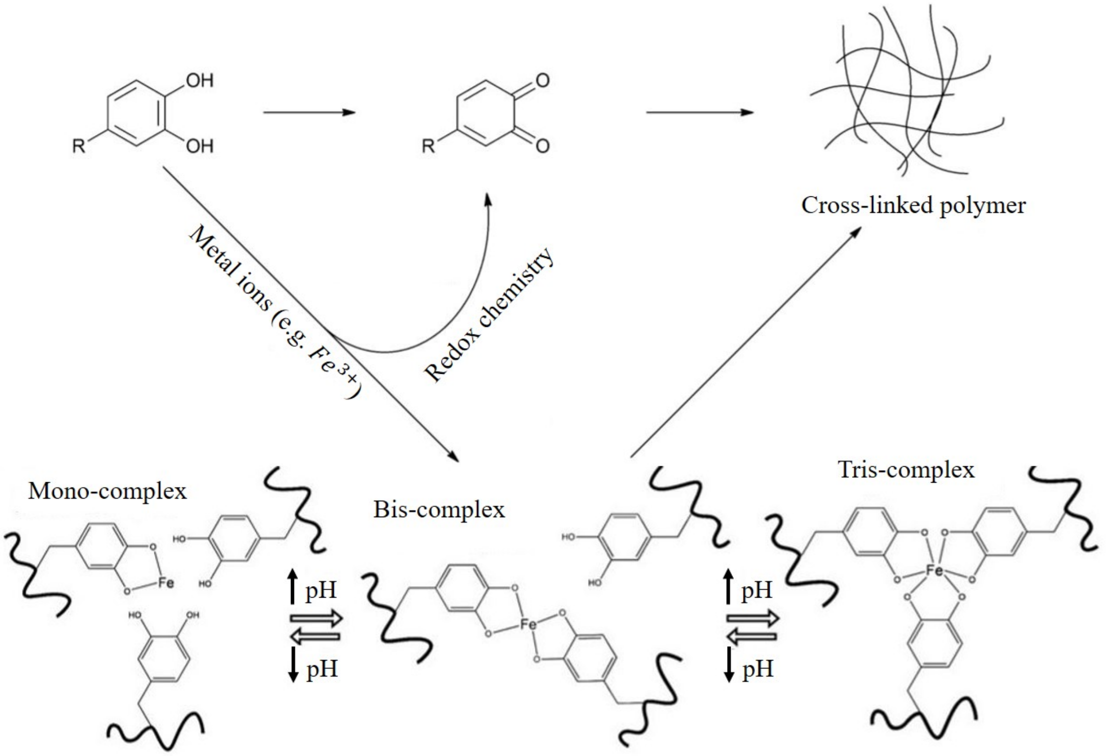

Figure 1.4. Cross-linked Pda formation in presence of metal ions.[117,124].

Interestingly, it was reported that Pda could be used as an efficient and adherent seed layer for metal plating by electroless (e.g. replacing the activation of the surface by Pd nuclei), even leading to the spontaneous reduction of several noble metal ions (Ag, Pd, ...) without the need of a reducing agent.[114,125–127] The adherence of Pda to metallic surface can be attributed to its catechol group, enabling a mix of hydrogen bonding and mono/bidentate bonding.[125,128–130] In contrast, its adherence to CNT (and other organic surfaces) can be attributed to the $\pi - \pi$ stacking and the Van der Waals interactions between the sp^2 hybridized carbon of CNT and the aromatic structure of dopamine.[115]

In conclusion, due to its high hydrophilicity, we expected that a Pda coating would improve the CNT dispersion and increase the copper filling depth. In addition, the adherence properties of Pda with both CNT and metals was expected to re-enforce the CNT-Cu interface. Furthermore, it is known that the rate of nucleation by electroplating is related to the amount of immobilized/attached ions to the surface,[113] we thus expected that the ions-chelating ability of the Pda would enhance the copper growth on the CNT surface. Based on the spontaneous reduction of noble metals by

Pda which is reported in the literature, we expected that Pda could act as an efficient seed layer for metallic growth using electroless plating and electroplating. Finally, the Pda-ions interactions were expected to lead to the positive charging of CNT, favoring a co-electrodeposition by electrophoretic migration.

CNT materials

Three types of CNT were used in this work: arc-discharged MWCNT (Sigma-Aldrich - L= 2.5-20 μm, D= 6-13 nm), CVD grown MWCNT (Nanotech lab - L= 200 μm, D=80-90 nm) and CVD grown MWCNT (Nanotech lab - L= 800 μm, D= 80-90 nm).

1.2.2 **CNT oxidization**

The CNT treatment begins with an oxidization step in acid. Oxidization is used to remove the impurities left in CNT during their fabrication (amorphous carbon, catalytic particles, ...). The impurities are more reactive and are digested faster than CNT. In comparison, CNT are attacked preferentially on their reactive sites, i.e. on their structural defects and on the CNT tips where the curvature (and the strain) is larger. As a consequence, the opening of the CNT tips is generally faster than the thinning and cutting of CNT.[131,132] Still, if oxidization is interesting to remove impurities, it can also create structural defects in CNT. Therefore, the oxidization degree should be carefully controlled and reduced to its minimum to maintain good transport properties in CNT.

In this work, we choose to use an oxidization in nitric acid (method inspired from Rosca et al.[132]). Typically, CNT were dispersed (7 mg.mL^{-1}) in nitric acid (52%) during 30 min using a sonication bath. The received CNT powders were highly aggregated and the sonication was used to break the aggregates, promoting an uniform digestion of the impurities and an uniform functionalization of the CNT surface. This oxidization can be considered as relatively gentle compared to existing methods involving generally several hours of treatment in heated acids.[133,134] This choice was motivated by the need to minimize the damage done to CNT while removing a maximum of impurities.

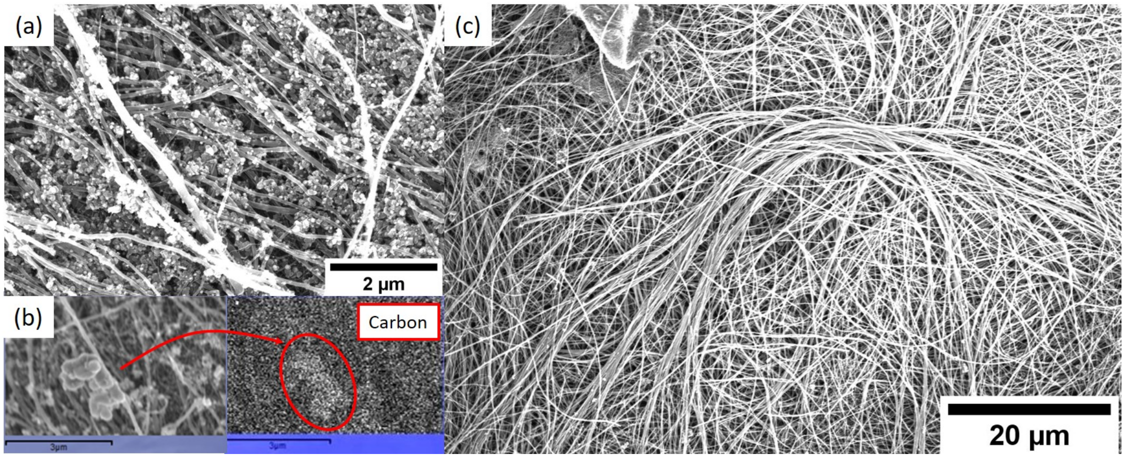

Figure 1.5. (a) SEM image of CVD grown MWCNT (200 μm long) before oxidization, (b) EDX image of an impurity (mainly composed of carbon), and (c) SEM image of the CNT after oxidization.

The effect of the oxidization was particularly visible on the CVD grown MWCNT which were particularly dirty when received (Fig. 1.5a). The particles that are visible on the surface of CNT were principally composed of carbon (Fig. 1.5b). Iron was also detected and attributed to the catalyst particles used during the CNT growth (8% of residual iron according to the commercial data-sheet). After 30 min of treatment and an extensive rinsing with DI water, the surface particles had almost completely disappeared (Fig. 1.5c). Furthermore, we observed MWCNT having a length $\geq$ 100 μm, suggesting that the treatment did not extensively cut/damaged the CNT. In comparison, no impurity was noticed in the arc-discharged MWCNT before (Fig. 1.6a) and after oxidization (Fig. 1.6b).

Finally, oxidization in HNO_3 is known to produces mainly carboxylic groups on the CNT surface.[132] As we will see in next sections, this functionalization was perceived as an advantage for the coating of CNT by polydopamine.

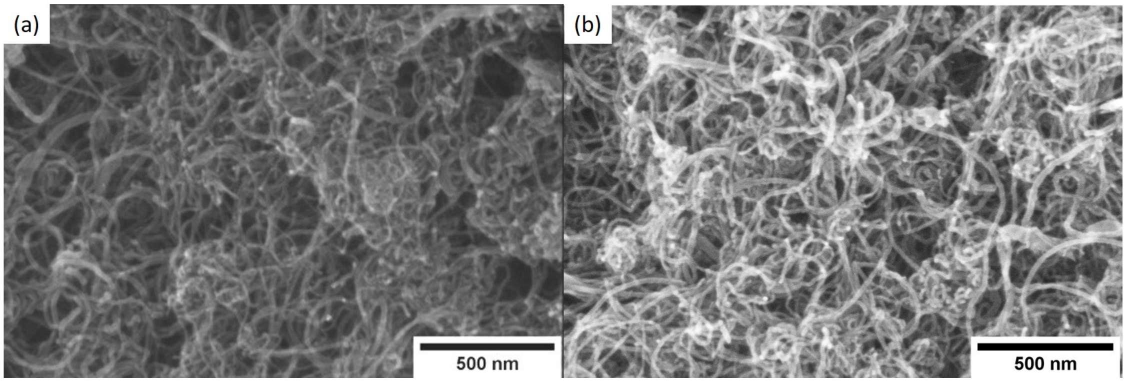

Figure 1.6. (a) SEM picture of the pristine arc-discharged MWCNT, and (b) after oxidization.

1.2.3 **Polydopamine coating on CNT (CNT@Pda)**

The polydopamine coating was used principally for the arc-discharged CNT and was inspired from the work of Shi et al.[115] The oxidized CNT (20 mg) are first dispersed in a small volume (50 mL) of a dopamine hydrochloride stock solution (0.1 mg.mL^{-1} = 0.5 mM). Pristine CNT powders are highly aggregated, preventing the coating solution to penetrate inside the clusters and to coat uniformly CNT. Therefore, the oxidization step was an important intermediary step to break the CNT aggregates, increasing also the hydrophilicity/dispersion of CNT into the coating solution. Still, the solution was first ultra-sonicated in the 50 mL solution to break the remaining clusters. Afterwards, dopamine stock solution was added until a volume of 606 mL was reached. The oxidized CNT were unstable in solution and tended to aggregate rapidly. Thus, CNT were kept dispersed in the solution during 30 min by using ultra-sonication (Power: 100%, pulse-time: 30 s every 5 min). The idea here was to favor the adsorption of an uniform layer of dopamine monomers on the CNT surface before launching the polymerization. The polymerization was triggered by the addition of 363 mL of Tris-HCl buffer (10 mM) which raised the pH of the solution from 5.9 to 7.9. The solution was then stirred during 24 h and CNT were recovered by filtration and rinsed with DI water. The verification of the coating presence was done by inspection of STEM images (Fig. 1.7a) where a clear contrast difference appeared between the CNT and the Pda coating. The coating had a thickness around 7 nm and seemed to cover uniformly the CNT.

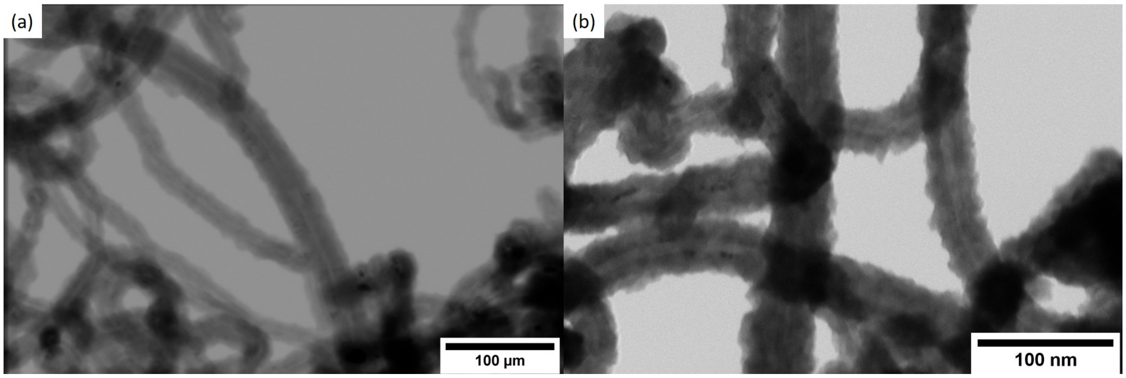

Figure 1.7. STEM picture of arc-discharged CNT coated with (a) polydopamine and (b) Cu-doped polydopamine.

When pristine and oxidized CNT were dispersed in water (Fig. 1.8), a large amount of CNT aggregates was visible, even if a slight improvement was observed after oxidization. In comparison, CNT coated with polydopamine are well dispersed in EtOH and in water, forming an "ink". The dispersion of CNT@Pda are stable over several days, while oxidized CNT and pristine CNT rapidly precipitate in the bottom of the vial.

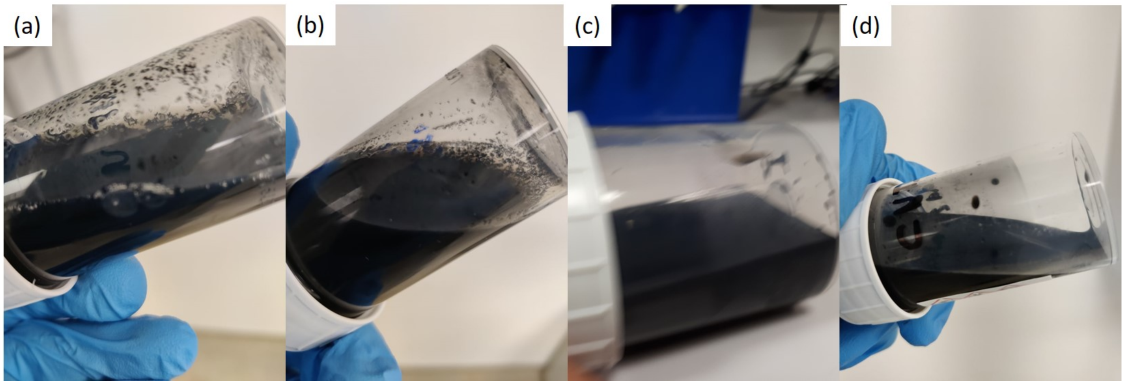

Figure 1.8. Photograph of a dispersion (1 mg.mL^{-1}) of arc-discharged (a) pristine CNT in H_2O, (b) oxidized CNT in H_2O, (c) CNT@Pda in H_2O, and (d) CNT@Pda in EtOH.

1.2.4 **Cu-doped polydopamine coating on CNT (CNT@PdaCu)**

The Cu-doped polydopamine coating was used for the arc-discharged and CVD grown CNT. For the arc-discharged CNT, the coating protocol was similar to the one of CNT@Pda except that we added $CuSO_4.5H_2O$ (0.6 mg.mL^{-1} = 2.5 mM) to the dopamine stock solution. Also the addition of the Tris-HCl led to a slightly lower pH (pH $\approx$ 7). Just before the filtration, we added NaOH ($\approx$ 0.0125 M) until a pH of 11-12 was reached to facilitate the filtration process.

A clear contrast difference between the CNT and the coating was also observed by STEM with this protocol (Fig. 1.7b). The coating had a higher roughness in comparison to un-doped polydopamine (Fig. 1.7a), its thickness being around 4 nm. Dispersions of the coated CNT in ethanol and water were, by eyesight, similar to the ones obtained with CNT coated with un-doped polydopamine (Fig. 1.9).

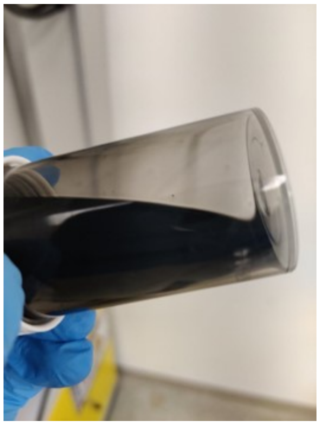

Figure 1.9. Photograph of a dispersion of arc-discharged CNT coated with Cu-doped polydopamine (1 mg.mL^{-1} in EtOH).

The addition of Cu ions in the dopamine solution before the addition of Tris-HCl was expected to favor the adsorption (on the CNT) of a layer containing a large amount of dopamine-Cu mono/bis/tris complexes. Indeed, the dopamine-Cu complexes can arrange themselves on the CNT surface by π-π stacking, Van der Waals, hydrogen bonding and Cu complexion interactions. In particular, the Cu ions in solution can also be immobilized on the CNT surface by the COOH groups formed by the oxidization, favoring the adsorption of dopamine by providing a complexation site on the CNT surface.

When the pH is raised, the deprotonation of dopamine is favored, leading to stronger Cu-Da interactions and favoring the formation of larger complexes (e.g. mono to bis/tris complexes as seen in Fig. 1.4). In addition, Cu^{2+} can act as oxidizing agent and, by having Cu^{2+} complexed by dopamine before the deprotonation, we believe to favor a redox reaction between dopamine and Cu ions (over a reaction between dopamine and O_2). When the pH is further raised to 11-12, the coating solution became darker, this was a sign of the further oxidative polymerization of the Pda.[135]

We observed a plugging of the filtration membrane by Cu-doped Pda particles when attempting to filtrate the solution at pH 7. The increase of the pH up to 11-12 just before the filtration promoted a better dispersion of the Pda particles, preventing the Pda aggregates to clog the membrane. To evaluate the size of the Pda particles (in comparison to the pore size of the membrane) and the effect of the pH on the aggregation of the Pda particles, we performed dynamic light scattering (DLS) and zeta potential (ζ-potential) characterization on doped and un-doped polydopamine solutions (without CNT) polymerized in the same conditions (Fig. 1.10). In the case of un-doped polydopamine, the hydrodynamic diameter of the particles/aggregates is slightly lower (Fig. 1.10b) than the filtration membrane pore size ($\varnothing \approx 400$ nm) at the pH of filtration (pH ≈ 7.9). It was attributed to the ζ-potential being around -40 mV (Fig. 1.10a), leading to a good dispersion of the Pda particles and preventing the clogging of the membrane. The ζ-potential is close to 0 at pH ≈ 2.5, leading to a strong aggregation (hydrodynamic diameter ≈ 5.3 μm). At lower pH, the ζ-potential becomes positive and the hydrodynamic diameter is reduced to $\sim$3 μm.

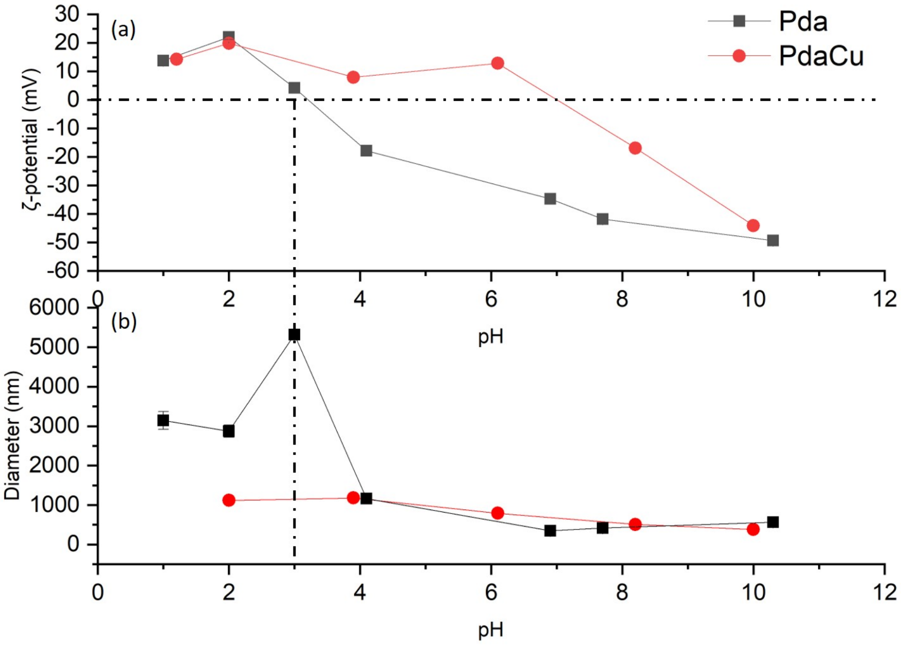

Figure 1.10. (a) ζ-potential and (b) hydrodynamic diameter (via DLS) characterization of polydopamine and Cu-doped polydopamine after 24 h of polymerization. The peak of diameter corresponds to a near zero ζ-potential.

In the case of Cu doped polydopamine, the ζ-potential remains positive up to a pH $\approx$ 7, featuring positive Cu ions in the doped Pda.[136] The near zero ζ-potential at pH $\approx$ 7 could explain the observed clogging of the membrane as it can lead to the particle aggregation. We observed an improvement of the filtration at pH $\geq$ 10, where the $\zeta \leq$ -44 mV and the particles are well dispersed ($\varnothing \leq$ 383 nm). At pH $\leq$ 4, the PdaCu is less aggregated ($\varnothing \approx$ 1.1 μm) than Pda ($\varnothing \geq$ 3 μm). Therefore, we believe that the coating of CNT with PdaCu could be interesting for Cu-CNT co-electrodeposition as it could enhance the dispersion of CNT in acidic plating solution (in comparison to CNT@Pda). In addition, the immobilized Cu positive ions at the CNT surface might favor an electrophoretic migration of the CNT towards the working electrode. However, it was beyond the scope of this thesis to investigate more deeply this interesting path of fabrication.

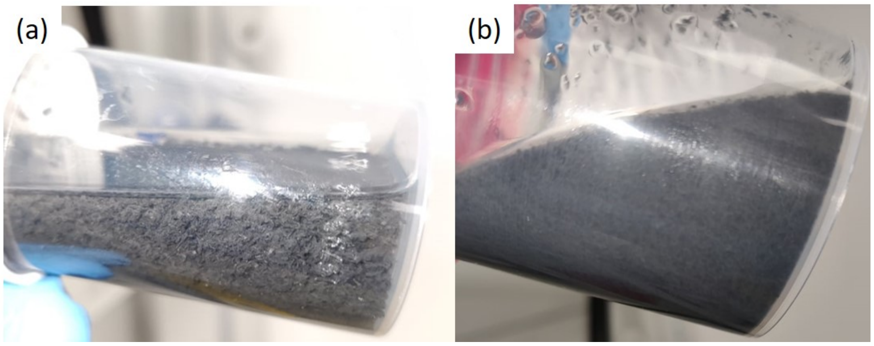

Figure 1.11. Photograph of dispersion (1 mg.mL^{-1} in etOH) of CVD grown (800 μm long) (a) pristine CNT and (b) coated with Cu-doped polydopamine.

CVD grown CNT were coated with Cu-doped Pda using similar conditions. Yet, these CNT are very long (200 and 800 μm) compared to arc-discharged CNT, and in order to limit their cutting, the ultra-sonication had to be done in a larger volume of solution and during a reduced time. Typically, we used 10 s of ultra-sonication to disperse the CNT in the dopamine stock solution (606 mL) and 10 s again when Tris-HCl is added (363 mL). The coating improved the CNT dispersion (Fig. 1.11) but an "ink" was never achieved. The CNT conserved a high length after the treatment (Fig. 1.12a). In comparison, after an extensive ultra-sonication (using the same coating conditions than for the arc-discharged CNT), the CNT were cut in small pieces (Fig. 1.12b). In this case, the CNT dispersion was greatly enhanced because of the CNT cutting (the dispersion was similar to the one in Fig. 1.9).

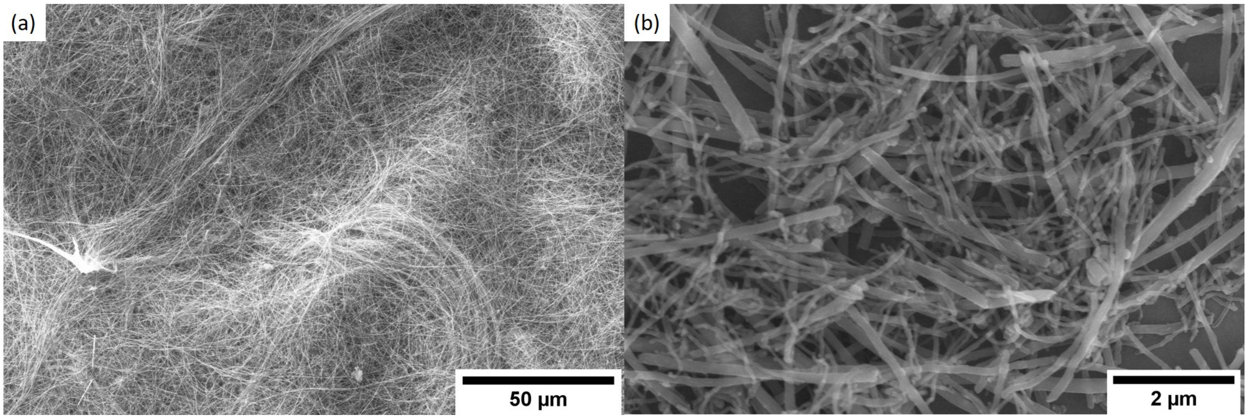

Figure 1.12. (a) CVD grown CNT (800 μm long) coated with PdaCu and (b) shortened CVD grown CNT (initially 800 μm long) coated with PdaCu under extensive ultra-sonication.

The presence of the Pda coating was not obvious when comparing the oxidized CNT to the CNT@PdaCu (Fig. 1.13). Also, the coating was not rough as observed previously with arc-discharged CNT@PdaCu. The increase of the hydrophilic character of the CNT and the noticeable improvement of the dispersion remained, for us, a signature of the coating presence. In addition, the coating was confirmed using XPS (See chapter 2).

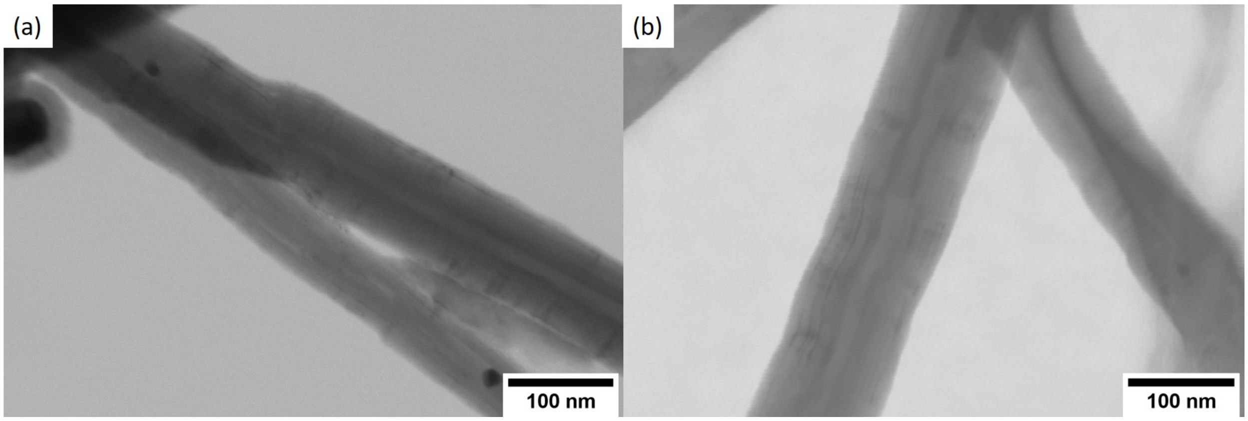

Figure 1.13. (a) Oxidized CVD grown CNT and (b) CVD grown CNT coated with Cu-doped polydopamine.

1.2.5 Alternative coating

In the context of our patent,[137] alternative molecules (to Pda) susceptible to enable the fabrication of Cu-CNT composites have been investigated. To do so, we aimed for molecules able to

- coat and improve the hydrophilic character of CNT.
- strongly chelate/cross-link metal ions.
- oxidize and act as e$^-$ source for the Cu ions reduction.

Among the possible molecules, polycatechol-amines, polycatechols, and polyphenols were identified.[138] In particular, we made an attempt using tannic acid which contains a large amount of phenol groups and can strongly chelate ions.[139] Its phenol groups can also oxidize into quinones (Fig. 1.14)[140] and tannic acid can be used to coat CNT, enhancing their hydrophilic character and dispersion.[141]

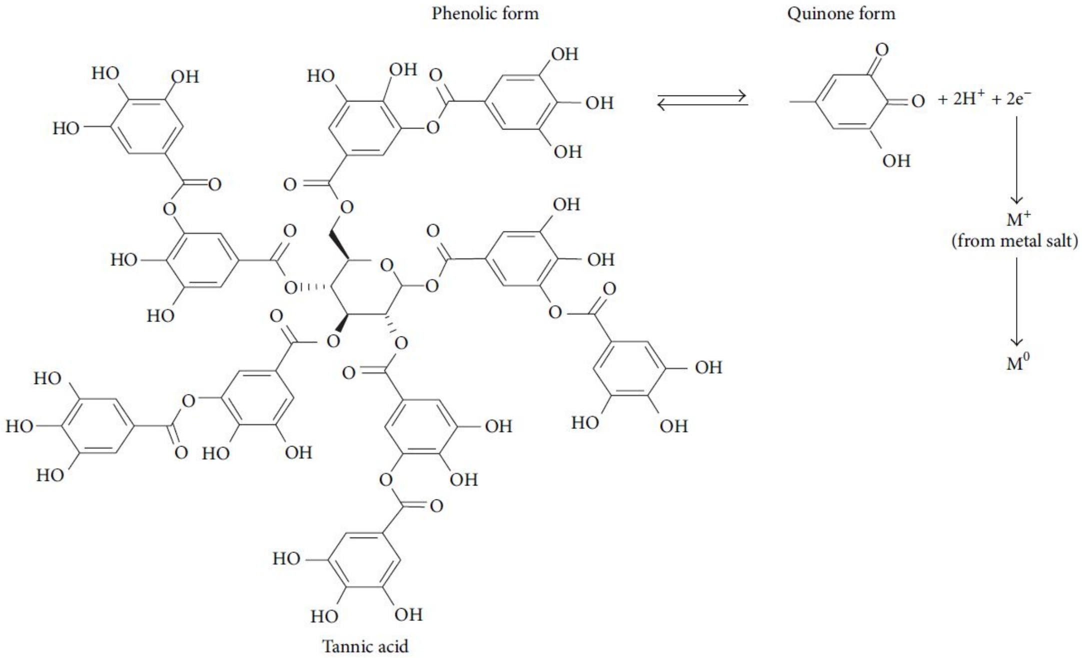

Figure 1.14. Tannic acid oxidation mechanism with metal salt reduction.[140]

A coating with Cu-doped tannic acid (TA) was attempted on arc-discharged CNT. The protocol of coating used was the same that the one of CNT@PdaCu except that we had to reduce the tannic acid concentration from 0.1 mg.mL^{-1} (concentration used with dopamine) to 0.01 mg.mL^{-1} to avoid a problem of filtration. Compared to CNT@PdaCu, CNT aggregates were still visible after dispersion in water despite of the Cu-doped TA coating (Fig. A.1c in appendix).

1.3 CNT CARPET FABRICATION

To fabricate CNT pre-deposit layers, we used a spray and a filtration method. The spraying method was used with arc-discharged CNT and 200 μm long CVD grown CNT. For longer CNT (800 μm), the filtration method was necessary.

The CNT deposition was done on various substrates. Briefly, copper foil was used in a first time (40-50 μm thick). Copper foil was gradually replaced by a Si/TaN(10 nm)/Ta(15 nm)/Cu(150 nm) substrate (SiCu) to reduce the contribution of the pure copper layer to the composite properties. Titanium plate covered with a thin layer ($\sim$ 130 nm) of copper (TiCu) was used when the composite had to be peeled-off from the substrate. A glass substrate was used for electroless plating and Si covered by a Al_2O_3 thin layer was used when CNT were used as working electrode.

1.3.1 CNT spraying

In order to spray CNT, we used two different instruments. We made our first spray attempts with a basic airbrush (manual airbrush - Fig. A.1a in appendix) to investigate roughly the importance of several spray parameters (pressure, distance, temperature of the substrate, ...). The thickness of the deposited layer was approximated from the volume of spayed solution. Still, the mass of deposited CNT never corresponds to the mass of CNT in the sprayed solution because the spray is always made partially outside the sample surface, and because a part of the aerosol is lost in the atmosphere. Thus, we could only predict the amount of deposited CNT empirically from the previous sprays while using the same spray parameters. Table 1.1 shows the repeatability that can be reached with such sprays. Using the parameters of Table 1.1, the mass loss of CNT during the spray remained around 80% and we calculated a deposition efficiency between 0.1 and 0.13 μm.mL^{-1}, or equivalently between 0.008 and 0.009 mg.(mL.cm^2)$^{-1}$. These values may be used to predict the deposition efficiency of the CNT independently of the substrate size.

	Spray 1	Spray 2	Spray 3
Solvent (H_2O/EtOH %)	50/50	50/50	50/50
CNT concentration (mg.mL^{-1})	0.5	0.5	0.5
Sprayed CNT amount (mg)	$\sim$ 5	$\sim$ 5	$\sim$ 10
Pressure (bar)	1.5	1.5	1.5
Temperature of substrate	90	90	90
Substrate area (cm^2)	12.25	12.6	12.6
Sprayer-substrate distance (cm)	$\sim$ 10	$\sim$ 10	$\sim$ 10
Thickness of the CNT layer (μm)	1.16 ± 0.15	1.03 ± 0.32	2.7 ± 0.57
Deposition efficiency (μm.mL^{-1})	0.12	0.1	0.13
Deposition efficiency* (mg.[mL.cm^2]$^{-1}$)	0.008	0.009	0.008
Mass of the CNT layer (mg)	1.04	1.15	2.01
CNT mass loss (%)	79	78	80

Table 1.1. CNT@PdaCu spray parameters used to evaluate the CNT spray repeatability with the basic airbrush. Thickness of the CNT layers was measured using SEM.

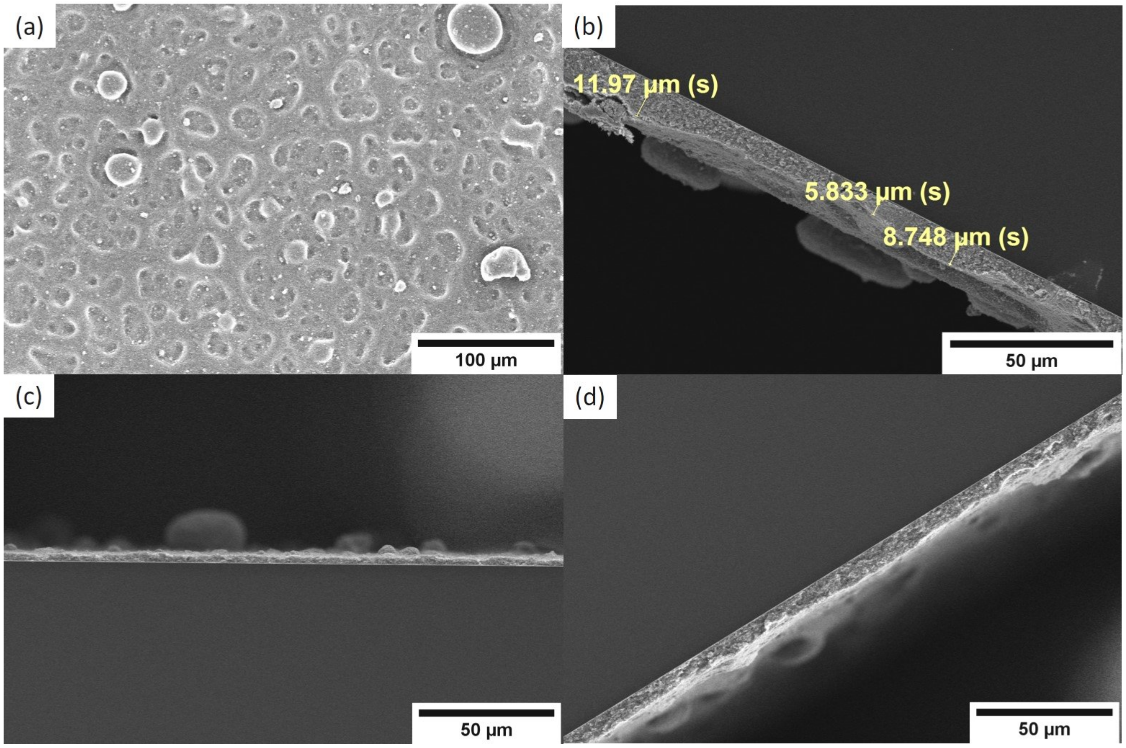

Figure 1.15. SEM (a) top-view and (b) cross-section of a spray (on SiCu) of a solution of CNT@PdaCu (0.5 mg.mL^{-1}) in 75%/25% (EtOH/H_2O). SEM cross-sections of sprays (on SiCu) of a solution of CNT@PdaCu in EtOH: (c) 0.5 mg.mL^{-1} and (d) 0.25 mg.mL^{-1}.

We observed that CNT are slightly better dispersed in water than in EtOH. However, water is difficult to evaporate rapidly and a mix of EtOH and water was initially used as a compromise between the evaporation rate and the quality of dispersion. However, the thickness uniformity of the spray is poor (Fig. 1.15a,b) using CNT@PdaCu dispersed in EtOH/H_2O (50/50 and 75/25%)

and worsens as the thickness of the layer increases. We observed a clear reduction of the undulating morphology when CNT are dispersed in EtOH (Fig. 1.15c). In addition, the aggregates density (Fig. 1.15a-c) is reduced by decreasing the CNT concentration in the solution (1.15d). The use of ultra-sonication just before the spray also has a noticeable impact on the aggregates reduction.

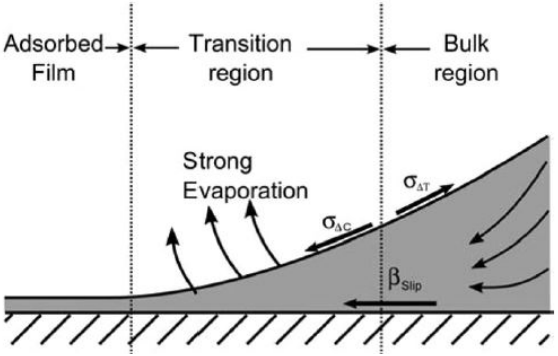

Figure 1.16. Schematic of the evaporation of a droplet in a completely wetting case.[142]

The disappearance of the undulating morphology may be attributed to the higher wetting of the SiCu substrates by EtOH than by water. Indeed, EtOH tended to form a continuous film on the Cu surface while water remained in a droplet form. The evaporation of a completely wetting droplet on a heated surface is described in Fig. 1.16. In this case, the droplet can be subdivided in three regions: the adsorbed film where solvent molecules interact strongly with the substrate, the transition region which is characterized by a high evaporation rate, and the bulk region which constitutes a solvent stock, feeding the transition region by capillary forces. During the evaporation, the adsorbed thin film reaches an equilibrium thickness and the height of the bulk region reduces until complete evaporation.[142] We think that the formation of an adsorbed film of solvent combined to a CNT dragging effect (from the bulk region to the thin film region) could contribute to the formation of a homogeneous CNT hydrophilic layer (Fig. 1.17). In contrast, in the non-wetting case, the evaporation of the droplets could favor the formation of CNT clusters. Afterwards, the next droplets could be preferentially absorbed by the hydrophilic clusters, preventing a homogeneous deposition of CNT and inducing the growth of the clusters (promoting an undulating morphology).

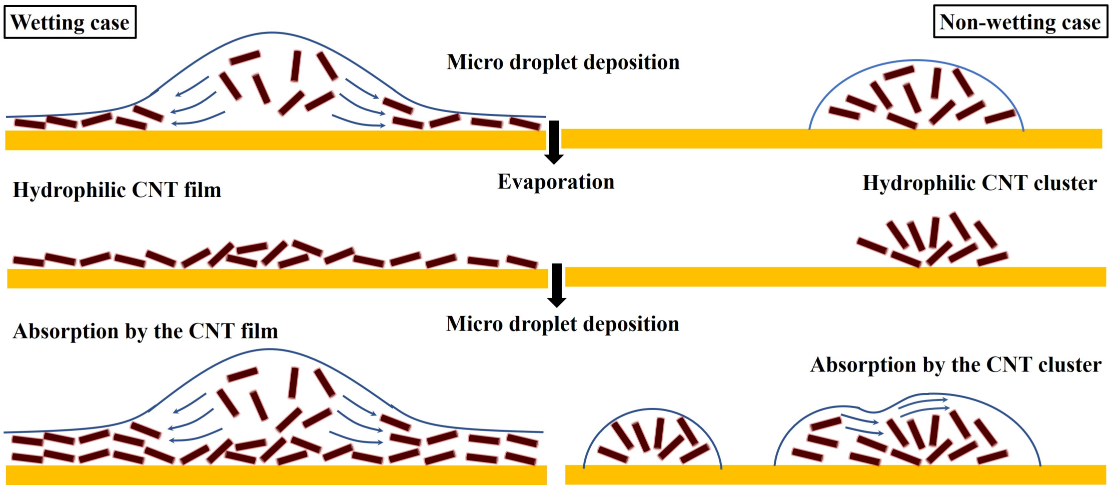

Figure 1.17. Proposed mechanism of CNT film deposition in the wetting and non wetting case.

	arc-discharged CNT@PdaCu	CVD grown CNT@PdaCu (200 μm)
Solvent	EtOH	EtOH
CNT concentration (mg.mL^{-1})	0.1	0.02
Nozzle-substrate distance (cm)	16	16
Canister pressure (bar)	1	0.5
Atomization pressure (bar)	2	2.5
Duty cycle (%)	35	100
Substrate temperature (°C)	100-110	100-110
Deposition efficiency (mg.[mL.cm^2]$^{-1}$)	1.3×10^{-4}	3.53×10^{-5}

Table 1.2. Combination of parameters leading to a good quality spray of CNT (CNT@PdaCu) and calculated deposition efficiency.

In a second phase, we used a sprayer prototype developed at LIST (Fig. 1.18). This prototype enabled a much higher degree of control, and thus optimization, of the spray parameters. The spray nozzle is designed to concentrate the aerosol on a horizontal line (e.g. instead of a cone). The sprayer can move vertically and the width of the covered area depends on the distance between the nozzle and the substrate. The sprayer is equipped with a heating plate where the substrate can be fixed. The flow rate of the sprayed solution is modulated by the pressure in the canister containing the solution. Atomization of the solution is made in the sprayer nozzle where pressured air is injected. An increase of the pressure in the nozzle decreases the size of the aerosol droplets. A duty cycle (varying from 0 to 100%) can also be implemented and consists in periodic switching (ON and OFF) of the sprayer (Fig. A.1b in appendix), adding another level of control to the flow rate of solution.

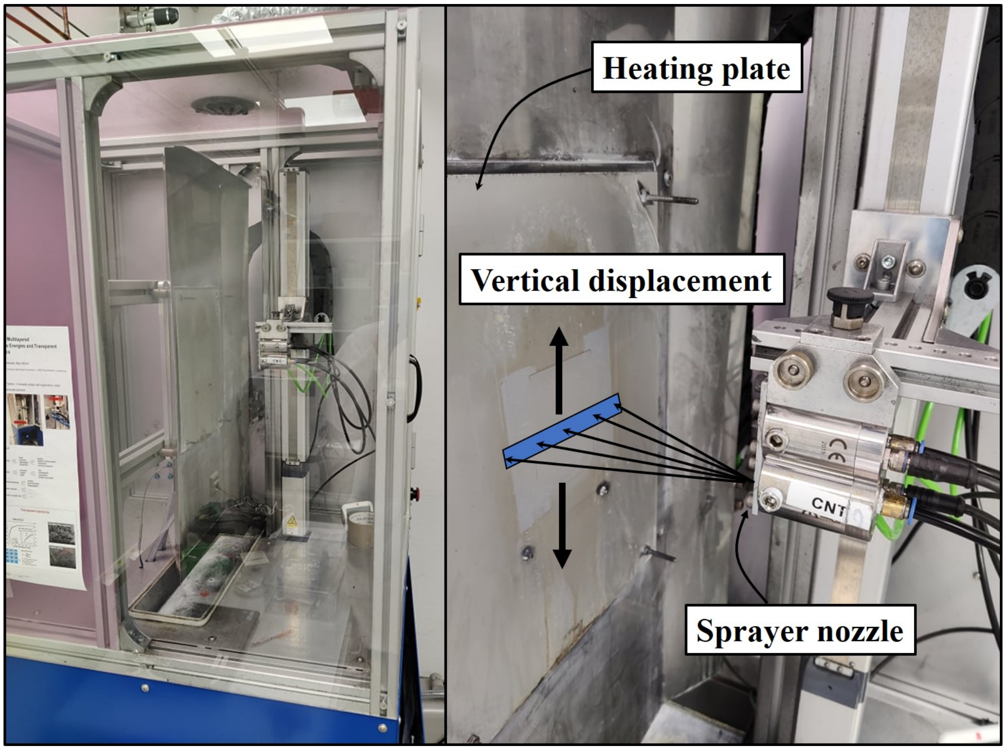

Figure 1.18. Photographs of the sprayer prototype.

In order to improve the quality of the sprayed layer, various parameter combinations were tested. We found a combination (Table 1.2) allowing to fabricate satisfying CNT layers. Beyond these parameters, several experimental rules should be respected for a successful spraying:

- The spray inevitably cools down the substrate due to evaporation of solvent, decreasing the evaporation rate. The spray has to be paused if liquid is observed on the surface to prevent a destructive downward flow.
- The spray should always begin outside the substrate area to ensure that a steady state is reached before spraying on the substrate. For the same reason, and because CNT aggregates tend to concentrate at the bottom of the canister, the end of the canister should never be sprayed.
- The solution should be ultra-sonicated just before the spray to maximize the dispersion of the CNT.

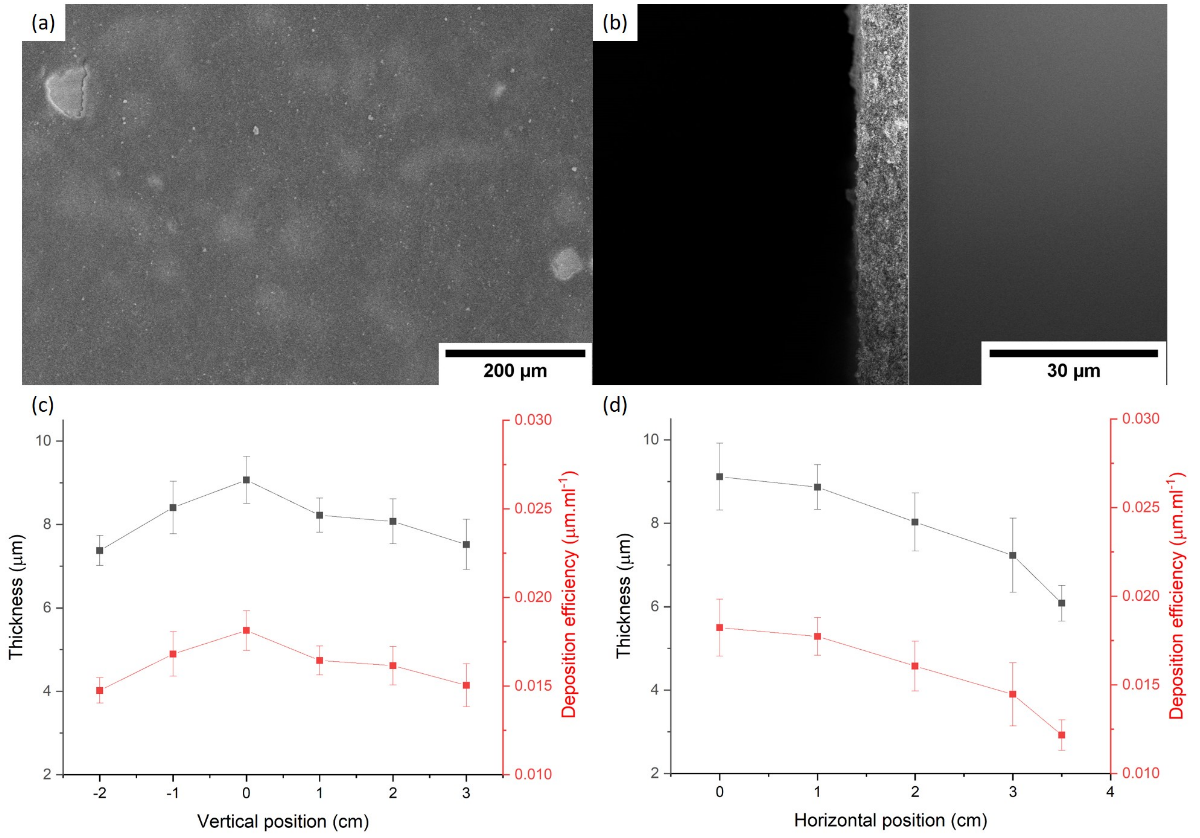

Figure 1.19. SEM picture of a spray of CNT@PdaCu (arc discharged) on SiCu obtained using the parameters in Table 1.2: (a) top-view and (b) cross-section. Thickness profile and deposition efficiency of the CNT spray versus the (c) vertical position and (d) horizontal position (0 represents the center of the sample/spray).

A CNT layer obtained using the parameters in Table 1.2 is shown in Fig. 1.19a,b. We observed a CNT film with very few aggregates and a very uniform thickness (e.g. in comparison to Fig. 1.15). Yet, few holes caused by undesired "high energy" droplets ("spit") appeared in the carpet. The variation of the layer thickness was small along the vertical axis (Fig. 1.19c). Along the horizontal axis (Fig. 1.19d), it rapidly decreased from 9 μm (at the spray center) to 6 μm (for an offset of 3.5 μm). The deposition efficiency (μm.mL^{-1}) was also calculated. In the context of fabrication of samples that were characterized as LSP, we up-scaled the spraying of CNT up to 8 inches diameter samples (20.3 cm) by spraying in two steps (Fig. 1.20) and by using the parameters in Table 1.2.

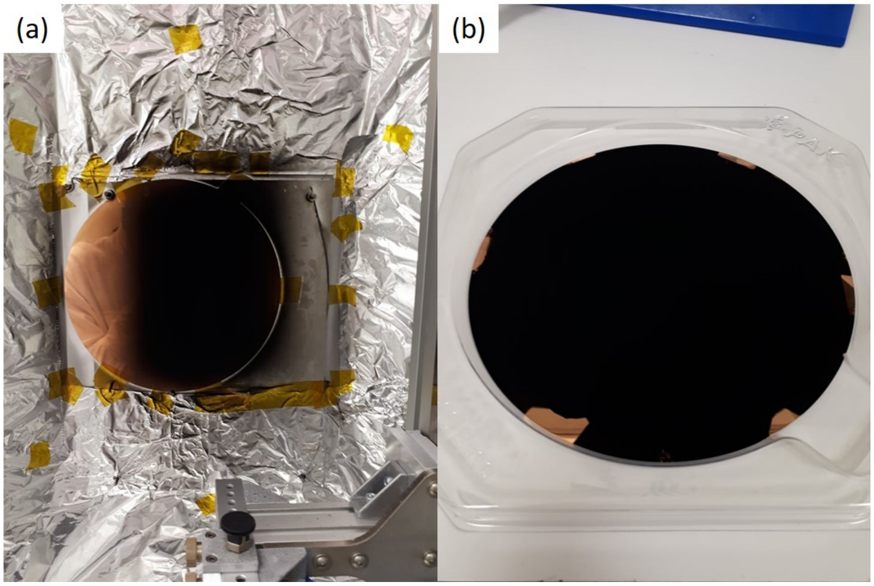

Figure 1.20. Photographs of arc-discharged CNT@PdaCu spray on a 8 inches SiCu wafer.

We also managed to spray CVD grown CNT@PdaCu (200 μm long). Spraying long CNT is challenging due to their fast aggregation in solution. The parameters used to successfully spray the CNT and the calculated rate of deposition are given in Table 1.2. To reduce the CNT aggregation, and the risk of sprayer clogging, the CNT were highly diluted in comparison to arc-discharged CNT. In addition, a lower canister pressure ($\sim$ solution flow rate) and a higher atomization pressure were used in order to reduce the size of the droplets, favoring the dispersion of the CNT clusters. The duty cycle was suppressed (100% opening) because we assumed that a rapid closure/opening of the spray nozzle could induce the clogging of the nozzle and cut CNT. A spray obtained using the parameters in table 1.2 is shown in Fig. 1.21. The CNT adopted a planar orientation in the carpet due to their large length in comparison to the thickness of the film. Large aggregates were always observed in these CNT carpets.

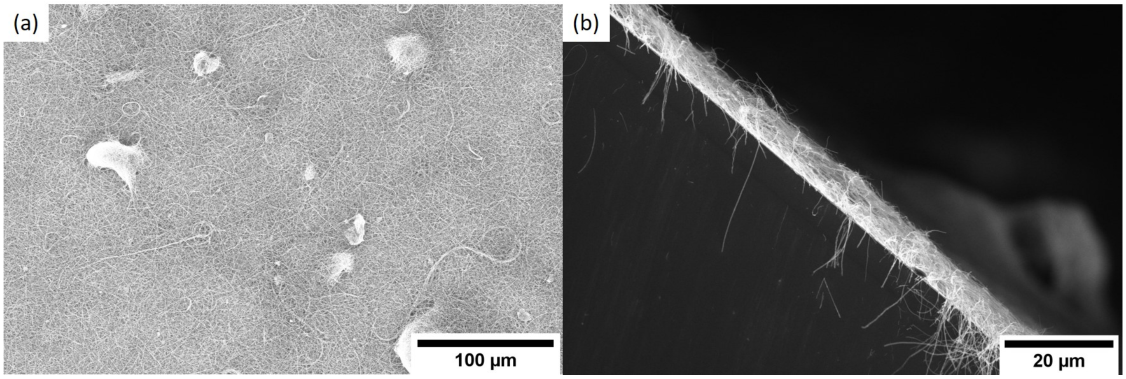

Figure 1.21. SEM (a) top-view and (b) cross-section of a spray of CVD grown CNT@PdaCu (200 μm) on SiCu.

A too high atomization pressure should be avoided as it can lead to the delamination the sprayed layer and to the formation of vertical structures (e.g. using a pressure of 3.5 bar - Fig. 1.22). We attributed the CNT lift-up to the strong air flow at the sample surface.

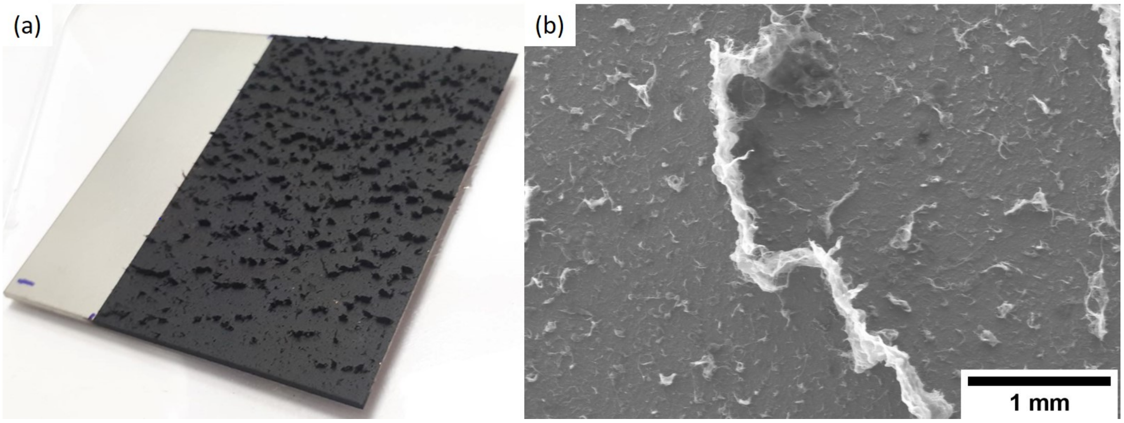

Figure 1.22. (a) Photograph and (b) SEM top-view of a spray of CVD grown CNT@PdaCu on a TiCu plate with vertical CNT structures.

1.3.2 **CNT filtration**

A spray of CNT, having a length of 800 μm, was successfully made but most of the attempts led to the sprayer clogging. Therefore, a method of filtration was developed to elaborate CNT carpets containing 800 μm long CNT (filtration can also be used with 200 μm long CNT). This simple and rapid method prevents the CNT mass loss observed when spraying. Its drawback is the difficulty to fabricate large samples due to the limited size of the filtration membrane. In addition, the fabrication of thin CNT layers is difficult and the obtained carpets are less uniform than the ones obtained with spraying.

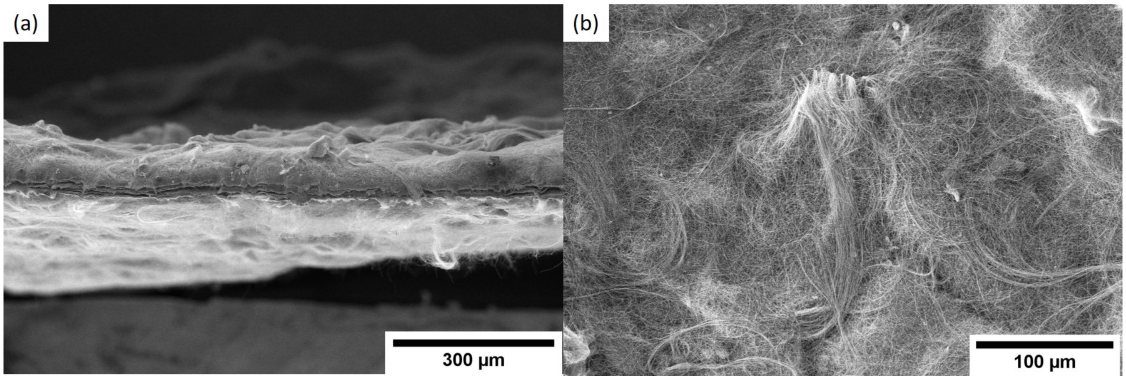

Figure 1.23. SEM (a) cross-section and (b) top-view a self-suspended layer of CNT@Pda (200 μm long) obtained by filtration ($\sim$ 1.7 mg.cm^{-2}).

The CNT carpets were fabricated by filtrating 50 mL of a CNT solution (CNT@Pda/CNT@PdaCu in EtOH - 0.1 mg.mL^{-1}) on a PTFE membrane (ø=3.9 cm). The filtrated CNT can be peeled manually from the membrane due to the self-cohesion of the layer, which was attributed to the length of CNT that promote a highly entangled system. The filtration of a smaller quantity of CNT led to brittle layers, preventing their peeling and handling. We also observed that oxidized CNT layers were more brittle than layers of CNT@Pda(Cu). Indeed, the polydopamine coating seemed to reinforce the cohesion of the CNT layer. In order to prevent their breaking, the quantity of filtrated oxidized CNT was doubled (100 mL) in comparison to CNT@PdaCu. Fig. 1.23 shows an example of a filtrated CNT@Pda layer (filtration of 20 mg of CNT). We observed thickness irregularities and a higher amount of CNT aggregates in comparison to sprayed layers. In the context of the fabrication of sample for the LSP characterization, we up-scaled the filtration system to a membrane having a diameter of 12 cm.

1.4 COPPER PLATING

1.4.1 On CNT@Pda

Electroplating

By coating the CNT with Pda, we aimed to promote the penetration of the aqueous plating solution inside the CNT layer. Using a water droplet, we observed an instantaneous penetration of the liquid inside a sprayed CNT@Pda layer (Fig. 1.24a). In comparison, the droplet slowly and partially penetrated inside an oxidized CNT layer (Fig. 1.24b).

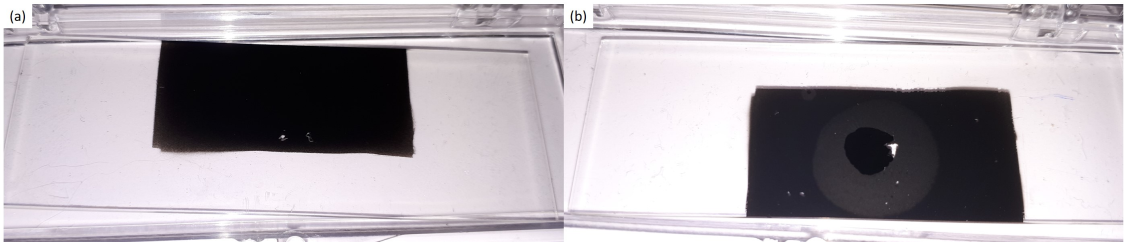

Figure 1.24. Photograph of a droplet of water deposited on a sprayed (on glass) arc-discharged (a) CNT@Pda carpet and (b) oxidized CNT carpet.

In Fig. 1.25, electroplating was used on a CNT@Pda layer sprayed on a copper foil (50 μm thick). The plating solution was composed of $CuSO_4.5H_2O$ (0.1 M) and H_2SO_4 (0.1 M - pH = 1). Chronoamperometry was made at - 0.4 V and - 0.2 V vs standard calomel electrode (SCE) in order to test two different deposition rates (14 and 5 mA.cm^{-2}, respectively), similar to the one used in the literature.[3] In addition, before the starting of the electroplating, the CNT layer was immersed 30 min in a solution of $CuSO_4.5H_2O$ (0.1 M) to favor the chelating of copper ions by the polydopamine at the CNT surface. Indeed, metal nucleation should be favored by the ions attachment at the CNT surface.[113,143] A low molar concentration of $CuSO_4.5H_2O$ (0.1 M) was initially chosen, in comparison to concentration usually used for copper plating (e.g. 1 M),[144] in order to increase the density of nucleating particles (Fig. A.2 in appendix).[145]

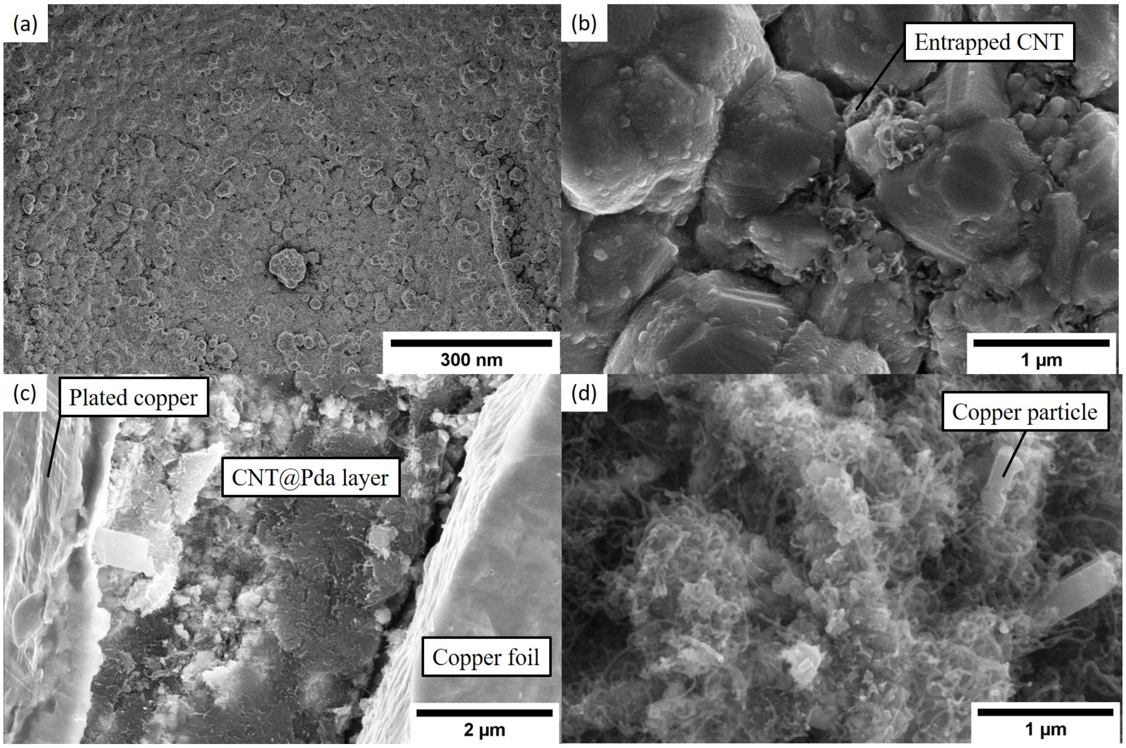

Figure 1.25. SEM pictures of a Cu-CNT@Pda "composite" (a,b) top-view, and (b,c) cross-section. Obtained by chronoamperometry (-0.2 V vs SCE).

The filling of the CNT@pda layer is slightly better when reducing the potential from -0.4 V to - 0.2 V vs SCE. The electroplating was stopped when the CNT@Pda layer was totally covered by copper (Fig. 1.25a). When looking at the top surface of the composite, we observed that CNT were entrapped in the grain boundaries (Fig. 1.25b). However, the system was poorly filled by copper, with only few copper particles dispersed inside the CNT carpet and a copper crust being formed on the surface of the CNT layer (Fig. 1.25c,d). Cu particles were seen next to the substrate surface, suggesting that the Pda coating promotes penetration of the plating solution inside the CNT network as we expected. This result highlights that CNT hydrophilicity alone is not sufficient to enable the fabrication of Cu-CNT composites. Furthermore, our attempt to improve the nucleation of copper by chelating Cu ions at the CNT surface using an immersion in the $CuSO_4$ solution was not successful.

We tried to plate Cu on an oxidized CNT layer but the CNT layer was very unstable when immersed in the plating solution, leading to its decohesion from the substrate. It was attributed to the higher hydrophoby of the oxidized CNT compared to the CNT@Pda. We did not further try to plate on oxidized CNT as results in literature already proved (see pp. 30-32) the inefficiency of this system for the fabrication of Cu-CNT composites by electroplating.

Electroless

Interestingly, we managed to fabricate a self-suspended foil of composite using electroless plating on a CNT@Pda layer sprayed on a glass slide (Fig. 1.24). To the best of our knowledge, no equivalent result was reported in literature. The experimental parameters were inspired from the

Chemicals	Concentration
$CuSO_4.5H_2O$	0.03 M
Ethylenediaminetetraacetic acid (complexing agent)	0.03 M
NaOH	pH adjusted to 12.1
Glyoxilic acid (reducing agent)	0.2 M
Parameters	**Value**
Temperature	55 °C
Time of plating	∼ 3 h
Substrate	glass
CNT	arc-discharged CNT@Pda

Table 1.3. Electroless plating parameters and solution composition.

literature[94,95,146] and are summarized in Table 1.3. During the electroless plating, the CNT layer were delaminated from the substrate and started to float at the surface of the solution due to the formation of hydrogen bubbles originating from the electroless reaction.[94] Interestingly, the CNT layer conserved its cohesion and continued to be plated by copper.

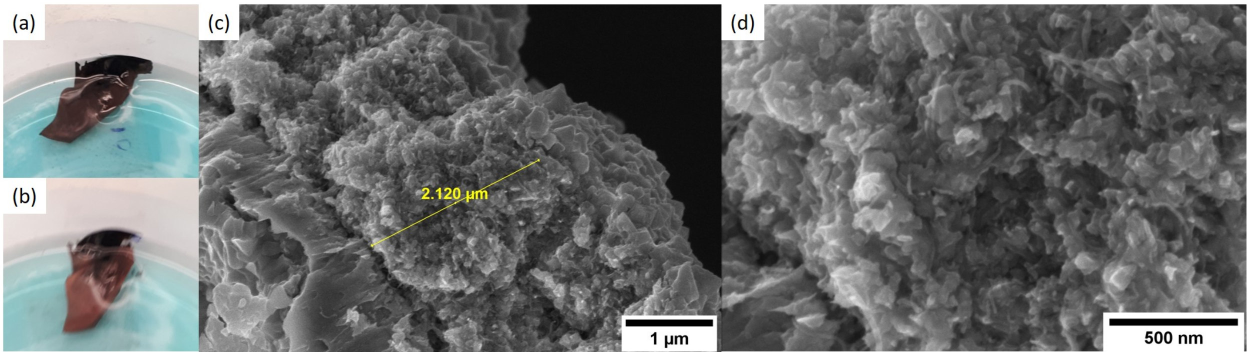

Figure 1.26. Photograph of the electroless plating of a CNT@Pda layer at (a) t≈ 0 and (b) t≈ 3 H. (c,d) SEM cross-section of the composite after plating.

1.4.2 On CNT@PdaCu

Electroplating

Arc-discharged CNT@PdaCu were sprayed on a copper foil and electroplated in same condition than CNT@Pda (-0.2 V vs SCE) until the CNT layer was totally covered by copper. Fig. 1.27a,b show that the copper filling is drastically enhanced thanks to the doping of the polydopamine by Cu ions. To the best of our knowledge, we reports for the first time an effective electroplating method using only an aqueous plating solution as an alternative to organic solutions.[3] Fractures were observed in the composite (Fig. 1.27a), disrupting the material continuity. The plating parameters were optimized to remove these discontinuities as it would affect negatively the material conductivity. Pulsed plating can improve the filling of small interstices and lead to smoother surfaces.[145,147,148] Fig. 1.27c,d show a composite obtained using potential pulses (-0.2 V vs SCE,

Chemicals	Concentration
$CuSO_4.5H_2O$	0.63 M
H_2SO_4	0.1 M (pH $\approx$ 1)
HCl	50 mg.L^{-1}
Bis(3-sulfopropyl)-disulfide (SPS)	15 mg.L^{-1}
Polyethylene glycol (PEG - M_n=6000 g)	100 mg.L^{-1}
Plating parameters	Value
Temperature	Room temperature
Pulsed current (time ON/OFF)	-85 mA.cm^{-2} (0.02/0.1 s)
Sitrring	No

Table 1.4. Optimized parameters of electroplating used to fabricate Cu-CNT composites.

0.01/0.01 s - ON/OFF). In this case, the composite features a smooth surface and is exempt of cracks. Interestingly, up to 45 μm thick Cu-CNT composites were obtained using this method (thicker composite was not attempted), highlighting a large filling depth compared to the results of the state of the art ($\leq$ 4 μm - pp. 28-32).

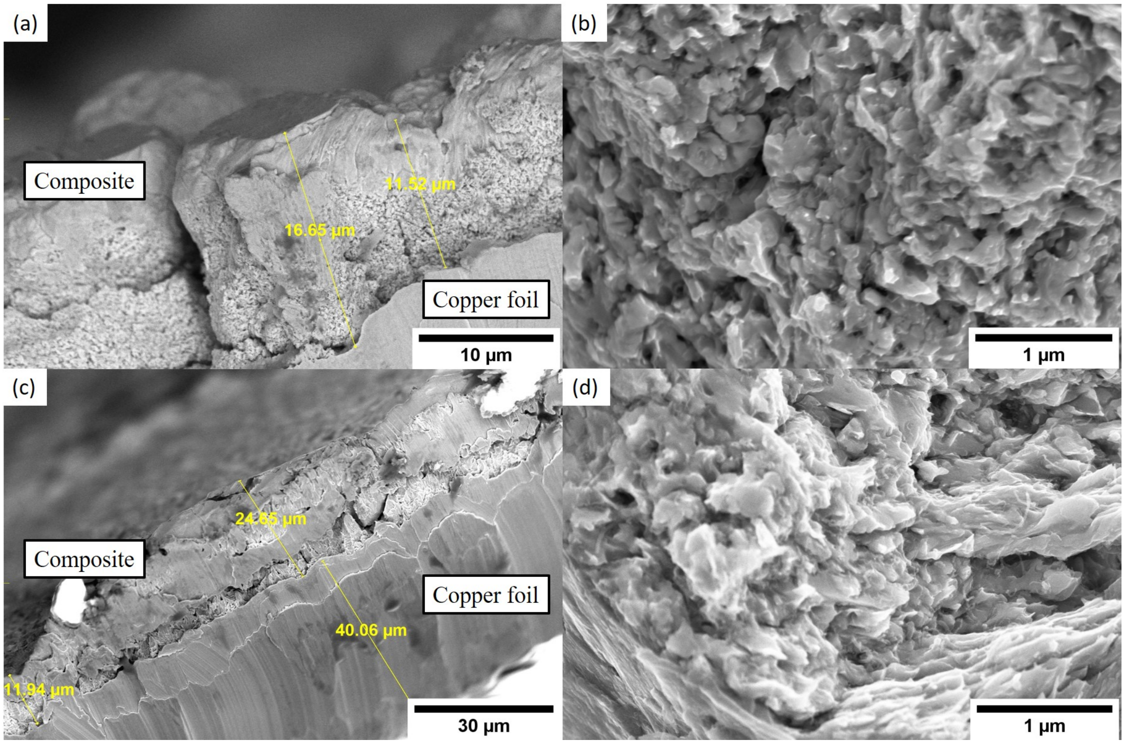

Figure 1.27. SEM pictures of cross-section of Cu-CNT@PdaCu composites obtained by chronoamperometry (a,b) and pulsed potential (c,d).

To decrease the contribution of the substrate on the measured material properties (non negligible for a 40-50 μm thick copper foil), we fabricated most of the following composites using SiCu substrates. In addition, we continued to optimize the plating solution and the plating parameters (Table 1.4).

Here, polyethylene glycol (PEG) and bis(3-sulfopropyl)-disulfide (SPS) act as suppressor and accelerator, respectively. SPS is a small molecule that can penetrate inside small cavities and catalyzes the reduction of Cu(II) into Cu(I), increasing the rate of filling inside the cavities. In contrast, PEG is a larger molecule that hardly penetrates inside small interstices and that binds to the copper surface (forming complex with Cu ions and Cl^-), slowing down the Cu deposition (Fig. A.3 in appendix). In our case, the additives were expected to accelerate the growth of copper inside the CNT carpet while slowing down the deposition of a copper crust.[149–153] We increased the current density of the pulses (-85 $mA.cm^{-2}$, 0.02/0.1 s - ON/OFF) because more nucleation sites are activated at higher potential (Fig. 1.29b), leading potentially to a more uniform copper growth.[145] We observed that copper undergoes a bottom-up filling of the CNT layer. In the initial stage, a copper layer can form and push-up the CNT layer (Fig. 1.28a). At some point, the copper starts to be injected into the CNT layer, preventing further pushing up, and initiating the copper filling process (Fig. 1.28b). After electroplating, the composites displayed an uniform copper filling with the CNT being mainly located at the grain boundaries (Fig. 1.28c,d). Therefore, these plating conditions were kept for the fabrication of the next composites. The CNT pushing-up was more often observed with CNT layers having a non-uniform thickness (typically with a CNT layer displaying an undulating morphology). We believe that an irregular thickness could lead to different rates of metal filling (because the ions diffusion towards the substrate is slower in thicker layer), inducing an internal stress and a delamination of the CNT layer (Fig. 1.28e). We remind here the critical merit of depositing an uniform CNT layer to avoid defects and obtain an uniform filling of copper (Fig. 1.28f).

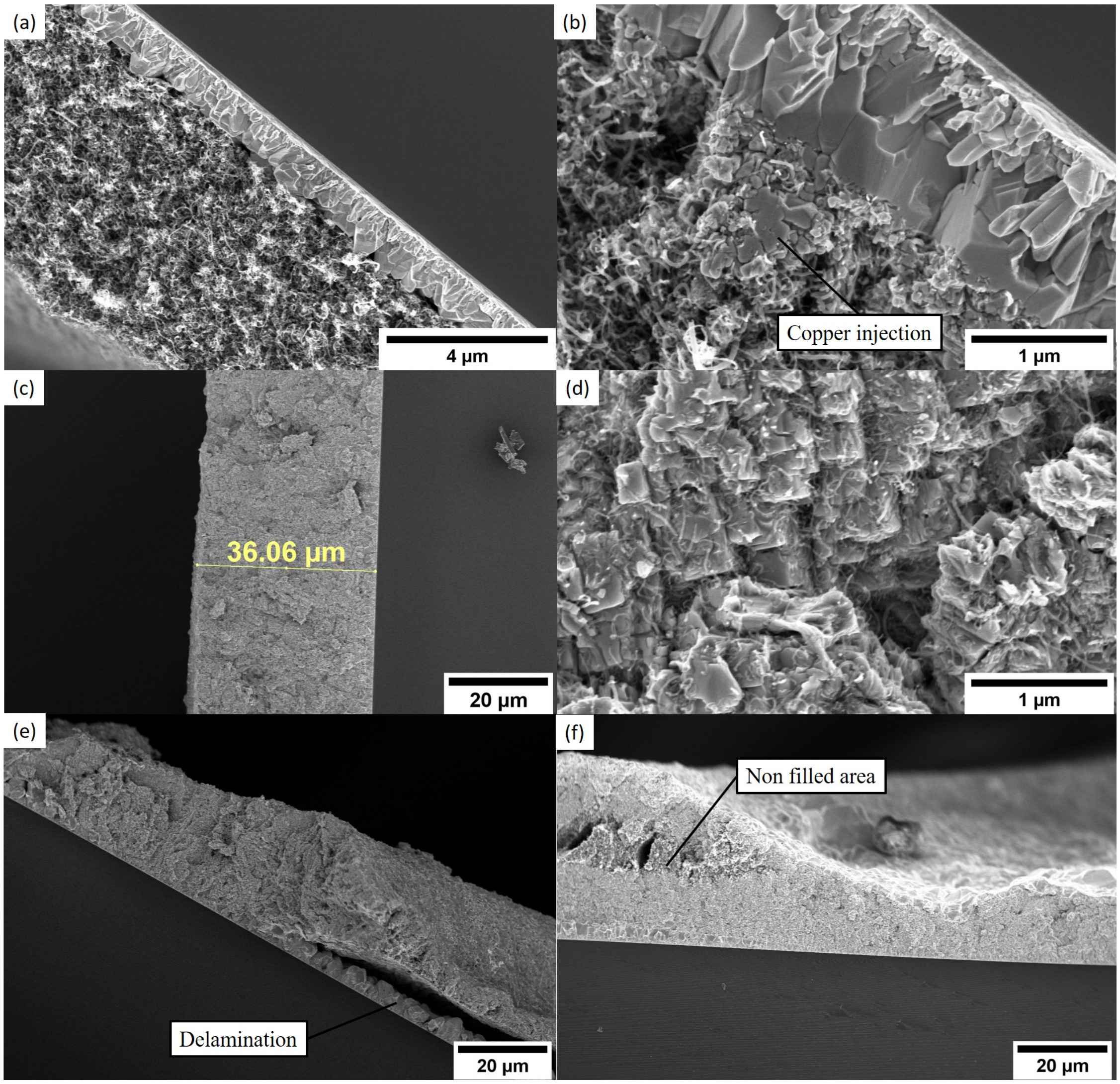

Figure 1.28. SEM picture of the cross-section of samples showing (a) the CNT pushing-up phenomenon during electroplating, (b) the start of the copper injection into the CNT layer, (c,d) a composite obtained with the optimized plating conditions, (e) a delamination observed with an irregular CNT layer, and (d) a defect induced by the irregularity of the CNT layer.

The stirring of the solution decreases the thickness of the diffusion layer (Fig. A.4a in appendix), increasing the limiting current of deposition. We monitored the plating current with and without magnetic stirring (Fig. 1.29a). After initiation of the magnetic stirring, no increase of the current of deposition was observed when using a fixed plating potential (-0.2 V vs SCE in 0.1 and 0.63 M $CuSO_4$ solutions) showing that the ion concentration did not increase in the CNT layer (see equation A.2 in appendix). We attributed this behavior to the CNT layer acting as physical barrier to the liquid movement near the substrate, leading to a diffusion layer thickness independent of the stirring. Furthermore, we observed that stirring could cause the delamination and the breaking of the CNT carpet into the plating solution. Independently of the plating solution composition, we observed the beginning of a plateau that corresponds to the moment where the composite is totally covered by copper (Fig. 1.29a). This was mainly attributed to a decrease of the surface area that is available for Cu deposition while the CNT layer is progressively filled. Finally, we used pulsed plating in order to feed more efficiently the ions into the CNT layer while avoiding their delamination (Fig. 1.29b).

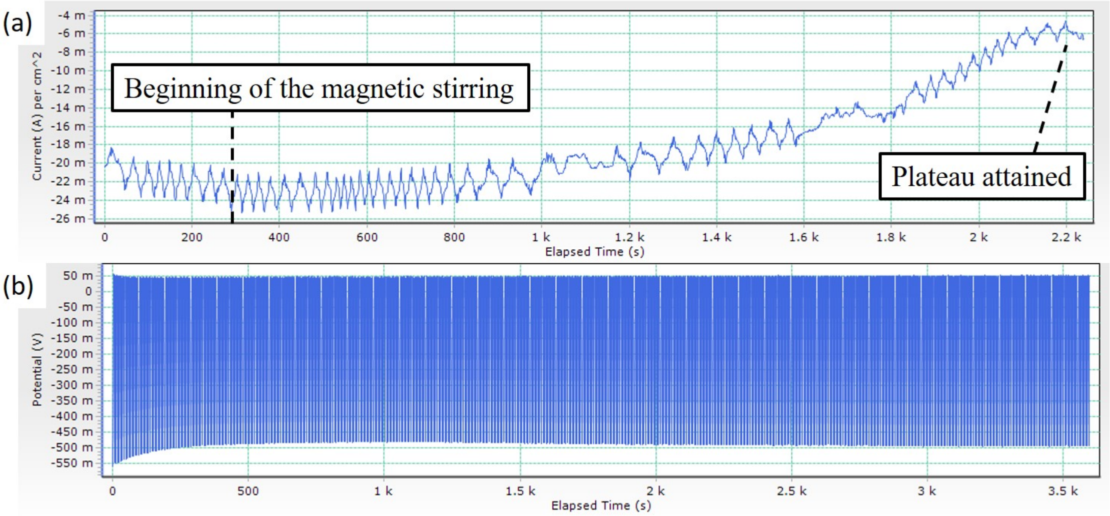

Figure 1.29. Plating curve of a Cu-CNT composite (on SiCu) obtained via (a) chronoamperometry (-0.2 V vs SCE in the optimized solution). Remark: the undulating current was an artifact caused by the reference electrode. (b) Plating curve of a Cu-CNT composite (on SiCu) obtained via pulsed plating (using parameters in Table 1.4).

Self-suspended composite foils

To measure the ampacity of the composite without any contribution of a substrate (e.g. of a thick copper foil substrate), we fabricated Cu-CNT composite self-suspended foils. Titanium drums are commonly used in industry to plate copper foils. Here, a titanium substrate was used to enable the peeling of the composite after the electroplating. Indeed, Ti oxide surface promotes an easy peeling of copper foils.[154] We observed that the native oxide formed on the Ti plate (exposed to air) was sufficient to promote such a peeling. Still, the composites peeled from the Ti substrates featured large defects of filling (Fig. 1.30a) because of the non-uniform initiation of the copper growth on the titanium. Indeed, looking at the surface of the composite (surface in contact with Ti), we observed large areas where copper growth was not well initiated (Fig. 1.30b). To promote a homogeneous growth of copper, we decided to coat the titanium surface with a thin layer of copper ($\sim$ 130 nm) by sputtering (parameters given in section A in appendix). Using such a layer, the composites were uniformly filled (Fig. 1.30c,d). When the composite thickness decreased, it became increasingly difficult to peel the foil without breaking it. Still, we managed to peel very thin composite foils without damaging them (e.g. a $\sim$ 2.5 μm thick foil is shown in Fig. 1.30e,f).

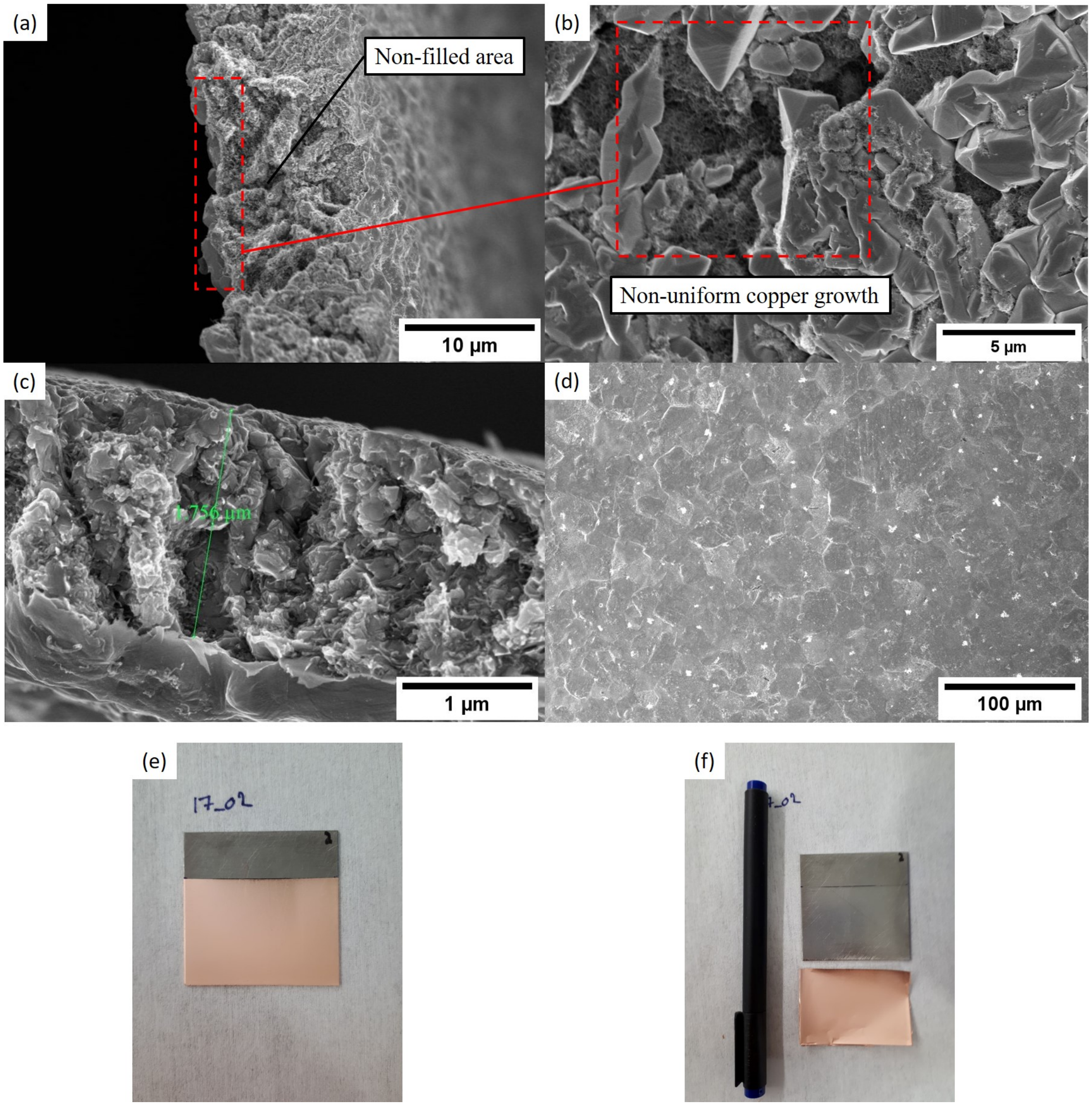

Figure 1.30. SEM (a) cross-section and (b) top-view (substrate side) of a composite foil peeled from Ti substrate. SEM (c) cross-section and (d) top-view (substrate side) of a composite foil peeled from Ti substrate pre-coated with copper. Photograph of a $\sim 2.5\ \mu$m thick Cu-CNT composite (e) before and (f) after peeling.

1.4.3 On CVD grown CNT

Electroplating on CVD grown CNT@PdaCu (200 μm long), which were sprayed on SiCu and TiCu, was carried in the same conditions (Table 1.4). Independently of the substrate, the composites were well filled and presented a CNT planar orientation. Fig. 1.31a show the composite obtained from the spray that is shown in Fig. 1.21b. Interestingly, we also managed to fabricate self-suspended composite foils (Fig. 1.31b) from spray made on a non-conductive substrate ($SiAl_2O_3$) by electrically contacting the CNT@PdaCu layer (200 μm long). The same thing was not possible with arc-discharged CNT@PdaCu due to a too high potential drop in the CNT layer.

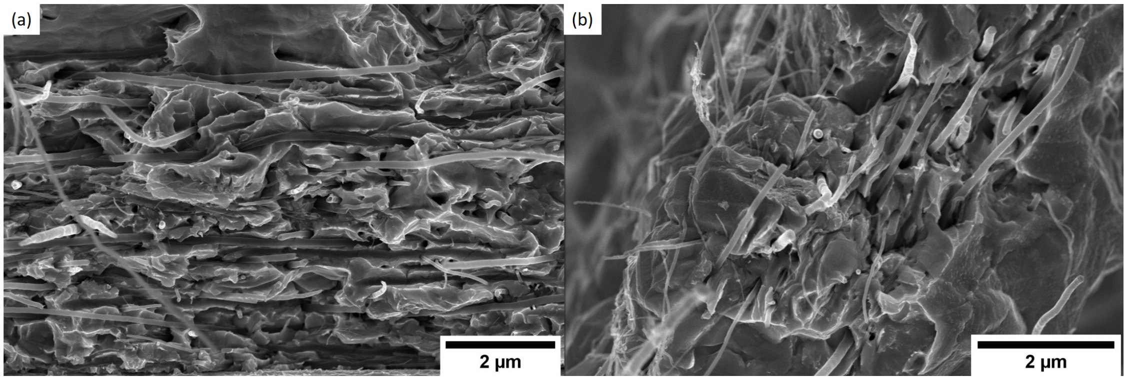

Figure 1.31. SEM cross-section of Cu-CNT@PdaCu (200 μm) composites obtained from a spray on (a) SiCu and (b) $SiAl_2O_3$.

1.4.4 **CNT volume percentage calculation**

As explained in our paper,[155] "the volume percentage of CNT (CNT vol. $\%$) of the composites can be calculated using

$$vol.\% = \frac{t_c - ((\frac{m_c - m_{cnt}}{A})/\gamma_{cu})}{t_c} \tag{1.1}$$

where t_c is the thickness of the composite, m_{cnt} is the mass of the CNT carpet, m_c is the mass of the composite, A is the area of the sample, and γ_{cu} is the density of Cu (8.96 g.cm^{-3})". The vol. $\%$ of CNT obtained in our Cu-CNT@PdaCu composites (Fig. 1.32) (arc-discharged CNT) was low (2.5$\%$ in average). Measured vol. $\%$ were sometimes very high or negative. This is because the mass of our CNT is low (few milligrams per substrate) in comparison to the mass of the deposited copper (several grams), and the error of mass measurement can easily lead to such inconsistencies. The calculated CNT vol. $\%$ in the composite layer could be slightly under-evaluated as a thin crust of pure copper is inevitably electroplated on the top of the Cu-CNT composite.

The CNT vol. $\%$ of composites containing CVD grown CNT@PdaCu was even more difficult to reliably evaluate as the measurements often led to negative values. Based on the maximum measured value, we considered that the CNT vol. $\%$ was less than 10$\%$ in these composites.

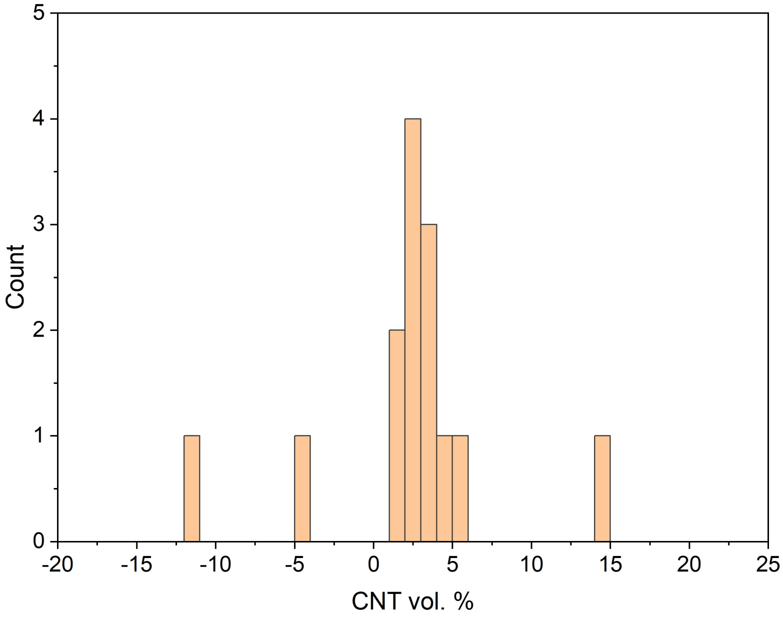

Figure 1.32. Distribution of calculated CNT vol. % in the Cu-CNT@PdaCu composites (arc-discharged).

1.5 CU-CNT COMPOSITE WITH HIGH CNT VOLUME PERCENTAGE

Our strategy to increase the CNT vol. % of the composites consisted in lowering the CNT layer porosity by using compression of the CNT layer before electroplating. Furthermore, we observed that the undulating morphology was mitigated by compression at 600 kg.cm^{-2} during 5 min (between a SiCu and a $SiAl_2O_3$ substrate), though few holes were still visible (Fig. 1.33).

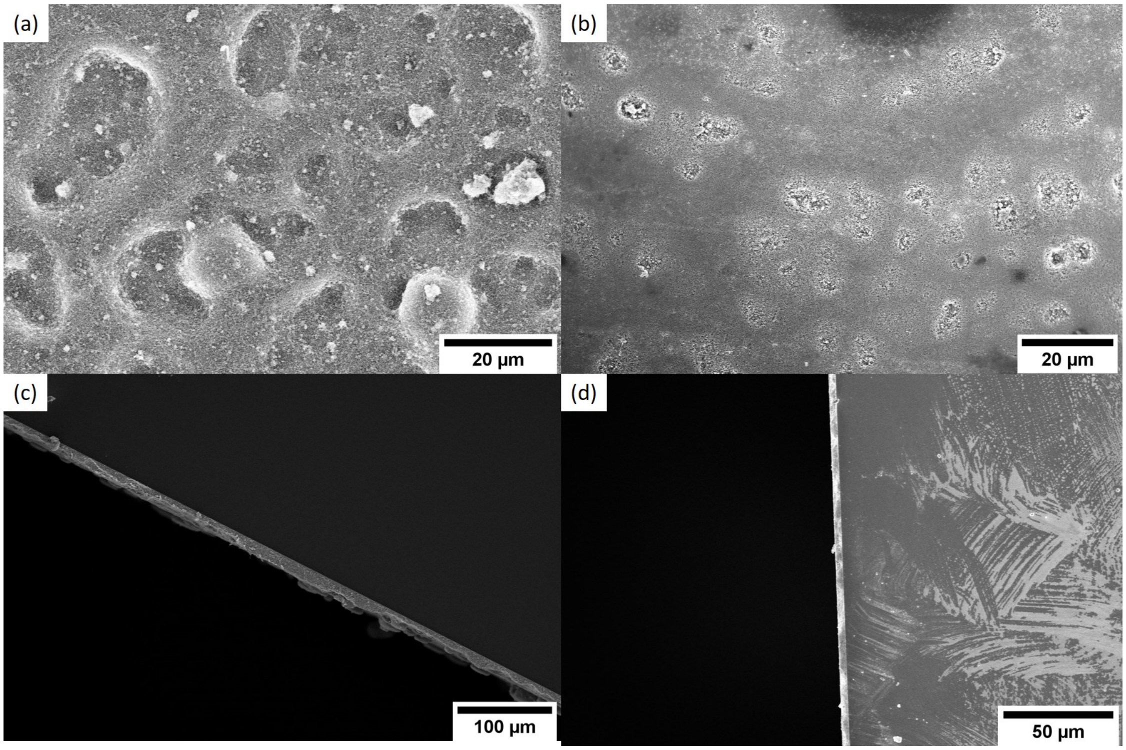

Figure 1.33. SEM images of arc-discharged CNT@PdaCu (a, c) before and (b, d) after compression at 600 kg.cm^{-2} during 5 min.

We compressed (arc-discharged) CNT@PdaCu layers at 200, 400, and 600 kg.cm^{-2} during 5 min and measured their thickness before and after compression (Fig. 1.34d). We defined the degree of compression as the ratio t_1/t_2 where t_1 and t_2 are the layer thicknesses before and after compression, respectively. We observed (Fig. 1.34a) that a pressure of 200 kg.cm^{-2} does not affect the film thickness while the thickness is divided by $\sim$ 1.4 and $\sim$ 4.2 (in average) after compression at 400 and 600 kg.cm^{-2}, respectively. Acknowledging the volume change of the CNT layer after compression at 600 kg.cm^{-2}, we calculated a porosity of at least 76% in the sprayed CNT layers. Indeed, this value is a lower bound assuming that the CNT layer is not necessarily perfectly packed after a compression at 600 kg.cm^{-2}. Then, we characterized the thickness of the Cu-CNT composite layer (t_3) after electroplating (using plating parameters in Table 1.4). We observed that t_3 was always higher than t_2, highlighting a swelling of the CNT layer during the electroplating (Fig. 1.34b). In addition, the swelling increased proportionally to the degree of compression, reaching a value $\sim$ 5.9 times that of the thickness of the CNT layer compressed at 600 kg.cm^{-2}.

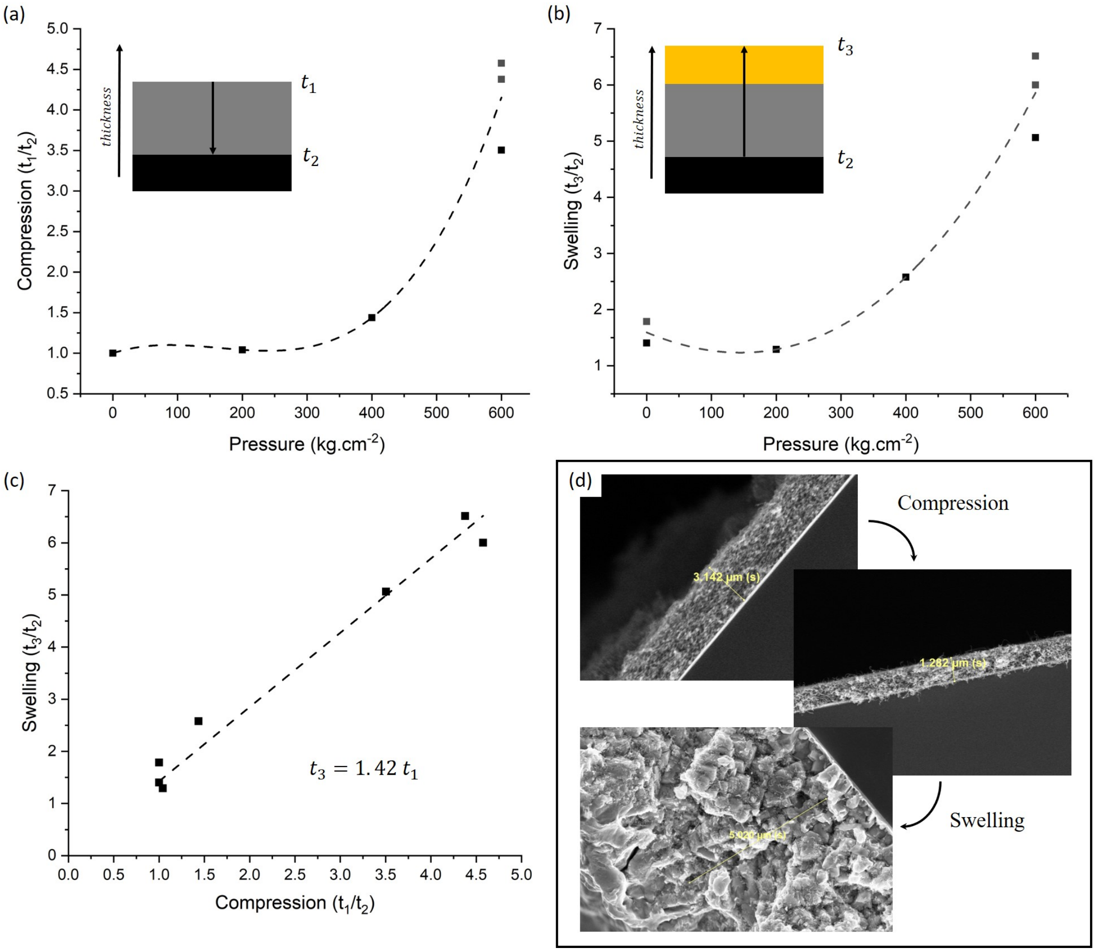

Figure 1.34. (a) Degree of compression of the CNT layer as a function of the pressure. (b) Degree of swelling of the compressed CNT layer after electroplating. (c) Degree of swelling as a function of the degree of compression. (d) Example of a CNT layer compression followed by a swelling after electroplating.

In fact, we observed a linear relation (Fig. 1.34c) between the degree of compression and the degree of swelling. By imposing $b = 0$ for $t_1 = 0$ in the $t_3 = at_1 + b$ expression, we used a least square linear regression to obtain

$$t_3 = 1.42t_1 \tag{1.2}$$

This relation highlights that the thickness of the composite layer is independent of the degree of compression of the CNT layer and is always 1.42 times higher than the one of the sprayed layer. Taking into account the swelling and based on the porosity of the sprayed CNT layer (calculated above: 76%), we determined an upper bound of 17% vol. of CNT which can be reached in the Cu-CNT composites (arc-discharged CNT):

$$\begin{cases} \dfrac{V_{CNT}}{V_{layer}} \leq 0.24 \\ \dfrac{V_{composite}}{V_{layer}} = 1.42 \end{cases} \implies \qquad \frac{V_{CNT}}{V_{composite}} \leq 0.17 \tag{1.3}$$

where V_{layer} is the apparent volume of the CNT layer (including porosity), V_{CNT} is the true CNT volume (without porosity), and $V_{composite}$ is the volume of the Cu-CNT composite. Remembering that CNT are principally located at the grain boundaries (Fig. 1.28d), we made the hypothesis that the grain size could be correlated with the magnitude of the swelling. Indeed, larger grains would lead to a lower amount of grain boundaries, lowering the CNT vol. $\%$. However, we also observed that coated CVD grown CNT layers swell significantly when in contact with ethanol, or water. Fig. 1.35 shows an example of such a carpet swelling from a thickness of $\sim$ 1 mm to $\sim$ 1 cm when immersed in ethanol.

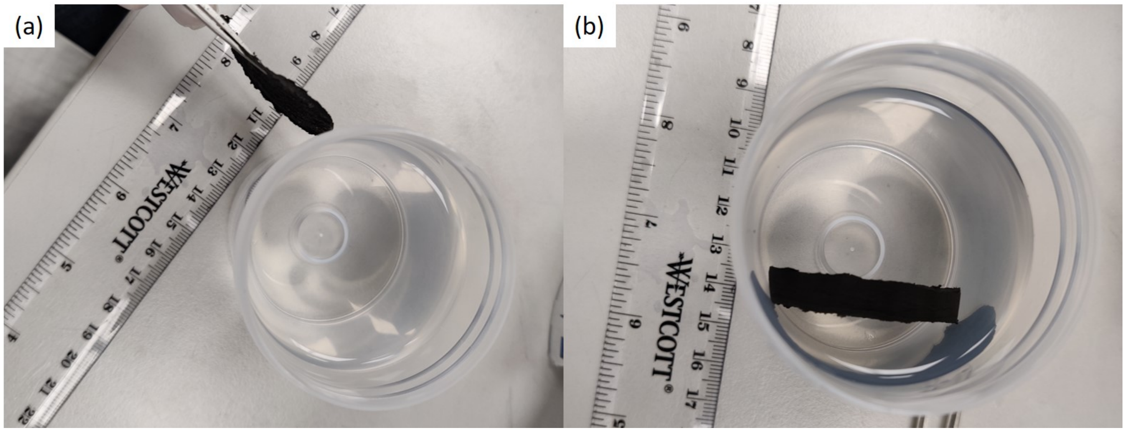

Figure 1.35. Photographs of a coated CVD grown CNT (800 μm long) layer (thickness $\approx$ 1 mm) before (a) and after (b) immersion in etOH (thickness $\approx$ 1 cm).

Based on this observation, we made the hypothesis that the swelling was mainly caused by the infiltration of the plating solution into the CNT network. Therefore, we developed a system (Fig. 1.36a,b) to mechanically maintain the CNT in their compressed state while being electroplated.

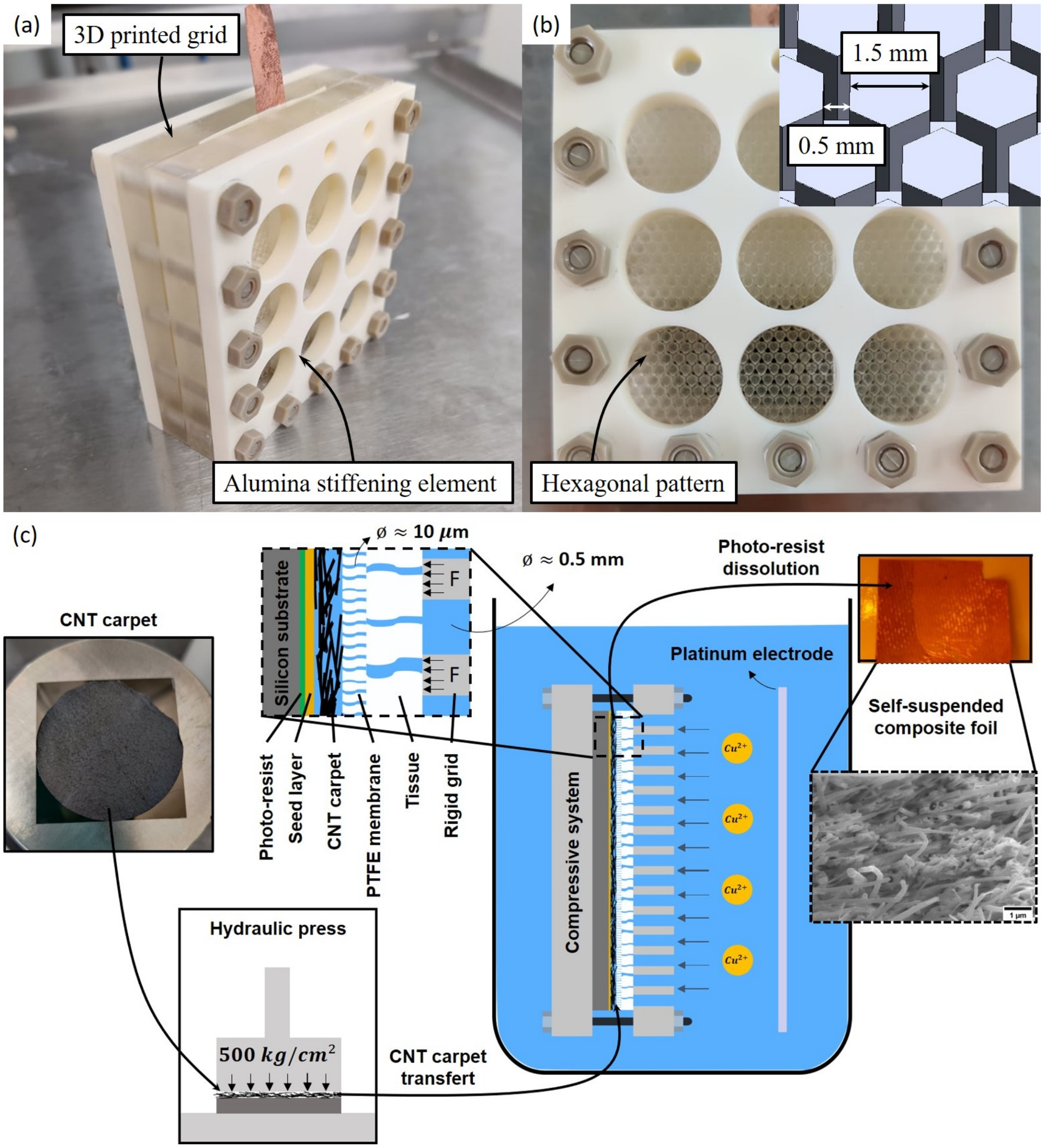

Figure 1.36. (a,b) Photographs of the compressing system. (c) Schematic of the Cu-CNT composite fabrication (high CNT vol. %) using a CNT layer compression in hydraulic press followed by electroplating in the compressing system. In the inset, F represent the force applied by the stiffening grid, the diameter of the pores in the PTFE membrane is 10 μm.[155] See section C.1 for information about the substrate preparation.

As described in our published paper,[155] the method of fabrication of Cu-CNT composites with high CNT vol. % can be described by the Fig. 1.36. The CNT layer is firstly compressed in a hydraulic press between two pieces of $SiAl_2O_3$. Afterwards, the free standing CNT carpet is placed onto the desired plating substrate: TiCu, SiCu, ... Next, the sample is clamped in the compression system and immersed in the electroplating solution (Table 1.4). Pulsed electroplating is then used (35 mA.cm^{-2}, 0.02/0.1s - ON/OFF) until the CNT layer is completely filled. The compression system is constituted of

- An external alumina stiffening element allowing the passage of the electrolyte and ensuring a homogeneous stress distribution on the sample (Fig. 1.36a,b).

- A 3D printed resist grid ("MJM high detail resin") as a second element to compress the sample, the 3D printing technique allowing to produce a grid with a more refined pattern compared to the alumina grid. In this work, the pattern was hexagonal, letting the electrolyte going through channels of 0.5 mm wide, increasing the surface of contact with the sample (compared to the alumina grid) and promoting a better stress distribution over the sample (Fig. 1.36b).

- A hydrophilic PTFE membrane (Omnipore - 10 μm pore size - 80 μm thick) that is directly in contact with the CNT layer. The goal of the membrane is to reduce the pore size to distribute even more homogeneously the stress over the CNT layer while keeping a sufficient penetration of the plating solution into the CNT layer. Various types of membranes were unsuccessfully tested, though this particular one was especially effective. We believe that the high membrane porosity ($\geq 80\%$) and its hydrophilic feature are significant to achieve a successful plating.

- A layer constituted of tissue (knitted polyester - VWR) that is placed between the PTFE membrane and the 3D printed grid. It has two purposes. It constitutes a layer with an intermediary pore size: without tissue, the soft PTFE membrane was observed to swell locally in the open channels of the 3D printed grid. We also observed that the tissue is instrumental for the distribution of the plating solution below the hexagonal "pillar" of the grid. Indeed, when the tissue was removed, the plating solution was not able to penetrate below the hexagonal pillar, leading to the growth of an hexagonal mesh. This is interesting as this layer can be modulated to promote the fabrication of either a plain composite foil or a patterned composite foil.

Using the compression system, the current density had to be reduced in order to obtain a composite with a high degree of metal filling. We believe that the tortuous compressing system lowers the rate of migration of ions towards the sample. Interestingly, the compression system enabled the use of sonication during the electroplating because it maintains the CNT layer integrity (preventing the CNT to be dispersed in solution by the ultrasounds). The sonication accelerates the migration of ions during electroplating.[156] When the electroplating is finished, the PTFE membrane can be slightly attached to the composite surface because copper can start to grow inside its pores. In this case, the PTFE can be removed by peeling followed by a gentle mechanical polishing. To overcome this problem, it would be interesting to find an equivalent membrane able to be easily dissolved in a solvent.

The CNT layer swelling was efficiently prevented when using the compression system, leading to Cu-CNT@PdaCu composites with 40-45$\%$ of CNT in volume. This is a huge improvement compared to the previous composites (Fig. 1.31a compared to Fig. 1.37a).

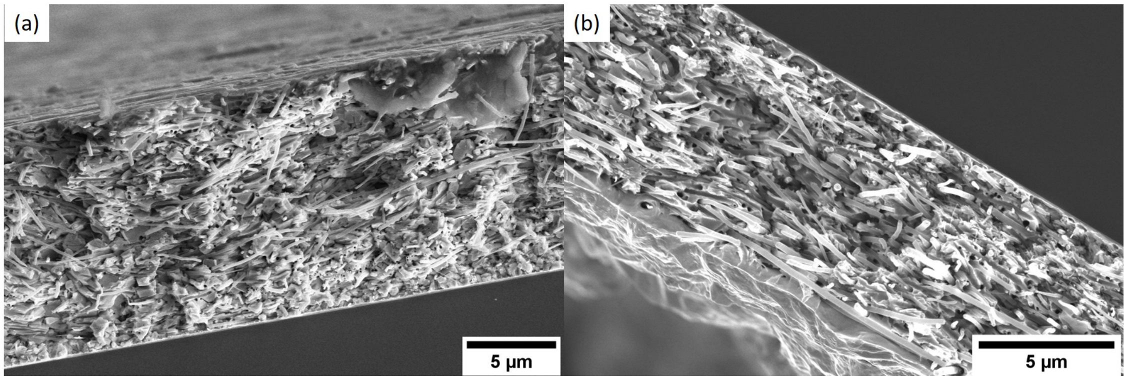

Figure 1.37. (a) Cu-CNT composite (CNT@PdaCu 800 μm) and (b) Cu-CNT composite (CNT@PdaCu-800 μm annealed at 673 K in Ar) obtained using the compression system.

In chapter 2, we will discuss the benefits of annealing the CNT@PdaCu carpet before electroplating. Here, we report that electroplating on annealed CNT@PdaCu was also possible up to annealing temperature of 873 K (in Ar) for both type of CNT (CVD grown and arc-discharged CNT). Fig. 1.37b presents an example of composite obtained using the compression system on CNT@PdaCu carpet (800 μm) annealed at 673 K in Ar (more information about the CNT annealing method is given in the appendix B.1). Beyond 873 K, the copper starts to grow preferentially on the top of the CNT layer, which may be attributed to the degradation of the Pda coating by the annealing (especially regarding an increase of the CNT hydrophoby).

1.6 COMPOSITE PATTERNING

As mentioned previously, we can adapt the compressing system in order to grow a patterned Cu-CNT composite instead of a plain foil. It is worth noting that the 3D grid was designed according to patterns typically used in lightning strike protections.[157] A patterned sample comprising sprayed CVD grown CNT@PdaCu (200 μm) was thus fabricated in the context of the lightning strike protection characterization (see chapter 4). After electroplating, black spots were seen on the sample surface (Fig. 1.38a) and correspond to poorly filled CNT areas that were in contact with the hexagonal pillars (Fig. 1.38c). Those CNT can be wiped off (Fig. 1.38b), leaving a Cu-CNT composite mesh (Fig. 1.38d). Interestingly, it enables a straightforward fabrication of patterned composites compared to methods usually required to fabricate these type of metal meshes (e.g. by stamping the copper foil).

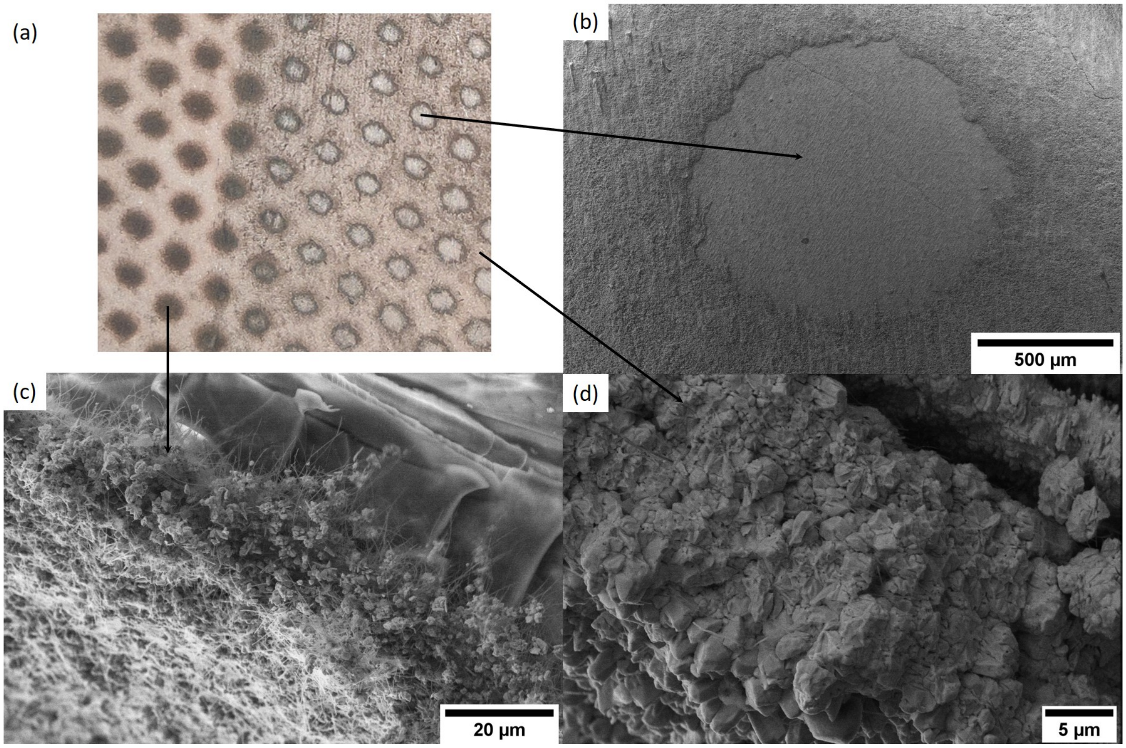

Figure 1.38. (a) Photograph of a composite mesh, (b) SEM top-view of an empty area after CNT removal, (c) SEM cross-section of the a CNT area poorly filled with copper before CNT removal, and (d) SEM cross-section of the Cu-CNT composite.

1.7 ALTERNATIVE CNT COATING AND ALTERNATIVE METALS

As previously discussed (section 1.2.5), we looked for an alternative coating enabling the fabrication of Cu-CNT composites. In this regard, we managed to fabricate a Cu-CNT composite by plating a carpet of arc-discharged CNT coated with Cu-doped tannic acid (CNT@TACu) using chronoamperometry in a solution composed of $CuSO_4.5H_2O$ (0.1 M), H_2SO_4 (0.1 M, pH = 1) at - 0.2 V vs SCE. Yet, the composite seemed more porous than with CNT@PdaCu (Fig. 1.39a,b). In addition, the composite had a thickness of about 5.4 μm and more investigation is required to know if this type of coating would be as efficient as Pda for the fabrication of thicker composites.

Fe plating		Ni plating	
Chemicals	Concentration	Chemicals	Concentration
$FeSO_4.7H_2O$	0.1 M	$Ni(SO_3NH_2)_2.4H_2O$	1.25 M
H_2SO_4	0.1 M	H_3BO_3	0.5 M
Plating parameters	Value	Plating parameters	Value
Temperature	313 K	Temperature	323 K
Chronoamperometry	-1.05 V vs SCE (∼ -6 mA.cm^{-2})	Pulsed current	-35 mA.cm^{-2} (0.02/0.1s - ON/OFF)

Table 1.5. Conditions of electroplating used to fabricate Ni/Fe-CNT composites.

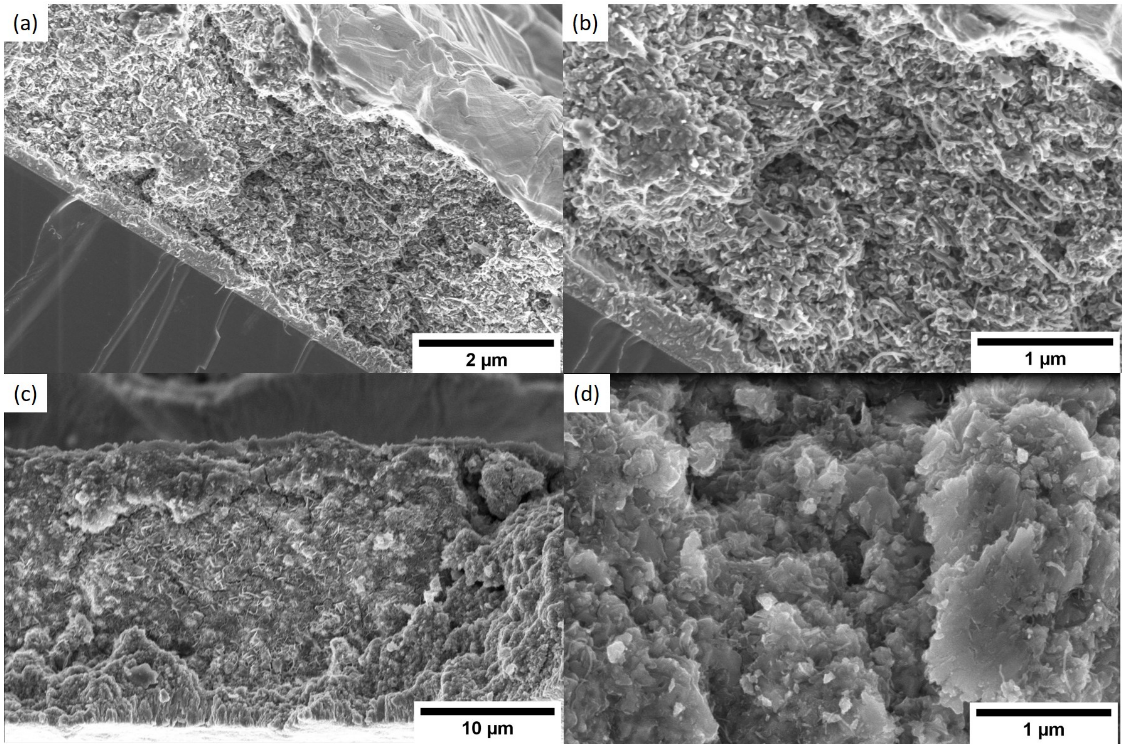

Figure 1.39. (a,b) SEM cross-section and zoom of a Cu-CNT@TACu composite. (c,d) SEM cross-section and zoom of a Fe-CNT@PdaCu composite.

Alternative metals had also been investigated. Using a Fe-doped Pda coating made using the same conditions than for the Cu-doped Pda ($CuSO_4.5H_2O$ being replaced by $FeSO_4.7H_2O$ in the coating solution - 0.417 g.L^{-1}), we attempted to plate Fe on the CNT@PdaFe layer but it led to the deposition of a Fe crust on the CNT layer. This was attributed to the observed higher hydrophoby of the CNT@PdaFe layer compared to CNT@PdaCu. Still, a Fe-CNT composite was successfully fabricated using PdaCu as a functional CNT chemical functionalization (Fig. 1.39c,d), the plating conditions being given in Table 1.5. In addition, we also investigated the properties of Ni-CNT composites (chapter 3). Such composite was fabricated with CNT (800 μm) coated with Ni-doped Pda, using the compression system (Fig. 1.36) and the plating parameters given in Table 1.5. The CNT vol. % of such Ni-CNT composite was estimated to be around 43%.

1.8 CHAPTER SUMMARY

In this chapter, we presented an innovative method to fabricate plain and patterned Cu-CNT composites. In our approach, CNT are functionalized with Cu-doped polydopamine, deposited as a CNT carpet (spray or filtration) and embedded into copper via electroplating. For the first time, Cu-CNT composites having a thickness reaching ~ 45 μm were fabricated using only an aqueous plating solution while displaying a high degree of copper filling. The spray method was optimized and up-scaled in order to deposit uniform layers of CNT (length of 2-20 μm and 200 μm) on large surface (up to 8 inches wafers). Indeed, we showed that the uniformity of the CNT layer was instrumental to fabricate Cu-CNT composites free from defects. In addition, we developed an alternative filtration method to fabricate carpet integrating longer CNT (800 μm).

We demonstrated that the doping of the polydopamine coating by Cu ions was disruptively efficient to promote a homogeneous growth of copper inside the CNT carpet. Addressing the current Cu-CNT fabrication challenges, the Cu-doped Pda coating promoted the penetration of the aqueous plating solution inside the CNT layer while acting as an efficient seed layer for the metal growth. In addition, the Pda coating greatly enhanced the dispersion of the CNT in the spraying solution, contributing to the high uniformity of the sprayed layers.

We also evidenced a swelling of the CNT layer during the electroplating leading to a low CNT vol. % in the composites (less than 10%), independent of the initial porosity of the CNT layer. Addressing this problem, we developed a new system maintaining CNT layers in their compressed state during the electroplating and leading to a CNT vol. % around 40-45%, which is a remarkable achievement. We also report the possible fabrication of Cu-CNT composites from CNT@PdaCu carpets annealed (at $T \leq 873$ K in Ar) prior to the electroplating.

An effort was made in order to fabricate self-suspended composite foils using substrate materials typically used in industry. In particular, we managed to fabricate and peel-off a very thin composite foil (~ 2.5 μm) from a titanium substrate. In addition, we showed the fabrication of self-suspended foils using an insulating substrate and by taking electrical contacts directly onto the CNT carpet (with CNT having a length ≥ 200 μm). For the first time, we also report the fabrication of a self-suspended Cu-CNT composite foil by using electroless plating (on a CNT coated with un-doped polydopamine).

Showing the flexibility of our proprietary method, we also managed to fabricate Fe-CNT and Ni-CNT composites using a Cu-doped and Ni-doped polydopamine coating, respectively. In addition, we showed that tannic acid may be an alternative coating molecule for the fabrication of Cu-CNT composites.

Chapter 2

Characterization of the CNT materials

2.1 INTRODUCTION

As reported in the background chapter, the properties of CNT are versatile, and targeting a low TCR and a low resistivity (desirable in the Cu-CNT composites), we characterized our CNT systems. In addition, an effort was made to increase the conductivity of the CNT layer, i.e. optimize the electrical properties of the polydopamine coating. In chapter 1, the presence of the coating on the CVD grown CNT was indirectly deduced but could not be undoubtedly observed via STEM. We thus investigated the surface chemistry and topography of the functionalized CNT before and after annealing, as well as their electrical properties. As discussed in our paper[158], "Li et al. reported the nucleation of copper particles from Cu-doped Pda when annealed, and an increased conductivity of the Pda due to the copper nuclei[159]. Daneshvar et al. showed that copper particles at the surface of functionalized CNT can enhance the conductivity of CNT carpets. In particular, they demonstrated a higher affinity between copper and CNT when a thiol-based functionality was used. However, electroless plating was used to grow the Cu particles on the CNT surface and the use of palladium seeding was required.[143]" In contrast, we report here the nucleating of metallic copper on the CNT surface by annealing of CNT@PdaCu carpets. It was thus interesting to investigate this system and evaluate their change of resistance and TCR upon annealing.

In a second time, we also investigated the possibility of increasing the CNT carpet conductivity by reducing the Pda coating amount. The change of TCR/resistance of the CNT carpets submitted to a compression step was also investigated as compression is used in the fabrication of the Cu-CNT composites. In chapter 3, CNT@PdaNi are used to fabricate Ni-CNT composites. Therefore, we characterize here the electrical properties of these CNT. Finally, we compare the specific resistivity of our coated systems the one containing oxidized CNT.

2.2 CHARACTERIZATION OF CARBON NANOTUBES COATED WITH CU-DOPED POLYDOPAMINE BEFORE AND AFTER ANNEALING

The following section is quoted from our published paper[158] and the precise methodology used in the paper is given in appendix (section B.1).

"XPS is a powerful mean to determine the oxidation state of metals and their oxides, hence it was used to investigate the mechanisms of growth of copper particles upon annealing of Cu-doped Pda coated CNT. Fig. 2.1 displays the Cu 2p and Cu LMM spectra of Cu-doped Pda before and after annealing at 673 and 773 K."

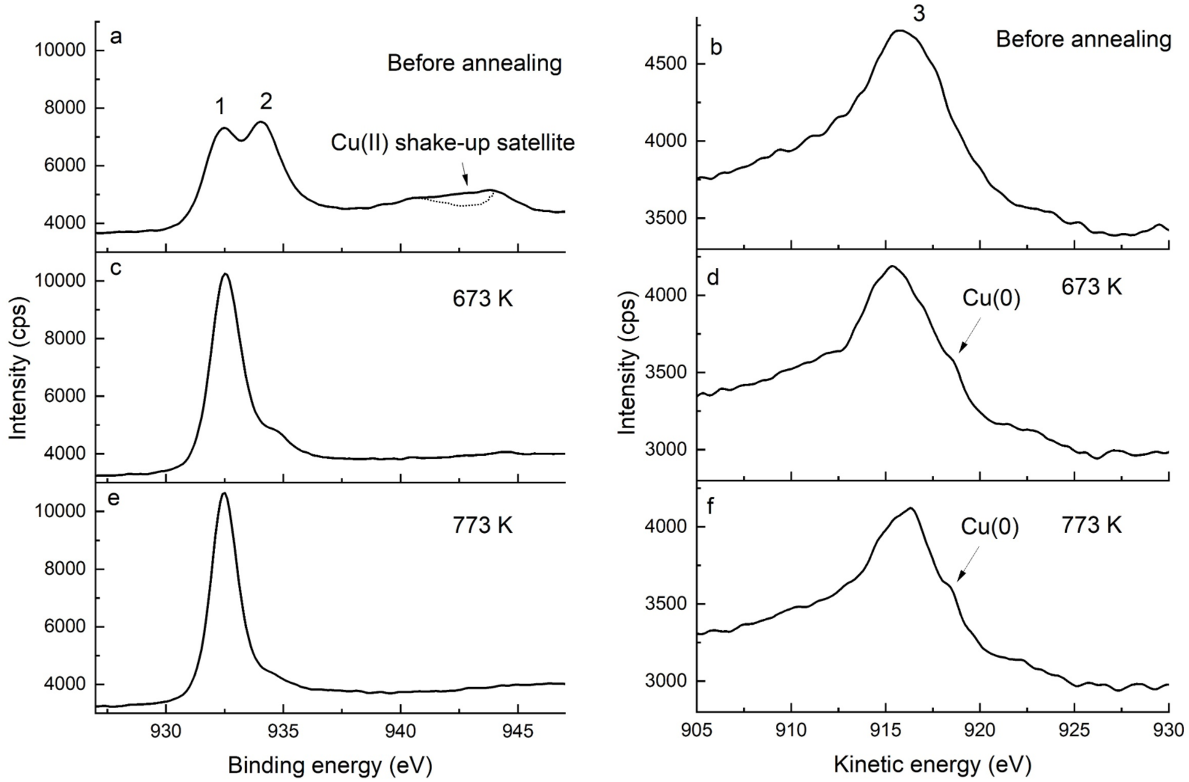

Figure 2.1. Cu 2p (left) and Cu LMM (right) spectra of (a-b) CNT@PdaCu, (c-d) CNT@PdaCu annealed at 673 K and (e-f) CNT@PdaCu annealed at 773 K. (1) peak at 932.45 eV related to Cu(I) species, (2) peak at 934.0 eV related to Cu(II) species, and (3) peak at 915.8 eV assimilated to Cu(I) and Cu(II) species.[158]

"The presence of copper in the Pda coating of CNT@PdaCu is confirmed by XPS (Fig. 2.1a,b). The shake-up satellite (Fig. 2.1a) is a clear indication of the presence of Cu(II).[160] Peak 1, at

	C %	Cl %	Cu %	N %	Na %	O %
Oxidized CNT	97.5	0.0	0.1	0.3	0.0	2.1
CNT@Pda	76.4	0.2	0.0	5.1	4.2	14.1
CNT@PdaCu	69.0	0.2	2.2	5.8	3.8	19.0
CNT@PdaCu 673 K	77.5	1.3	2.0	7.2	2.1	9.9
CNT@PdaCu 773 K	81.3	1.1	1.5	6.5	2.0	7.6

Table 2.1. XPS elemental composition in atomic %.[158]

932.45 eV, is attributed to Cu(I). The possibility of Cu(I) being present as CuCl was excluded using the elemental composition (Table 2.1), which showed that CuCl cannot represent a major contribution of the Cu 2p line. One can notice that the peak position has slightly shifted compared to the Cu_2O bulk value (932.18 eV[160]). This energy shift may be attributed to Cu(I) ions coordinated to catechol/quinone/amine groups of Pda.[123,125] Similarly, we attribute the peak at 934 eV to Cu(II) being coordinated by Pda. Indeed, the lack of indentation in the shake-up satellite (see dotted line in Fig. 2.1a) precludes the presence of CuO.[160] We might conclude that Cu(II) and Cu(I) are coordinated in the polydopamine coating and that the Cu(II) introduced from $CuSO_4$ is partially reduced into Cu(I) during the dopamine polymerization. This reduction is attributed to the several oxidation steps involved in the dopamine polymerization. In particular, the oxidation of catechol to quinone releases two electrons which can reduce the chelated metal ions.[125,161]"

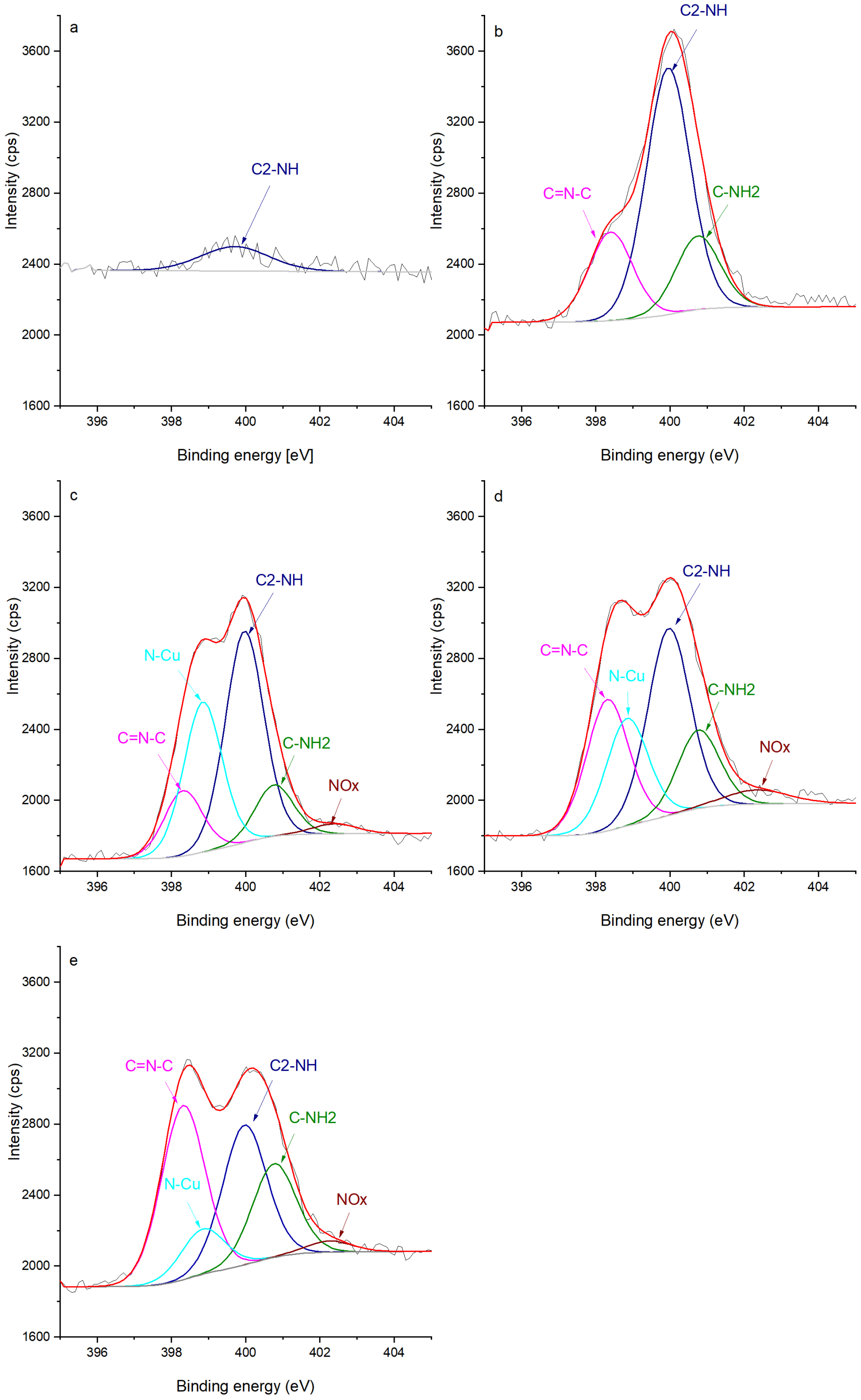

Figure 2.2. N 1s spectra of (a) oxidized CNT, (b) CNT@Pda, (c) CNT@PdaCu, CNT@PdaCu annealed at (d) 673 K and (e) 773 K.[158]

	C=N-C %	N-Cu %	C2-NH %	C-NH2 %	NOx %
Oxidized CNT	0.0	0.0	100.0	0.0	0.0
CNT@Pda	21.9	0.0	60.9	17.2	0.0
CNT@PdaCu	13.7	30.5	43.3	10.1	2.4
CNT@PdaCu 673 K	25.4	20.2	35.9	14.5	4.1
CNT@PdaCu 773 K	38.4	8.8	30.6	19.6	2.7

Table 2.2. N 1s peak components and their relative contribution in the peak fit %.[158]

"Additionally, the chemical evolution of the samples can be depicted from the N 1s, C 1s and O1s spectra (Fig. 2.2, Fig.2.3 and Fig. 2.4 respectively). The reference sample (Fig. 2.2a) is featured by CNT doped with nitrogen due to oxidation in nitric acid (peak at 400±0.1 eV associated to C2-NH).[162–165] One can recall that in the CNT@Pda sample (Fig. 2.2b), the C2-NH (pyrrolic nitrogen) and C=N-C (pyridinic nitrogen) components feature cyclic units of Pda as formed via the Michael addition reaction.[125] The CNT@PdaCu sample (Fig. 2.2c) features a peak at 398.8 eV attributed to nitrogen copper interactions.[162,164,166] Interestingly, the relative contribution of the Cu-N component (Table 2.2) decreases upon annealing from 30.5% (CNT@PdaCu) to 20.2% (CNT@PdaCu annealed at 673 K) and towards 8.8% (CNT@PdaCu annealed at 773 k) meaning that the amount of Cu ions chelated in Pda decreases with the annealing temperature. In the Cu 2p spectra (Fig. 2.1c,e), the thermal annealing of CNT@PdaCu at 673 and 773 K shows a drastic decrease of the shake-up satellite and peak at 934 eV, highlighting that Cu(II) is disappearing. The Cu LMM spectra (Fig. 2.1d,f) feature a shoulder at 918.5 eV, corresponding to the formation of Cu(0) during annealing.[160] We also observe a shift of peak number 3 from 915.8 to 916.4 eV at 773 K. We attribute this shift to the progressive surface oxidation of the grown copper particles (Fig. 2.5) into Cu_2O (which has an expected peak position of 917.0 eV).[167,168] As seen above in the N 1s spectra, the Cu-N chelation component still represents 8.8% of the nitrogen amount after annealing at 773 K. We might thus conclude that, after annealing at 773 K, Cu(I) is still partially coordinated in Pda while a part of Cu(I), in the Cu_2O form, appears at the copper nuclei surface due to exposition to air. The presence of C=N-C, N-Cu, C2-NH, C-NH2 components in figures 2.2d,e confirms the preservation of the Pda coating after annealing at 673 and 773 K. Nevertheless, the Pda structure is altered by the annealing; the C=N-C bonding (Table 2.2) in annealed CNT@PdaCu (25.4 and 38.4% at 673 and 773 K, respectively) is significantly higher than in non-annealed CNT@PdaCu (13.7%). The C2-NH contribution in CNT@PdaCu (43.3%) decreases when annealed at 673 and 773 K (35.9 and 30.6%, respectively). These results suggest a progressive suppression of pyrrolic nitrogen in favor of pyridinic nitrogen during annealing.[169,170]"

	CNT	C-(C,H)	C*-COO	C-N	C=N	C-O	C=O O-C-O	O-C=O	$\frac{C-O}{C=O}$
CNT@Pda	57.2%	16.9%	1.9%	7.5%	1.0%	8.2%	5.3%	1.9%	1.5
CNT@PdaCu	40.2%	19.2%	3.4%	9.2%	1.1%	15.2%	8.3%	3.4%	1.8
CNT@PdaCu 673 K	52.3%	26.1%	2.0%	6.3%	1.4%	4.6 %	5.2%	2.0%	0.9
CNT@PdaCu 773 K	61.8%	22.4%	1.5%	5.4%	1.7%	2.1%	3.6%	1.5%	0.6

Table 2.3. C 1s peak components, their relative contribution in the peak fit (%) and ratio $\frac{C-O}{C=O}$.[158]

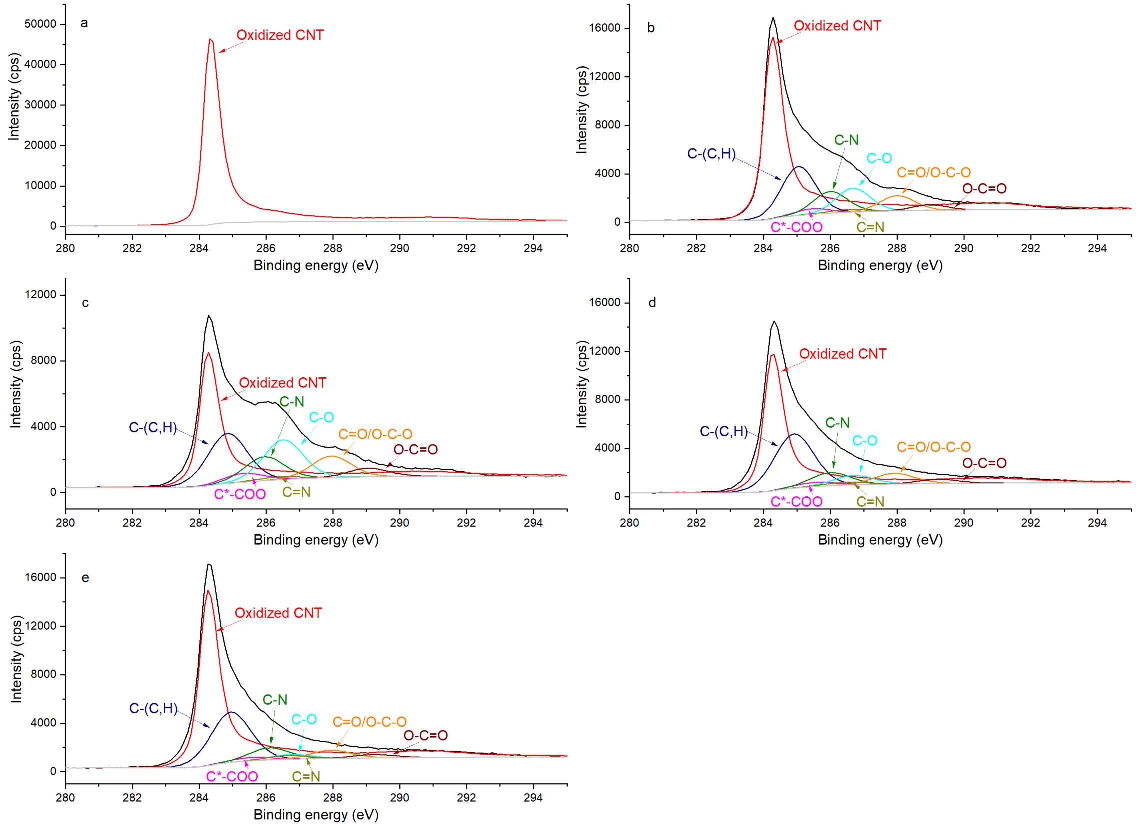

Figure 2.3. C 1s spectra of (a) oxidized CNT, (b) CNT@Pda, (c) CNT@PdaCu, (d) CNT@PdaCu annealed at 673 K and (e) CNT@PdaCu annealed at 773 K.[158]

"The lower ratio (Table 2.3) of C-O/C=O in CNT@Pda (Fig. 2.3b) than in CNT@PdaCu (Fig. 2.3c) suggests that catechol/semi-quinone groups are present in higher quantities than quinone when copper is coordinated in Pda. Barrett et al.[171] suggested that catechol groups could be partially protected by the coordination of metal ions during polymerization in alkaline conditions. Interestingly, when CNT@PdaCu samples are annealed at 673 and 773 K, the same ratio drops to 0.9 and 0.6, respectively, illustrating an even more important quinone component. We believe that the thermal treatment induces further oxidation of polydopamine providing a continuous source of electrons that enable the efficient reduction of copper ions as revealed by the detailed analysis of the XPS spectra of copper. This conclusion is further supported by carefully analyzing the O 1s spectra which evidences a drastic decrease of the C-O component of CNT@PdaCu (curve 1 in Fig. 2.4) after thermal treatment (curve 3-4 in Fig. 2.4). Finally, we could attribute the drop in oxygen (Table 2.1) from 19% before annealing to 7.6% after annealing at 773 K respectively to the catechol dehydration as suggested by Kong et al..[170]"

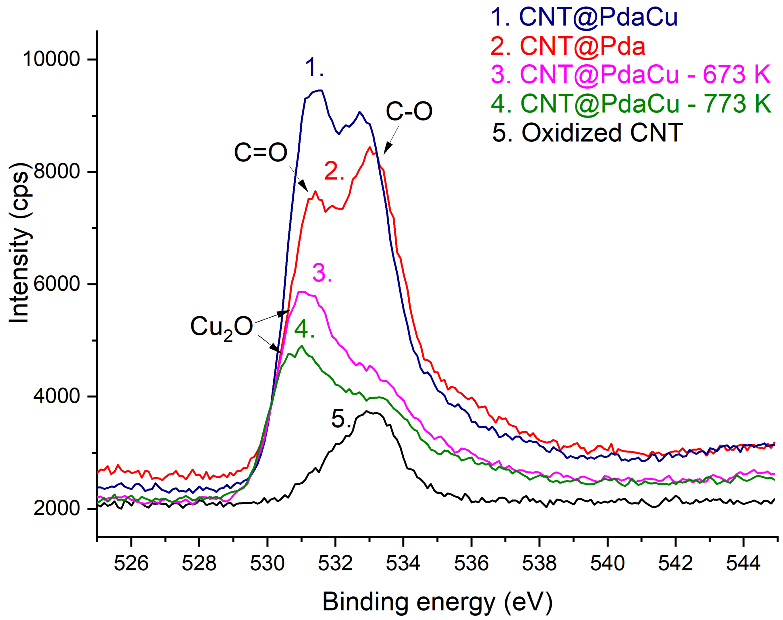

Figure 2.4. O 1s spectra of (1) CNT@PdaCu, (2) CNT@Pda, (3,4) CNT@PdaCu annealed at 673 and 773 K respectively and (5) oxidized CNT.[158]

"One can note an evolution of the O 1s peak shape for Pda-coated CNT (curve 2 and 5 in Fig. 2.4) which features an increase in both the O=C and O-C contributions, at 531.4 and 533 eV respectively,[172,173] corresponding to the catechol and quinone groups of the Pda. The Cu doping of the Pda coating (curve 1 in Fig. 2.4) leads to a higher component located at 531.4 eV and is attributed to Cu(II) chelated by Pda, as previously observed in the Cu 2p spectra. One can note a shift of this peak maximum towards 531.1 and 531.0 eV when samples are annealed at 673 and 773 K, respectively. This shift is attributed to the apparition of Cu_2O at the surface of the Cu nanoparticles as already seen in the Cu 2p spectra.[160,167,168,174,175]"

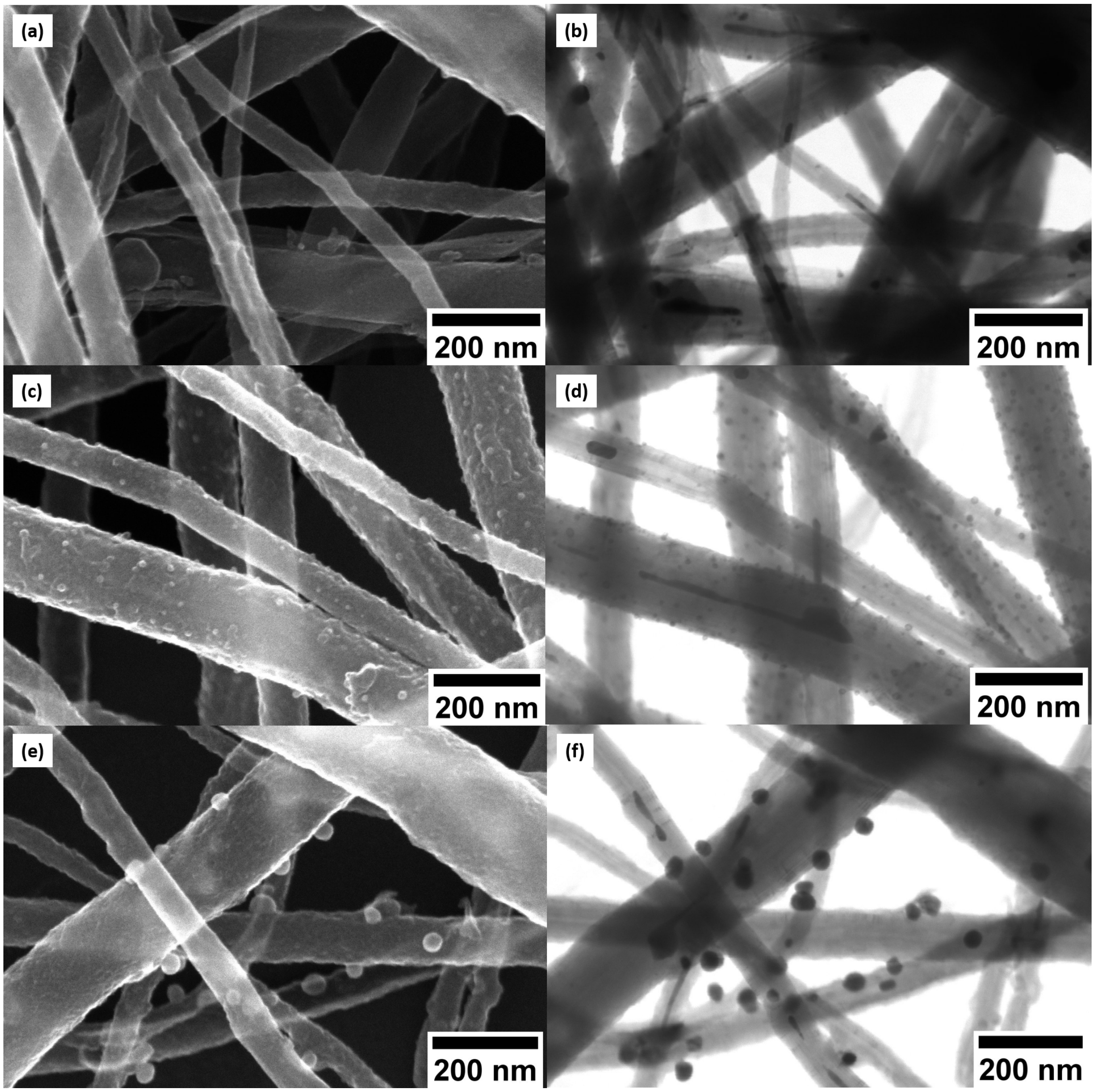

Figure 2.5. (a) SEM and (b) STEM image of CNT@PdaCu. (c) SEM and (d) STEM image of CNT@PdaCu annealed at 573 K. (e) SEM and (f) STEM image of CNT@PdaCu annealed at 773 K.[158]

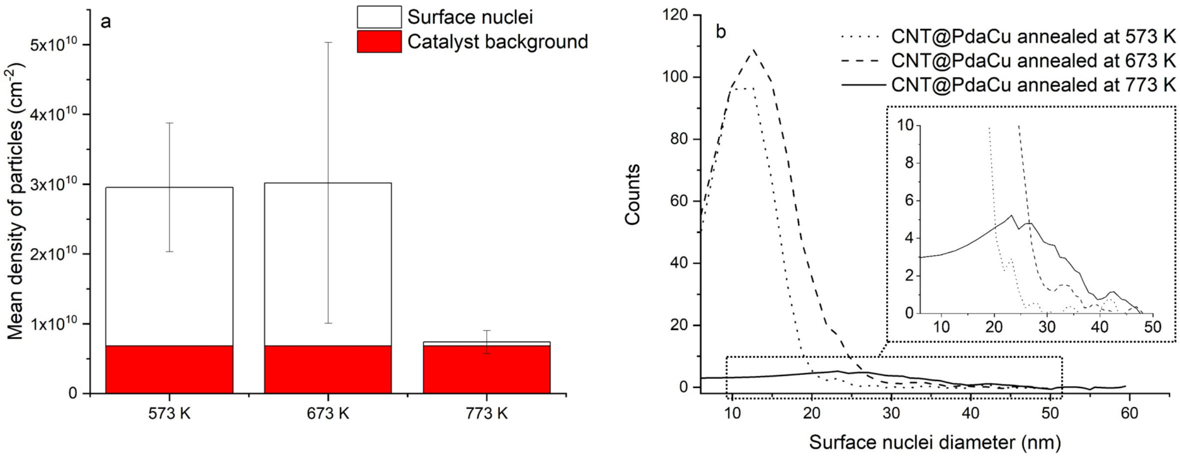

Figure 2.6. (a) Mean density of particles and (b) nuclei size distribution.[158]

"Figure 2.5a of CNT@PdaCu without annealing shows distribution of CNT with a diameter ranging from 33 to 195 nm. The same sample observed by STEM (Fig. 2.5b) shows inner particles (black spots) corresponding to typical catalysts used to grow CNT. We calculate the average diameter of catalyst being around 18 nm featuring a density of 6.8×10^{9} particles.cm^{-2} (Fig. 2.6a,b). Catalysts are present in all analyzed samples. Figure 2.5c (CNT@PdaCu annealed at 573 K) reveals the growth of nuclei rather than a homogeneous coating distributed over the CNT surface. The STEM image (Fig. 2.5d) shows a strong contrast with the CNT corresponding to those particles and enables their main features to be counted precisely: size and density. CNT@PdaCu annealed at 773 K (Fig. 2.5e) shows bigger particles on most of the CNT except the largest one. Nevertheless, observations in other areas of the same sample have shown that the growth of particles is not dependent on the diameter of the CNT. The STEM image of the same sample in figure 2.5f further confirms the rather high material density (contrast-dependent) of the grown particles. Furthermore, additional image contrast enhancement reveals the growth of particles on the back side of the largest CNT. Only the images of the samples annealed at 573 and 773 K are reported here but similar observations can be made for the sample annealed at 673 K. After annealing at 573 K, one can observe a high particle density (2.27×10^{10} particles.cm^{-2}) related to the apparition of a new population of nuclei with an average diameter of 13 nm (Fig. 2.6). When the sample is annealed at 673 K, the particle density remains almost the same (2.34×10^{10} particle.cm^{-2}) while the mean diameter of nuclei grows slightly (15 nm). At 773 K, the quantity of particles decreases drastically (5.7×10^{8} particles.cm^{-2}) while their average diameter shifts towards 27 nm. The small decrease of the Cu content detected by XPS during annealing (table 2.1) is thus attributed to the gradual formation of copper nuclei with a diameter larger than the XPS probing depth (<10 nm)."

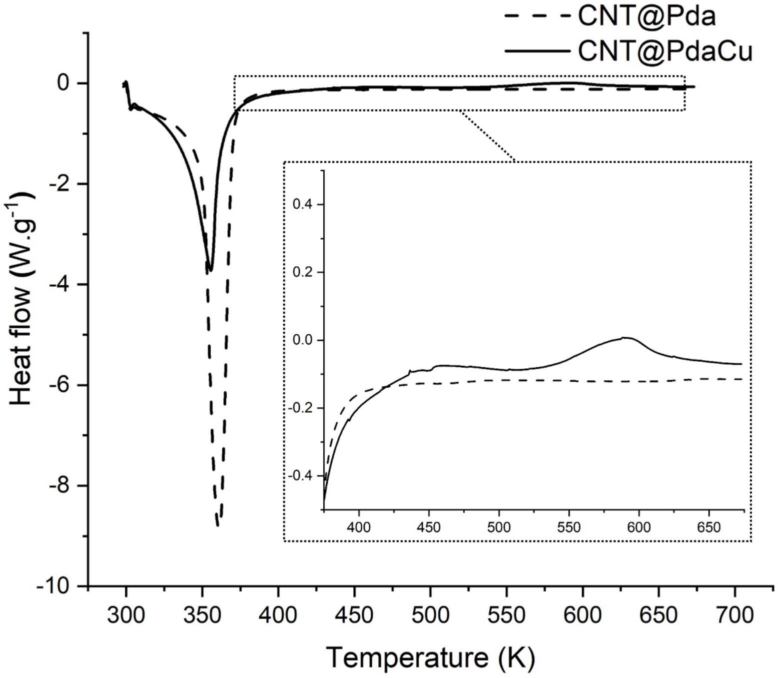

Figure 2.7. Differential scanning calorimetry of CNT@Pda and CNT@PdaCu. Inserted figure: magnification showing the exothermic peak in CNT@PdaCu sample.[158]

Annealing temperature	Oxidized CNT	CNT@Pda	CNT@PdaCu
573 K	/	/	33 ± 1.3%
673 K	/	/	36.9 ± 6.7%
773 K	-8.8 ± 12.0%	32.4 ± 3.6%	37.6 ± 12.2%

Table 2.4. Drop in resistance of CNT carpet samples after annealing at 573, 673, and 773 K in comparison to their resistance before annealing. The resistance drop is expressed as $100\times$ (1-$R_{annealed}/R_{notannealed}$) %.[158]

"Figure 2.7 shows the comparative DSC measurements of CNT@Pda and CNT@PdaCu samples in order to further understand the chemical mechanisms governing the nucleation of particles onto the CNT surfaces. In both cases, the first endothermic peak below 373 K is attributed to the evaporation of ethanol contained in the Pda hydrophilic layer. The most specific feature of the CNT@PdaCu sample is the exothermic peak around 573 K. Li et al. have attributed this peak to the apparition of metallic nuclei during the annealing of Cu-doped Pda coated on fused silica.[176] In our case, this exothermic peak occurs between 540 K and 660 K and concurs with the observation of surface particles in samples annealed at 573, 673 and 773 K. As shown by the Cu LMM spectra, the presence of metallic Cu is detected for samples annealed beyond 673 K. We believe that this peak might be related to the energy variation arising from the redox reaction between copper and Pda as well as the decrease of free energy due to the reduction of the surface area of the Cu particles.[177] Fig. 2.8 a,b (SEM and HIM-SIMS, respectively) highlights the presence of copper (in blue) and its homogeneous distribution on the CNT@PdaCu surface after annealing at 773 K."

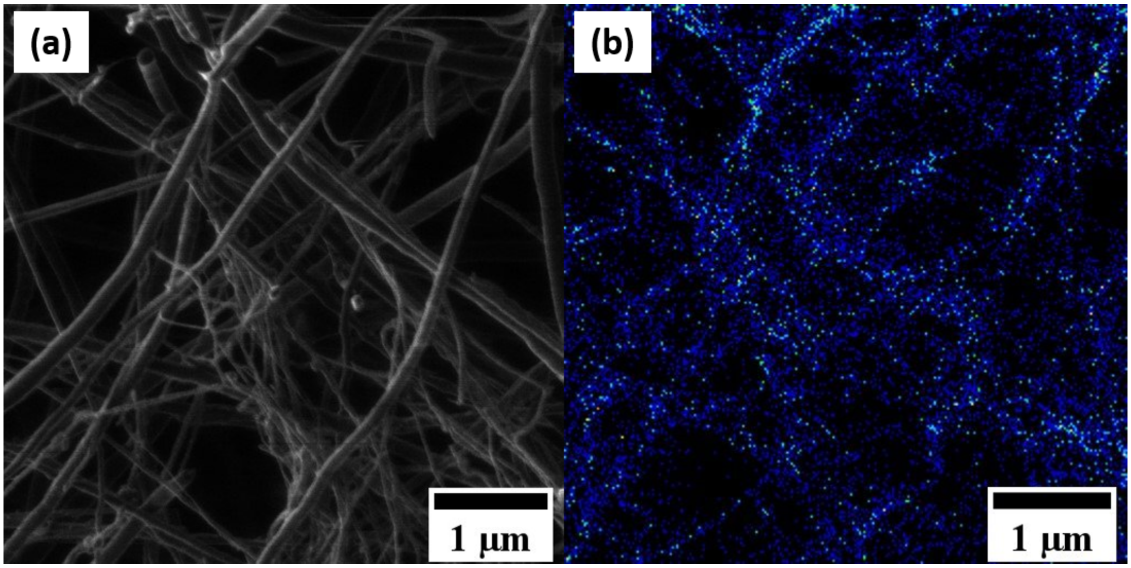

Figure 2.8. (a) Secondary electron and (b) HIM-SIMS picture of the same zone of CNT@PdaCu annealed at 773 K.[158]

"Figures 2.9 a and b show a photograph and SEM image, respectively, of a CNT@PdaCu carpet sample annealed at 673 K and used for the resistance measurements. The CNT are randomly oriented within an horizontal plane. All CNT carpet samples displayed a similar morphology. Table 2.4 summarizes the drop in resistance (at room temperature) of CNT carpets after annealing at 573, 673, and 773 K, in comparison to their resistance before annealing. It shows that there is no drop in resistance for the oxidized CNT reference sample (-8.8±12.0%). Lekawa-Raus et al. reported that a small increase of resistance could be observed in CNT fibers after annealing due to humidity removal.[178] One can observe a drop in resistance of 32.4±3.6% for the CNT@Pda sample after annealing at 773 K. Several authors reported the increase in conductivity of Pda after annealing,[169,170,179] which could explain the drop in resistance of the Pda-coated CNT carpet. There is no significant difference among the CNT@PdaCu samples annealed at 573, 673, and 773 K; indeed the resistance drops are 33±1.3, 36.9±6.7 and 37.6±12.2%, respectively. This means that the carpet resistance is independent of the copper particle size and density. One can recall that copper particles on the CNT surface have a high density with a smaller size at 573 K and are bigger with a lower density at 773 K (Table 2.6). Finally, there is no significant difference between CNT@Pda and CNT@PdaCu when both are annealed at 773 K. This is surprising since Li et al.[159] attributed a higher conductivity of Cu-doped Pda coating (on fused silica) annealed at 873 K (in comparison to undoped Pda annealed at the same temperature) to the nucleation of copper particles in the Cu-doped Pda coating. In our case, the Cu 2p spectra showed that copper particles are partially oxidized in Cu_2O after annealing at 773 K which might explain the independence of the resistance from the particle size and density. The resistance decrease in CNT@PdaCu samples is attributed to the progressive suppression of pyrrolic nitrogen (C2-NH) in favor of pyridinic nitrogen (C=N-C) as previously observed in table 2.2.[169,170,179] As seen in table 2.5, the temperature coefficient of resistance is negative for annealed and non-annealed oxidized CNT reference samples. An interesting work from Naeemi et al.[42,55] theoretically attributed the negative TCR of MWCNT to their large diameter. The TCR of the CNT@Pda sample slightly increased when annealed at 773 K while the TCR of CNT@PdaCu samples remained apparently unaffected after annealing at 573, 673, and 773 K. Polydopamine conductivity displayed a $\log(\sigma) \propto -1/T$ semiconductor behavior in a dry environment[180,181] and could partially contribute to the negative TCR of coated CNT."

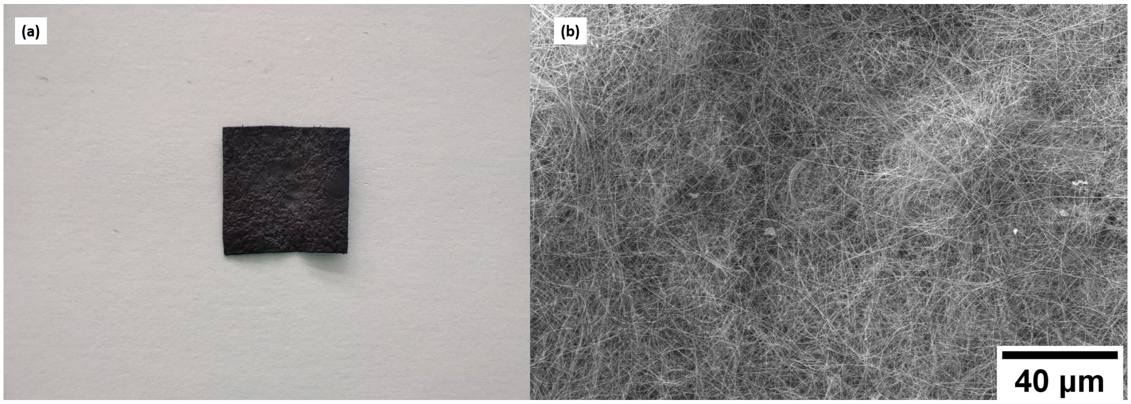

Figure 2.9. (a) Photography and (b) SEM picture of CNT@PdaCu carpet sample annealed at 673 K.[158]

Annealing temperature	Oxidized CNT	CNT@Pda	CNT@PdaCu
Not annealed	$-1.44\times10^{-3}\pm 3.17\times10^{-5}$	$-2.73\times10^{-3}\pm 1.89\times10^{-4}$	$-2.21\times10^{-3}\pm 4.59\times10^{-4}$
573 K	/	/	$-1.85\times10^{-3}\pm 9.09\times10^{-5}$
673 K	/	/	$-1.73\times10^{-3}\pm 1.03\times10^{-4}$
773 K	$-1.44\times10^{-3}\pm 4.05\times10^{-5}$	$-2.26\times10^{-3}\pm 1.39\times10^{-4}$	$-2.35\times10^{-3}\pm 1.02\times10^{-4}$

Table 2.5. Temperature coefficient of resistance of CNT carpets before and after annealing at 573, 673, and 773 K.[158]

2.3 REDUCTION OF THE PDA COATING AND CARPET COMPRESSION

Following the use of annealing, we investigated the reduction of the Pda coating to decrease the resistivity of the CNT@PdaCu carpets. We measured the resistance of CNT carpets constituted of CNT@PdaCu obtained by different concentrations of dopamine in the coating solution. Yet, as discussed above, the comparison between the sheet resistance of different CNT carpets is difficult because its value depends of the CNT quantity in each sample. As reported in our published paper,[155] we take this into account by normalizing the resistivity and defining inverse of the specific conductivity that is derived from the following equations:

$$R_s = \frac{\rho}{t} = \frac{\rho_{carpet}}{\lambda}\gamma_{carpet} \tag{2.1}$$

and

$$R_s\lambda = \rho_{carpet}\gamma_{carpet} = (\frac{\sigma_{carpet}}{\gamma_{carpet}})^{-1} \tag{2.2}$$

where ρ is the resistivity, λ is the measured mass per square centimeter (area density) of the CNT carpet, and γ is the density. The specific resistivity of CNT@PdaCu carpets (800 μm), obtained with different concentrations of dopamine in the coating solution, is shown in Fig. 2.10. The specific resistivity of the CNT@PdaCu carpets (black squares) drops of 90.3$\%$ when the dopamine concentration is lowered to 0.0625 mM (compared to 0.5 mM). At lower dopamine concentration, the specific resistivity increases slightly. The Pda coating contributes to the carpet cohesion and we believe that 0.0625 mM of dopamine was just low enough to promote adhesion between the CNT (promoting larger CNT-CNT surface of contact) while reducing the contribution of the coating to the CNT-CNT contact resistance. We also investigated the impact of a strong compression (800 kg.cm^{-2} during 5 min, red circle). After compression, the specific resistivity is reduced by 85 and 29$\%$ for 0.5 and 0.125 mM of dopamine, respectively. At lower dopamine concentration, the compression did not further reduce the specific resistivity. Here, annealing of the compressed sample (at 673 K in Ar) leads to a decrease of 13 and 28$\%$ for dopamine concentration of 0.5 and 0.125 mM, respectively. Annealing had no effect on the measured resistance below 0.0625 mM. Therefore, a dopamine concentration $\leq$ 0.0625 mM may be used in the coating solution to reduce effectively the drop of CNT conductance caused by the Pda coating.

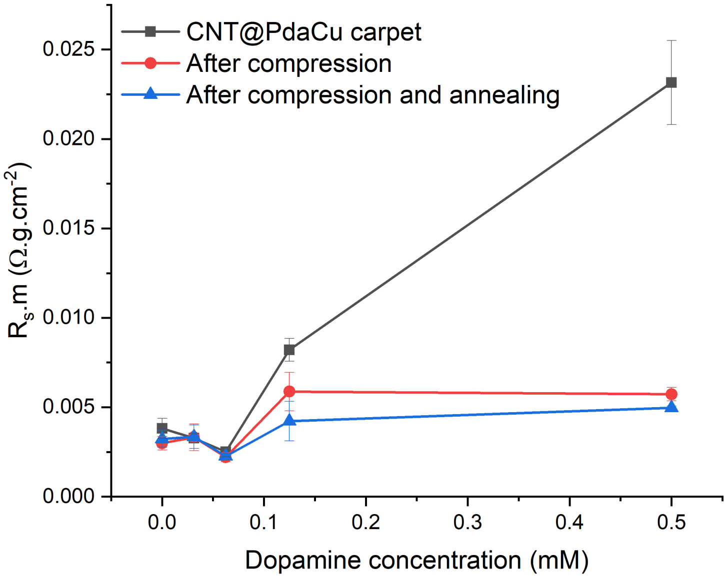

Figure 2.10. Specific resistivity of (square) CNT@PdaCu carpet (800 μm) samples obtained with different concentration of dopamine in the coating solution. The samples are successively (circle) compressed at 800 kg.cm^{-2} and (triangle) annealed at 673 K (in Ar).

We also characterized the resistance of a carpet containing arc-discharged CNT@PdaCu (0.5 mM of dopamine). We measured a sheet resistance of $8.9*10^4$ Ω for a carpet with a thickness around 12 μm. In the case of the CNT characterized above (800 μm - 0.5 mM of dopamine), the thickness was (roughly) between 7 and 10 μm while having a sheet resistance of 55.3 Ω. The sheet resistance of the arc-discharged CNT@PdaCu carpet was thus $\sim 10^3$ times that of the CVD grown CNT@PdaCu carpet. Although a more precise characterization should be done, this large difference of sheet resistance suggested that the long CVD grown CNT were more effective to carry electrons over macroscopic distances.

In chapter 3 (pp. 96-109), we fabricate Cu-CNT and Ni-CNT composites using compressed (500 kg.cm^{-2}) CNT@PdaCu and CNT@PdaNi carpets (0.0625 mM of dopamine), that we characterize here. The following section is quoted from our published paper,[155] and the precise methodology used in this section is given in appendix (section C.1).

"The Cu/Ni presence was confirmed by EDX (Fig. C.2 in appendix) in the CNT@PdaCu/Ni carpets (800 μm - 0.0625 mM of dopamine). Fig. 2.11 shows SEM pictures of CNT carpets, made with (a,b) Oxidized CNT, (c,d) CNT@PdaCu, and (e,f) CNT@PdaNi, before (left) and after compression (right) at 500 kg.cm^{-2}. The CNT carpets feature an entangled network of CNT with planar isotropic orientation. CNT carpets obtained by filtration have an irregular thickness characterized by bulges (Fig. 2.11a,c,e). A compression step at 500 kg.cm^{-2} reduces the height of the bulges and flattens the sample (Fig. 2.11b,d,f)."

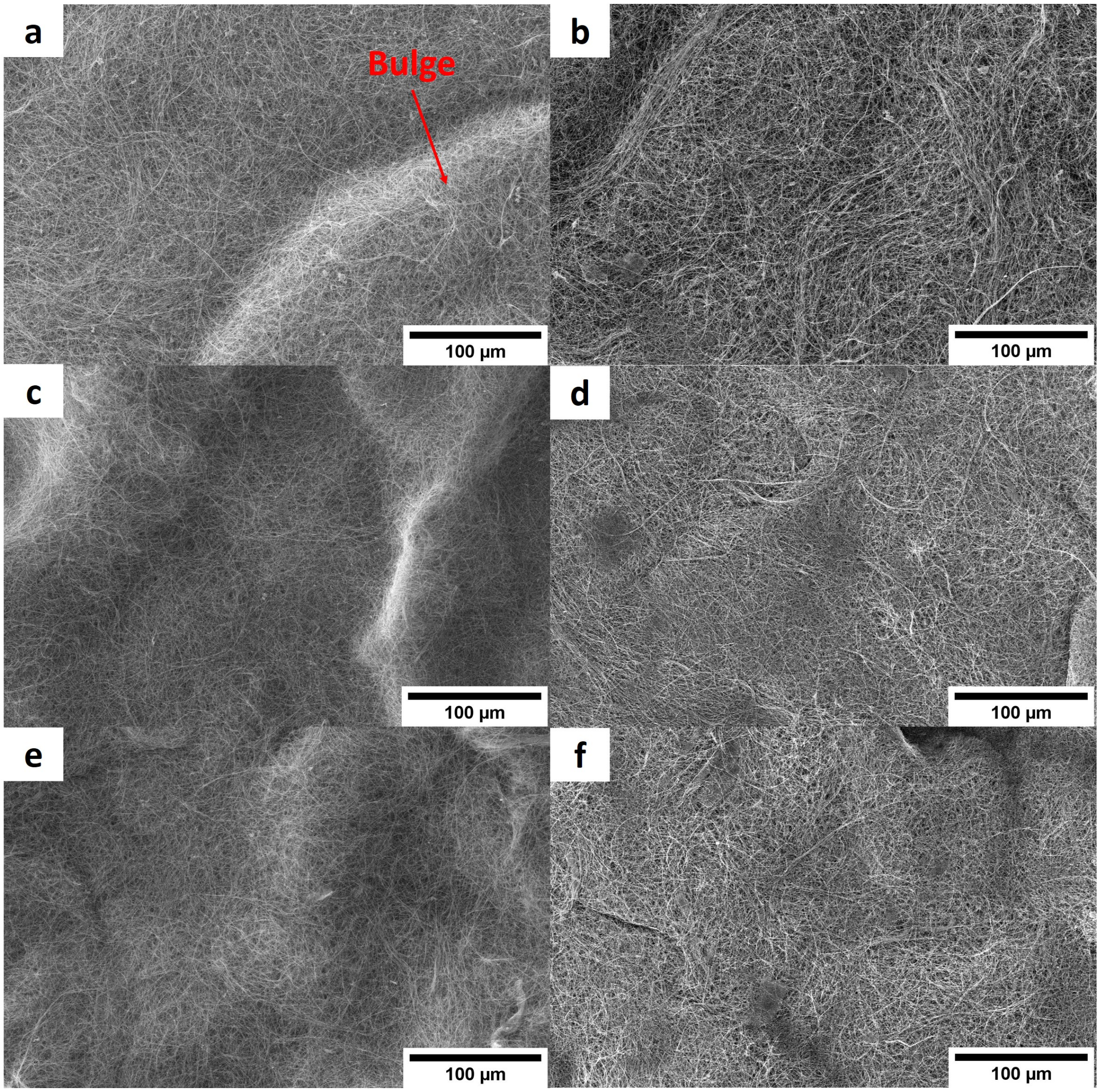

Figure 2.11. SEM top-views of Oxidized CNT (a,b), CNT@PdaCu (c,d), and CNT@PdaNi (e,f) carpets before (left) and after compression (right).[155]

"As highlighted in Fig. 2.12a, the sheet resistance of the compressed layers of oxidized CNT, CNT@PdaCu, and CNT@PdaNi are similar to their respective values before compression (comprised within the error bar). The large difference of sheet resistance between the oxidized CNT, the CNT@PdaCu and the CNT@PdaNi samples is due to a variation of the quantity of CNT in each kind of sample. In order to factor in this difference, we used the equation 2.2. Fig. 2.12b shows that compressed CNT@PdaCu, CNT@PdaNi, and un-compressed CNT@PdaNi carpets have a similar specific resistivity to oxidized CNT carpets, suggesting that the Pda coating does not hinder the electron conduction through the CNT carpets. Interestingly, the un-compressed carpet of CNT@PdaCu would be even more conductive than the non-coated system, although the rationale of this remains unclear. The TCR of all the samples is negative (Fig. 2.12) as expected for large diameter MWCNT[42,55,158] and has a similar value independent of the coating or compression steps. In comparison to our previous work,[158] we find that the TCR of our systems is similar to the TCR of systems constituted of oxidized CNT with a length of 200 μm and a diameter of 80-90 nm (Table 3.11), meaning that the variation of the CNT length does not drastically affect the TCR. Furthermore, in our previous paper, we also observed that the TCR of coated CNT was lower than un-coated CNT. In this paper, values of TCR are similar for all samples. This is attributed to the much lower amount of the dopamine used in this coating solution (0.0625 mM instead of 0.527 mM). This result suggests that a higher concentration of Pda in the coating solution can lead to the TCR value of CNT carpets being tailored (decreased), and could be attributed to the log(σ)$\propto$-1/T semi-conductor behavior of dry Pda.[180,181]" Though, the understanding of this phenomenon calls for additional experiments.

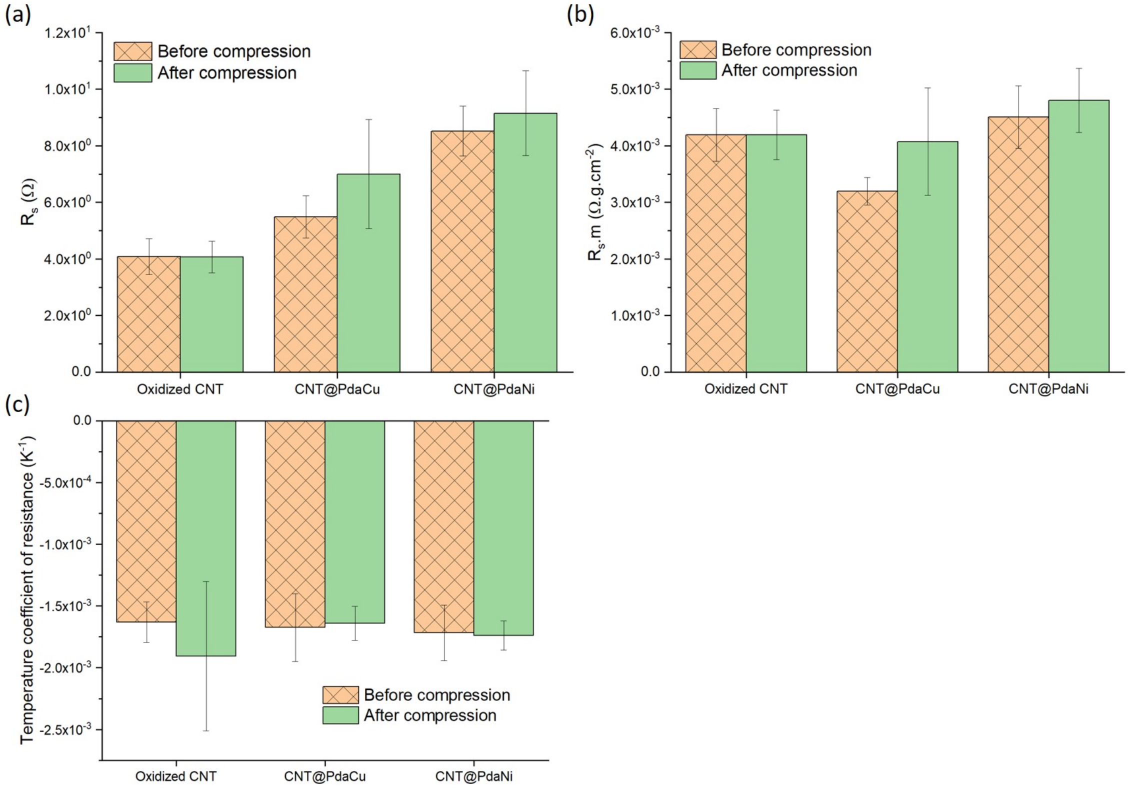

Figure 2.12. (a) Sheet resistance, (b) specific resistivity, and (c) TCR of CNT carpet samples before and after compression.[155]

The oxidized CVD grown CNT (800 μm) were also characterized using Raman spectroscopy (method described in appendix B.1) before and after compression at 500 kg.cm^{-2} to further ensure that the high pressures used during the composite fabrication do not deteriorate the CNT structure, and hence, their electrical properties. In Fig. 2.13, the G band is associated to the in-plane bond stretching mode of the C-C bonds in the hexagonal lattice. For pristine graphene, the G band is a single Lorentzian peak while it broadens for defective carbon materials. The G' band is related to the vibration mode of the breathing of six carbon atoms in an hexagon (of the hexagonal lattice of graphene) and has no direct relation to the level of defect. The D band is related to hybridized vibration modes associated with graphene edges and its intensity increases with the level of defect in the CNT structure and with decreasing CNT length. In very defective materials (such as amorphous carbon), the G and D band overlap each other. Therefore, the G and D bands are mainly considered to measure the quality of the CNT.[182] In particular, the ratio of intensity I_D/I_G is related to the average average distance between defects in CNT, indicating a low level of defect for low I_D/I_G.[183] I_D/I_G was 0.2 ± 0.05 in the compressed sample and 0.2 ± 0.03 in the non-compressed sample, suggesting that CNT are not damaged/cut by the compressing step. The large intensity of the G' band compared to the D band can be attributed to the large diameter of the our CNT.[184,185] Finally, our CNT contains a certain amount of defect as it is expected for CVD grown CNT but the impact of the defects on the CNT conductivity remains difficult to evaluate and calls for additional measures.

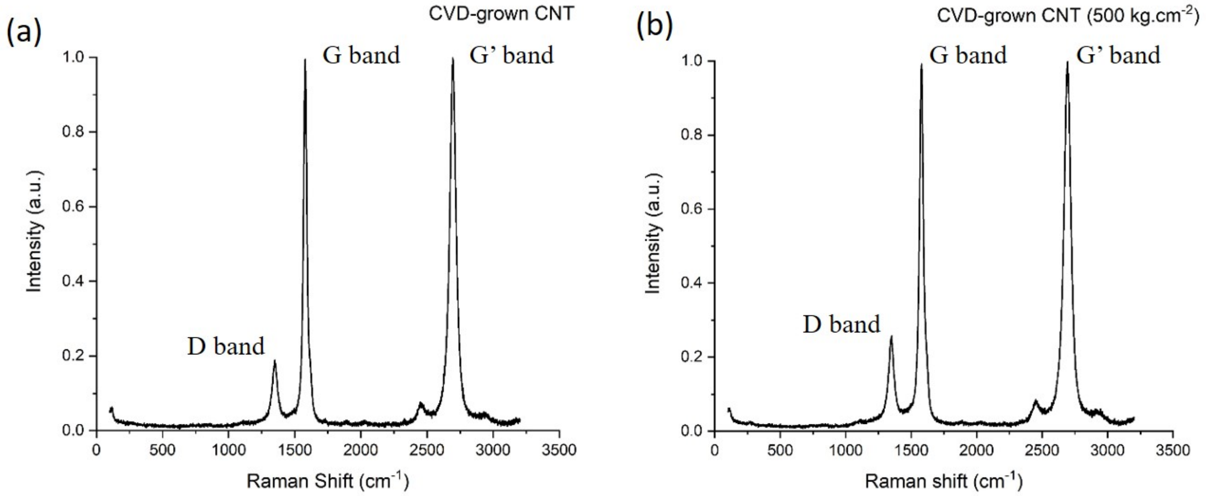

Figure 2.13. Raman spectra of (a) oxidized CVD grown CNT (800 μm) and (b) CVD grown CNT (800 μm) compressed at 500 kg.cm^{-2}. The spectra are normalized on the maximum intensity.

2.4 CHAPTER SUMMARY

"We evidenced the nucleation and growth of metallic copper nanoparticles onto the surface of CNT coated with Cu-doped polydopamine when annealed in an Ar environment at temperatures varying from 573 to 773 K. Based on the XPS characterization of these materials, the copper nucleation mechanism is attributed to the reduction of Cu ions by the electrons released during the oxidation of catechol into quinone moieties upon annealing. The nuclei are quite homogeneously distributed on the CNT surface, independent of the CNT diameter. The nuclei diameter ranges from 13 to 27 nm after annealing at 573, and 773 K, respectively, and the particle density drops from 2.27×10^{10} to 5.7×10^{8} particles.cm^{-2}, respectively. The carpets of CNT coated with Cu-doped Pda displayed a decrease in resistance quite independent of the annealing temperature (ranging from 33 ± 1.3 to $37.6\pm12.2\%$). This resistance drop upon annealing is attributed to pyridinic nitrogen formation into the Pda structure. Furthermore, this variation of resistance is independent of the growth of the copper particles. We believe that it could be attributed to the progressive oxidation of copper particles when exposed to air. In addition, we showed a negative TCR for our metallic CNT carpet, which is promising for obtaining low TCR Cu-CNT composites. The easy nucleation of metallic copper particles at the surface of CNT, combined with the negative TCR and drop in resistance after soft annealing are particularly promising material features to fabricate high performance Cu-CNT composite materials."[158] In addition, we observed[155] that CNT carpets coated in a solution containing $\leq$ 0.0625 mM of dopamine (for both Cu and Ni-doped Pda) are as much conductive as oxidized CNT carpets and display a similar TCR. It seems that the TCR of CNT carpets can be tailored (decreased) by coating the CNT with a larger amount of Cu-doped polydopamine. When coated in a solution containing $\geq$ 0.0625 mM of dopamine, a compression step is efficient to reduce the resistance of the CNT carpets.

In conclusion, aiming to fabricate lightning strike protections with a low resistivity, a low TCR and a high ampacity, it seems judicious to anneal the CNT carpet (prior to electroplating) when the concentration of dopamine used to coat the CNT is 0.5 mM. However, the resistance drop is around 37% and a reduction of the polydopamine coating is more efficient as it leads to a resistance drop of about 90%. Therefore, using 0.0625 mM of dopamine in the coating solution may be preferred over the annealing, considering that annealing of the coated CNT (0.0625 M) does not change their resistance. Furthermore, it seems that a reduction of the dopamine concentration below 0.0625 mM is not necessary as the specific resistivity of the carpets is similar to the one of oxidized carpets. The compression of the carpets does not seem to damage the structure of the CNT and may be used in the fabrication of the composites. Finally, carpets containing long CNT (CVD grown) may be more appropriate to carry electrons over macroscopic distance as they were significantly more conductive than carpet containing arc-discharged CNT.

Chapter 3

Characterization of the metal-CNT composites

3.1 INTRODUCTION

As previously discussed in the background chapter (pp. 24,34), several characteristics should be researched to obtain a Cu-CNT composite with high electrical conductivity, low TCR and high ampacity. In this regard, the effect of the degree of metal filling is investigated by comparing homogeneously and poorly filled Cu-CNT composites. As seen above, long and large CVD grown MWCNT (800 μm, 80-90 nm) carpets have a negative TCR and have a lower resistance than arc-discharged CNT (2.5-20 μm, 6-13 nm), and may in principle be beneficial for Cu-CNT composites. Theoretically, Lee et al. reported a decrease of the composite self-heating using long CNT[112]. Naeemi et al. reported that the increase of the length and diameter of a MWCNT increases its conductivity because of the higher number of conduction channels coupled to a ballistic conduction over a longer distance.[42,55] In addition, the reducing of the band gap in the semi-conducting walls is expected to increase the number of walls actually participating to the current conduction in comparison to low diameter MWCNT. Practically, experiments have shown that large MWCNT and Cu-CNT composites containing long CNT can display an extremely high ampacity.[3,53]

Based on the fabrication guidelines defined previously (p. 34), an increase of the contribution of CNT to the material properties is investigated by comparing Cu-CNT composites with different vol. % of CNT. The alignment of the CNT is also identified as an instrumental feature for an interconnect application. Yet, in lightning strike protection, we may expect that an isotropic orientation of the CNT could be more beneficial as the current is dispersed radially.

Our previous study (chapter 2) showed that the resistance of CNT@PdaCu carpets was reduced after annealing and we managed to fabricate Cu-CNT composites from annealed CNT@PdaCu carpets (chapter 1). Therefore, we could improve the conductivity of our Cu-CNT composites by using annealing of the CNT carpet before electroplating. In addition, adsorbed molecules (e.g. NO_2, O_2, ...) can affect the electronic structure of the CNT outer-wall.[186] Based on the 90% drop of specific resistivity observed when coating with less Pda, we fabricated composites integrating

CNT coated with 0.0625 mM of dopamine.

Finally, we investigate the tuning the Cu-CNT interface with nickel. Indeed, due to the strong cuprophoby of the CNT, copper is weakly interacting with the CNT surface leading difficult electron transfer between the Cu matrix and the CNT. A good wettability should be preferred to form ohmic contact between CNT and the metal. In transitions metals, metals with 3d outermost orbitals (like copper) have a higher wettability on CNT than 4d and 5d metals. In addition, the wettability increases with the number of vacancies in the 3d orbitals,[187] leading to Ni (2 vacancies) forming stronger ohmic contact than Cu (1 vacancy).[187,188]

Metals can strongly affect the electronic structures of CNT[188] and are separated in 3 categories:

- Strongly interacting metals (chemisorbed, as Ni and Ti) which modify the band structure and the DOS of CNT. This is particularly evidenced by the disappearing of the Van Hove singularities and the energy band gap around E_F.
- Weakly interacting metals (physisorbed, as Pd, Pt and Cr) which preserve the CNT band structure.
- Intermediary interacting metals (as Cu, Al and Au) which partially modify the DOS and the band structure of CNT.

Depending on the metal used, it was shown that a SWCNT would act as an "effective" tube with different electrical properties. For semi-conducting SWCNT, calculation have shown that the use of Ti and Ni would lead to high contact resistance, compared to Cu.[188] Yet, this result cannot be applied to all types of CNT. Better electrical contact using Ni and Ti, compared to Cu, was also reported. Milowska et al.[189] calculated that, on (5,5) and (10,10) SWCNT (semi-metallic), metal-CNT electron transfer depends mainly on three factors: favorable interface geometry and bonding, small contact resistance, and high DOS at the CNT-metal interface. In particular, Ni would be able to improve the conductance of metal-MWCNT systems because it can increase the DOS at the Cu-CNT interface, providing additional conduction channels able to contribute to the electron transfer between Cu and CNT. In addition, Ni can form an alloy with copper, providing an interesting buffer layer to strongly bond copper to CNT, and leading to good ohmic contact. Yet, it was also predicted that specific contact geometries would have a negative impact on the system conductance. In particular, nickel fully embedding a SWCNT would rather hinder the CNT conductance because of a strong spatial localization of the DOS along the "effective" CNT. Instead, dot type contact on the side of CNT or a CNT being connected only at its ends should be preferred in order to promote local injection of electron into the CNT while preserving a delocalized DOS along the CNT. Yet, these calculations were made for SWCNT. In the case of MWCNT, inner-walls could be protected from the metal alteration. Furthermore, literature showed[189] the possibility of electrically contacting the inner-walls of a MWCNT by a forming Ni carbide phase (Ni reacting with the CNT) using annealing of a Ni-CNT system.[189]

It was experimentally shown that addition of Ni at the interface between CNT and copper could increase the conductivity and ampacity of the system in comparison to CNT-Cu systems but the characterization of the TCR is generally missing.[189–192] Furthermore, the studied composites were poorly filled with metals and featured by a metallic layer deposited onto the top of a CNT fiber/carpet (Fig. 3.1a-c). In contrast, we investigate highly filled/embedded systems (Fig. 3.1d) before and after annealing, providing experimental measures to compare with theoretical predictions.

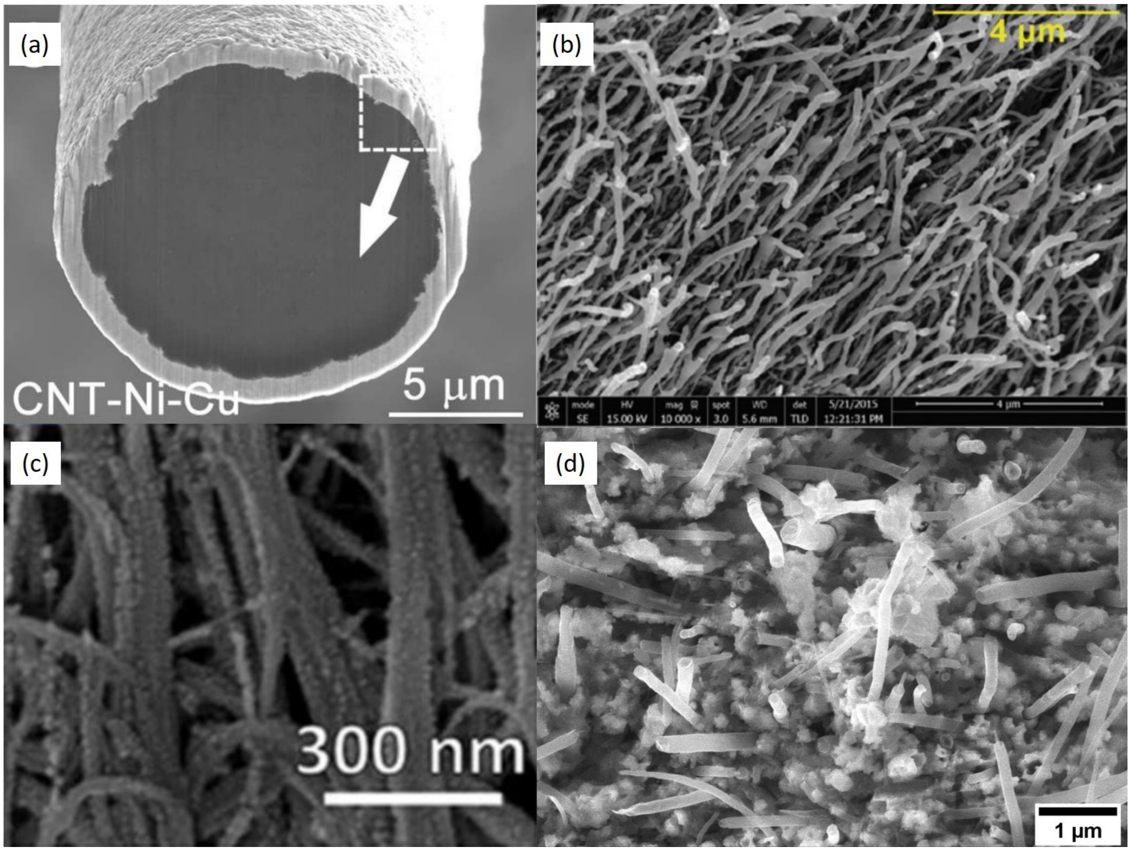

Figure 3.1. Example of (a) a Cu-Ni-CNT composite obtained via electroplating on a CNT fiber,[190] (b) Cu-Ni-CNT composite obtained via deposition by CVD,[189] (c) Ni-CNT composite obtained via deposition by metal evaporation,[192] and (d) our Ni-CNT composite obtained via electroplating.[155]

Following the discussion above and remembering that Cu alloying by Ni can dramatically deteriorates the resistivity and TCR of Cu (Table 1), the potential beneficial effect of Ni in our composites should be done first by comparing "pure" Cu-CNT and Ni-CNT composites with similar CNT vol. $\%$ and degree of filling. In addition, we study the effect of the annealing on such systems. Furthermore, we summarize the current results of the literature treating of the electrical properties of Cu-CNT composites (Table 3.1) and discuss them in the light of our own results. Indeed, and as discussed in our paper,[155] "the composite of Subramaniam et al. remains unmatched and it remains unclear today how Cu-CNT material with an ampacity 100 × that of copper[3] can be produced as the results reported in recent papers are controversial (Table 3.1), ranging from smaller ampacity gains (at most 82$\%$)[104] to ampacity loss.[193] Similarly, the reported resistivity ranges from 1.65×10^{-8} to 5.1×10^{-5} $\Omega.m$[97,102] and the reported TCR from 1.7×10^{-3} K^{-1} to values similar to pure copper.[97,111]"

CNT type	CNT vol. %	CNT alignment	ampacity (A.cm^{-2})	resistivity (Ω.m)	TCR (K^{-1})	Reference
MWCNT	N/A	not aligned	1.54×10^{4} Cu: 9.38×10^{3}	2.44×10^{-8}	N/A	Chen et al.[22]
MWCNT	20	not aligned	N/A	$\sim3.83\times10^{-8}$	N/A	Daoush et al.[93]
MWCNT	N/A	aligned	N/A	5.1×10^{-5}	N/A	Feng et al.[102]
MWCNT	N/A	aligned	N/A	2.45×10^{-7}	N/A	Xu et al.[103]
MWCNT	1	aligned	1.16×10^{4} (32%) Cu: 8.84×10^{3}	2.13×10^{-8}	< Cu	Shuai et al.[106]
SWCNT	0-10	not aligned	N/A	1.65×10^{-8}	≈ Cu	Yang et al.[97]
SWCNT	45	aligned	6×10^{8} Cu: 10^{6}	2.12×10^{-8}	7.5×10^{-4}	Subramaniam et al.[3,107]
MWCNT	45	aligned	6.3×10^{4} (28%) Cu: 4.9×10^{4}	1.6×10^{-7}	1.7×10^{-3}	Sundaram et al.[110,111]
N/A	20-50	aligned	N/A	4.19×10^{-7}	2.1×10^{-3}	Sun et al.[109]
MWCNT	40	partially aligned	2.74×10^{5} (~82%)** Cu: $\sim1.5\times10^{5}$	1.82×10^{-8}	N/A	Bazbouz et al.[104]

Table 3.1. Recent results obtained in the literature. For each paper, the ampacity value of pure copper is also given where measured (composite ampacity gain in comparison to pure copper given in %). ** Study over several line lengths, ampacity taken for 17 mm.[155]

3.2 METHOD OF MEASUREMENT OF THE RESISTIVITY AND AMPACITY

We specifically developed a Van der Pauw (section D.1 in appendix) measurement setup (Fig. 3.2b) constituted of a four-probe support immersed in a temperature-controlled dielectric oil bath (Wacker AK 100 silicone oil - Lauda ECO RE 415). In order to carefully evaluate the contribution of the CNT to the electron transport in the composites, it was crucial to precisely monitor the temperature while measuring the resistivity of our samples. In addition, a Van der Pauw measurement was more repeatable than a standard four probe measurement on small samples (0.5 × 0.5 cm) and the oil bath protected the samples from the oxidation by air.

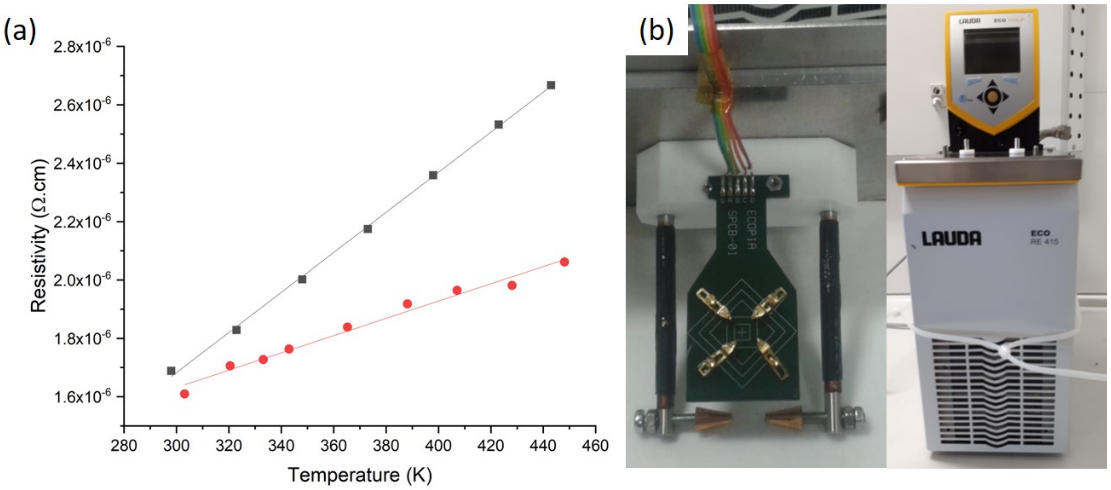

Figure 3.2. (a) Resistivity vs temperature of pure copper measured with (red) a hot-plate coupled with a 4 probe setup and (black) with our Van der Pauw setup (shown in Fig. b). (b) Photograph of our resistivity vs temperature measurement setup (left: sample support - right: temperature controlled oil bath).

Indeed, when measured with a standard 4 probe measurement setup coupled with a temperature-controlled hot plate, we observed that the measured TCR (0.00184 K^{-1} - Fig. 3.2a, red curve) of pure copper was very different from its theoretical value (between 0.00369 and 0.00409 K^{-1} at room temperature).[13] In comparison, the TCR measured with our system led to a value of 0.00406 K^{-1} (Fig. 3.2a, black curve). We attributed this difference to the heat loss of the sample to the environment (air) and to an imperfect contact between the sample and the hot plate, leading to a non-uniform temperature in the sample and to its overall over-estimation. It also highlights the strong requirement to have the relevant measurement setup and illustrates the strong variation that may be reported in the literature depending on the measurement method.

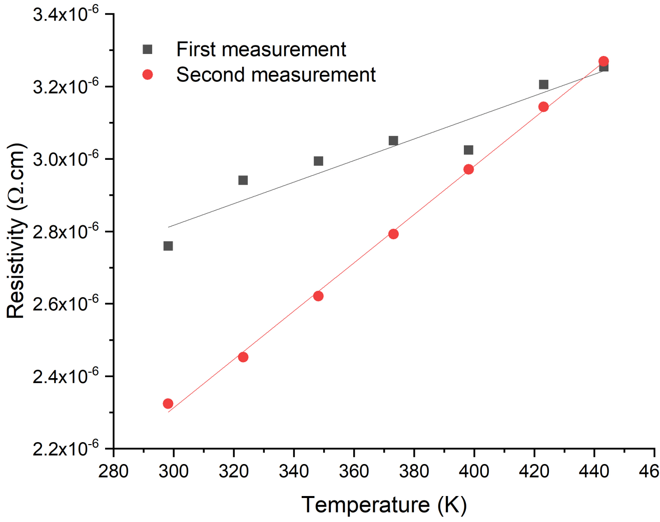

Figure 3.3. Resistivity vs temperature of a Cu-CNT composite sample (arc-discharged CNT): (black) first and (red) second measurement.

We systematically observe a difference of resistivity between the first and second measurement for all the Cu-CNT composite samples (Fig. 3.3). The resistivity always has the same value in the two measurements at 443 K and becomes significantly lower at room temperature in the second measurement. We considered three potential origins to this instability:

- The dielectric oil could cause an unwanted reaction with the sample during the measurement.
- The polydopamine coating of CNT is highly hydrophilic and some water could be retained at the CNT-copper interface, leading to a higher contribution of the CNT to the current transport in the composite (as wet Pda is more conductive than dry Pda[180,181]) and to a lower TCR. This effect being removed at the second measure due to water removal at $T \geq 373$ K.
- The copper grain could slightly grow due to the temperature increase, reducing the composite resistivity.

The first hypothesis was rejected as no instability is observed when our samples are annealed (at $T \geq 400$ K), clearly highlighting a temperature-related effect. The second hypothesis was rejected because the resistivity of the sample is higher at room temperature during the first measurement showing that the CNT contribution to the current conduction would be lower during the first measurement. Regarding the last hypothesis, it is known that the use organic additive in plating solution can lead to smaller copper grains. These type of grain can self-anneal (growth of the Cu grain) at room temperature over few days/weeks, leading to a reduced internal stress and electrical resistance. In fact, carbon impurities (from additives) can occupy the interstitial sites of the Cu crystal, creating internal stress. The movement of the grain boundaries, induced by the grain growth, concentrates the impurities into the grain boundaries and towards the surface of the sample. In addition to the lower amount of grain boundaries, this cleansing effect also decreases the electron scattering (Fig. C.1).[194,195] In Cu-CNT composites, CNT can be located at the grain boundaries or inside the grains and reduce the copper grain size.[196] We suspect that the resistance drop observed in our Cu-CNT composites could be due to a fast grain self-annealing at low temperature, induced by the organic additives used in the plating solution and/or the CNT. Still, the clear understanding of this phenomenon calls for additional experiments. In order to measure an un-biased resistivity and TCR, we always used the values of the second measurement.

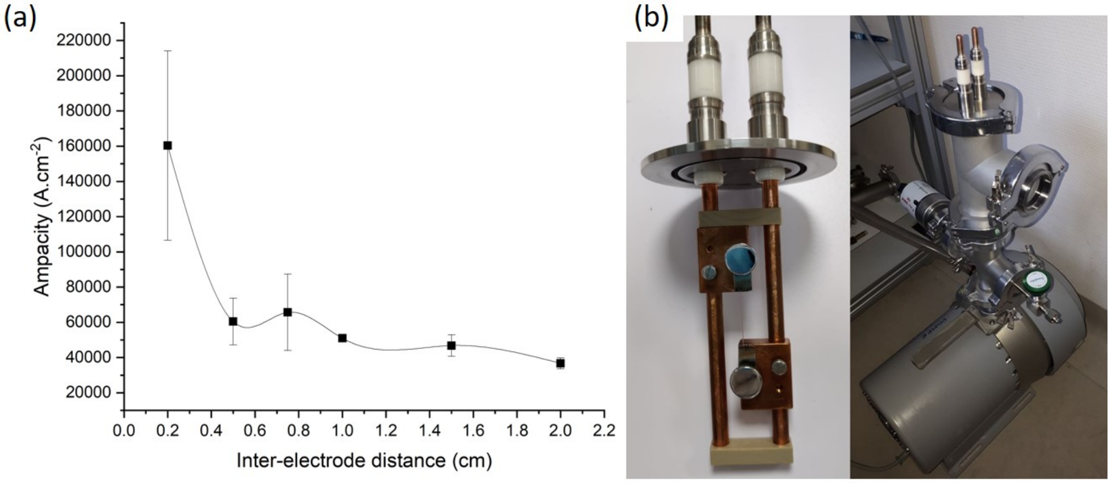

Figure 3.4. (a) Ampacity of pure copper lines (30 μm thick, 250 μm width) with a varying inter-electrode distance. (b) Photograph of the ampacity measurement setup (left: sample support, material lines are clipped between the two electrodes - right: vacuum chamber where the sample support is inserted).

In this work, the ampacity of our materials was characterized with lines of composite materials made by stamping between two razor blades clamped together (line width = 250 μm - measured by optical microscopy). The lines were placed in a homemade setup (Fig. 3.4b) enabling the control of the pressure and the distance between electrodes. While characterizing pure copper lines (thickness = 30 μm) at low pressure (0.5 mbar), the decrease of the inter-electrode distance led to an increase of the ampacity (Fig. 3.4a), highlighting the great impact of the measurement parameters on the ampacity of a given material. This was understood as the heat (from Joule heating) being more easily evacuated via the massive electrodes (heat sink) when the inter-electrode distance decreased. The material parameters influencing the ampacity of our composites will be thoroughly discussed in section 3.4.

3.3 COMPOSITE RESISTIVITY

All our Cu-CNT composites have a higher resistivity than that of pure copper (Fig. 3.5a). In addition, we observed that Cu-CNT composites integrating the different types of CNT (arc-discharged and CVD grown) had generally a similar resistivity. More specifically, it was difficult to draw any conclusions on the effect (on the resistivity) of changing the CNT type, given the error made on the measure of the resistivity (arising mainly from the measurement of the composite thickness). We also observed that porous Cu-CNT composites have a higher resistivity than homogeneously filled Cu-CNT composites. Here, the porosity of the sample was the result of a bad copper growth initiation on a titanium substrate that was not covered with a thin copper layer beforehand.

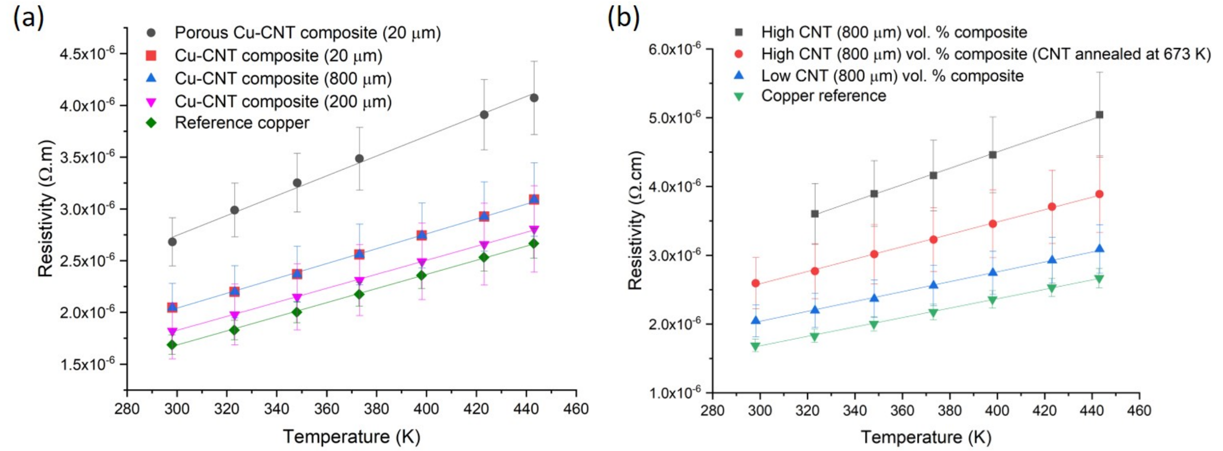

Figure 3.5. Resistivity vs temperature of (a) Cu-CNT composites containing arc-discharged CNT@PdaCu (L=20 μm) and CVD grown CNT@PdaCu (L=200 and 800 μm), and (b) Cu-CNT composite containing CVD grown CNT (L=800 μm) with low CNT vol. % (< 10%), high CNT vol. % ($\sim$ 40%) and high CNT vol. % ($\sim$ 40%) with CNT being annealed at 673 K (in Ar) before electroplating.

Reminding that CNT should have a lower TCR than pure copper, it was surprising to see that the resistivity slope (vs temperature) of the composites is always similar or higher than that of pure copper. In addition, porous composites have a higher resistivity slope than that of homogeneously filled one. We extract the TCR (α) of the composites and pure copper from the equation 8 (Table 3.2). All the composites have a lower TCR than the one of pure copper.

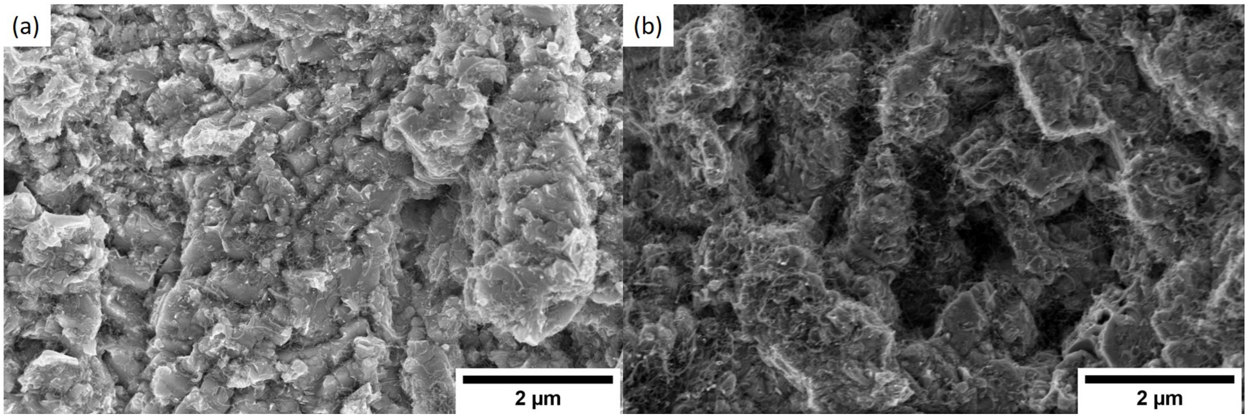

Figure 3.6. SEM cross-section of (a) a Cu-CNT composite (20 μm) and (b) a Cu-CNT composite (20 μm) poorly filled with copper.

It can be understood from the expression of the sample resistivity (surface area: A, width:w, thickness:t, length: L) as a function of the measured resistance R

$$\rho = R\frac{A}{L} = R\frac{wt}{L} \tag{3.1}$$

When measuring the thickness of the sample, we do not take into account the porosity of the system and we overestimate the area of the cross-section of the sample, leading to an overestimated

Temperature coefficient of resistance (K^{-1})		
Low CNT vol. %	Poreous Cu-CNT composite (20 μm)	0.0035
	Cu-CNT composite (20 μm)	0.0031
	Cu-CNT composite (200 μm)	0.0037
	Cu-CNT composite (800 μm)	0.0035
High CNT vol. %	Cu-CNT composite (800 μm)	0.0033
	Cu-CNT composite (800 μm) - 673 K	0.0035
Copper reference		0.0041

Table 3.2. Temperature coefficients of pure copper and Cu-CNT composites related to the Fig. 3.5.

resistivity for a given value of the resistance. Therefore, we introduce a parameter θ (between 0 and 1) reflecting the porosity

$$t_{true} = t_{measured}\theta \tag{3.2}$$

This expression is used in the equation above to get the expression of the resistivity of a material exempt of porosity (ρ_{true})

$$\frac{\rho_{measured}}{\rho_{true}} = \frac{1}{\theta} \tag{3.3}$$

From equation 8, the resistivity vs temperature slope (c) can be written by

$$c_{measured} = \alpha\rho_{measured} = \alpha\frac{\rho_{true}}{\theta} \tag{3.4}$$

For different samples with a same TCR (α), $c_{measured}$ can thus be higher because $\rho_{measured}$ is higher. Thus, the resistivity slope does not necessarily reflect an intrinsic property of the material but more an artifact caused by an error made on the cross-section of the sample due to porosity. To reliably evaluate the contribution of CNT on the resistivity slope, the TCR was thus considered in priority. This model is simplified and does not take into account the electron scattering induced by the porosity. Yet, we can expect that the scattering rate increases proportionally to the porosity, contributing to the resistivity increase. Still, the elastic scattering of electrons by static defects is not expected to modify the TCR of a material (see Matthiessen's rule, pp. 4, 22).

We believe that, in our composites (Fig. 3.5a), misaligned CNT (versus the current direction) increase drastically the residual resistivity of the system while enabling only a slight amount of CNT to contribute efficiently to the electron transport. The small contribution of CNT to the current conduction is reflected by the slightly lower TCR of the composites compared to pure copper. In addition, the decrease of the TCR is not sufficient to compensate the effect of the increase of residual resistivity on $c_{measured}$.

Following this result, we expected that a drastic increase of the CNT vol. % would increase the contribution of the CNT to the electron transport, decreasing the measured TCR of the composite (Fig. 3.5b). However, comparing Cu-CNT composites (800 μm) having a low and a high CNT vol. % ($<$ 10 and $\sim$ 40%, respectively), a relatively stable TCR (Table 3.2) together with an increase of the resistivity at higher CNT vol. % are observed. Thus, independently of their alignment, the CNT poorly carry electrons.

As previously discussed, we observed an increase of the CNT@PdaCu carpet conductivity after annealing, therefore, we compared a Cu-CNT composite (high vol. % - 800 μm - Fig. 1.37a) with a Cu-CNT composite obtained from a CNT@PdaCu carpet annealed at 673 K in Ar (high vol. % - 800 μm - Fig. 1.37b). If the resistivity of the second sample was slightly lower than the first one, the TCR appeared to be stable (Table 3.2).

3.4 **CU-CNT INTERFACE TUNING**

At this point, we postulate that the weak transport of electrons by the CNT is the result of the weak electronic interaction between copper and CNT. Indeed, we observed a weak bonding between copper and CNT independently of the coating and annealing steps (Fig. 3.7). Aiming to improve the electron transfer between Cu and CNT, we investigated the tuning of the Cu-CNT interface with a second metal. The following discussion is quoted from our published paper[155] and the methodology used in this study is given in appendix (section C.1).

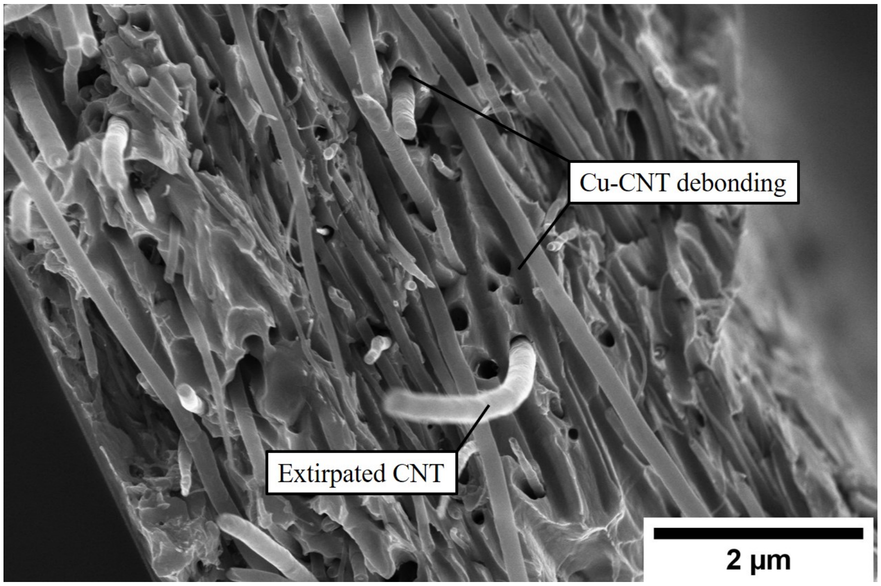

Figure 3.7. SEM cross-section of Cu-CNT composite (800 μm) showing a debonding between the CNT and the Cu matrix.

Samples	CNT vol. %	Density (g.cm^{-3})
Cu-CNT composite not annealed	45.9 ± 2.2	5.05 ± 0.20
Cu-CNT composite 673 K	41.7 ± 2.6	5.46 ± 0.24
Cu-CNT composite 873 K	36.2 ± 4.1	5.95 ± 0.38
Cu-CNT composite 1073 K	46.1 ± 8.4	5.03 ± 0.79
Average of Cu-CNT composites samples	42.5±6.3	5.38±0.59
Ni-CNT composite not annealed	47.8 ± 2.8	4.87 ± 0.26
Ni-CNT composite 673 K	40.9 ± 7.8	5.45 ± 0.62
Ni-CNT composite 873 K	38.7 ± 13.3	5.6 ± 1.22
Ni-CNT composite 1073 K	47.8 ± 4.1	4.89 ± 0.38
Ni-CNT composite 1173 K	41.2 ± 4.3	5.41 ± 0.39
Average of Ni-CNT composites samples	43.3 ± 8.1	5.24 ± 0.73

Table 3.3. CNT vol. % and density of Cu-CNT and Ni-CNT composites samples used for the conductivity measurements (measured before annealing).[155]

"High metal filling (Fig. 3.8) and CNT vol. % as high as 42.5 and 43.3% were obtained in the Cu-CNT and Ni-CNT composites, respectively (Table 3.3). The average density of Cu-CNT and Ni-CNT composites is 5.38 and 5.24 g.cm^{-3}, respectively, which is significantly lower than pure Cu (8.96 g.cm^{-3}) and Ni (8.9 g.cm^{-3}).[12] The variation of CNT vol. % in Table 3.3 originates from the increase of the current density on the sample edges;[197] leading to metal over-deposition on the top of the composite layer for the pieces taken from the sample edges."

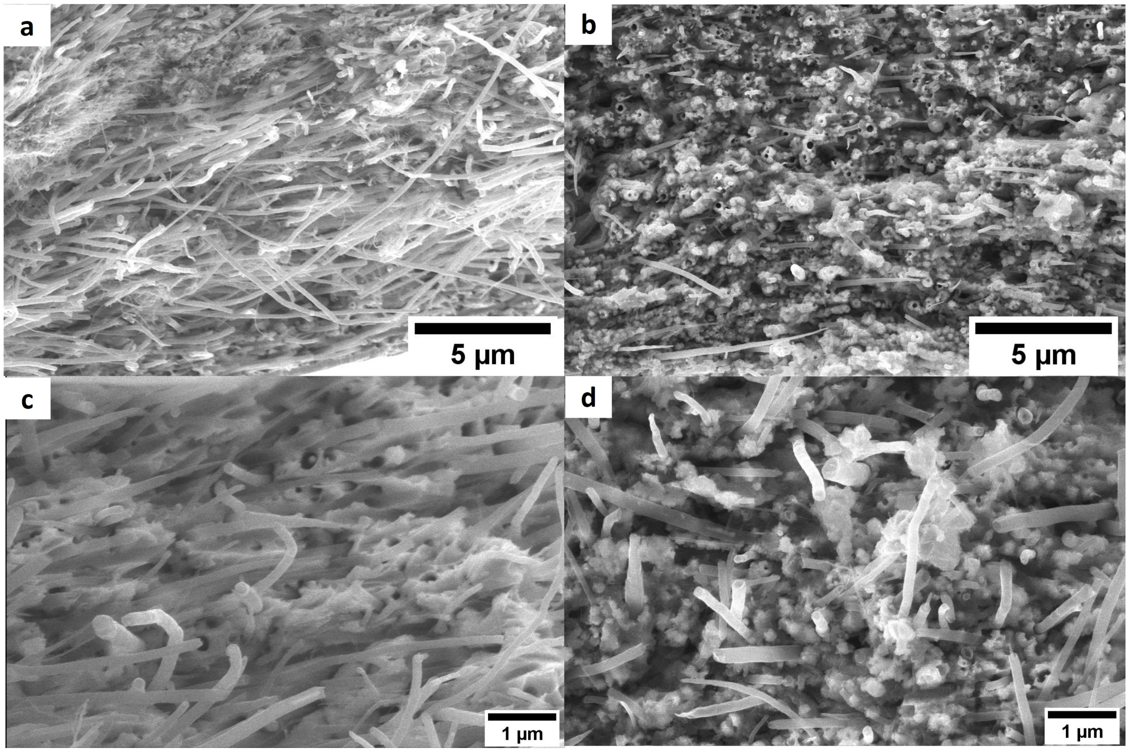

Figure 3.8. SEM cross-sections of Cu-CNT (a, c) and Ni-CNT (b, d) composites before annealing.[155]

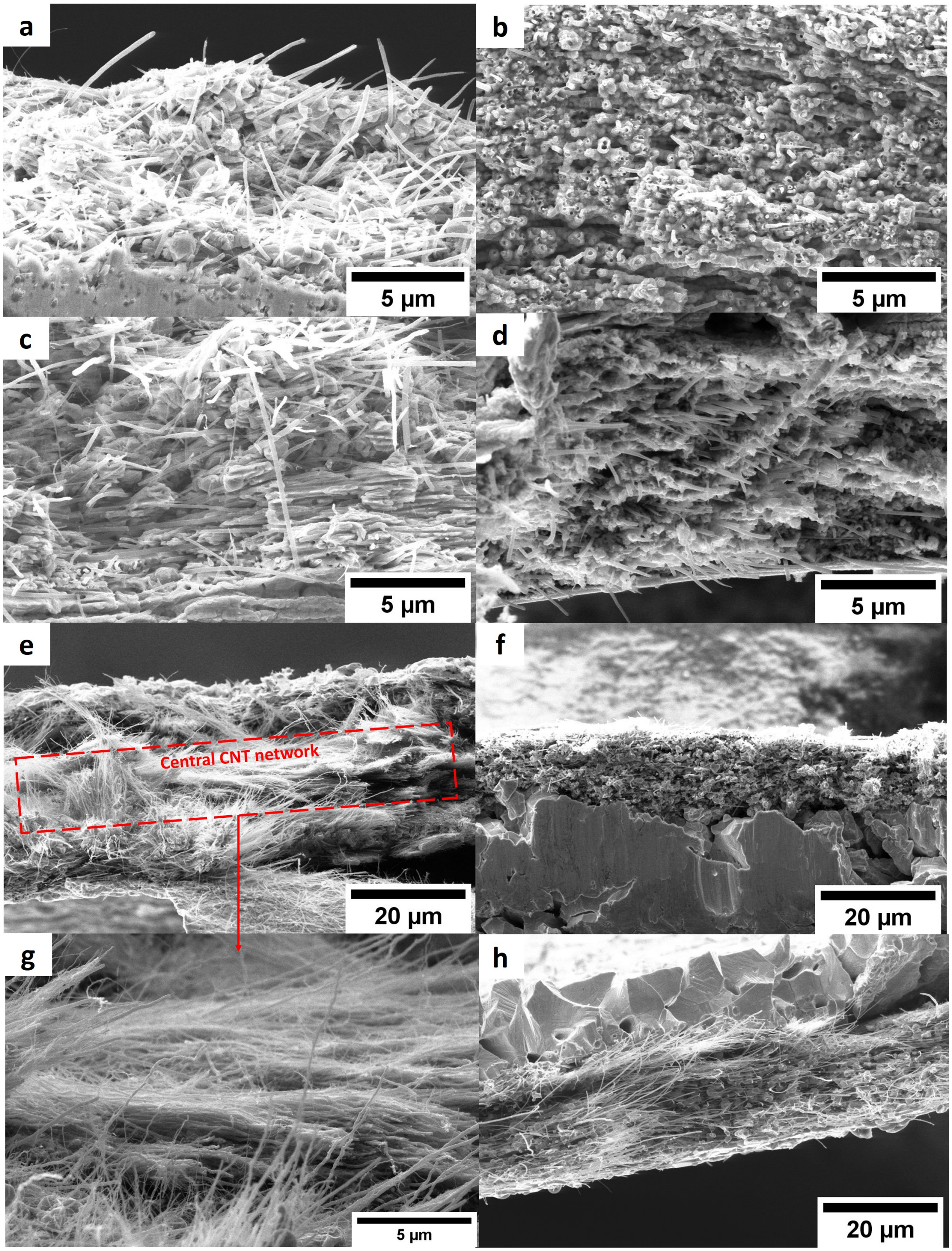

Figure 3.9. SEM cross-sections of Cu-CNT (left) and Ni-CNT (right) composites annealed at 673 (a,b), 873 (c,d), 1073 (e,f), and 1173 K (h). Zoom of the central CNT network of Cu-CNT annealed at 1073 K (g).[155]

"The morphology of the composites appears un-affected by annealing at 673 and 873 K (Fig. 3.9a-d). Annealing at 1073 and 1173 K triggers a phase separation between metals and the CNT network; in the Cu-CNT composite annealed at 1073 K (Fig. 3.9e,g), the central CNT network seems almost completely depleted of Cu. In the Ni-CNT composite, a large number of Ni nodules are still visible in the vicinity of the CNT network when samples are annealed at 1073 K and 1173 K (Fig. 3.9f,h). We attribute this difference to the preferred wetting ability of Ni onto CNT (in comparison to Cu).[187] Furthermore, Ni can form strong chemical bonding with CNT[188] and can even lead to carbide phases when CNT are annealed at high temperatures ($\geq$ 1073 K).[85,189]"

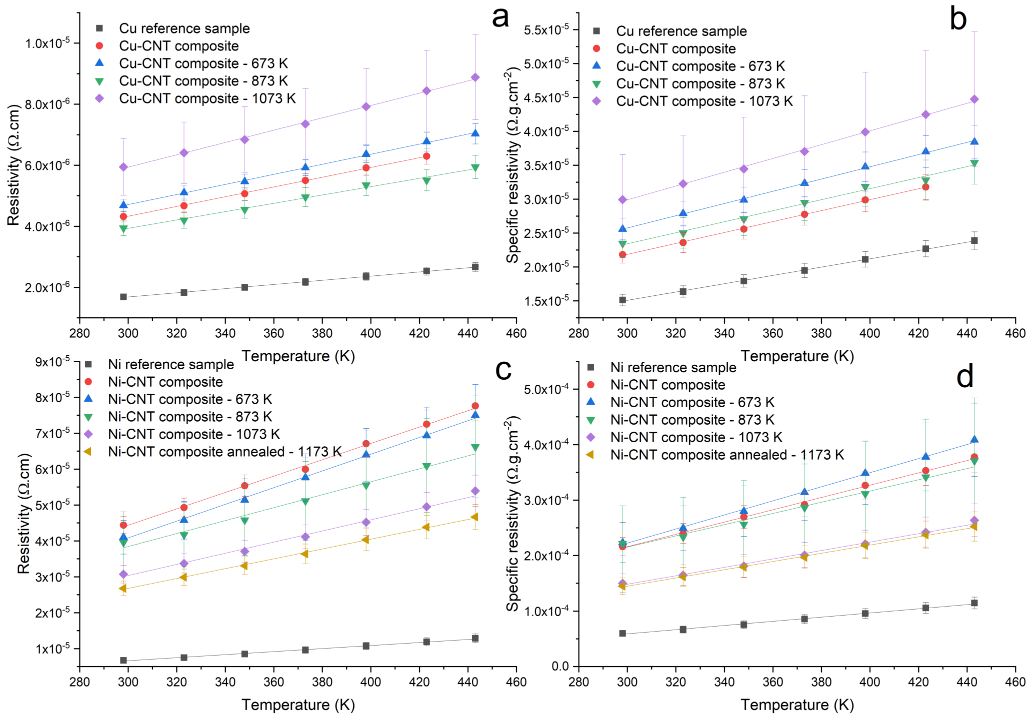

Figure 3.10. Resistivity ρ and specific resistivity $(\frac{\sigma}{\gamma})^{-1}$ versus temperature of Cu-CNT (a,b) and Ni-CNT (c,d) composites.[155]

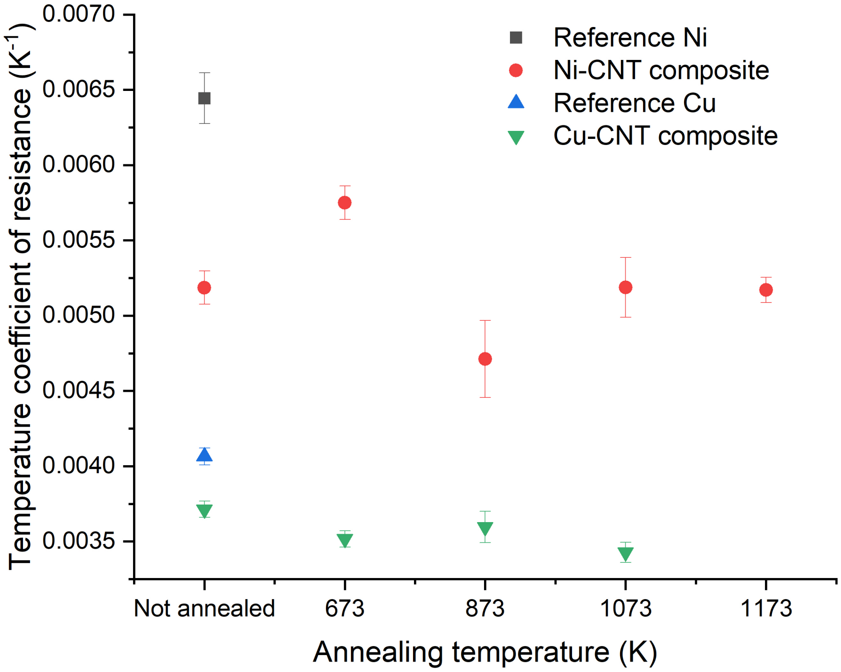

Figure 3.11. Temperature coefficient of resistance of Ni-CNT and Cu-CNT composites.[155]

"The resistivity of the Cu-CNT composite sample is 4.32×10^{-6} Ω.cm and is 2.5 × that of the reference copper (at 298 K - Fig. 3.10a). Compared to the Cu-CNT composites reported in the literature, we find that our composite with non-aligned MWCNT shows a resistivity (at room temperature) about four times lower than the resistivity of a highly filled Cu-MWCNT composite (45% of CNT in volume) with aligned CNT (Sundaram et al. in Table 3.1). We may expect that the alignment of the CNT along the flow of the electrical current leads to the decrease of the overall resistivity of the composite.[85,198,199] However, one should note that the diameter of the MWCNT used by Sundaram et al. is 20 nm while ours is 80-90 nm. Acknowledging that electron mean free path grows in proportion with the diameter of the wall and that more conduction channels are available to electrons in larger diameter walls,[55] Naeemi et al.[42] calculated that, for a sufficient CNT length, increasing the diameter of a MWCNT can significantly increase its conductivity (e.g. for $l \approx 100$ μm, a MWCNT with a diameter of 100 nm would have a conductivity ~3 × higher than that of an MWCNT with a diameter of 20 nm). Hence, our lower resistivity, compared to published results, could be partially attributed to the large dimensions of our MWCNT. When samples are annealed at 673, 873 and 1073 K, the composite resistivity becomes 2.77, 2.34, and 3.52 × higher than that of the reference copper, respectively. It should be recalled that CNT vol. % is not equal in all samples and can induce different contributions to resistivity. We account for this by looking at the specific resistivity (Fig. 3.10b) of the composite (2.18×10^{-5} Ω.g.cm^{-2}) which is 1.44 × higher than the specific resistivity of pure copper, and becomes 1.69, 1.55 and 1.98 × higher when annealed at 673, 873, and 1073 K, respectively. The TCR of the Cu reference sample (0.00406 K^{-1} in Fig. 3.11) is close to values reported in literature (between 0.00369 and 0.00409 K^{-1} at room temperature[13]). The TCR of the Cu-CNT composites vary from 0.00343 K^{-1}, when annealed at 1073 K, to 0.00371 K^{-1} when not annealed. This represents a decrease of 15.5% and 8.6%, respectively, in comparison to the value measured for the reference copper. The non-alignment of CNT is expected to decrease their contribution to the current conduction as electron is mainly transported along the tube axis.[3,31,111] Sundaram et al.[111] shows that the TCR drops progressively with the filling degree of the Cu-CNT composite (from 0.003, when poorly filled, to 0.0017 K^{-1} when highly filled) due to the increase of the CNT-Cu contact surface. We look closely at the morphology of the composites (Fig. 3.8 and Fig. 3.9) to explain a large resistivity increase (at 1073 K) alongside a stable TCR, in comparison to non-annealed composites. We suggest that after annealing at 1073 K (Fig. 3.9e), the central network of CNT has a very large resistivity in the direction perpendicular to the foil because of the Cu-CNT contact surface reduction. The resistivity increase is attributed to the lower contribution of the CNT network to electron transport and to the confinement of the current in the top copper crust (where electrical contact was taken for the measurement). The stability of the TCR in the composite after annealing (compared to before annealing) is attributed to a decrease of the effective TCR of the CNT network (Fig. 3.12a,b), because of the CNT-CNT side contacts favoring electron transport only through the outer walls[52] (outer walls have a lower TCR than inner walls[55]) counteracting the lower contribution of the CNT network to electron transport."

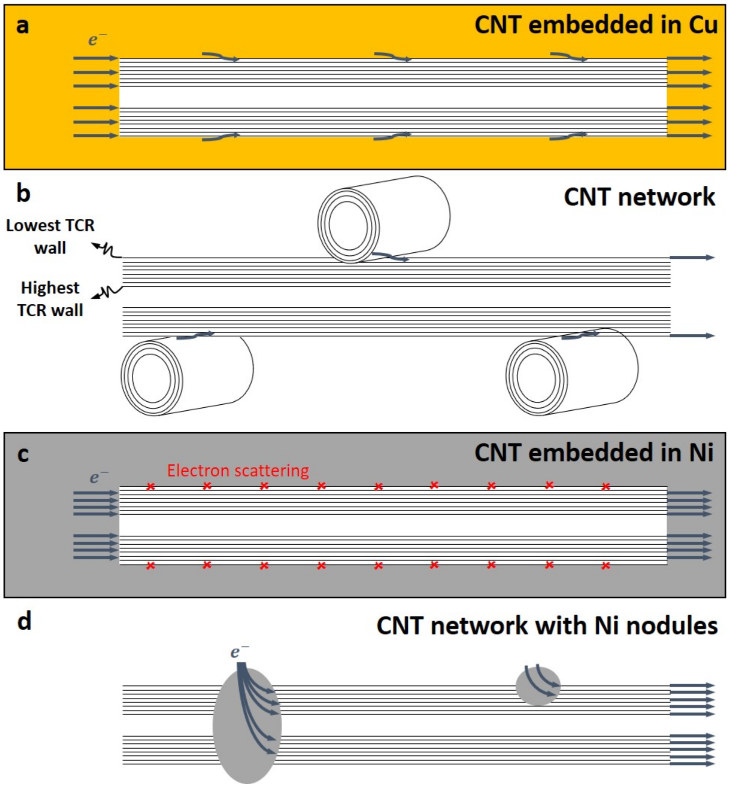

Figure 3.12. Schematic of proposed mechanisms of electron transport in case of (a) CNT embedded in Cu in Cu-CNT composite, (b) CNT central network in Cu-CNT composite after annealing at 1073 K, (c) CNT embedded in Ni in CNT-Ni composite, and (d) CNT network highly interconnected with Ni nodules after annealing at 1073 and 1173 K.[155]

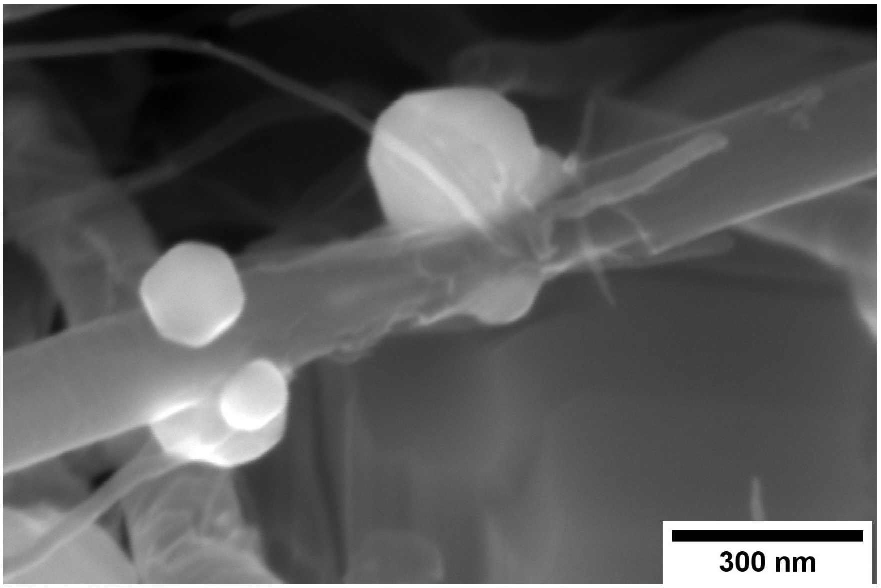

Figure 3.13. SEM images of Ni-CNT composite annealed at 1173 K.[155]

"In Fig. 3.10c, the resistivity of the non-annealed Ni-CNT composite (4.44×10^{-5} Ω.cm) is 6.6 × higher than that of pure nickel. Annealed samples have resistivities that are 6.1, 5.9, 4.6, and 4.0 × higher than pure nickel when annealed at 673, 873, 1073, and 1173 K, respectively. The specific resistivity (at room temperature) of the Ni-CNT composite (2.16×10^{-4} Ω.g.cm^{-2}) is 3.6 × higher than pure Ni and remains the same after annealing at 673 and 873 K. The specific resistivity of Ni-CNT composites annealed at 1073 and 1173 K (1.44 and 1.5 $\times10^{-4}$ Ω.g.cm^{-2}, respectively) drops by 33.3 and 30.5% , respectively, to reach values that are roughly 2.5 × higher than those of pure Ni. The TCR of the Ni-CNT composite is 0.00519, representing a 18.9% decrease in comparison to pure Ni (0.00644 K^{-1}). It ranges from 0.00575 to 0.00471 (10.7 and 26.8% decrease) when annealed at 673 and 873 K, respectively. It stabilizes around 0.00519 when annealed at 1073 and 1173 K. In comparison to the Cu-CNT composite, the higher magnitude of the TCR decrease in Ni-CNT system indicates that the current flowing through CNT is favored when Ni is used. It is still being debated whether Cu-CNT has a higher or lower contact resistance than Ni-CNT.[188,189] However, the calculations of Milowska et al.[189] have shown that Ni would be able to increase the local density of state at the CNT-Ni interface thus increasing the injection of electrons into CNT in comparison to Cu-CNT materials. For our Ni-CNT composite, CNT are fully embedded within the Ni matrix, promoting electrical contact on CNT sides and ends. When the Ni-CNT system is annealed at 1073 and 1173 K, it leads to a layered system constituted of pure Ni and a layer of CNT highly interconnected by Ni nodules. In the fully embedded system, electrons can be efficiently injected, at the CNT end contact, into all the CNT walls (Fig. 3.12c). When annealed at 1073 and 1173 K, Ni nodules make electrical contact with CNT inner walls (Fig. 3.13a) due to the high carbon solubility in Ni[189] (Fig. 3.12d). The apparent TCR remains equivalent before and after annealing; in both cases, the electrons are efficiently injected into the inner walls of the CNT. After annealing at 1073 and 1173 K, the resistivity is decreased, because of the formation of a pure and dense Ni layer on top of a CNT network highly interconnected with Ni nodules. In the CNT-Ni layer, CNT are highly interconnected with Ni nodules while the CNT outer walls got rid of Ni encapsulation, which is known to promote localized electronic states[189] all along the CNT-Ni interface. Hence, we believe that the CNT network with Ni-dot contacts, which enable the electronic conduction through the inner walls of CNT, is a key feature for fabricating highly conductive Ni-CNT systems."

3.5 COMPOSITE AMPACITY

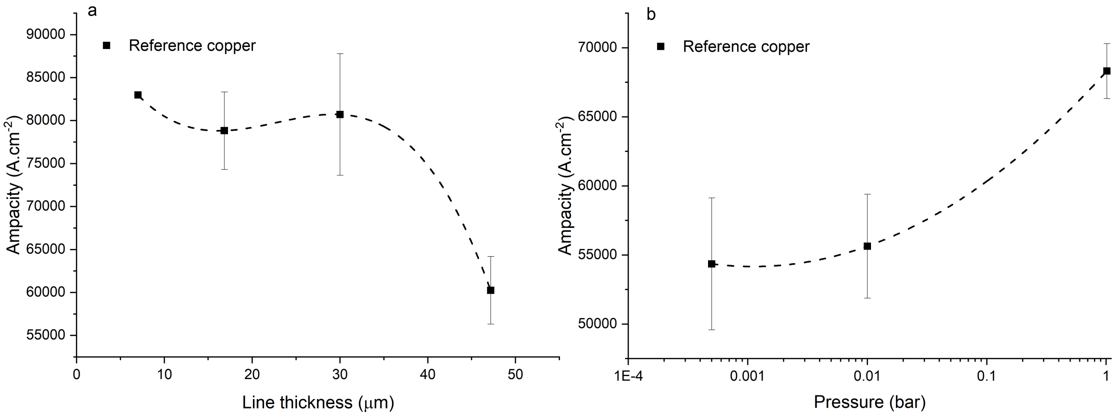

Figure 3.14. Ampacity of reference copper for (a) different line thicknesses, and (b) different pressures (at same thickness and distance between electrodes).[155]

"For the reference copper (Fig. 3.14a), we observed a higher ampacity with thinner lines (for a same inter-electrode distance and same line width). The ampacity of an electrical line is principally determined by the exchange of heat with its environment.[8,9] When the line reaches a temperature higher than its operational temperature (depending on the failure mechanism, e.g. melting or electromigration), it is doomed to fail. We use a rapid ramp of current increase (0.5 A.s^{-1}), and, in our case, we attribute the failure of the line to metal melting. In our ampacity measurement setup, the line was clipped at the electrodes (heat sink) and the surface of contact between the electrode and the line was proportional to the width of the line. Thus, the heat produced by Joule heating increases with the line thickness while the heat dissipated at the electrode is limited by the line width, leading to a 38% increase in ampacity for thin lines (7 μm) in comparison to thicker lines (47 μm). Furthermore, for pure copper, we observed a 25% increase in ampacity when the line was exposed to air, in comparison to low pressure conditions (Fig. 3.14b). We attribute this behavior to the heat dissipation improvement in the presence of air. Literature reported that the line ampacity would be decreased when exposed to air due to oxidation.[3,111] We attribute our higher ampacity, when exposed to air, to our higher current increase rate while testing the line (0.5 A.s^{-1} vs e.g. 1 mA.s^{-1}),[111] leading to a significantly shorter time of exposure to oxidation. We deduce that, for a high current increase rate, heat dissipation by air leads to higher ampacity. It is worth noting that the literature also reports an increase in ampacity for shorter lines.[104,106] This is, according to us, expected to be highly dependent on the measurement method (presence of a heat sink as atmosphere, substrate, ...). Here, we highlight the importance of measuring reference lines and composite lines of the same geometry as the resulting ampacity variation can be in the same range of composite ampacity gain vs copper reported in the literature (~32%,[106] ~28%,[111] ≥82%[104]). More generally, we stress the importance of measuring ampacity on reference lines and composite

Atmosphere	Current ramp	Substrate	Lines dimensions	Ampacity	Reference
N/A	N/A	free standing	40 mm x 1 mm x 20.4 μm	1.54 x 10^4 A.cm^{-2} (63%)	Chen et al.[22]
			Cu: 40 mm x 1 mm x 18.3 μm	Cu: 9.4 x 10^3 A.cm^{-2}	
Ar	N/A	free standing	50 mm x 2 mm x $60 \leq t \leq 80 \mu$m	1.16 x 10^4 A.cm^{-2} (32%)	Shuai et al.[106]
			Cu: 50 mm x 2 mm x 50 and/or 75 μm*	Cu: 8,84 x 10^3 A.cm^{-2}	
10^{-3} Pa	1 mA.s^{-1}	free standing	$\varnothing$ =100 μm	6.3 x 10^4 A.cm^{-2} (28%)	Sundaram et al.[111]
			Cu: similar	Cu: 4.9 x 10^4 A.cm^{-2}	
Air	N/A	free standing	$\varnothing \approx$10.88 μm for $1.5 \leq l \leq 17$ mm	2.74 x 10^5 A.cm^{-2} ($\sim$82%)**	Bazbouz et al.[104]
			Cu: $\varnothing$ = 50 μm for $1.5 \leq l \leq 17$ mm	Cu: $\sim$1.5 x 10^5 A.cm^{-2}	
1.3 x 10^{-4} Pa	N/A***	substrate	50μm x 800nm x 900nm	6 x 10^8 A.cm^{-2} (10000%)	Subramaniam et al.[3,107]
			Cu: similar	Cu: 6 x 10^6 A.cm^{-2}	

Table 3.4. Summary of the measurement parameter in the literature. Line dimensions are given as length x width x thickness. The ampacity gain of Cu-CNT vs Cu is given in %. * means that the value given in the paper was unclear/supposed for/by the reader. ** Study over several line lengths, ampacity taken for 17 mm. *** Cu-CNT composite ageing experiment was also carried at 10^8 A.cm^{-2} over 1200 h.[155]

lines in the same conditions to allow a non-ambiguous comparison between copper and composite. The ampacity measurement parameters and ampacity values vary widely between the papers (Table 3.4). There is also sometimes deviation or potential deviation between the parameters used to measure reference Cu and Cu-CNT composites. As a consequence, it is difficult to compare the ampacity gains obtained in different works as they can involve different heat exchanges, chemical environments and probably failure mechanisms (e.g. electromigration vs melting)."

"In our work, the failure zone of the Cu-CNT composite (Fig. 3.15a) lines is few hundred μm long and is featured by a swelled layer of CNT that is highly depleted of copper (only few copper globules remain). The failure zone had a similar morphology independent of the annealing of the composites and hence, of the initial degree of the copper filling. In the Ni-CNT composite case (Fig. 3.15b), the failure zone is not swelled and the remaining content of Ni in the CNT network is significantly larger than in the Cu-CNT composite lines (see also Fig. C.3). Also, in the case of Ni-CNT materials, the morphology of the failure zone is independent of the annealing of the composite. We note the presence of Ni nodules, fusing CNT (Fig. 3.15c,d) and in Ni-CNT lines (failure zone) after the ampacity measurement and which are formed by Joule heating."

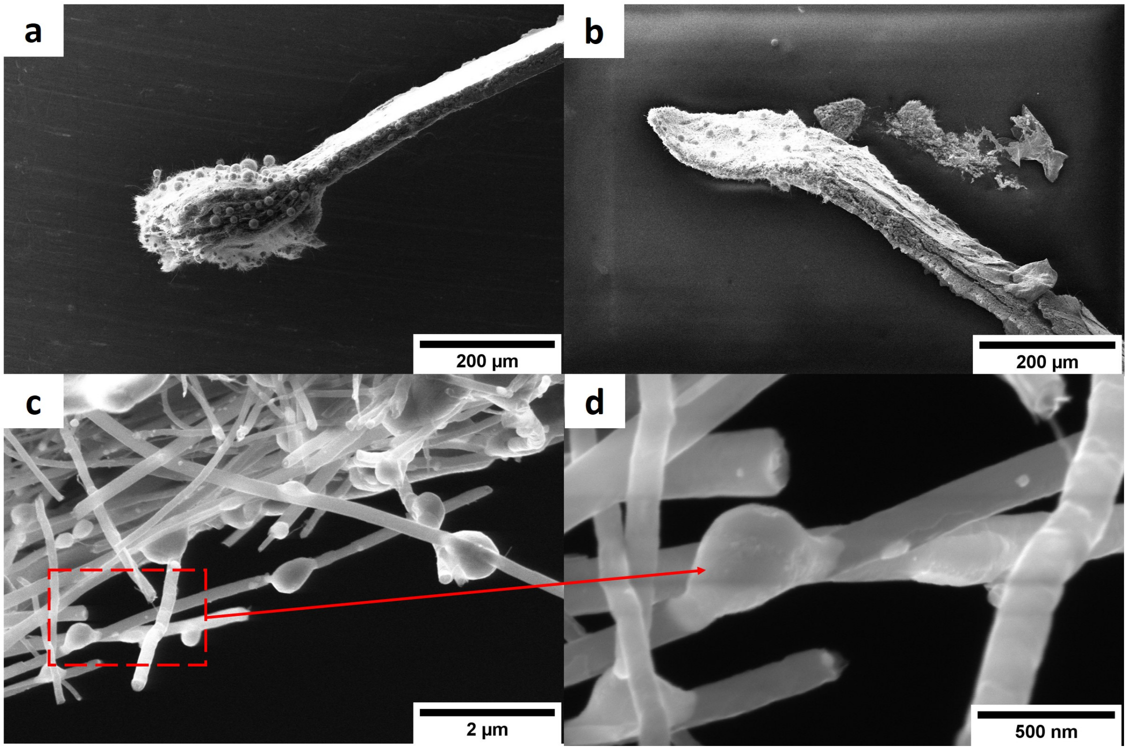

Figure 3.15. SEM image of the failure zone of (a) Cu-CNT and (b) Ni-CNT composites lines (both annealed at 873 K) after the ampacity measurement. Zoom on the line of Ni-CNT composite (annealed at 873 K) after ampacity measurement in the failure zone showing Ni nodules fused with CNT (c,d).[155]

"The composite ampacity is compared to the ampacity of reference copper lines with a similar thickness, the same measured pressure, same line width, and same inter-electrode distance. Most of the Cu-CNT lines had an ampacity between 40276 and 52929 A.cm^{-2} (Fig. 3.16a) and a specific ampacity (Fig. 3.16b) between 7591 and 9930 A.cm.g^{-1}. A few lines displayed a specific ampacity of 9409, 9722, and 9930 A.cm.g^{-1} (Cu-CNT composite, Cu-CNT composite annealed at 1073 K, and Cu-CNT composite annealed at 873 K, respectively), which is higher than pure copper (around 9000 A.cm.g^{-1}). In contrast with a recent paper,[22] our results indicates that a composite characterized by a randomly aligned CNT carpet highly filled by copper has a lower ampacity than pure copper. Shuai et al.[106] also reported an ampacity increase of 32% (with 1.04 vol. % of aligned MWCNT). Sundaram et al.[111] reported a 28% increase in a composite constituted of 45% vol. of aligned MWCNT (but with a room temperature resistivity four times higher than ours). And finally, Subramaniam et al. reported an ampacity one hundred times higher than pure copper. For Ni-CNT composite samples, most of the lines had an ampacity between 8250 and 13500 A.cm^{-2} while pure Ni displayed ampacity between 23900 and 25400 A.cm^{-2} (Fig. 3.16c). The majority of the lines had a lower specific ampacity than pure Ni, while a few lines presented a specific ampacity of 3150 and 3560 A.cm.g^{-1} in comparison to a value of around 2700 A.cm.g^{-1} for pure Ni (Fig. 3.16d). Interestingly, the lowering of the resistivity in Ni-CNT composites when annealed at 1073 and 1173 K did not improve the ampacity of the system while, similarly, the increasing of the resistivity of the Cu-CNT composite when annealed at 1073 K did not significantly lower its ampacity. Alongside the resistivity changes, the change of metal-CNT composite morphology (e.g. highly filled CNT matrix to depleted CNT matrix in the Cu-CNT annealed sample at 1073

K) did not seem to impact the ampacity."

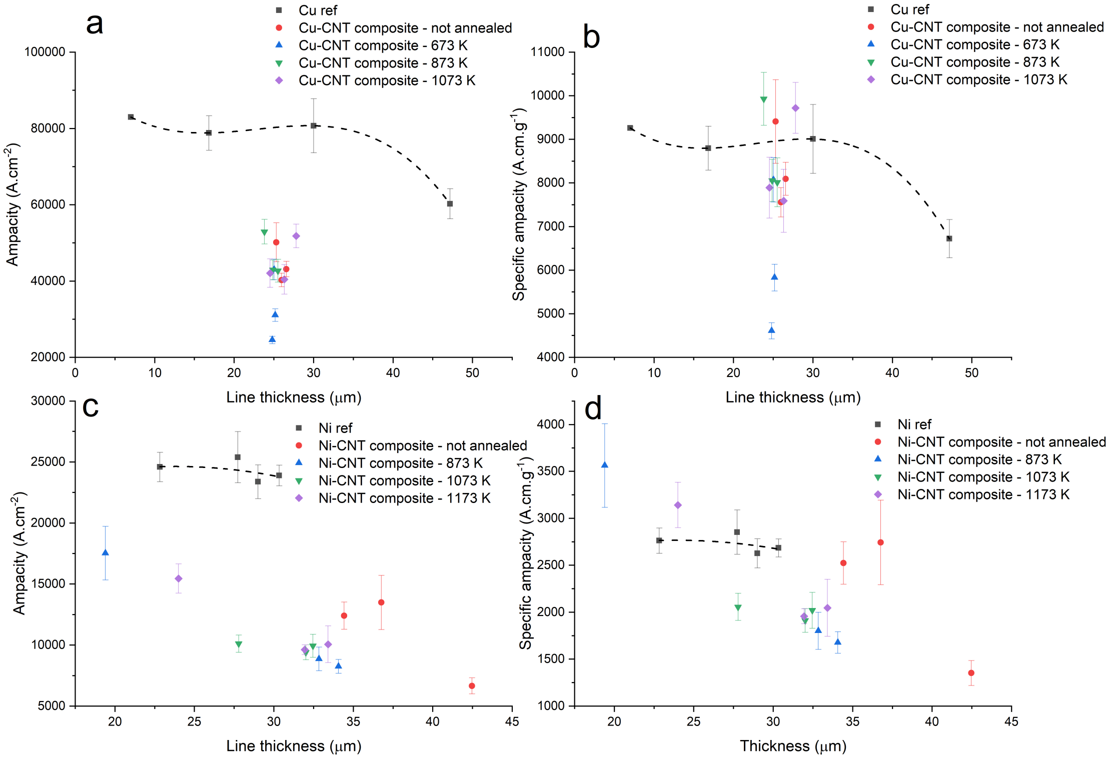

Figure 3.16. Ampacity and specific ampacity of the Cu-CNT composite lines (a,b) and Ni-CNT lines (c,d).[155]

Fig. 3.17a shows the ampacity of Cu-CNT composites integrating CNT@PdaCu (coated with 0.5 mM of dopamine in solution) having length of 20 and 200 μm, and with a low CNT vol. %. As previously showed in Fig. 3.2c, the ampacity of the composites lines should always be compared to a reference copper line having the same length. All the samples had a lower or equivalent ampacity to reference copper. The specific ampacity was not determined here because the measurement of the CNT vol. % was not precise enough to reliably evaluate the low vol. % of CNT in these composites (as discussed in sections 1.4.3 and 1.4.4). In addition, we can assume that the high value of ampacity of the composite integrating 200 μm could arise from a very low amount of CNT in the composite, leading to an ampacity close to that of pure copper. A segregation of the Cu and CNT phases was also observed in all of the tested lines. After the measurement, the composite integrating 200 μm long CNT (Fig. 3.17e,f) has a morphology similar to the previous results (Fig. 3.15a). For composites integrating 20 μm long CNT (Fig. 3.17b), the copper migrated rapidly outside the CNT network in the line region (Fig. 3.17c) that was close to the failure zone (Fig. 3.17d).

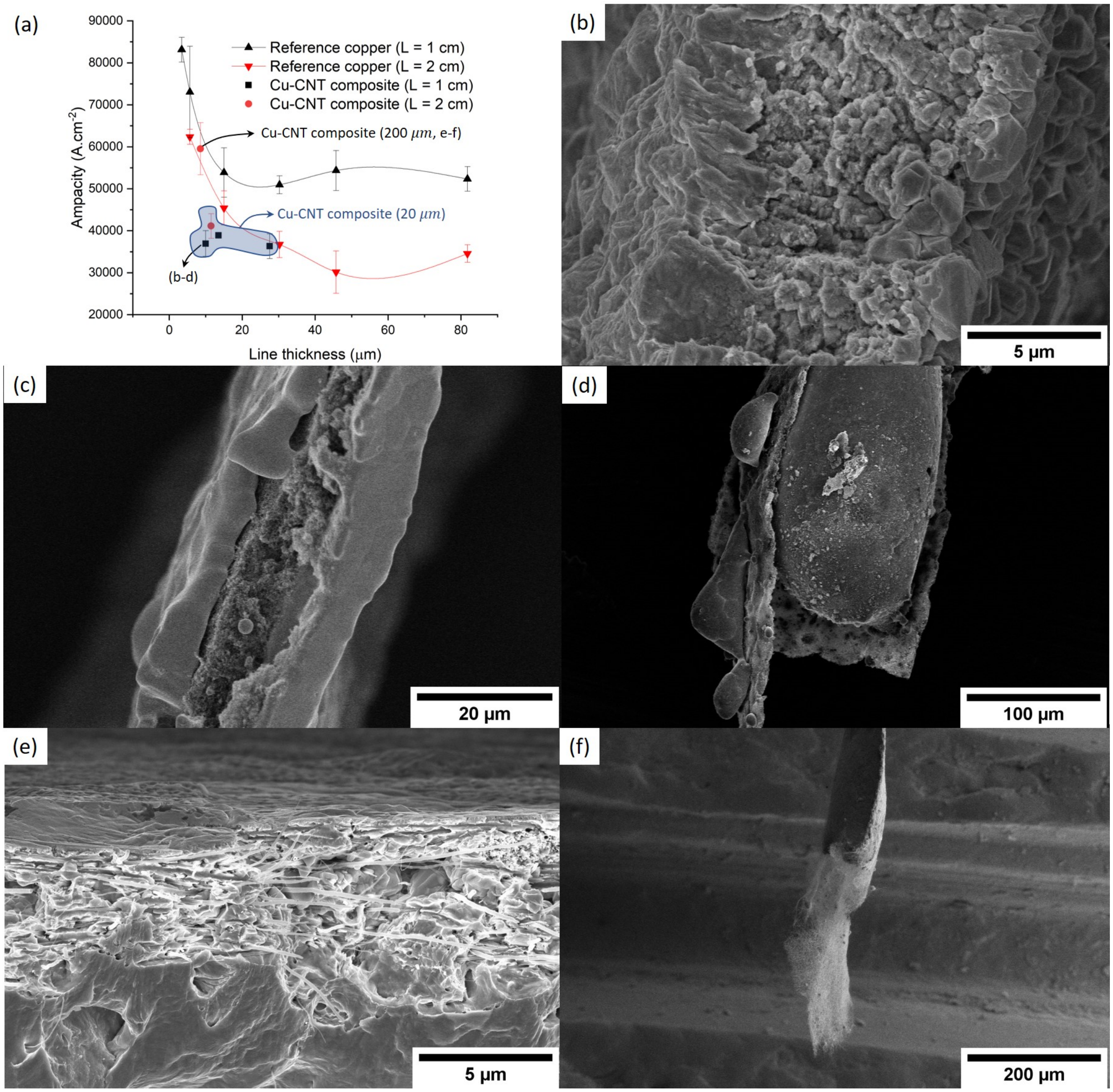

Figure 3.17. (a) Ampacity of reference copper for different line lengths (1 and 2 cm) and different line thicknesses. Ampacity of Cu-CNT composites (20 and 200 μm) with low CNT vol. % and coated with 0.5 mM of dopamine. SEM cross sections of a characterized Cu-CNT composite (20 μm) (b) before the ampacity measurement and after the ampacity measurement (c) close to and (d) in the failure zone. Cu-CNT composite (200 μm) (e) before and (f) after the ampacity measurement.

3.6 CHAPTER SUMMARY

We developed new setups to precisely measure the resistivity, TCR and ampacity of our materials. The measure of the resistivity when varying temperature should always be run two times due to an artifact appearing systematically during the first measurement. The resistivity of our Cu-CNT composites (low CNT vol. %) integrating short arc discharged CNT@PdaCu and long CVD grown CNT@PdaCu display a higher resistivity than the one of pure copper while having a TCR slightly lower. We showed that a high degree of copper filling is crucial to reduce the composite resistivity. The annealing of the carpets prior to the electroplating as well as the reduction of the Pda coating was unsuccessful to increase the CNT contribution to the electron transport (stable TCR). When comparing our systems integrating a high vol. % of MWCNT to the literature, "we highlight that long and large MWCNT could be used in the Cu-CNT composite to reach low resistivity. Also, the CNT contribution to the electronic transport was higher in the Ni-CNT composite than in the Cu-CNT composite. In addition, the resistivity of the CNT network, featuring dot-contacts by Ni particles (after annealing of the Ni-CNT composite), is lower than the Ni-CNT composite, where CNT are fully embedded in Ni; featuring the potential interest of tailoring the CNT-Cu interface with such Ni electrical contacts to promote effective electronic transport in the Cu-CNT composite. In this regards, we showed that a composite annealing was beneficial in a Ni-CNT system while it is detrimental in a Cu-CNT system. Controversially to the literature, we report a loss of ampacity in our metal-CNT composites compared to the pure reference metal. Also, we show that the atmosphere used for the measurement and the dimension of the sample can have a significant impact on its ampacity, leading to variations typically in the range of the ampacity gains of Cu-CNT composite (compared to reference copper), which can be seen in the literature. Therefore, we stress the importance of controlling and disclosing the experimental parameters of the ampacity measurement accurately in order to provide reliable comparisons of published results between the Cu-CNT composites and pure copper."[155]

Chapter 4

Lightning strike protection

4.1 INTRODUCTION

Lightning strikes are the result of electrical charges generated by collisions between ice and/or water particles, being separated rapidly (up to 20 m.s^{-1}) by vertical winds within thunderclouds. An electric field is generated from the separation of the positive charges (at the top of the clouds) and the negative charges (at the bottom of the clouds). The difference of potential between the ground and the thunderclouds is around 100 MV. Such a high field promotes the formation of an ionized channel (leader) that travels progressively downward, forming several branches (Fig. 4.1a.1). When a leader reaches close to the ground, an upward leader initiates and connects the downward leader, triggering a "return stroke" having high intensity and flowing from the ground to the cloud (Fig. 4.1a.1,2).[200] At this point, if additional negatives charges are available in the thundercloud, they can start to travel downward via the existing leader, provoking additional/subsequent return strokes.

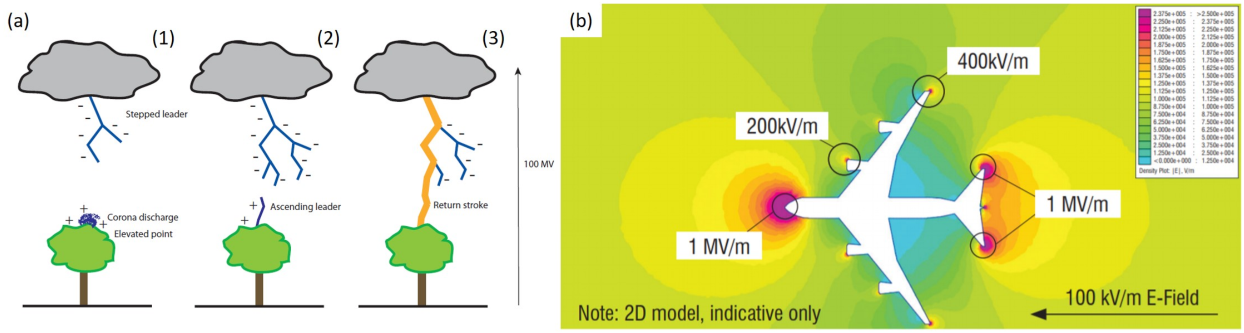

Figure 4.1. (a) Mechanisms of the initiation of a lightning: (1) stepped leader formation, (2) initiation of an upward leader, and (3) return stroke. (b) Indicative electrostatic model of an airplane in a 100 kV.m^{-1} ambient field. Sharp curvatures in the structure lead to the electric field concentration at the aircraft extremities.[200,201]

Most of the lightning strikes on an aircraft happens within the thunderclouds, during the climb and descent phases of the flight because most of the lightning activity is between 1500 and 4500 m of altitude.[202] An airplane can be exposed to natural lightning or lightning initiated by the aircraft. For natural lightning (Fig. 4.2a), the leader originating from the cloud propagates and comes close to the aircraft. The electric field, generated by the charges in the leader, concentrates around the tips/edges/extremities of the aircraft (Fig. 4.1b), ionizing the air around these spots (corona effect) and generating a junction leader. At the same time, another junction leader appears at the other extremity of the aircraft, propagating towards the opposite charge. An aircraft travelling around a charged region can also trigger a lightning strike if the electric field at the aircraft extremities is high enough to trigger the appearance of bi-directional leaders (Fig. 4.2b). In both cases, the places where the bi-directional leaders appear are called the initial attachment points.[203]

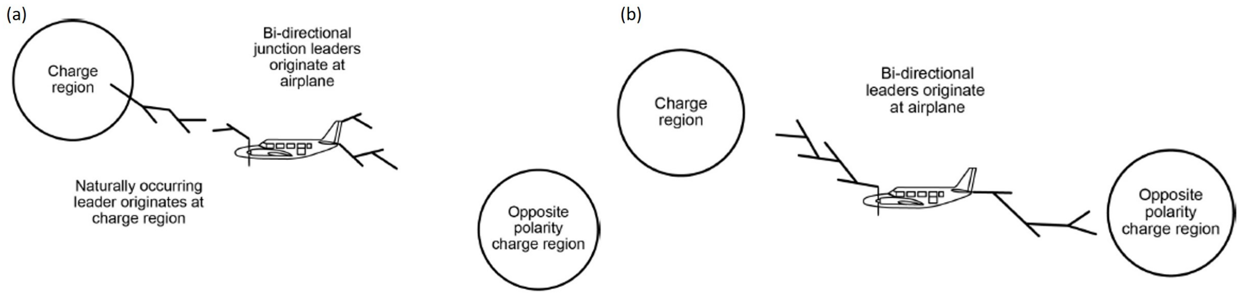

Figure 4.2. Schematic of (a) a naturally occurring lightning strike and an aircraft initiated lightning strike.[203]

Because the airplane is moving while the ionized channel is fix, subsequent attachment points are created along the leader sweeping path (Fig. 4.3a), leading to "swept stroke" damaging (Fig. 4.3b).[202] An aircraft can be separated in different zones depending on their probability to be struck by a lightning (Fig. 4.4a). The zone 1 is susceptible to be affected by a first return stroke (initial attachment point). The zone 2 is the swept stroke zone where a return stroke of reduced amplitude is likely. In zone 3, lightning attachment is unlikely but it can conduct the current between two attachment points. Furthermore, zone 1 and 2 can be subdivided in zones A and B depending on the probability of the lightning to remain attached for a short (A) or longer period (B) (e.g. lightning are more likely to remain attached at the trailing edges of the wings).[201,202]

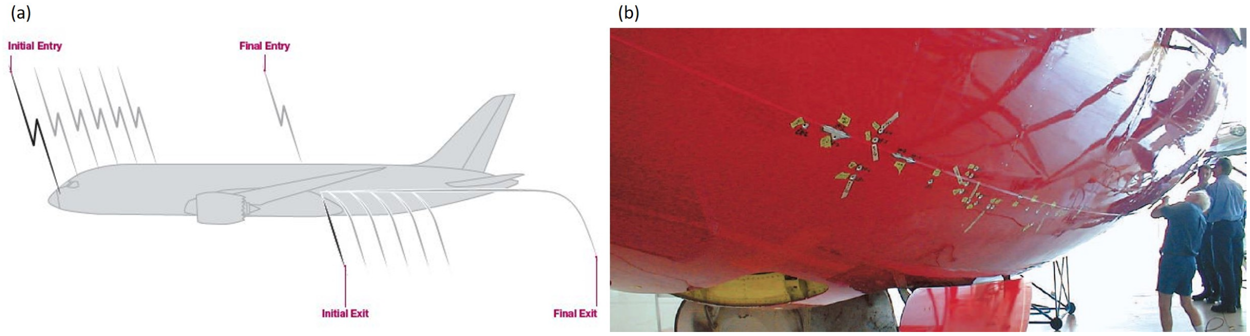

Figure 4.3. Schematic of (a) the attachment of a lightning strike on an airplane. The lightning attaches to one ionized edge of the airplane and is conducted through the conducting materials of the airplane, exiting to the ground. While the aircraft moves, the lightning can successively attach to different locations. (b) Photograph of a "swept stroke" damage caused when the lightning attachment point moves along the aircraft.[202]

A standardized current waveform is usually used to model the lightning strike principal features (Fig. 4.4b). The component A is associated to the initial return stroke attachment (e.g. near the nose and tail of the airplane) and is characterized by a very high current (200 kA) over a short time (≤ 0.5 ms). The component D is similar but reflects return strokes of reduced amplitude (100 kA) that can occur when the arc is swept along the aircraft. The components A and D cause most of the damaging: the joule heating can lead to the explosive fusing of thin conductors, causing damaging over-pressures. Damaging over-pressures can also arise from the fast heating of the air in the lightning leader. In addition, the very high current of the lightning induces magnetic forces which can pull apart the conductors. The magnetic field generated by the high current travelling in the airplane can induce voltage variation in the wiring, damaging the electronic systems. Furthermore, the current conducted through the aircraft can induce arcing/sparking at the conductor junctions (e.g. fasteners), potentially igniting the fuel vapors. In comparison, the components B and C are characterized by lower currents (4.2 kA and 400 A, respectively) over a significantly longer period ($\leq$ 5 ms and $0.25 \leq \tau \leq 1$ s, respectively) and are called the intermediate and continuing currents, respectively. The damaging of components B/C are greatly reduced in comparison of components A/D, and usually leads to the heating of the surface of the aircraft, vaporizing the surface resist.[201]

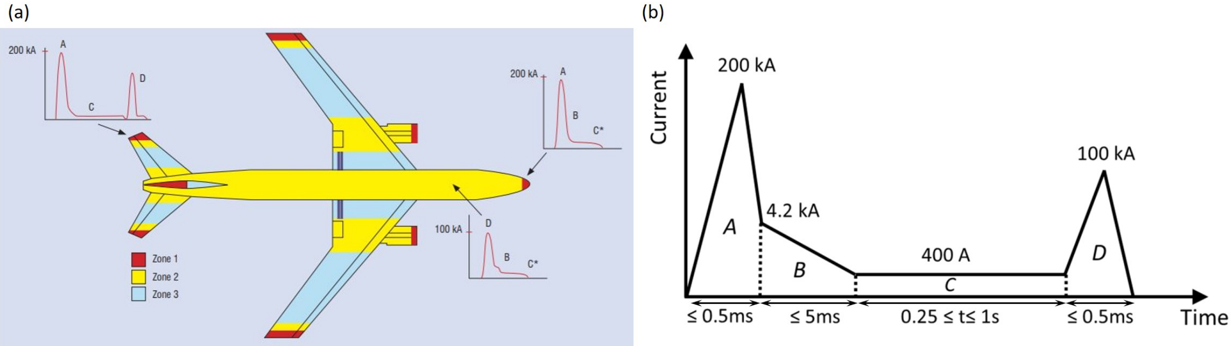

Figure 4.4. (a) Simplified schematic of the zones of an airplane that are prone to lightning strikes. Zone 1 area is likely to be affected by the initial attachment of a strike (entry or exit). Zone 2 is the area with a high probability to have the lightning being swept from the first attachment point. Zone 3 may experience conducted currents but with a low probability of attachment of the strike. (b) Standardized current waveform of a lightning strike.[201,204]

To protect effectively the plane from the lightning strikes, conductive materials are strategically integrated in the different zones of the aircraft. Metal having a high conductivity (Al, Cu, ...) are usually embedded into the composite outer ply of the aircraft as a plain foil or as a metallic mesh. Metallic meshes (expanded foils) are usually used to reach a compromise between the mass and the resistance of the lightning strike protection (LSP). The copper has a lower resistivity than Al (1.69 vs 2.68×10^{-6} Ω.cm)[12] but Cu has a higher density (8.96 vs 2.7 g.cm^{-3})[12] leading to specific resistivity (resistivity $\times$ density) of 15.14 and 7.23 Ω.g.cm^{-2} for Cu and Al, respectively. Aluminum is thus more interesting than copper regarding the mass of material needed to achieve a LSP of equal conductance. Yet, metals can be corroded by the carbon fiber-polymer composite when moisture infiltrates the protecting ply of the aircraft, drastically lowering the conductivity of the LSP. Aluminum being far less noble than copper, it is much faster corroded, and copper becomes preferably used instead of aluminum.[1]

4.2 CHARACTERIZATION TO LIGHTNING STRIKE

To characterize the resistance of our materials to lightning strikes, we fabricated samples of 8 inches (20.3 cm) of diameter. Our substrates were constituted of a glass fiber/CR4 epoxy resin support on which a layer of copper/Ni (t_{cu} $\approx$2-3 μm and t_{ni} is few nm) was deposited (provided by Circuit Foil). The preparation of the substrate is depicted in Fig. 4.5. A copper foil having a thickness of 2-3 μm is very fragile and should be deposited on a thicker copper carrier foil. The thin copper foil side was pressured while heating on the epoxy support to promote adherence. Afterwards, the copper carrier can be peeled thanks to the thin Ni intermediate layer. The CNT are then deposited on the substrate and the electroplating is made afterwards. To mimic the polymer-composite structure of an aircraft, the samples were glued on a 1 mm thick FR4 substrate (glass fiber-epoxy composite).

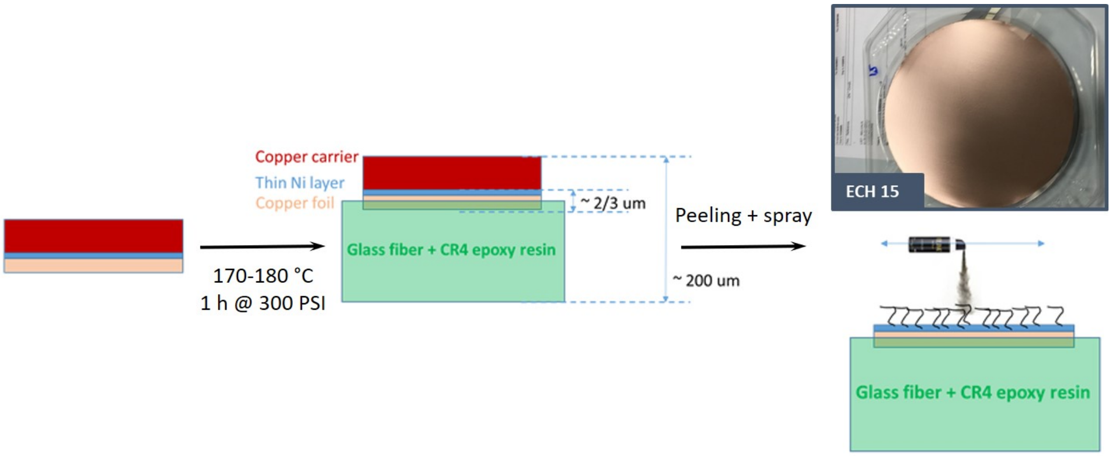

Figure 4.5. Schematic of the substrate preparation for the characterization of the composite samples to lightning strikes.

To perform the lightning strikes tests, the samples were placed in a metallic support that is shown in Fig. 4.6. Lightning strikes are generated at the center of the samples using the component D of the current waveform (100 kA - Fig. 4.4b).

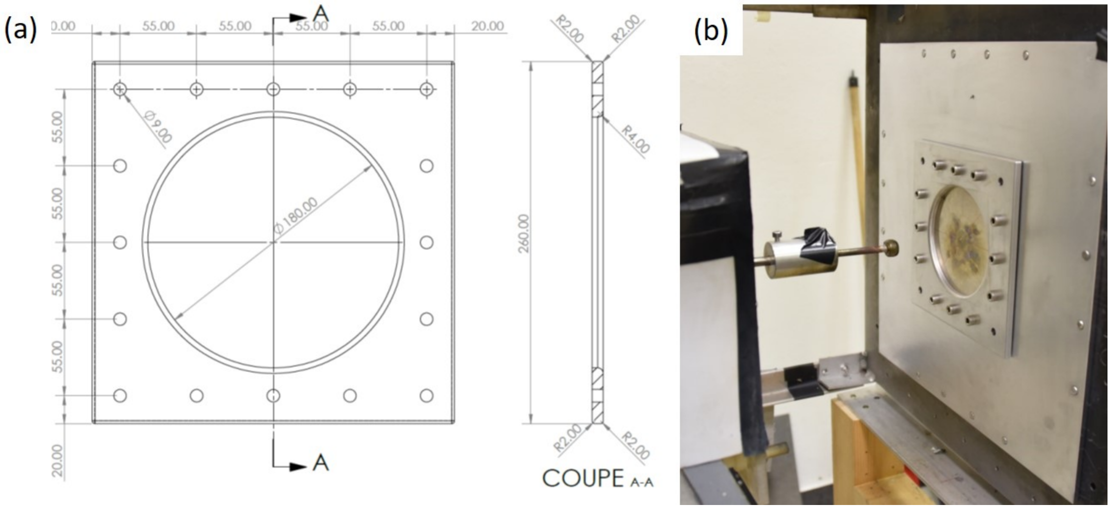

Figure 4.6. (a) Schematic and (b) photograph of the support used at Onera to perform the lightning strike tests.

Here, we choose to consider the size of the holes left in the sample by the lightning to evaluate the resistance of our composites to lightning strikes (for a same area density). It was assumed that the energy of sublimation of the material comes mainly from the energy dissipated by the Joule effect that is calculated by integrating the power dissipated in the sample over the time of the lightning strike. Considering the expression of the radial resistance of a thin sample,[205] it can be written as

$$E_{Joule} = \int^{\tau} RI^2 d\tau = \frac{1}{\sigma 2\pi t} \ln \frac{r_{ext}}{r_{int}} \int^{\tau} I^2 d\tau \tag{4.1}$$

where R is the resistance, σ is the conductivity, t is the sample thickness, and r_{ext} and r_{int} correspond to the radius of the support and the radius of the injected arc, respectively. The energy of vaporization is given by

$$E_{vap} = mH = \gamma t S H \tag{4.2}$$

where m is the mass (g), γ is the density (g.cm^{-3}), S is the surface of vaporization and H is the specific enthalpy of sublimation (J.g^{-1}). Equalizing E_{Joule} with E_{vap}, we can write

$$\frac{1}{2\pi} \ln \frac{r_{ext}}{r_{int}} \int^{\tau} I^2 d\tau = \gamma \sigma t^2 S H \tag{4.3}$$

Where the first part of the equation is approximated as a constant considering that the measured integrals of $I^2 d\tau$ were similar for all the samples. As consequence, we can compare composite samples to pure copper samples using

$$\gamma_1 \sigma_1 t_1^2 S_1 H_1 = \gamma_2 \sigma_2 t_2^2 S_2 H_2 \tag{4.4}$$

leading to

$$\frac{\sigma_1 t_1 H_1}{\sigma_2 t_2 H_2} = \frac{\gamma_2 t_2 S_2}{\gamma_1 t_1 S_1} \tag{4.5}$$

and using the sheet resistance ($R_s^{-1} = \sigma t$) and the area density of the sample ($\lambda = \gamma t$ [g.cm^{-2}]), we have

$$\frac{R_{s2} H_1}{R_{s1} H_2} = \frac{\lambda_2 S_2}{\lambda_1 S_1} \tag{4.6}$$

This equation allows to link the amount of vaporized material to its sheet resistance and to the specific enthalpy of sublimation. This is a simplified model as we neglect numerous phenomenons such as the variation of resistance with temperature, the loss of heat by radiation, etc ... Still, we believe that it can be used to evaluate the main trends. In particular, we took $\lambda * S$ as figure of merit knowing that the aeronautic industry seeks to reduce the area density of the LSP (λ) while

Sample	Description	$\frac{S_{cu}}{S_{compo}}$
Sample 5	Arc-discharged CNT@PdaCu	1.0
Sample 7	200 μm CVD grown CNT@PdaCu	∞*
Sample 12	200 μm CVD grown CNT@PdaCu	1.6
Sample 14	200 μm CVD grown CNT@PdaCu (free standing, made on $SiAl_2O_3$)	2.1
I21	800 μm CVD grown CNT@PdaCu (compressing system)	24.06*
A1L1	200 μm CVD grown CNT@PdaCu	7.6
A1L2	200 μm CVD grown CNT@PdaCu	3.7
B4L2	200 μm CVD grown CNT@PdaCu (compressing system)	14.4
C7L1	Arc-discharged CNT@PdaCu	2.0
D10L1	200 μm long CVD grown CNT@PdaCu (0.0625 mM of dopamine)	28.4*
P1	Patterned composite, 200 μm CVD grown CNT@PdaCu (compressing system)	0.92
P2	Patterned composite, 200 μm CVD grown CNT@PdaCu (compressing system)	0.69

Table 4.1. List of the samples characterized with lightning strikes and ratio of vaporized area (sample compared to pure copper at same area density). All samples except I21, B4L2, P1 and P2 were made by chronopotentiometry at current density between 10 and 20 mA.cm^{-2}. Samples I21, B4L2, P1 and P2 were obtained using the compressing system and current pulses of 35/0 mA.cm^{-2} - 0.02/0.1 s. (*) Calculated with the value of the bottom vaporized surface.

keeping a minimum of damage (S). Our samples (described in Table 4.1) were characterized in two campaigns (Fig. 4.7) and compared to pure copper samples having different area densities. The vaporized surface of the samples was averaged from three measures (using ImageJ) and increases for lower area densities (Fig. 4.7a and Fig. 4.8a). It can be understood considering that E_{Joule} increases as the area density decreases and that the mass per square centimeter to vaporize (thus E_{vap}) decreases at the same time. As comparison, composites integrating short CNT@PdaCu (sample 5 - Fig. 4.8b) showed a result very similar to pure copper. When comparing to composites integrating 200 μm long CNT (sample 12, 14 - Fig. 4.8c), a beneficial impact of the length of the CNT seems to emerge as the vaporized area decreases slightly in comparison to pure copper (Table 4.1). Interestingly, we observed an unexpected behavior characterized by a preferential vaporization of the top layer, leaving a black under-layer (sample 7 - Fig. 4.8d). In this case, the vaporized area was measured distinctively for the top layer and the bottom layer. We believe that this preferential vaporization can be linked to the bi-layered architecture of our systems (the composite layer on the top of the thin pure copper substrate). This could be interesting for LSP as it would probably favor a superficial damaging of the aircraft structure. In addition, the black under-layer was still conductive, potentially enabling a repairing by electroplating.

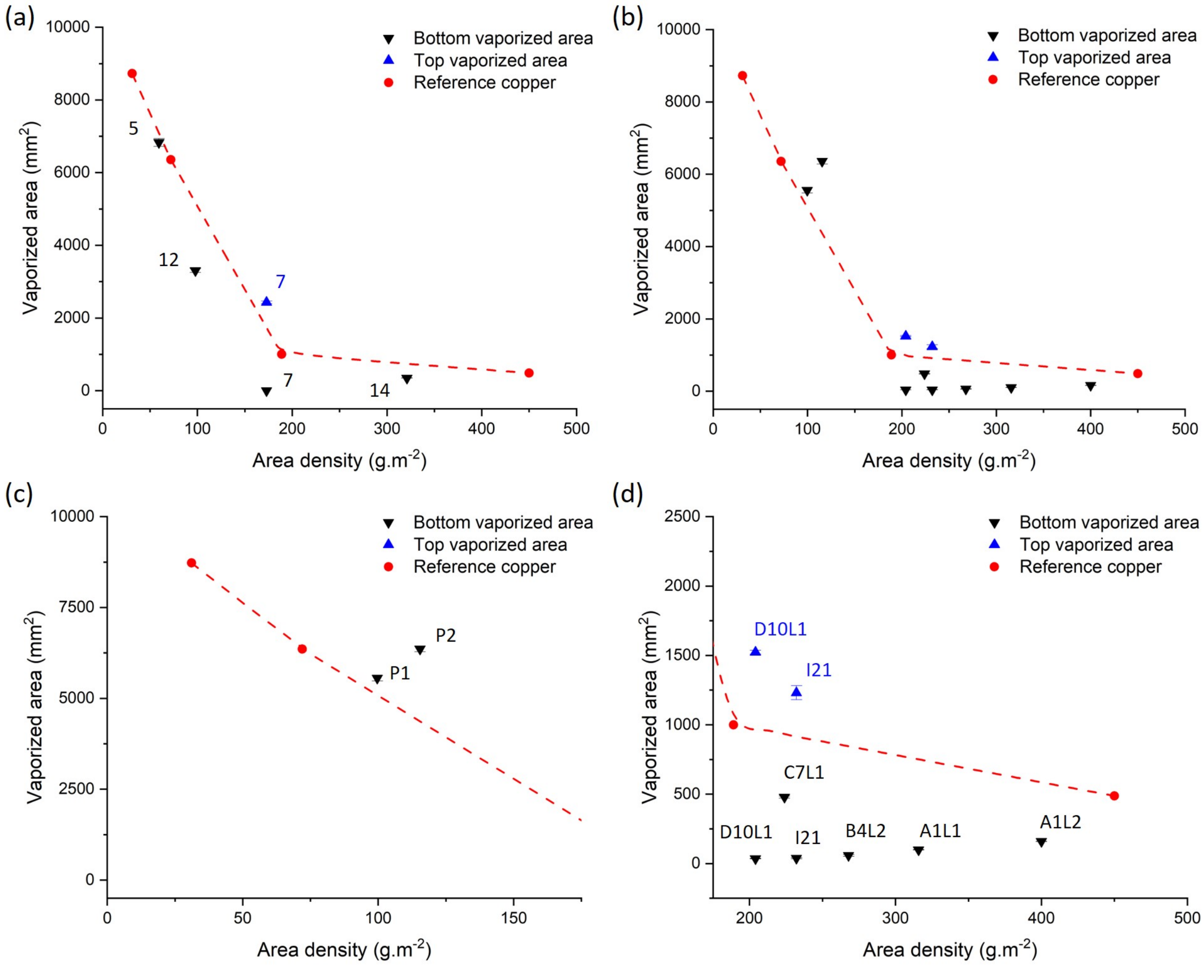

Figure 4.7. Vaporized surface vs area density of reference copper samples and Cu-CNT composites: (a) first campaign of analysis, (b) second campaign of analysis and (c,d) zoom in graph b.

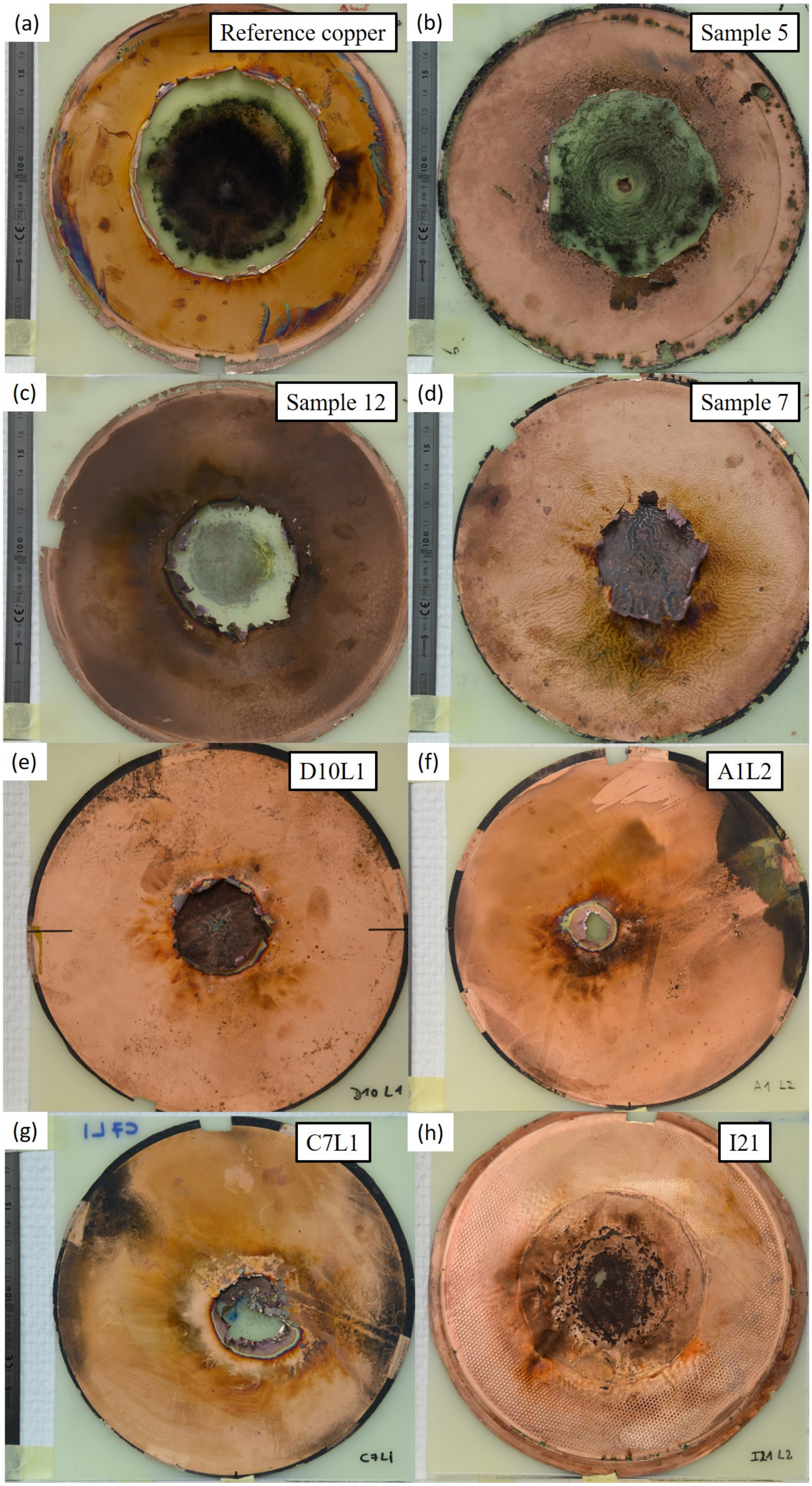

Figure 4.8. Photographs of the samples after the characterization to lightning strike.

The occurrence of a top-layer preferential vaporization was clearly confirmed during the campaign 2 (Fig. 4.7b-d) in the sample D10L1 (Fig. 4.8e), also containing 200 μm long CNT (coated with 0.0625 mM of dopamine). In addition, other samples containing 200 μm long CNT (A1L1 and A1L2 - Fig. 4.8f) seemed more efficient than the composite containing short CNT (C7L1 - Fig. 4.8g). The difference of ratio S_{cu}/S_{compo} between A1L1 and A1L2 remains unclear (Table 4.1) but the higher area density of A1L2 suggests that a higher amount of copper could have been over-plated on the top of the composite, leading to a result closer to the one of pure copper. The sample I21 (Fig. 4.8h) was obtained by integrating a carpet (diameter = 12 cm) of 800 μm long CNT at the center of the sample while using the compressing system. The center of the disk was a composite while the external ring was pure copper. The sample showed a good resistance to the lightning strike in comparison to copper, with a tendency to evaporate preferentially the top layer. We believe that the most promising result was obtained with the sample B4L2 (Fig. 4.9a,b - 200 μm long CNT - use of the compressing system) which resisted to the lightning strike with almost no vaporization of the composite ($S_{cu}/S_{compo} = 14.4$). Indeed, it seems that the holes being seen in the sample after the lightning strike correspond to defects (lack of electroplating due to air bubbles being trapped) already present before the test. This result suggests that a composite containing a high $\%$ of long CNT could resist to lightning strike without significant damaging. We also characterized patterned grids of composites obtained using the compressing system. The resistance of the sample was equivalent or less good than pure copper. However, the samples contained significant defects of electroplating (Fig. 4.9c,d) which probably contributed to the lesser performance.

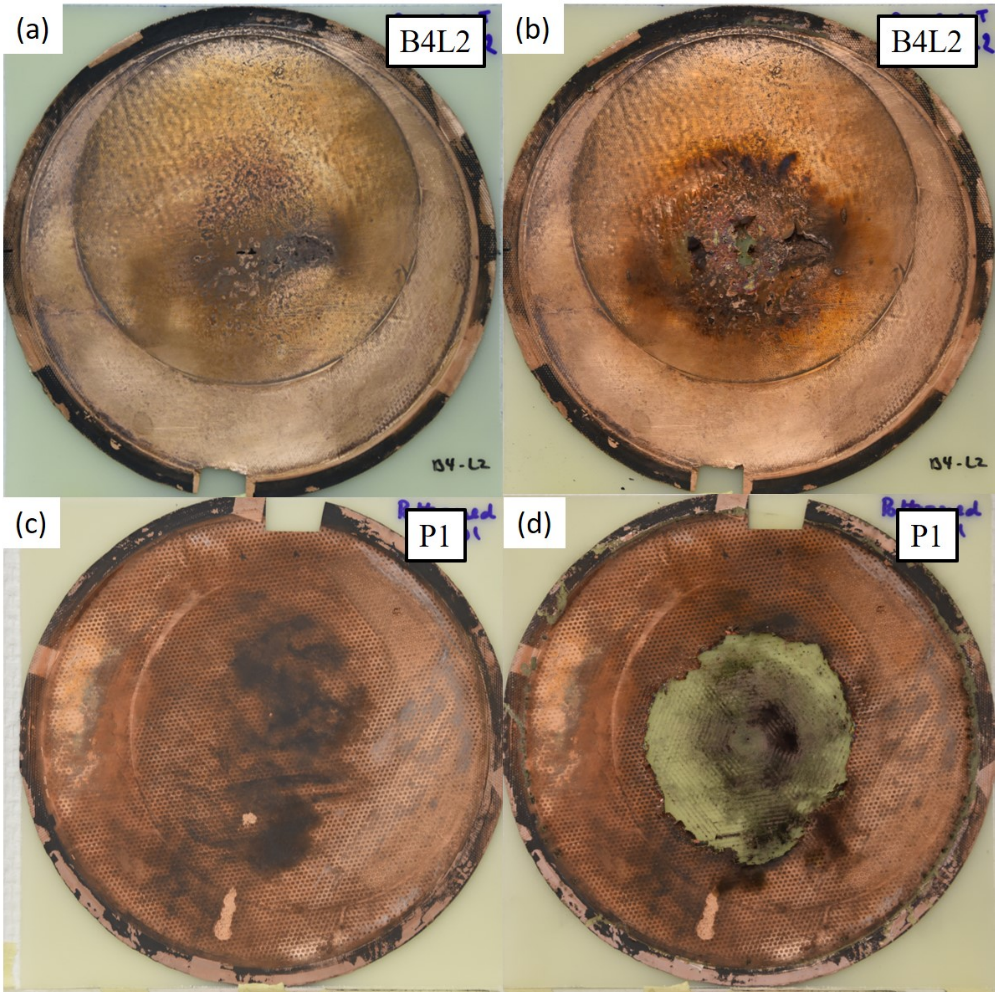

Figure 4.9. Photographs of the samples before (left) and after (right) the characterization to lightning strike.

While the beneficial effect of integrating CNT to the composite seems undoubtedly established, it is difficult for us to reach an understanding of the underlying physical mechanisms. Still, we allow ourselves to invoke several strong hypothesis to initiate a discussion. Based on the equation 4.6, it seems crucial to evaluate the specific enthalpy of sublimation H of our composite. First, we derive the expression of the volumetric enthalpy of sublimation of the composite h_{compo} (J.cm^{-3}). The total energy that is needed to sublimate a given volume of composite is given by the sum of the energies needed to sublimate each of its components:

$$V_{compo}h_{compo} = V_{cu}h_{cu} + V_{cnt}h_{cnt} \tag{4.7}$$

leading to

$$h_{compo} = \frac{V_{cu}h_{cu} + V_{cnt}h_{cnt}}{V_{compo}} = \beta_{cu}h_{cu} + \beta_{cnt}h_{cnt} \tag{4.8}$$

where β_{cu} and β_{cnt} are the volume fraction of Cu and CNT, respectively. We calculate H from

$$H_{compo}\gamma_{compo} = h_{compo} = \beta_{cu}h_{cu} + \beta_{cnt}h_{cnt} \tag{4.9}$$

Developing the equation, we get

$$H_{compo} = \frac{\beta_{cu}H_{cu}\gamma_{cu} + \beta_{cnt}H_{cnt}\gamma_{cnt}}{\gamma_{compo}} \tag{4.10}$$

The data on the enthalpy of sublimation of CNT are lacking in the literature and are very scarce regarding the graphene. Calculations have shown that graphene has a specific enthalpy of sublimation similar to that of graphite ($\sim$ 58.17 and 59.27 kJ.g^{-1}, respectively). The slight difference arising from Van der Walls bonding between the stacked graphene layers in bulk graphite.[12,206] Therefore, we took the value of the specific enthalpy of sublimation of graphene to roughly approximate the one of CNT. Constituting another strong hypothesis, this value is used to elaborate a piece of explanation that would nevertheless require to be confirmed by the evaluation of the specific enthalpy of CNT. The specific enthalpy of sublimation of copper was taken as 5.3 kJ.g^{-1}.[12,207] As we previously discussed, the density of CNT greatly vary from one CNT to another, therefore it is important to evaluate the density of our own CNT. The density of the CNT (γ_{cnt}) can be extracted from the density of our composite

$$\gamma_{compo} = \frac{m_{cnt} + m_{cu}}{V_{tot}} \tag{4.11}$$

and further developing

$$\begin{cases} \dfrac{V_{cnt}}{V_{tot}} = \beta_{cnt} \\ \dfrac{V_{cu}}{V_{tot}} = \beta_{cu} \end{cases} \implies \gamma_{cnt} = \frac{\gamma_{compo} - \gamma_{cu}\beta_{cu}}{\beta_{cnt}} \tag{4.12}$$

Injecting this expression in equation 4.10 and using the average value of γ_{compo} and $\beta_{cu} = 1 - \beta_{cnt}$ in Table 3.3 for a Cu-CNT composite having a high vol. $\%$ of CNT (5.38 g.cm^{-3} and 57.5$\%$, respectively), we calculate γ_{cnt}= 0.54 g.cm^{-3} and we get an approximation of H for our composites obtained when using the compressing system (typically B4L2 and I21)

$$H_{compo} = \frac{\beta_{cu}H_{cu}\gamma_{cu} + H_{graphene}(\gamma_{compo} - \gamma_{cu}\beta_{cu})}{\gamma_{compo}} = 7.54[kJ.g^{-1}] \tag{4.13}$$

leading to a ratio

$$\frac{H_{compo}}{H_{cu}} = 1.42 \tag{4.14}$$

The increase of H in a composite having a high vol. $\%$ of CNT seems significant and is likely to reduce drastically the mass of material vaporized by the lightning strike. Similarly, the specific heat of the composite C_{compo} can be obtained using the rule of mixture[208] and was calculated using the data in Table 1 and Table 3.3 with

$$C_{compo} = \frac{(C_{cnt}\gamma_{cnt})\beta_{cnt} + (C_{cu}\gamma_{cu})\beta_{cu}}{\gamma_{compo}} = 0.3867(J.[g.K]^{-1}) \tag{4.15}$$

where $C \times \gamma$ is the volumetric heat capacity (J.[cm^3.K]$^{-1}$). The specific heat of the composite is similar to that of pure copper (0.386 J.[g.K]$^{-1}$) and should not significantly increase the energy absorbed by the composite in comparison to pure copper. But if we consider that CNT sublimate at higher temperature than the copper phase, then the energy absorbed by the composite would be higher than pure copper. The sublimation temperature of graphene can be approximated by the sublimation temperature of graphite.[209] We calculate the energy required to heat up the CNT and the Cu phase to their respective evaporation temperature (graphite: 4098 K, Cu: 2833 K)[209,210] by

$$E_{h-compo} = \frac{C_{cnt}\beta_{cnt}\gamma_{cnt}\Delta T_{cnt} + C_{cu}\beta_{cu}\gamma_{cu}\Delta T_{cu}}{\gamma_{compo}} = 1003.8(J.g^{-1}) \tag{4.16}$$

The energy absorbed by the composite could thus be higher than pure copper (980.4 J.g^{-1}). Still, this gain of energy (23.4 J.g^{-1}) is one hundred times lower than difference (between the composite and copper) of specific enthalpy of sublimation (2240 J.g^{-1}) and may be negligible. Again, taking the temperature of sublimation of graphite to approximate the one of CNT constitutes another strong hypothesis. However, in view of this result, we could consider that the variation of energy caused by a deviation from the real sublimation temperature of the CNT would also be negligible in comparison to the gain of energy of sublimation.

The above discussion called strong assumptions on the temperature and enthalpy of sublimation of CNT but highlighted that the energy necessary to vaporized the composite could have a non negligible effect on its resistance to lightning strikes. Still, the ratio $H_{compo}/H_{cu} = 1.42$ is not sufficient to explain the reduction of vaporized surface in sample B4L2 (Table 4.1) compared to pure copper (having a same area density) using the equation 4.6:

$$1.42\frac{R_{scu}}{R_{scompo}} = 14.4 \tag{4.17}$$

It suggests that CNT also have a beneficial effect that is not related to their specific sublimation enthalpy and therefore, we discuss additional possibilities.

Considering the potential high thermal conductivity of CNT (Table 1), a faster radial dispersion of the heat could promote a reduction the amount of vaporized material at the center of the sample. Based on the measure of resistivity previously done on our composites, it is likely that the sheet resistance of the composites tested to lightning strike is higher than pure copper. But in this case, the current flows radially from the center of the sample, and considering the isotropic orientation of the CNT in the foil, it could drastically decrease the resistivity and the TCR of the composite. As already discussed, the number of conduction channels available to the electrons depends on their energy. In this case, we can assume that the temperature and the electrical field are high enough to promote the conduction of the electrons through a maximum of conduction channels favoring a significant contribution of the CNT to the electron transport. Furthermore, conduction through all the shells of the CNT could be promoted. In this case, the ampacity of the composite could attain high values as a high current density would flow through the CNT before leading to material failure (e.g. CNT carry 100 × the current density of copper).[53] In the previous chapter, the resistivity/TCR measurement was made on 0.5 × 0.5 cm samples up to 443 K while using electrical field of about 20 mV.m^{-1} to generate current that are lower than 1 A. The current generated by the component D of a lightning is around 100 kA, it is safe to assume that the electrical field generating the electrical current in the LSP is much higher than in our laboratory, while also leading to temperatures that are largely superior. It is thus difficult to extrapolate, from our laboratory measurements, the features that our composite could display when impacted by a lightning strike. Yet, we may assume a non-linear variation of the composite resistivity as the electrical field and temperature increase drastically. Therefore, further lightning strike tests should be carried out to potentially highlight the gap with the properties measured in our laboratory, and bring out the benefits of CNT for the composite in this specific application.

4.3 CHAPTER SUMMARY

In this chapter, we characterized the resistance of Cu-CNT composites as lightning strike protection. To evaluate the performance of the materials, we took $\lambda \times S$ as figure of merit (area density × vaporized surface) as the aeronautic industry seeks to reduce the mass of the LSP while keeping a minimum damaging of the aircrafts. Compared to pure copper, the majority of our composites containing long CNT (200 and 800 μm) have shown striking results while composites containing the arc discharged CNT were more similar to the copper. In particular, a composite obtained using the compressing system (high vol. $\%$ of 200 μm long CNT) seemed to resist very well to the lightning strike with almost no vaporization of material, the vaporized area of copper being 14.4 × larger than the one of the composite. It was difficult for us to reach an understanding of the underlying physical mechanisms. Invoking several hypothesis, it was possible to link the figure of merit to the sheet resistance and the energy absorbed by the composite (mainly due to vaporization). We approximated that the specific enthalpy of sublimation of our composite, having a high vol. $\%$ to 7.54 kJ.g^{-1}, is 1.42 times that of pure copper. The specific heat of the composite was calculated to be similar to the one of pure copper (0.3867 J.[g.K]$^{-1}$). Assuming that the CNT would heat up to a higher temperature than copper before vaporizing, the energy required to heat up the composite to the sublimation temperature would be higher than the energy of pure copper (1003.8 vs 980 J.g^{-1}) but leading to a negligible impact in comparison to the large difference of specific sublimation enthalpy (2.24 kJ.g^{-1}). However, this gain of vaporization energy seems to be not sufficient to explain our results. Indeed, our composites could have electrical properties that are different from the one measured within the range of temperature/electrical field available in our laboratory. Also, the isotropic orientation of the CNT could be beneficial in this case as the current is flowing radially from the center of the sample. Also, the extreme conditions (high electric filed, high temperature, ...) could favor the electron conduction through all the walls of the CNT, and by a large number of conduction channels. In this case, the ampacity of the composite could be higher than pure copper. In addition, an unexpected preferential vaporization of the composite top layer, protecting the LSP under-layer, was observed in several cases. However, a more advanced investigation is called to clarify the main underlying mechanisms/properties of materials that lead to the noticeable improved performances in LSP.

Summary and conclusion

In this thesis, we investigated the fabrication of Cu-CNT composites with the objective of integrating them into lightning strike protections. Here, we provide a summary of the different chapters of our work, drawing our main conclusions from them.

In **chapter 1**, we presented an innovative method to fabricate Cu-CNT composites that outperforms the current state of the art and enables the fabrication of Cu-CNT composites with a thickness of up to $\sim 45\ \mu$m using only an aqueous plating solution where an organic solvent-based solution was required before. Addressing the current challenges of fabrication, we demonstrated that the doping of the CNT polydopamine coating with copper ions disruptively enhanced the filling of the CNT carpet with copper in comparison to undoped polydopamine. A swelling of the CNT carpet during the electroplating was also evidenced, drastically limiting the maximum CNT vol. $\%$ in the composite. Addressing this problem, we developed an innovative compressing system allowing us to perform the electroplating of the CNT carpet while it is being compressed, and thus reaching a CNT vol. $\%$ of around 40-45$\%$. Aiming to integrate CNT into the composite with an isotropic orientation and with various dimensions, we fabricated CNT carpets using a filtration method for the longest CNT (800 μm) and used a spraying method for the shorter ones (2-20 and 200 μm). In particular, we showed that the spraying method was suitable for the production of large samples (20.3 cm of diameter). While our method enabled the fabrication of thick layers, we also demonstrated the fabrication of self-standing ultra-thin composite foils ($\sim$ 2.5 μm) when using a titanium substrate. Finally, we showed that the polydopamine coating enabled the fabrication of the Cu-CNT composite using electroless plating, while also being extremely powerful in the fabrication of various metal-CNT composites.

In **chapter 2**, we characterized our CNT carpet systems before and after an annealing treatment. We highlighted the reducing activity of the polydopamine during its polymerization, leading to a partial reduction of the copper ions used as dopant. In addition, the post-annealing of the CNT between 573 and 773 K (in Ar) evidenced an additional reduction of the copper contained in the polydopamine coating, leading to the apparition of copper nuclei at the surface of the CNT. We also showed that the electrical resistance of the coated CNT (200 μm long) carpets could be reduced by $\sim$ 33 to 37$\%$ using annealing. The TCR of these carpets was negative, an encouraging attribute when targeting Cu-CNT composites with a low TCR. In addition, the TCR was independent of the annealing conditions but seemed to be decreased by increasing the coating on CNT. In this regard, carpets of CNT coated with Cu or Ni-doped polydopamine reached a similar specific resistivity to that of carpets containing oxidized CNT when the dopamine concentration in the coating solution was decreased to 0.0625 mM (the specific resistivity decreased by 90% in comparison to 0.5 mM). Finally, we estimated that carpets made of long CNT (200 and 800 μm) coated with Cu-doped Pda were significantly more conductive than similarly-coated carpets containing shorter CNT (2-20 μm).

In **chapter 3**, we characterized the resistivity, TCR and ampacity of our composites. We observed that all of our composites had a higher resistivity than pure copper while the TCR was slightly lower. The decrease of the CNT coating and the CNT carpet annealing prior electroplating or after electroplating was ineffective in lowering the resistivity and TCR of Cu-CNT composites. Similarly, the increase of the CNT % from less than 10% to 40-45% rather increased the resistivity of the composite while conserving a similar TCR. Comparing our results to the literature, it seems that the use of large and long MWCNT is an interesting path to reach low resistivity composites. Aiming to improve the conduction of electrons through the MWCNT, we also explored the use of nickel as an interfacing metal between copper and CNT. Investigating Ni-CNT composites in comparison to Cu-CNT composites, we highlighted a higher contribution of the CNT to the electron transport when nickel is used. While the annealing of the Cu-CNT composites at high temperatures led to a phase separation between the CNT and the copper, increasing its resistivity dramatically, the annealing of Ni-CNT composites at the same temperature led to a CNT network that was highly interconnected by Ni nodules, featuring a great reduction of the resistivity of the composites. In controversy with the results of literature, we showed that all our Cu and Ni-CNT composites had a similar or lower ampacity than that of pure copper and nickel, respectively. However, we also showed that several parameters, such as the dimension of the sample, can have a significant impact on the measured ampacity, leading to variations which are typically in the range of the ampacity gains of Cu-CNT composites (compared to the reference copper). The importance of controlling and accurately disclosing the experimental parameters when measuring the ampacity was stressed in order to provide reliable comparisons of published results between the Cu-CNT composites and pure copper.

In **chapter 4**, Cu-CNT composites containing long CNT (200 and 800 μm) have proven potentially interesting as lightning strike protection. In several cases, we observed the preferential vaporization of the top composite layer, protecting the copper under-layer, and thus potentially concentrating the damage on the outer skin of the aircrafts. More striking, a composite containing a high vol. % of long CNT (200 μm) has shown a great resistance to the lightning strike with almost no vaporization of the material, clearly showing the interest of using the Cu-CNT composite in LSP. Further investigations are needed to better understand this result. Still, we propose that the higher LSP performance of the composite (compared to copper) could be attributed partially to its specific enthalpy of sublimation, estimated as being 1.42 times that of pure copper. Yet, the difference of specific sublimation enthalpy alone is not sufficient to explain the large reduction of vaporized area (14.4 $\times$ lower than pure copper for a same area density) and we stressed that the isotropic orientation of the CNT in the composite could benefit its conductivity in the case of a current being propagated radially in the sample. Finally, the high temperature and electric field generated by a lightning strike could favor electron conduction through the CNT, maximizing the contribution of their outstanding electrical properties to the lightning strike resistance.

Outlooks

Throughout this work, there are several paths that remain unexplored and questions that arose. Here we discuss them chapter by chapter.

In **chapter 1**, we developed a reliable method of fabricating Cu-CNT composites by electroplating. Initially, we also designed the coating of CNT to potentially enable CNT co-electrodeposition. It would be interesting to explore this fabrication method as the doping of Pda by Cu ions increases its ζ-potential and improves the Pda particle dispersion in an acidic environment. Therefore, the Cu-doped Pda coating of CNT could favor the dispersion of CNT in an acidic plating solution, as well as their electrophoresis during the co-electrodeposition. Also, we showed for the first time (to the best of our knowledge) the successful fabrication of a Cu-CNT composite using electroless plating. It would be interesting to explore this fabrication route further, as we did not characterize this sample electrically. Regarding our electroplating method, we were able to fabricate composites with a thickness never before demonstrated in the literature using only an aqueous plating solution and it would be interesting to evaluate the maximum thickness that could be obtained. Furthermore, we developed a new method to fabricate composites with a high vol. $\%$ of CNT but this was only used with long CNT (200 and 800 μm); it would be interesting to see whether the swelling is also suppressed when using short CNT (2-20 μm). Regarding this compressing system, one of the drawback of the current method is the use of a PTFE membrane that has to be removed from the composite surface by peeling and gentle polishing. Finding an equivalent membrane that could be easily removed (e.g. by being dissolved in a solvent) would simplify the fabrication of the composite greatly. Furthermore, it would be interesting to find a stiffer membrane than PTFE for the fabrication of the patterned composite, as the membrane could deform slightly when the tissues are removed, leading to a slight swelling of CNT in the patterned lines. We also saw that the compressing system enables the use of ultrasound during electroplating, which could interestingly increase the deposition rate of copper in the CNT layer. In addition, we believe that the Pda coating protocol could be used/adapted to functionalize a vertically aligned CNT forest that is grown by CVD on a substrate, enabling a path to the fabrication of composites integrating vertically or horizontally aligned CNT. The Pda coating was efficient in promoting the growth of various metals, and aiming to improve the copper-CNT interface, we believe that it should be used to functionalize the CNT with nickel prior to the copper electroplating. Finally, we observed a migration of the copper outside the CNT network when the Cu-CNT composite was annealed at high temperatures. Based on the melt infiltration method (equation 32), it may be possible to prevent this migration by putting the composite under compressing stress during the annealing.

In **chapter 2**, we characterized the physical properties of the CNT carpets and optimized some of the experimental parameters to improve their conductivity prior to their integration into the composite. It would be greatly enriching to develop methods allowing the characterization of individual CNT, permitting us to screen and select the most suitable CNT for a given application, in terms of ballistic conduction, resistivity, TCR, and ampacity. In addition, it is reported in the literature that CVD grown CNT can have low thermal conductivity due to their defective nature. In the context of the ampacity, where heat conduction plays a major role, it seems interesting to characterize the thermal conductivity of our CNT and to consider an annealing step at high temperatures (3000 °C) prior to their coating to improve their crystallinity (see p. 23). Similarly, it would be interesting to evaluate the drop of CNT conductivity caused by the presence of defects in the CNT structure, and a study involving Raman spectroscopy and electrical characterization of CNT after different steps of oxidization/sonication could be useful.

In **chapter 3**, we observed that our CNT contributed to the current conduction only poorly, despite the variation of the CNT type and a great increase of the CNT vol. %. We believe that the measured resistivity of the Cu-CNT composite was dramatically increased by the isotropic orientation of the CNT. As a result, the magnitude of the variation of conductivity/TCR/ampacity, resulting from the composite features variation (change of CNT type and vol. %, optimization of the Pda coating, annealing, ...), was "masked" by the small amount of CNT actually aligned with the direction of the current flow. To investigate the CNT-copper interactions, a system with aligned CNT that maximizes the contribution of the CNT to the electron transport, and therefore maximizes the gain/loss of conductivity when changing a fabrication parameter, is required. We also demonstrated that Ni could act as an effective interface to promote electron conduction through the CNT. Indeed, the annealing of the Ni-CNT composite leads to an highly interconnected CNT network by Ni nodules and is beneficial to composite conductivity. It would be now interesting to adapt this configuration to a Cu-Ni-CNT composite system. However, nickel can alloy copper and dramatically reduce its conductivity. Therefore, we believe that if an annealing step has to be used to create electric contact with the inner walls of CNT, it should be done prior to the copper electroplating.

In **chapter 4**, we saw that composites with a high vol. % of long CNT were more efficient in protecting the materials from the lightning strike. In this case, we calculated that the specific enthalpy of sublimation of the composite was 1.42 times that of pure copper, which may contribute to the lower quantity of vaporized material. It would be interesting to characterize additional composite samples with various CNT vol. % to correlate the amount of vaporized material with the CNT vol. %. In addition, a post-characterization of the samples would be necessary to determine the composition and morphology of the samples after a lightning strike. It would also be interesting to repeat the experiments while reducing the area density of the sample below 200 g.cm^{-2} where the difference with the copper curve would be even more pronounced. It would also be interesting to optimize the patterning method to obtain composite meshes with a high vol. % of CNT, while drastically reducing the area density of the LSP.

Publications and conferences

ARTICLES IN PEER-REVIEWED JOURNALS

1. Antoine Duhain, Jérôme Guillot, Guillaume Lamblin, Damien Lenoble. "Copper–CNT interfacing with Cu-doped polydopamine in CNT carpet: copper nucleation and resistance decrease upon soft annealing", RSC Advances, **2021**, 11, 11900 - 11909.
2. Antoine Duhain, Guillaume Lamblin, Damien Lenoble. "On the Resistivity, Temperature Coefficient of Resistance, and Ampacity of Cu-CNT and Ni-CNT Composites", RSC Advances, **2021**, 11, 40159 - 40172.

PATENTS

1. Antoine Duhain, Guillaume Lamblin, Marc Michel, Damien Lenoble. Metal-CNT composite, production method and materials therefor, WO2020043590A1, **2020**.
2. Antoine Duhain, Guillaume Lamblin, Damien Lenoble. Patterned Cu-CNT composite fabrication, LU102334.
3. Antoine Duhain, Guillaume Lamblin, Marc Michel, Damien Lenoble. Bi-layered Cu-Cu-CNT Composite, LU102368.

ORAL PRESENTATIONS IN CONFERENCES

1. Antoine Duhain, Guillaume Lamblin, Damien Lenoble. Metal-CNTs Composites for High Ampacity Materials: A New Fabrication Route. Electrochemical Micro & Nano system technologies. From August 28 to September 1, 2018, Milan, Italy.
2. Antoine Duhain, Jérôme Guillot, Guillaume Lamblin, Damien Lenoble. Thermal Annealing of Polycatecholamine Coated Carbon Nanotube: A New Path for Copper-Carbon Nanotube Composites Fabrication. ECS, ECSJ, & KECS Joint Meeting. Held virtually from October 4 – 9, 2020.

Appendix A

Chapter 1: supplementary information

Fig. A.1d shows that the thickness of layers, obtained by spraying CVD grown CNT (200 and 800 μm), is difficult to reliably evaluate reliably due to the layer porosity.

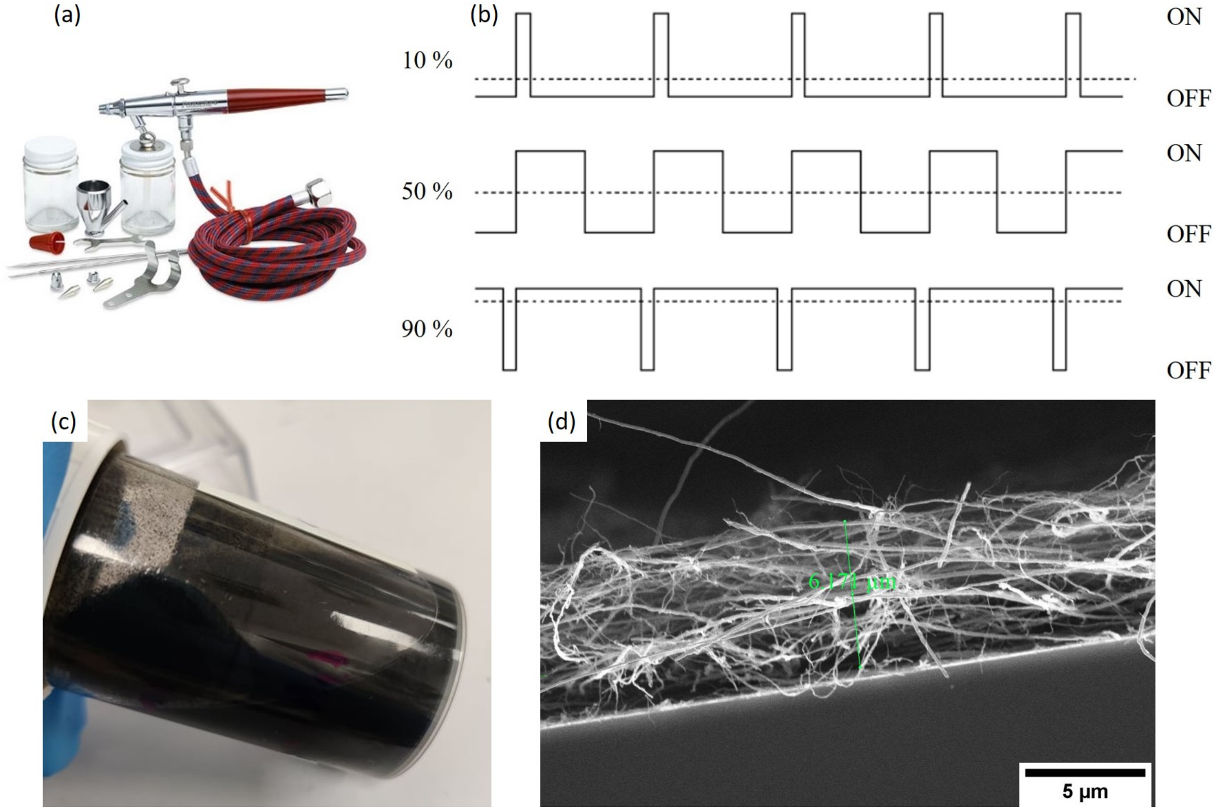

Figure A.1. (a) Picture of the airbrush used to manually spray CNT, (b) illustration of a duty cycle of 10, 50, and 90%, (c) photograph of a dispersion of arc-discharged CNT coated with Cu-doped tannic acid in water, and (d) cross-section spray of CVD grown CNT@PdaCu on $SiAl_2O_3$.

The following parameters were used to deposit a thin layer of copper on the titanium substrates by sputtering:

- Distance electrode-substrate: 6 cm
- Current: 120 mA
- Time: 150 s
- Argon pressure: $10-2$ bar
- Initial vacuum pressure: 5×10^{-5} bar

Fig. A.2 illustrates the nucleation of copper at different stages of the chronoamperometry and for two different concentrations of $CuSO_4$ in a plating solution. In the two first stage of the chronoamperometry, the current of deposition is high because a large amount of ions are available next to the substrate surface. Afterward, a diffusion layer depleted from the Cu ions takes place and the deposition current reaches an equilibrium depending on the diffusion speed of the ions. A lower concentration of copper ions favors the formation of a larger density of small nuclei compared to the case of a high ions concentration that favors a lower density of larger nuclei.

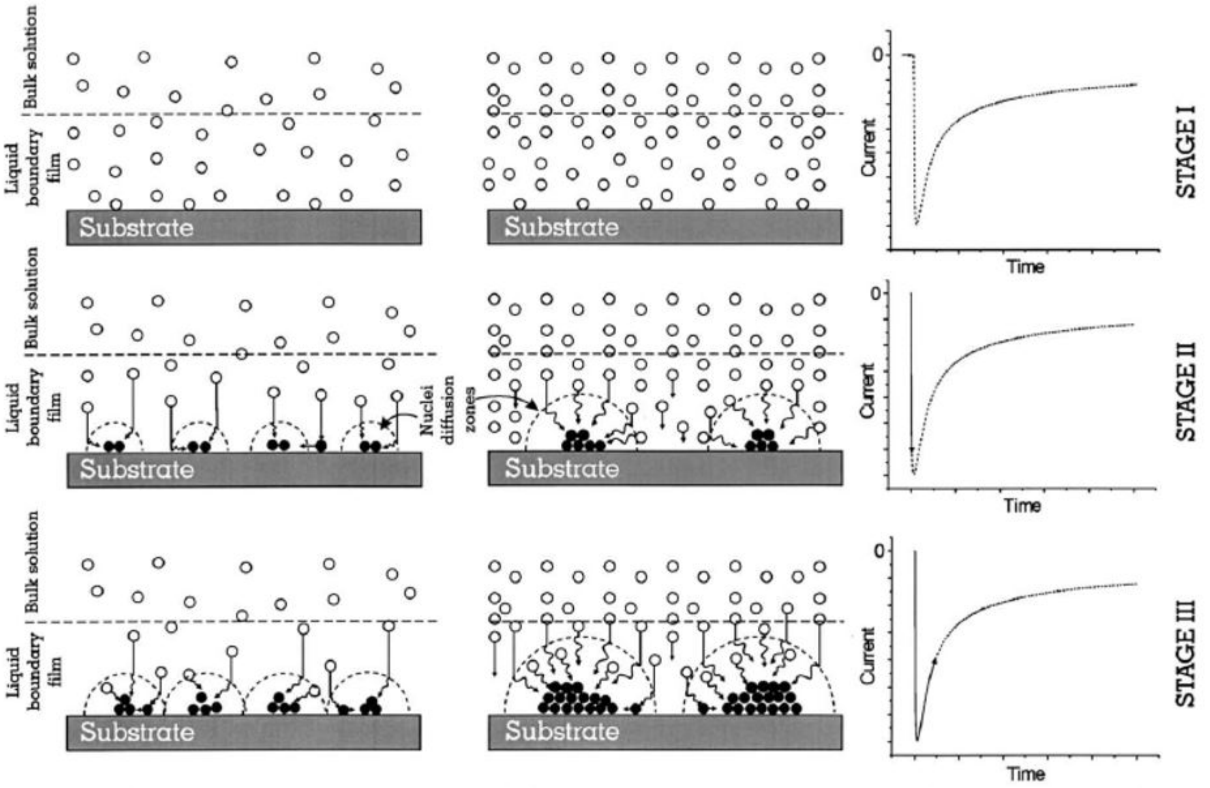

(a) Lower metal concentration (b) Higher metal concentration (c) Corresponding CAs

Figure A.2. Schematic of nucleation of copper for (a) low and (b) high $CuSO_4$ concentration in solution at (c) different chronoamperometry stage[145].

Fig. A.3 illustrates the effect of organic additives on the electroplating of copper. Accelerators and suppressors define two types of molecules / organic additives that accelerate and slow down the deposition rate of copper, respectively. By controlling the location of the molecules on the plated surface, it is possible to control where the plating will be accelerated or slowed down (Fig. A.3c). Polyethylene glycol (PEG) and bis(3-sulfopropyl)-disulfide (SPS) are commonly used as suppressor and accelerator , respectively. PEG (Fig. A.3)d can bind copper ions and adsorbs at the copper surface, preventing the further copper deposition. It is also a large molecule that hardly diffuse in small cavities, thus PEG tends to concentrate at the upper surface of a substrate. In contrast, SPS (Fig. A.3e) is much smaller and can readily be adsorbed in small cavities. There it reduces the Cu(II) in Cu(I), catalyzing the further electro-reduction of the copper in the cavities. The combined action of PEG and SPS lead to a speed up of the copper deposition in cavities and a slow down of the copper deposition at the surface. As a consequence, the use of the two additives enable the complete filling of small cavities such as trenches in silicon (Fig. A.3a,b).

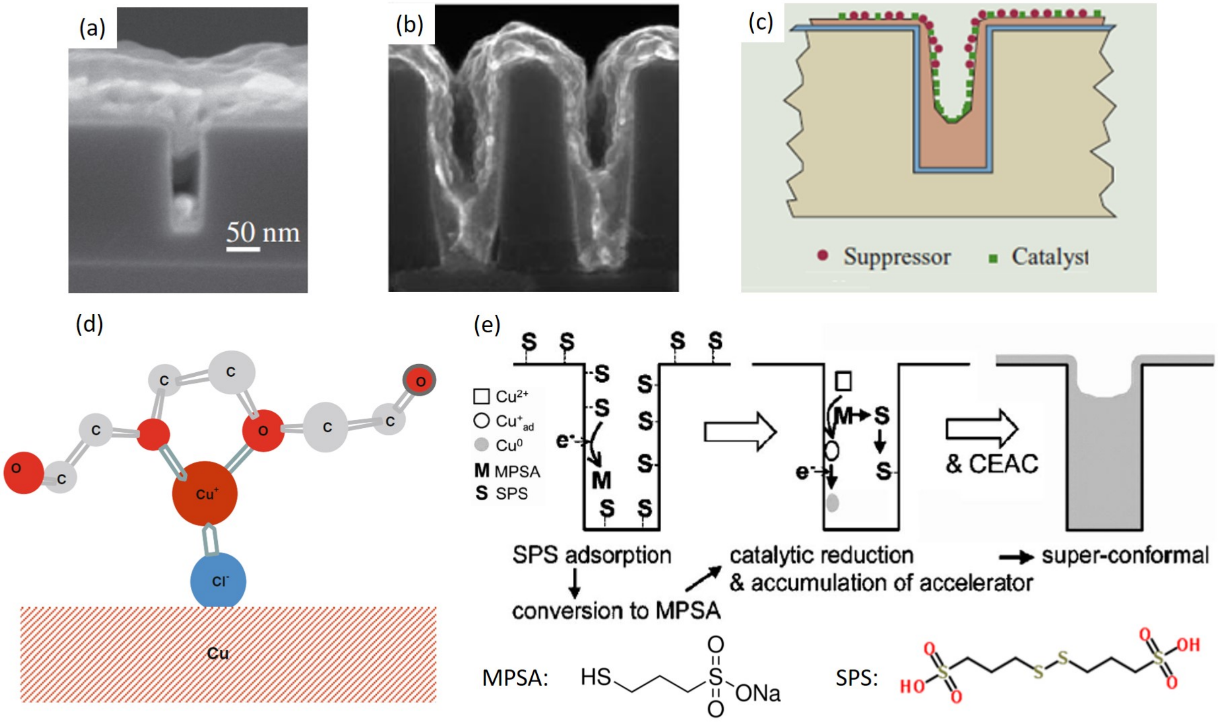

Figure A.3. SEM picture of a cavity plated with copper (a) without and (b) with additives (PEG: 100 mg.L^{-1}, SPS: 15 mg.L^{-1}). (c) Schematic of the super-filling mechanism using additives. (d) Mechanism of suppression of copper deposition via formation of a PEG-Cu^{+}-Cl^{-} at the copper surface. (e) Mechanism of plating acceleration by SPS in cavity.[149–153]

Fig. A.4a is a schematic of the diffusion layer that appears at the working electrode. The ions are consumed at the surface of the working electrode, lowering their concentration. A gradient of concentration appears between the surface and the bulk solution, and depends on many parameters (concentration in bulk solution, applied current, stirring, pulse of current, temperature, ...). The diffusion rate of the ions through this layer follows the Fick law (equation A.1): the higher is the gradient of concentration, the faster the diffusion is. When the thickness of the diffusion layer is lowered, the diffusion of the ions is sped-up.[211] The maximum density of current (Fig. A.4b) that can be used is thus limited by the rate of diffusion and is calculated by the equation A.2. Beyond this value, the plated surface becomes "burned" as it appears darker due to the powdery structure forming on the substrate.[211,212]

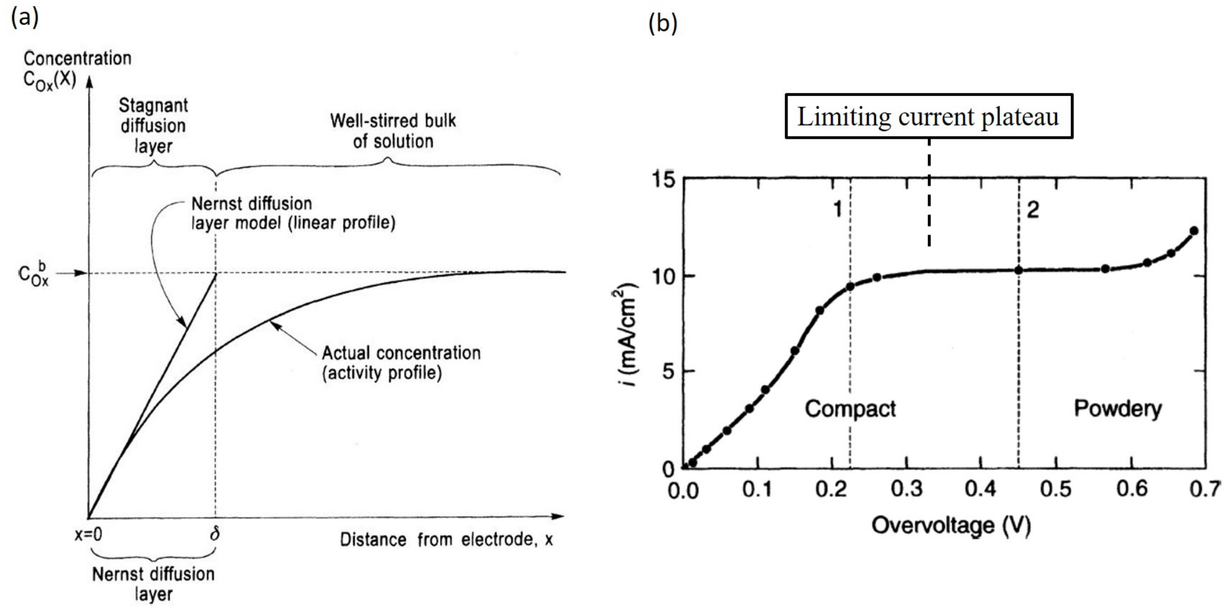

Figure A.4. (a) Schematic of the diffusion layer appearing between the working electrode and the bulk solution, and (b) graphic of the current of plating vs the over-potential.[212]

Fick law:

$$J = -D(\frac{\partial C}{\partial x}) \tag{A.1}$$

where J is the ions flux, D is the diffusion coefficient, C is the concentration of ions.

Limiting current:

$$I_L = \frac{\eta F D}{\delta} C_b \tag{A.2}$$

where I_L is the limiting current, η is the number of electrons of the reaction, F is the Faraday constant, D is the diffusion coefficient, and C_b is the bulk concentration of ions.

Appendix B

Chapter 2: supplementary information

B.1 CHARACTERIZATION OF THE CNT MATERIALS: MATERIALS AND METHOD

The following section is quoted from our paper:[158]

CNT preparation

"Commercial MWCNT (average diameter 80-90 nm; average length 200 μm) were bought from NanoTechLabs, Inc. (NTL). Dopamine hydrochloride and nitric acid (65%) were bought from Sigma-Aldrich. Hydrochloric acid (37 %, AnalaR NORMAPUR) and Ethanol absolute (>99.8% AnalaR NORMAPUR) were bought from VWR.

CNT oxidization

Following a protocol inspired from Rosca et al.[132], 350 mg of CNT were oxidized through sonication in 50 mL of nitric acid 52% for 30 minutes at room temperature. Oxidized CNT were then filtrated and rinsed with DI water. Oxidation in nitric acid produces principally carboxylic groups at the CNT surface.[132]

Pda coating on CNT (CNT@Pda)

A protocol inspired by Shi et al.[115] was used to prepare Pda-coated CNT samples. 150 mg of oxidized CNT were dispersed in 937.5 mL of a solution of dopamine hydrochloride (DA) (0.1 mg.mL^{-1}). The solution was ultra-sonicated for 10 s then vigorously stirred for 25 min in the solution in order to promote the adsorption of the DA monomers on the CNT surface, which occurred due to Van der Waals and π-π stacking interaction between the aromatic dopamine and the sp^2 hybridized carbon of the CNT.[115] Furthermore, the CNT oxidation can promote the adsorption of DA monomers on the CNT due to the formation of hydrogen bonds between carboxilic groups at the CNT surface and catechol groups of dopamine.[213] The DA polymerization was triggered by addition of 562.5 mL Tris-HCl (0.01 M) and the solution was successively ultra-sonicated for 10 s. It was then vigorously stirred for 24 h. 18.75 mL of NaOH 1 M was added to the dispersion and the CNT were recovered by filtration. The CNT were then dispersed in 100 mL of absolute ethanol (EtOH). The CNT dispersion was then filtered, rinsed twice with 200 mL EtOH and re-dispersed in 100 mL EtOH.

Cu-doped Pda coating on CNT (CNT@PdaCu)

To prepare CNT@PdaCu, 150 mg of oxidized CNT were coated using the same protocol as shown above, except that $CuSO_4.5H_2O$ was added to the dopamine solution (2.4 mM and 0.5 mM, respectively). Cu(II) was expected to be chelated by amine and catechol groups of DA.[123,125] In addition to the hydrogen bonding between DA and the oxidized CNT surface, the -COOH groups were also expected to provide a binding spot for Cu(II) ions and promote the adsorption of the DA-Cu(II) complexes.[123,125,143]

Annealing of samples

The CNT annealing experiments were performed in a Carbolite Gero CWF furnace upgraded with an internal retort allowing the atmosphere to be controlled. CNT@PdaCu samples were annealed in a fully inert atmosphere (Ar), rising from room temperature to 573, 673 and 773 K at a 5 $K.min^{-1}$ heating rate. When the desired temperature was reached, the furnace was cooled down overnight to room temperature.

Physical characterization

	XPS	SEM/STEM	HIM-SIMS	DSC	TCR/R_s
Oxidized CNT	x				x
Oxidized CNT 773 K	x				x
CNT@Pda	x			x	x
CNT@Pda 773 K					x
CNT@PdaCu	x	x		x	x
CNT@PdaCu 573 K		x			x
CNT@PdaCu 673 K	x	x			x
CNT@PdaCu 773 K	x	x	x		x

Table B.1. Summary of characterized samples.

X-ray photoelectron spectroscopy (XPS)

The Cu 2p, N 1s, C 1s, O 1s photoelectron spectra and Cu LMM Auger electron spectra of samples reported in table B.1 were acquired using Kratos Axis Ultra DLD apparatus equipped with a monochromatic Al Kα X-ray source running at 150 W (10 mA, 15 kV). The spectra were carried out on an analysis area set to 300×700 μm^2 with 20 eV-pass energy for the narrow scans, leading to a FWHM of 0.6 eV on the Ag $3d_{5/2}$ line of a cleaned reference silver foil. The electron spectrometer had previously been calibrated on the Cu $2p_{3/2}$ and Au $4f_{5/2}$ lines at 932.6 eV and

84.0 eV respectively. Without any further charge correction, the main C 1s component, corresponding to sp2 carbon atoms in CNT, is found at 284.35±0.05 eV for every sample. The spectra were analyzed with the CasaXPS software. It has been verified that annealing the oxidized CNT at 773 K leaves the C 1s line shape unchanged. This spectrum has subsequently been used as the CNT component in the C 1s peak reconstruction of every samples (Fig. 2.3). It allowed us to discriminate the oxidized CNT contribution from the polydopamine coating contribution. The relative intensities of C-N and C=N components in C 1s were fixed using their at. % ratio, which was determined from the N 1s spectra and the nitrogen percentage in the sample. Except for the oxidized CNT, the O 1s spectra present a large tail on the high binding energies, over 535.0 eV, a feature of the sodium Auger peaks.[214] The sodium contribution has been fitted with a single component centred at 534.8±0.1 eV. The intensity of this peak represents between 12 and 20 percent of all the O 1s peaks and its evolution is in accordance with the sodium amount detected in the samples after the various synthesis steps and thermal treatments. This contribution has systematically been removed from the O 1s peaks to accurately determine the elemental composition. The low % of Cl detected in the CNT@PdaCu samples (Table 2.1) results from contamination by the buffer (Tris-HCl) and/or residual hydrochloride salts coming from the dopamine-hydrochloride. Although there were two rinsing steps with EtOH after the polymerization step of DA, small quantities of some salts can sometimes remain in the CNT@PdaCu filtered layer. The detection of Cl in annealed samples is therefore not specifically linked to the annealing process.

Scanning electron microscopy (SEM) and scanning transmission electron microscopy (STEM)

SEM and STEM (FEI; Helios NanoLab™ 650) were used to record high resolution images of CNT. CNT were deposited on typical holey carbon -supported Cu grids. Pictures were taken using a 1.0 μm field of view with an acceleration voltage of 30 kV. Pictures were post-processed with ImageJ to estimate the number of particles per square centimetre and the nuclei size distribution. The mean nuclei density and error bars shown in figure 2.6a are calculated from all the distinct images analyzed for each sample. Catalyst particles typically used to grow CNT are present in all samples; for this reason, the mean size and density of copper nuclei were extracted by subtracting the catalyst background calculated from CNT@PdaCu before annealing.

Helium ion microscopy-secondary ion mass spectroscopy (HIM-SIMS)

HIM-SIMS analysis were performed with a Helium Ion Microscope instrument (Zeiss, Peabody, MA, USA) coupled with a mass spectrometer developed at the Luxembourg Institute of Science and Technology.[215] Electron microscopy images were performed using a 25 kV helium beam and a primary current of 0.5 pA. The analytical information was provided by the Secondary Ion Mass Spectroscopy technique. SIMS measurements were acquired in imaging mode using a primary bombardment of Ne^+ accelerated at 20 kV. The probe ranged from 20 to 40 nm in diameter, with an intensity of 3 pA. The raster size was 5×5 μm^2 for a matrix of 512×512 pixels^2. This technique was specifically used to investigate the spatial distribution of chemical elements at the surface of CNT@PdaCu annealed at 773 K compared to reference oxidized CNT.

Differential scanning calorimetry (DSC)

DSC (Mettler Toledo DSC3+) was used to measure the variation of enthalpy during CNT annealing and was carried in Ar gas to reproduce the annealing conditions. 11.5 mg of CNT@Pda and 5 mg of CNT@PdaCu were placed in an aluminum crucible. Due to the small quantity of reacting material, the samples were heated with a 20 K.min^{-1} ramp to 673 K (instead of the 5 K.min^{-1} as used during the annealing) in order to increase the DSC signal intensity.[216]

Temperature coefficient of resistance and sheet resistance measure

- TCR measurements were carried between 298 and 433 K with a four-probes setup coupled with a temperature-controlled hot plate. The probes have a space of 1 mm and measurements were performed on 1×1 cm CNT carpet samples. Those samples were obtained through the filtration of the CNT solutions (Oxidized, CNT@Pda, CNT@PdaCu) followed by a peeling of the CNT layer from the filtration membrane.
- The sheet resistance of CNT carpets was measured at room temperature. As the thickness of CNT carpets is difficult to measure accurately, the one-to-one comparison of sheet resistance between samples is not reliable. Thus, we decided to compare the drop in resistance of the CNT carpets after annealing at 573, 673 and 773 K to their resistance before annealing. The drop in resistance is expressed as $100\times(1\text{-}R_{annealed}/R_{notannealed})$ %."

Raman Spectrocopy

A carpet sample was obtained by filtration of $\sim$ 5 mg of oxidized CVD grown CNT (800 μm). The carpet was cut in two and one piece was compressed during 5 min at 500 kg.cm^{-2}. Each sample was characterized at five different spots using a Renshaw inVia micro-Raman spectrometer with a 2.53 mW laser (excitation wavelength: 532 nm) on a 0.87 μm diameter spot (exposure time: 10 s). The intensity of the five D and G bands were used to calculate the average ratio I_D/I_G.

Appendix C

Chapter 3: supplementary information

C.1 CHARACTERIZATION OF THE METAL-CNT COMPOSITES: MATERIALS AND METHOD

The following section is quoted from our published paper:[155]

"The fabrication of Cu-CNT composite with high CNT vol. % (i.e. 40-50%) fabrication remains challenging and is commonly obtained by electroplating in an organic solvent based solution.[3,110] Here, we use an innovative method to produce Ni-CNT and Cu-CNT composites with a high CNT vol. % and a continuous metal matrix using only aqueous solutions.

CNT treatment

Commercial MWCNT (average length 800 μm; average diameter 80-90 nm) were bought from NanoTechLabs, Inc. (NTL). The MWCNT treatment was inspired by the protocol used in our preceding work.[158]

CNT oxidization

The CNT were oxidized via sonication in nitric acid (52%) for 30 min (at room temperature). They were then filtrated and rinsed with DI water.

Metal-doped polydopamine coating on CNT

CNT coated with Cu doped polydopamine (CNT@PdaCu) were obtained by stirring oxidized CNT (100 mg) for 30 min in a solution (625 mL) composed of dopamine hydrochloride (0.0625 mM) and $CuSO_4.5H_2O$ (0.3 mM). Then, Tris-HCl (375 mL, 10 mM) was added to the solution to trigger the polymerization of the dopamine. The solution was left under stirring for 24 hours. NaOH (12.5 mL) was then added to the solution. The CNT were filtrated, rinsed with EtOH, and dispersed in EtOH (100 mL). Similarly, CNT coated with Ni doped polydopamine (CNT@PdaNi) were obtained by replacing the $CuSO_4.5H_2O$ by $NiSO_4$ (0.3 mM) in the previous protocol.

CNT carpet fabrication

CNT carpets were obtained directly by filtrating the CNT solution, and the filtrate was peeled from the membrane (ø=3.9 cm). Oxidized CNT layers were more brittle than CNT@PdaCu and CNT@PdaNi layers. In order to facilitate their peeling and handling, 10 mL of oxidized CNT solution was filtrated for each CNT layer instead of 5 mL for the CNT@PdaCu and CNT@PdaNi layers. The peeled CNT were dried at 353 K for 2 min to evaporate the remaining ethanol. Compressed CNT layers were obtained using a hydraulic press (500 kg.cm^{-2} for 5 min).

Metal-CNT composites and pure metal sample fabrication

Reference copper foils were provided by Circuit Foil Luxembourg Sarl. Hydrophilic PTFE membranes (Omnipore - 10 μm pore size) were bought from Sigma-Aldrich. Tissues were bought from VWR.

Cu-CNT composite sample fabrication

Photo-resist was spin-coated onto a standard silicon substrate and then covered with a seed layer of copper by sputtering (thickness $\approx$ 400 nm). The compressed CNT@PdaCu layer was placed on the substrate and successively clamped in the compression system described in Figure 1.36. The system was then immersed in an electroplating solution composed of $CuSO_4.5H_2O$ (0.63 M), H_2SO_4 (0.1 M), HCl (50 ppm), polyethylene glycol (100 ppm), and Bis-(sodium sulfopropyl)-disulfide (15 ppm). Electroplating was done at room temperature using current pulses of 35 mA.cm^{-2} (ON - 0.02 s) and 0 mA.cm^{-2} (OFF - 0.1 s) until the CNT layer was completely filled by Cu. The composite foil was separated from the substrate by dissolution of the resist in acetone. The PTFE membrane was slightly attached to the composite surface and was removed by peeling followed by gentle mechanical polishing. The composite sample was then cut into separate pieces for further characterization.

Ni-CNT composite and pure Ni sample fabrication

Ni-CNT composite was obtained following a similar protocol. In this case, the Ni seed layer was sputtered instead of Cu and a CNT@PdaNi compressed layer was used. The electroplating solution was composed of Ni sulphamate tetrahydrate (400 g.L^{-1}) and boric acid (30 g.L^{-1}). The plating was done at 323 K with same current pulses until the CNT@PdaNi layer was filled by Ni. The Ni-CNT composite foil was then recovered, polished and cut into pieces using the same method as detailed above. A pure Ni sample was fabricated in the same conditions but without using the compression system.

Annealing of composite samples

A Carbolite Gero CWF furnace upgraded with an internal retort was used to anneal pieces of Cu-CNT and Ni-CNT composites at 673, 873, 1073 and 1173 K under Argon. The heating rate was fixed at 5 K.min^{-1} and the target temperature was maintained for 30 min (but only 15 min at 1173 K). The furnace was then left to cool down overnight until room temperature was reached.

	Sheet resistance	TCR	SEM	Ampacity	EDX
Oxidized CNT carpet	✓	✓	✓		✓
CNT@PdaCu carpet	✓	✓	✓		✓
CNT@PdaNi carpet	✓	✓	✓		✓
Compressed Oxidized CNT carpet	✓	✓	✓		✓
Compressed CNT@PdaCu carpet	✓	✓	✓		✓
Compressed CNT@PdaNi carpet	✓	✓	✓		✓
Cu-CNT composite	✓	✓	✓	✓	
Annealed at 673 K	✓	✓	✓	✓	
Annealed at 873 K	✓	✓	✓	✓	
Annealed at 1073 K	✓	✓	✓	✓	
Ni-CNT composite	✓	✓	✓	✓	
Annealed at 673 K	✓	✓	✓	✓	
Annealed at 873 K	✓	✓	✓	✓	
Annealed at 1073 K	✓	✓	✓	✓	
Annealed at 1173 K	✓	✓	✓	✓	

Table C.1. Summary of the characterized samples.

Physical characterization

Scanning electron microscopy (SEM) and energy dispersive x-ray spectroscopy (EDX)

SEM and EDX were carried with an FEI Helios NanoLab^{TM} 650 instrument. Sample cross-sections were observed using a 10 kV acceleration voltage in order to evaluate the degree of metal filling in the composite layers. Furthermore, all composite lines used for ampacity characterization were individually measured to determine their thickness accurately. CNT layers were also observed before and after compression. EDX was used to confirm the presence of copper and nickel in the CNT@PdaCu and CNT@PdaNi carpet samples.

Composite CNT volume percentage and density characterization

The volume percentage of CNT (CNT vol. $\%$) of the composite was calculated using

$$vol.\% = \frac{t_c - ((\frac{m_c - m_{cnt}}{A})/\gamma_{Cu})}{t_c} \tag{C.1}$$

where t_c is the thickness of the composite, M_{cnt} is the mass of the CNT carpet, M_c is the mass of the composite, A is the area of the sample, and γ_{Cu} is the density of Cu (8.96 g.cm^{-3}) and Ni (8.9 g.cm^{-3}).[12] The CNT vol. $\%$ was also determined for each sample used in the resistivity measurements. The average thickness of each sample was obtained from 15 measurements taken with a micrometer. The CNT vol. $\%$ and density errors both originate from the thickness variation.

Sheet resistance and TCR measurement on CNT layer samples

A four-probe measurement (1 mm space between probes) was used to obtain the sheet resistance and TCR of the oxidized CNT, CNT@PdaCu, and CNT@PdaNi carpets before and after compression. The TCR of the CNT carpets was obtained by measuring the sheet resistance between 298 and 443 K (using a temperature-controlled support and a Keithley 2634B source-meter). The TCR and sheet resistance measurements were taken each time on three carpets of each type. The TCR was calculated from

$$R = R_0(1 + \alpha(T - T_0)) \tag{C.2}$$

where R_0 is the sheet resistance at room temperature and α is the TCR.

Resistivity and TCR measurement on CNT-metal composite samples

The resistance was measured between 298 and 443 K on 0.5 × 0.5 cm^2 samples using the Van der Pauw method. The samples were immersed in a temperature-controlled dielectric oil bath (Wacker AK 100 silicone oil - Lauda ECO RE 415). Resistance was measured three times at each temperature. Composites, annealed composites and reference samples (pure Ni and pure Cu) were characterized. The resistivity standard deviation arose mainly from the standard deviation of thickness (Figure 3.10). The TCR is independent of the thickness. The TCR error is low and arises only from the errors made during the resistance measurement.

Ampacity measurement

Ampacity measurements were performed using a homemade setup (Fig. 3.4b) allowing to control the distance between electrodes (set to 0.5 cm) and the pressure (set to 0.5 mbar) to be carefully controlled. The lines were fabricated by stamping the foils with two razor blades clamped together. The width of the lines were measured by optical microscopy (250 μm). The current was increased at a 0.5 A.s^{-1} rate while the voltage was measured. The maximum current density (at line failure) was taken as ampacity. The ampacity was measured on three lines of each type of material system. The main contribution of the ampacity standard deviation arose from the standard deviation of the line thickness."

C.2 **COPPER SELF-ANNEALING**

Fig. C.1 illustrates the fast self-annealing that freshly electroplated copper can undergo at relatively low temperature, leading to a fast growth of the copper grains. As a consequence, the resistance of the sample is rapidly lowered as the sample is heated because the grain growth is accelerated as the temperature raises. It also appears that the TCR is not affected by the self-annealing.[194] But, if not accounted for, this effect can lead to biased measure and conclusion about the resistance/TCR of a sample.

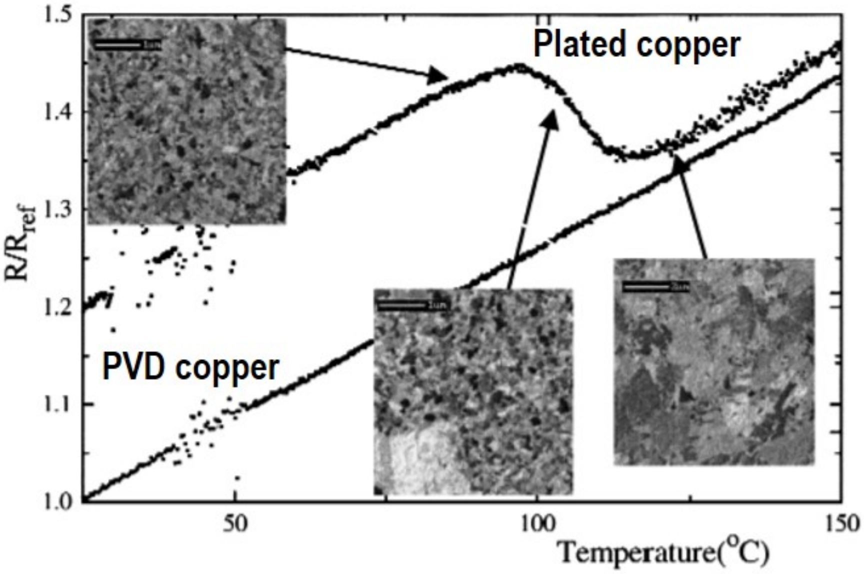

Figure C.1. Measure of the normalized resistance of a PVD Cu layer and a electroplated Cu layer. The insets shows the growth of the Cu grains in the electroplated layer at several temperature of annealing.[194]

C.3 COMPOSITE CHARACTERIZATION

EDX spectra (Fig. C.2) confirm the presence of Cu and Ni in the CNT@PdaCu and CNT@PdaNi carpets, respectively. It was verified that the detected Al and S came from the support used for EDX and that Fe (present in all the samples) came from the catalysts used to grow the CNT.

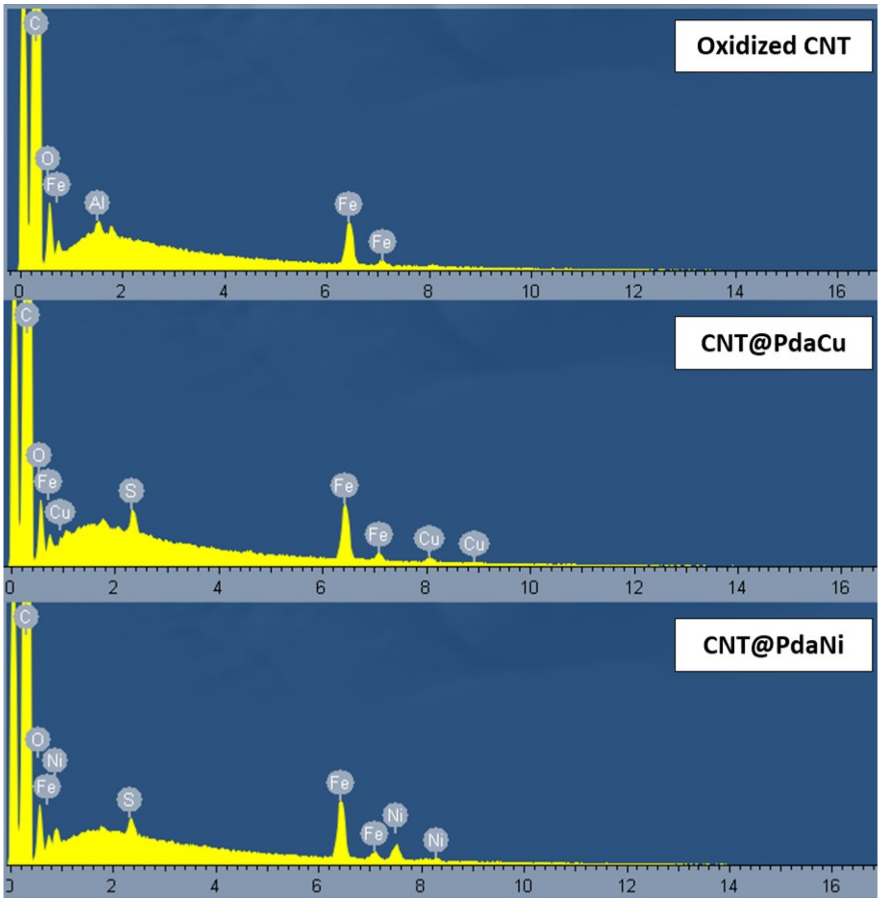

Figure C.2. EDX spectra of oxidized CNT, CNT@PdaCu, and CNT@PdaNi carpets.

Fig. C.3 shows the highly interconnected CNT network of a Ni-CNT composite line in the failure zone after an ampacity measurement.

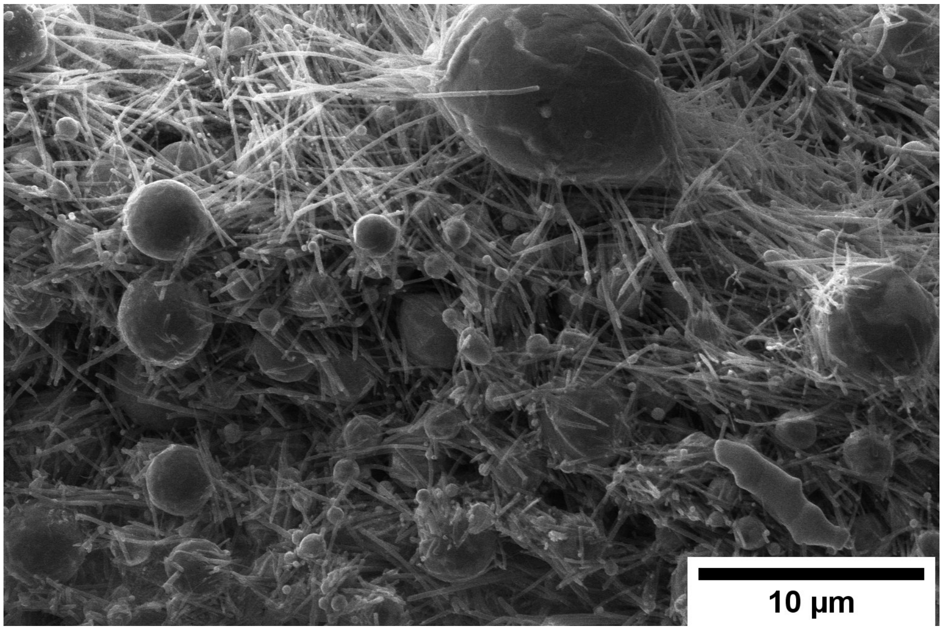

Figure C.3. Zoom on the Ni-CNT ampacity line failure zone (annealed at 873 K).

Appendix D

Characterization techniques

D.1 ELECTRICAL MEASUREMENTS

Two/four-probe measurement

To measure the resistivity of a sample, two-probe and four probe techniques are commonly used. In the first one, the current is flowing across the sample via two electrodes and the voltage drop is measured by the same electrode (Fig. D.1a). In this case, the measure of the resistance of the sample is not reliable because R also contains the contributions of the resistance of contact, the resistance of the contact wires and the resistance of the equipment. A four-probe measurement is usually preferred to accurately measure the resistance (and resistivity) of a material. In this method, the potential drop is measured via two additional electrodes placed onto the inner part of the sample (Fig. D.1b). Here, no current flow through the two electrodes used to measure the voltage drop thanks to the high impedance of the measurement system (Keithley, ...), therefore the voltage does not contain the contributions of the contact and wire resistances. As a consequence, the resistance R of the sample is given by[217]

$$R = \frac{V}{I} \tag{D.1}$$

where V is the voltage drop and I is the current. The resistivity can then be calculated by

$$\rho = \frac{Vwt}{IL'} \tag{D.2}$$

where w is the width of the sample, t is its thickness, and L' is the distance between the two inner probes.

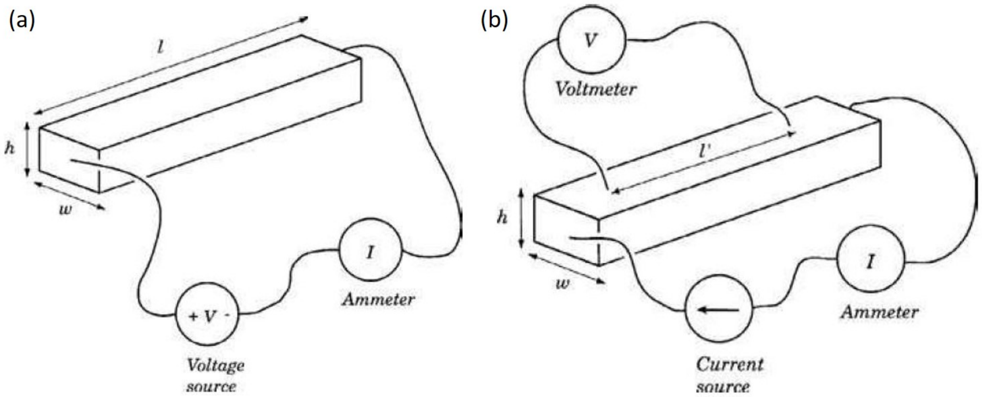

Figure D.1. Schematics of (a) a two-probe method and (b) a four-probe method that are used to measure the resistivity of a sample.[217]

This method is particularly adapted to a sample having a wire geometry. When the resistivity of a thin film has to be measured, one measure the sheet resistance instead. It is also made by using a four-probe configuration where the probe are placed onto the surface of the film. The sheet resistance (Ω) expression varies in function of the sample dimensions. For a sample with $\frac{t}{s} \leq 0.5$ (where s is the spacing between the probe), the sheet resistance R_s is given by

$$R_s = C\frac{V}{I} \tag{D.3}$$

where C is a correction factor that depends on the sample geometry (Fig. D.2).[218] In practical, we have to take account on the thermal junction that appears between the electrodes and the sample, inducing a temperature dependent voltage V_{th}. The measured voltage is

$$V = V_{sample} + V_{th} \tag{D.4}$$

To cancel the V_{th} contribution and measure an unbiased value of V_{sample}, we use

$$R_s = C\frac{V_+ - V_-}{2I} \tag{D.5}$$

where V_+ and V_- are reversed polarity potentials.[219] The resistivity of the sample can be calculated by

$$\rho = R_s t \tag{D.6}$$

In our case, the thickness of our film was always significantly lower than the probe spacing (s = 1 mm) thus equation D.5 was always used. Yet, if the film had to be much thicker, leading to a non negligible voltage drop in the sample thickness, the equation D.5 should be adapted.[218]

(a)

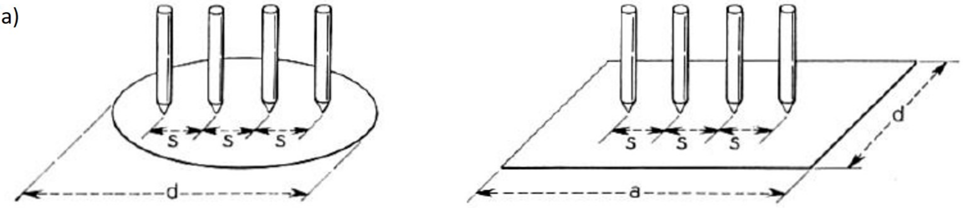

(b)

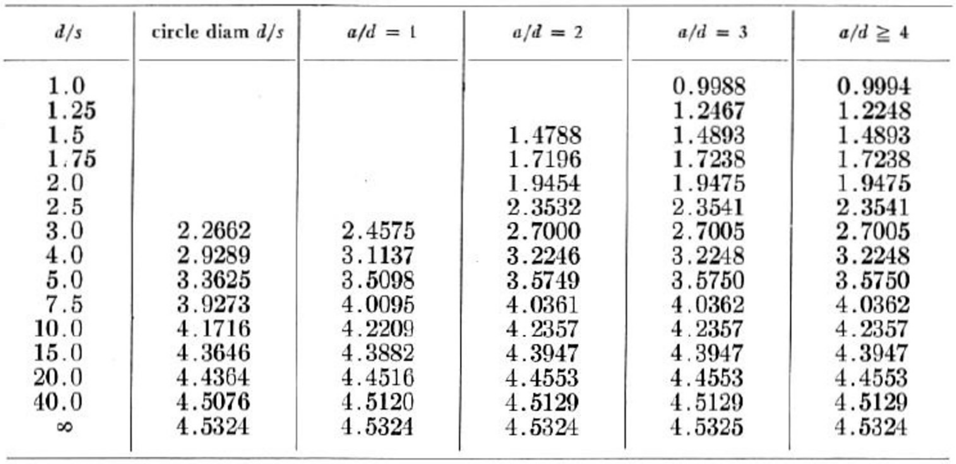

d/s	circle diam d/s	$a/d = 1$	$a/d = 2$	$a/d = 3$	$a/d \geq 4$
1.0				0.9988	0.9994
1.25				1.2467	1.2248
1.5			1.4788	1.4893	1.4893
1.75			1.7196	1.7238	1.7238
2.0			1.9454	1.9475	1.9475
2.5			2.3532	2.3541	2.3541
3.0	2.2662	2.4575	2.7000	2.7005	2.7005
4.0	2.9289	3.1137	3.2246	3.2248	3.2248
5.0	3.3625	3.5098	3.5749	3.5750	3.5750
7.5	3.9273	4.0095	4.0361	4.0362	4.0362
10.0	4.1716	4.2209	4.2357	4.2357	4.2357
15.0	4.3646	4.3882	4.3947	4.3947	4.3947
20.0	4.4364	4.4516	4.4553	4.4553	4.4553
40.0	4.5076	4.5120	4.5129	4.5129	4.5129
∞	4.5324	4.5324	4.5324	4.5325	4.5324

Figure D.2. (a) Schematics of the measurement of the sheat resistance using a four-probe method for a circular and square sample. (b) Correction factor C for the different sample geometries.[218]

Van der Pauw measurement

As we seen above, the measurement of the sheet resistance via a four-probe method is highly dependent on the sample size and geometry, decreasing the precision and repeatability of the measurement. Therefore, we switched to the Van der Pauw method that has the advantage to be independent of the sample geometry and to not require the knowledge of all the sample dimensions.[217,220] In this measurement method, it is preferable to have an uniform thickness in the sample. Remembering that electroplating usually produce samples that are thicker on the edges, we cut our samples to take square pieces at their centre while minimizing their lateral size (0.5 × 0.5 cm) to minimize the thickness gradient. The contact were always made at the square sample corners. The procedure to measure the sheet resistance using the Van der Pauw method is quoted from the work of M. B. Heaney:[217]

1. "Define a resistance $R_{ij,kl}$ (V_{kl}/I_{ij}), where V_{kl} $(V_k - V_l)$ is the voltage between points k and l, and I_{ij} is the current flowing from contact i to contact j.
2. Measure the resistances $R_{21,34}$ and $R_{32,41}$. Define $R_>$ as the greater of these two resistances and $R_<$ as the lesser of these two resistances.
3. Calculate the ratio $R_>/R_<$ and find the corresponding value of the function $f(R_>/R_<)$ from Fig. D.3.
4. Calculate the resistivity ρ_a using:

$$\rho_a = \frac{\pi t(R_> + R_<) f(R_>/R_<)}{ln(4)} \tag{D.7}$$

where t is the sample thickness.

5. Switch the leads to measure $R_{43,12}$ and $R_{14,23}$. Repeat steps 3 and 4 to calculate ρ_b using these new values for $R_>$ and $R_<$. If the two resistivities ρ_a and ρ_b are not within 10% of each other, either the contacts are bad, or the sample is too non-uniform to measure reliably. Try making new contacts. If the two resistivities ρ_a and ρ_b are within 10% of each other, the best estimate of the material resistivity ρ is the average:"

$$\rho = \frac{\rho_a + \rho_b}{2} \tag{D.8}$$

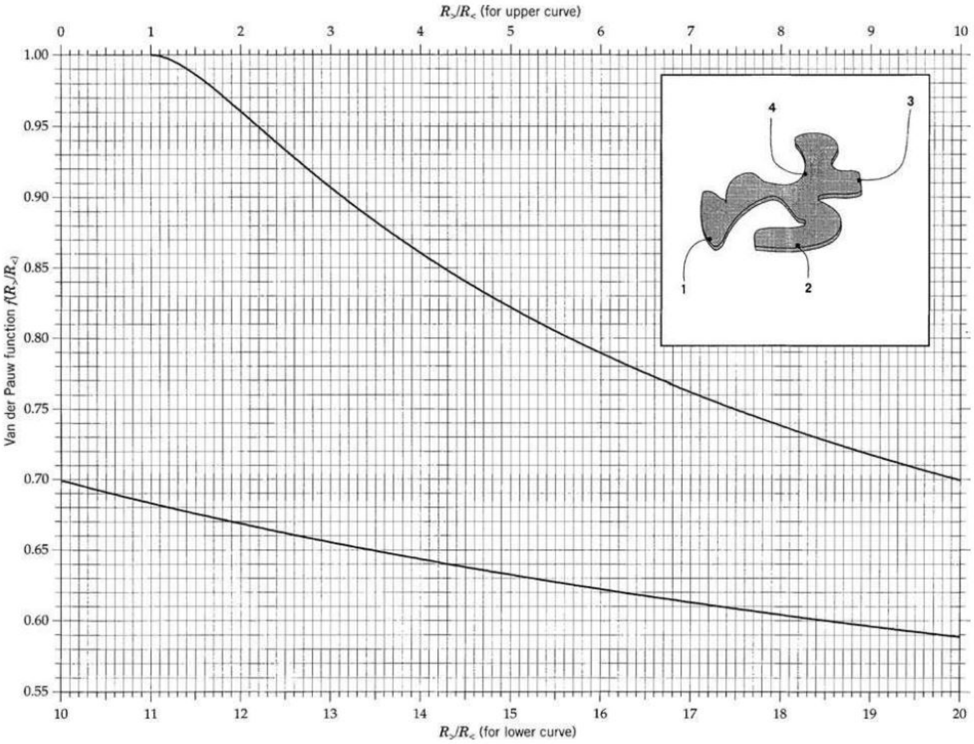

Figure D.3. Graph of the function $f(R_>/R <)$. In the inset, one possible geometry of sample is shown.[217]

Bibliography

[1] B. Zhang, V. Patlolla, D. Chiao, D. Kalla, H. Misak, R. Asmatulu, *Int J. Adv. Manuf. Technol.* **2012**, *67*, 1317–1323.

[2] S. Iijima, *Nature* **1991**, *354*, 56–58.

[3] C. Subramaniam, T. Yamada, K. Kobashi, A. Sekiguchi, D. Futaba, M. Yumura, K. Hata, *Nat. Commun.* **2013**, *4*, 2202.

[4] C. Kittel, *Introduction to Solid State Physics*, 8th ed., Wiley, **2004**.

[5] J. Manca, M. Nesladek, M. Neelen, C. Quaeyhaegens, L. De Schepper, W. De Ceuninck, *Microelectron. Reliab.* **1999**, *39*, 269–273.

[6] G. Eranna, *Crystal growth and evaluation of Silicon for VLSI and ULSI*, 1st ed., CRC Press., **2014**.

[7] S. Kasap, C. Koughia, H. E. Ruda in *Springer Handbook of Electronic and Photonic Materials*, (Eds.: S. Kasap, P. Capper), Springer International Publishing, **2017**.

[8] T. Linenbrink, *Consulting Specifying Engineer* **2014**, *61*, 50.

[9] J. H. Neher, M. H. McGrath, *Transactions of the American Institute of Electrical Engineers. Part III: Power Apparatus and Systems* **1957**, *76*, 752–764.

[10] N. National Fire Protection Association, *NFPA 70: National Electrical Code (NEC) Handbook, 2011 Edition*, 12th, NFPA, **2011**.

[11] J. Lienig, M. Thiele, *Fundamentals of Electromigration*, **2018**, pp. 13–60.

[12] In *Metals Reference Book*, (Ed.: C. J. Smithells), Butterworth-Heinemann, **1976**, pp. 940–974.

[13] J. Dellinger, *J. Frankl. Inst.* **1910**, *170*, 213–216.

[14] Amercian Elements, The Advanced Element Manufacturer, https://www.americanelements.com/copper-nickel-alloy-12357-13-0, (accessed 2021).

[15] K. Zhang, G. Stocks, J. Zhong, *Nanotechnology* **2007**, *18*, 285703.

[16] W. Yi, L. Lu, Z. Dian-lin, Z. W. Pan, S. S. Xie, *Phys. Rev. B* **1999**, *59*, R9015–R9018.

[17] Z. Han, A. Fina, *Prog. Polym. Sci.* **2011**, *36*, 914–944.

[18] C. Laurent, E. Flahaut, A. Peigney, *Carbon* **2010**, *48*, 2994–2996.

[19] R. Byron Pipes, S. Frankland, P. Hubert, E. Saether, *Compos. Sci. Technol.* **2003**, *63*, 1349–1358.

[20] C.-L. Liu, *physica status solidi (b)* **2001**, *226*, 47–56.

[21] J. Black, *P. IEEE* **1969**, *57*, 1587–1594.

[22] X. Chen, J. Tao, J. Yi, Y. Liu, R. Bao, C. Li, *J. Alloys Compd.* **2018**, *735*, 163–171.

[23] M. B. Bazbouz, A. Aziz, D. Copic, M. De Volder, M. E. Welland, *Adv. Electron. Mater.* **2021**, *7*, 2001213.

[24] S. Iijima, T. Ichihashi, *Nature* **1993**, *363*, 603–605.

[25] M. Dresselhaus, P. Avouris in *Introduction to Carbon Materials Research*, *Vol. 80*, **2001**, pp. 1–9.

[26] H. Dai in *Nanotube Growth and Characterization*, *Vol. 80*, **2001**, pp. 29–53.

[27] N. Arora, N. Sharma, *Diamond Relat. Mater.* **2014**, *50*, 135–150.

[28] R. Das, Z. Shahnavaz, M. E. Ali, M. M. Islam, S. B. A. Hamid, *Nanoscale Res. Lett.* **2016**, *11*, 510.

[29] H. Sugime, T. Sato, R. Nakagawa, T. Hayashi, Y. Inoue, S. Noda, *Carbon* **2021**, *172*, 772–780.

[30] M. Kumar, Y. Ando, *J. Nanosci. Nanotechnol.* **2010**, *10*, 3739–3758.

[31] R. Saito, G. Dresselhaus, M. S. Dresselhaus, *Physical Properties of Carbon Nanotubes*, Imperial College Press, **1998**.

[32] P. Avouris, Z. Chen, V. Perebeinos, *Nat. Nanotechnol.* **2007**, *2*, 605–615.

[33] Y. Zhang, L. Zheng, *Nanoscale* **2010**, *2*, 1919–1929.

[34] S. Nanot, E. H. Hároz, J.-H. Kim, R. H. Hauge, J. Kono, *Adv. Mater.* **2012**, *24*, 4977–4994.

[35] I. P. Batra, *Surf. Sci.* **1998**, *395*, 43–45.

[36] S. Datta, *Electronic Transport in Mesoscopic Systems*, Cambridge University Press, **1995**.

[37] Y. Imry, R. Landauer, *Rev. Mod. Phys.* **1999**, *71*, S306–S312.

[38] P. McEuen, M. Fuhrer, H. Park, *IEEE Transactions on Nanotechnology* **2002**, *1*, 78–85.

[39] M. S. Dresselhaus, R. Saito, A. Jorio, *AIP Conf. Proc.* **2005**, *772*, 25–31.

[40] J. Ma, J.-N. Wang, C.-J. Tsai, R. Nussinov, B. Ma, *Front. Mater. Sci.* **2010**, *4*, 17–28.

[41] C. Dekker, *Phys. Today* **1999**, *52*, 22–28.

[42] A. Naeemi, J. Meindl, *IEEE Electr. Device L.* **2006**, *27*, 338–340.

[43] S. Datta, *Quantum Transport: Atom to Transistor*, 2nd, Cambridge University Press, **2005**.

[44] L. Forró, C. Schoenenberger in *Physical Properties of Multi-wall Nanotubes*, *Vol. 80*, **2001**, pp. 329–391.

[45] P. Poncharal, C. Berger, Y. Yi, Z. L. Wang, W. A. de Heer, *J. Phys. Chem. B* **2002**, *106*, 12104–12118.

[46] M. S. Dresselhaus, G. Dresselhaus, P. C. Eklund, *Science of Fullerenes and Carbon Nanotubes: Their Properties and Applications*, Academic Press, **1996**.

[47] C. Schoenenberger, A. Bachtold, C. Strunk, J.-P. Salvetat, L. Forró, *Appl. Phys. A: Mater. Sci. Process.* **1999**, *69*, 283–295.

[48] A. Bachtold, M. S. Fuhrer, S. Plyasunov, M. Forero, E. H. Anderson, A. Zettl, P. L. McEuen, *Phys. Rev. Lett.* **2000**, *84*, 6082–6085.

[49] S. Frank, P. Poncharal, Z. L. Wang, W. A. d. Heer, *Science* **1998**, *280*, 1744–1746.

[50] O. Hjortstam, P. Isberg, S. Söderholm, H. Dai, *Appl. Phys. A: Mater. Sci. Process.* **2004**, *78*, 1175–1179.

[51] B. Bourlon, C. Miko, L. Forró, D. C. Glattli, A. Bachtold, *Phys. Rev. Lett.* **2004**, *93*, 176806.

[52] A. Bachtold, C. Strunk, J.-P. Salvetat, J.-M. Bonard, L. Forró, T. Nussbaumer, C. Schönenberger, *Nature* **1999**, *397*, 673–675.

[53] H. J. Li, W. G. Lu, J. J. Li, X. D. Bai, C. Z. Gu, *Phys. Rev. Lett.* **2005**, *95*, 086601.

[54] S. Lee, K. Teo, G. Amaratunga, W. Milne, M. Chhowalla, D. Hasko, H. Ahmed, *J. Vac. Sci. Technol. B* **2003**, *21*, 996–999.

[55] A. Naeemi, J. D. Meindl, *IEEE Electr. Device L.* **2007**, *28*, 135–138.

[56] A. Chiariello, A. Maffucci, G. Miano, *IEEE T. Electromagn. C.* **2012**, *54*, 158–166.

[57] J. Jiang, J. Dong, H. T. Yang, D. Y. Xing, *Phys. Rev. B* **2001**, *64*, 045409.

[58] C. T. White, T. N. Todorov, *Nature* **1998**, *393*, 240–242.

[59] M. Nihei, D. Kondo, A. Kawabata, S. Sato, H. Shioya, M. Sakaue, T. Iwai, M. Ohfuti, Y. Awano in Proceedings of the IEEE 2005 International Interconnect Technology Conference, **2005**, pp. 234–236.

[60] A. Naeemi, J. Meindl, *IEEE Electr. Device L.* **2006**, *27*, 338–340.

[61] T. Ando, *Semicond. Sci. Technol.* **2000**, *15*, R13–R27.

[62] V. Krsti ć, S. Roth, M. Burghard, *Phys. Rev. B* **2000**, *62*, R16353–R16355.

[63] J.-Y. Park, S. Rosenblatt, Y. Yaish, V. Sazonova, H. Üstünel, S. Braig, T. A. Arias, P. W. Brouwer, P. L. McEuen, *Nano Lett.* **2004**, *4*, 517–520.

[64] T. Ando, T. Nakanishi, R. Saito, *J. Phys. Soc. Jpn.* **1998**, *67*, 2857–2862.

[65] V. L. Gurevich, V. I. Kozub, *J. Phys.: Condens. Matter.* **2011**, *23*, 245303.

[66] T. Lan, T. Ragab, C. Basaran, *Comp. Mater. Sci.* **2018**, *149*, 397–408.

[67] G. T. Meaden in *Electrical Resistance of Metals*, Springer US, Boston, MA, **1965**, pp. 59–94.

[68] X. Zhou, J.-Y. Park, S. Huang, J. Liu, P. L. McEuen, *Phys. Rev. Lett.* **2005**, *95*, 146805.

[69] V. Perebeinos, J. Tersoff, P. Avouris, *Phys. Rev. Lett.* **2005**, *94*, 086802.

[70] P. L. McEuen, M. Bockrath, D. H. Cobden, Y.-G. Yoon, S. G. Louie, *Phys. Rev. Lett.* **1999**, *83*, 5098–5101.

[71] N. W. Ashcroft, N. David Mermin, *Solid State Physics*, 1st ed., Brooks Cole, **1976**.

[72] S. Suzuki, *Physical and Chemical Properties of Carbon Nanotubes*, InTech, **2013**.

[73] R. Landauer in Non linearity in Condensed Matter, (Eds.: A. R. Bishop, D. K. Campbell, P. Kumar, S. E. Trullinger), Springer Berlin Heidelberg, **1987**, pp. 2–22.

[74] D. K. Ferry, S. M. Goodnick, J. Bird, *Transport in Nanostructures*, 2nd ed., Cambridge University Press, **2009**.

[75] M. P. Das, F. Green, *AIP Conf. Proc.* **2008**, *1063*, 26–34.

[76] M. Das, F. Green, *J. Phys. Condens. Matter.* **2005**, *17*, 46.

[77] E. Bringuier, "The dissipation in Landauer's ballistic resistor", working paper or preprint, **2016**.

[78] J. Heremans, I. Rahim, M. S. Dresselhaus, *Phys. Rev. B* **1985**, *32*, 6742–6747.

[79] W. Zhang, Z. Zhu, F. Wang, T. Wang, L. Sun, Z. Wang, *Nanotechnology* **2004**, *15*, 936.

[80] J. X. Cao, X. H. Yan, Y. Xiao, J. W. Ding, *Phys. Rev. B* **2004**, *69*, 073407.

[81] S. Mensah, F. Allotey, G. Nkrumah, N. Mensah, *Physica E* **2004**, *23*, 152–158.

[82] A. Agarwal, S. Bakshi, D. Lahiri, *Carbon Nanotube Reinforced Metal Matrix Composites*, **2010**.

[83] S. R. Bakshi, D. Lahiri, A. Agarwal, *Int. Mater. Rev.* **2010**, *55*, 41–64.

[84] W. A. D. M. Jayathilaka, A. Chinnappan, S. Ramakrishna, *J. Mater. Chem. C* **2017**, *5*, 9209–9237.

[85] D. Janas, B. Liszka, *Mater. Chem. Front.* **2018**, *2*, 22–35.

[86] J. Molina, R. Saravanan, R. Arpón, C. Garcıa-Cordovilla, E. Louis, J. Narciso, *Acta Mater.* **2002**, *50*, 247–257.

[87] W. Chen, J. Tu, L. Wang, H. Gan, Z. Xu, X. Zhang, *Carbon* **2003**, *41*, 215–222.

[88] X. Chen, J. Xia, J. Peng, W. Li, S. Xie, *Compos. Sci. Technol.* **2000**, *60*, 301–306.

[89] B.-K. Jang, Y. Sakka, *Mater. Trans.* **2010**, *51*, 192–195.

[90] M. A. U. Rehman, Q. Chen, A. Braem, M. S. P. Shaffer, A. R. Boccaccini, *Int. Mater. Rev.* **2020**, 1–30.

[91] C. Zhao, J. Wang, *Phys. Status Solidi A* **2014**, *211*, 2878–2885.

[92] D. Zhang, Z. Zhan, *J. Alloys Compd.* **2016**, *658*, 663–671.

[93] W. Daoush, B. Lim, C. Mo, D. Nam, S. Hong, *Mat. Sci. Eng. A-Struct.* **2009**, *513-514*, 247–253.

[94] S. Arai, T. Osaki, *J. Electrochem. Soc.* **2014**, *162*, D68–D73.

[95] S. Arai, T. Osaki, M. Hirota, M. Uejima, *Material Today Communications* **2016**, *7*, 101–107.

[96] F. Yan, L. Liu, M. Li, M. Zhang, L. Shang, L. Xiao, Y. Ao, *Compos. Part A-Appl. S.* **2019**, *125*, 105530.

[97] Y. Yang, Y. Wang, Y. Ren, C. He, J. Deng, J. Nan, J. Chen, L. Zuo, *Mater. Lett.* **2008**, *62*, 47–50.

[98] H. Rennhofer, B. Zanghellini, *Nanomaterials* **2021**, *11*, 6.

[99] Y. Feng, G. E. McGuire, O. A. Shenderova, H. Ke, S. L. Burkett, *Thin Solid Films* **2016**, *615*, 116–121.

[100] D. Ning, A. Zhang, H. Wu, *Materials* **2019**, *12*, 3.

[101] X. Chen, J. Tao, J. Yi, Y. Liu, R. Bao, C. Li, *J. Alloys Compd.* **2018**, *735*, 163–171.

[102] Y. Feng, S. L. Burkett, *J. Vac. Sci. Technol. B* **2015**, *33*, 022004.

[103] G. Xu, J. Zhao, S. Li, X. Zhang, Z. Yong, Q. Li, *Nanoscale* **2011**, *3*, 4215–4219.

[104] M. B. Bazbouz, A. Aziz, D. Copic, M. De Volder, M. E. Welland, *Adv. Electron. Mater.* **2021**, *7*, 2001213.

[105] P.-M. Hannula, J. Aromaa, B. Wilson, D. Janas, K. Koziol, O. Forsén, M. Lundström, *Electrochim. Acta* **2017**, *232*, 495–504.

[106] J. Shuai, L. Xiong, L. Zhu, W. Li, *Compos. Part A Appl. S.* **2016**, *88*, 148–155.

[107] C. Subramaniam, A. Sekiguchi, T. Yamada, D. N. Futaba, K. Hata, *Nanoscale* **2016**, *8*, 3888–3894.

[108] C. Subramaniam, Y. Yasuda, S. Takeya, S. Ata, A. Nishizawa, D. Futaba, T. Yamada, K. Hata, *Nanoscale* **2014**, *6*, 2669–2674.

[109] S. Sun, W. Mu, M. Edwards, D. Mencarelli, L. Pierantoni, Y. Fu, K. Jeppson, J. Liu, *Nanotechnology* **2016**, *27*, 335705.

[110] R. Sundaram, T. Yamada, K. Hata, A. Sekiguchi, *Jpn. J. Appl. Phys.* **2018**, *57*, 04FP08.

[111] R. Sundaram, T. Yamada, K. Hata, A. Sekiguchi, *Sci. Rep.* **2017**, *7*, 9267.

[112] J. Lee, S. Berrada, F. Adamu-Lema, N. Nagy, V. P. Georgiev, T. Sadi, J. Liang, R. Ramos, H. Carrillo-Nunez, D. Kalita, K. Lilienthal, M. Wislicenus, R. Pandey, B. Chen, K. B. K. Teo, G. Goncalves, H. Okuno, B. Uhlig, A. Todri-Sanial, J. Dijon, A. Asenov, *IEEE Trans. Electron Devices* **2018**, *65*, 3884–3892.

[113] G. Zangari, *Coatings* **2015**, *5*, 195–218.

[114] H. Lee, S. M. Dellatore, W. M. Miller, P. B. Messersmith, *Science* **2007**, *318*, 426–430.

[115] C. Shi, C.-H. Deng, X. Zhang, P.-Y. Yang, *ACS Appl. Mater. Interfaces* **2013**, *5*, 7770–7776.

[116] F. Bernsmann, V. Ball, F. Addiego, A. Ponche, M. Michel, J. J. d. A. Gracio, V. Toniazzo, D. Ruch, *Langmuir* **2011**, *27*, PMID: 21332218, 2819–2825.

[117] J. Yang, M. A. Cohen Stuart, M. Kamperman, *Chem. Soc. Rev.* **2014**, *43*, 8271–8298.

[118] L. Wang, L. Hu, S. Gao, D. Zhao, L. Zhang, W. Wang, *RSC Adv.* **2015**, *5*, 9314–9324.

[119] Q. Lyu, N. Hsueh, C. L. L. Chai, *Polym. Chem.* **2019**, *10*, 5771–5777.

[120] J. Liebscher, R. Mrówczyński, H. A. Scheidt, C. Filip, N. D. Hădade, R. Turcu, A. Bende, S. Beck, *Langmuir* **2013**, *29*, 10539–10548.

[121] D. R. Dreyer, D. J. Miller, B. D. Freeman, D. R. Paul, C. W. Bielawski, *Langmuir* **2012**, *28*, 6428–6435.

[122] M. Arzillo, G. Mangiapia, A. Pezzella, R. K. Heenan, A. Radulescu, L. Paduano, M. d'Ischia, *Biomacromolecules* **2012**, *13*, 2379–2390.

[123] Z. Xu, *Sci. Rep.* **2013**, *3*, 2914.

[124] N. Holten-Andersen, M. J. Harrington, H. Birkedal, B. P. Lee, P. B. Messersmith, K. Y. C. Lee, J. H. Waite, *Proc. Natl. Acad. Sci. U. S. A.* **2011**, *108*, 2651–2655.

[125] Y. Liu, K. Ai, L. Lu, *Chem. Rev.* **2014**, *114*, 5057–5115.

[126] H. Lee, Y. Lee, A. R. Statz, J. Rho, T. G. Park, P. B. Messersmith, *Adv. Mater.* **2008**, *20*, 1619–1623.

[127] Y. Liu, G. Li, R. Qin, D. Chen, *Langmuir* **2016**, *32*, 13675–13686.

[128] Q. Ye, F. Zhou, W. Liu, *Chem. Soc. Rev.* **2011**, *40*, 4244–4258.

[129] T. H. Anderson, J. Yu, A. Estrada, M. U. Hammer, J. H. Waite, J. N. Israelachvili, *Adv. Funct. Mater.* **2010**, *20*, 4196–4205.

[130] S. T. Martin, J. M. Kesselman, D. S. Park, N. S. Lewis, M. R. Hoffmann, *Environ. Sci. Technol.* **1996**, *30*, 2535–2542.

[131] N. Yao, V. Lordi, S. X. C. Ma, E. Dujardin, A. Krishnan, M. M. J. Treacy, T. W. Ebbesen, *J. Mater. Res.* **1998**, *13*, 2432–2437.

[132] I. Rosca, F. Watari, M. Uo, T. Akasaka, *Carbon* **2005**, *43*, 3124–3131.

[133] V. Datsyuk, M. Kalyva, K. Papagelis, J. Parthenios, D. Tasis, A. Siokou, I. Kallitsis, C. Galiotis, *Carbon* **2008**, *46*, 833–840.

[134] M. Fatin, A. Rahim Ruslinda, S. Norhafizah, M. A. Farehanim, M. K. Md Arshad, R. Ayub, U. Hashim in 2014 IEEE Conference on Biomedical Engineering and Sciences (IECBES), **2014**, pp. 686–689.

[135] H. Mei, Z. Gao, Q. Wang, H. Sun, K. Zhao, P. Zhang, J. Hao, M. Ashokkumar, J. Cui, *Ultrason. Sonochem.* **2021**, *74*, 105571.

[136] V. Ball, J. Gracio, M. Vila, M. K. Singh, M.-H. Metz-Boutigue, M. Michel, J. Bour, V. Toniazzo, D. Ruch, M. J. Buehler, *Langmuir* **2013**, *29*, 12754–12761.

[137] A. Duhain, M. Michel, G. Lamblin, D. Lenoble, Metal-CNT composite, production method and materials therefor, WO2020043590A1, **2020**.

[138] E. Faure, C. Falentin-Daudré, C. Jérôme, J. Lyskawa, D. Fournier, P. Woisel, C. Detrembleur, *Prog. Polym. Sci.* **2013**, *38*, 236–270.

[139] H. Fan, L. Wang, X. Feng, Y. Bu, D. Wu, Z. Jin, *Macromolecules* **2017**, *50*, 666–676.

[140] T. Ahmad, *J. Nanotechnol.* **2014**, *2014*, 1–11.

[141] D. Lin, B. Xing, *Environ. Sci. Technol.* **2008**, *42*, PMID: 18767645, 5917–5923.

[142] J. L. Plawsky, M. Ojha, A. Chatterjee, P. C. W. Jr., *Chem. Eng. Commun.* **2008**, *196*, 658–696.

[143] F. Daneshvar, T. Zhang, A. Aziz, H.-J. Sue, M. E. Welland, *Carbon* **2020**, *157*, 583–593.

[144] J. W. Dini, D. D. Snyder in *Modern Electroplating*, John Wiley & Sons, Ltd, **2010**, Chapter 2, pp. 33–78.

[145] D. Grujicic, B. Pesic, *Electrochim. Acta* **2002**, *47*, 2901–2912.

[146] E. Stenhäuser, S. Roseler, S. Wiese, T. C. L. Nguyen, L. Stamp, Formaldehyde-free electroless copper plating solution, US20140242264A1, **2014**.

[147] W.-C. Tsai, C.-C. Wan, Y.-Y. Wang, *J. Electrochem. Soc.* **2003**, *150*, C267.

[148] G. Devaraj, S. Guruviah, S. Seshadri, *Mater. Chem. Phys.* **1990**, *25*, 439–461.

[149] S.-K. Kim, J. J. Kim, *Electrochem. Solid-State Lett.* **2004**, *7*, C98.

[150] Z. V. Feng, X. Li, A. A. Gewirth, *J. Phys. Chem. B* **2003**, *107*, 9415–9423.

[151] J. W. Gallaway, M. J. Willey, A. C. West, *J. Electrochem. Soc.* **2009**, *156*, D287.

[152] Y. Sasajima, T. Satoh, K. Tamahashi, J. Onuki, *Mater. Trans.* **2012**, *53*, 1507–1514.

[153] P. M. Vereecken, R. A. Binstead, H. Deligianni, P. C. Andricacos, *IBM J. Res. Dev.* **2005**, *49*, 3–18.

[154] H. K. Chang, B.-H. Choe, J. K. Lee, *Mater. Sci. Eng. A* **2005**, *409*, 317–328.

[155] A. Duhain, G. Lamblin, D. Lenoble, *RSC Adv.* **2021**, *11*, 40159–40172.

[156] C. Qianwen, W. Zheyao, C. Jian, L. Litian, *Microelectron. Eng.* **2010**, *87*, 527–531.

[157] L. S. HEBERT, Lightning strike protection film, WO2019234693, **2019**.

[158] A. Duhain, J. Guillot, G. Lamblin, D. Lenoble, *RSC Adv.* **2021**, *11*, 11900–11909.

[159] H. Li, T. Marshall, Y. Aulin, A. Thenuwara, Y. Zhao, E. Borguet, D. Strongin, F. Ren, *J. Mater. Sci.* **2019**, *54*, 6393–6400.

[160] M. Biesinger, *Surf. Interface Anal.* **2017**, *49*, 1325–1334.

[161] B. Vincent, I. Nguyen, M. Haupt, C. Oehr, C. Arnoult, V. Toniazzo, D. Ruch, *J. Colloid Interface Sci.* **2011**, *364*, 359–365.

[162] D. Bulushev, A. Chuvilin, V. Sobolev, S. Stolyarova, Y. Shubin, I. Asanov, A. Ishchenko, G. Magnani, M. Ricco, A. Okotrub, L. Bulusheva, *J. Mater. Chem. A* **2017**, *5*, 10574–10583.

[163] T. Susi, T. Pichler, P. Ayala, *Nanotechnol.* **2015**, *6*, 177–192.

[164] W. Tamakloe, D. Agyeman, M. Park, J. Yang, Y.-M. Kang, *J. Mater. Chem. A* **2019**, *7*, 7396–7405.

[165] Y. Liao, Y. Wang, X. Feng, W. Wang, F. Xu, L. Zhang, *Mater. Chem. Phys.* **2010**, *121*, 534–540.

[166] V. R. S, S. Kandaiah, *J. Mater. Chem. A* **2016**, *5*, 2052–2065.

[167] Y. Sohn, D. Pradhan, L. Zhao, K. Leung, *Electrochem. Solid-State Lett.* **2012**, *15*, K35.

[168] A. Radi, D. Pradhan, Y. Sohn, K. Leung, *ACS nano* **2010**, *4*, 1553–1560.

[169] K. Ai, Y. Liu, C. Ruan, L. Lu, M. Lu, *Adv. Mater.* **2013**, *25*, 998–1003.

[170] J. Kong, W. A. Yee, L. Yang, Y. Wei, H. G. Ong, J. M. Ang, X. Li, X. Lu, *Chem. Commun. (Cambridge U. K.)* **2012**, *48*, 10316–10318.

[171] D. Barrett, D. Fullenkamp, L. He, N. Holten-Andersen, K. Y. Lee, P. Messersmith, *Adv. Funct. Mater.* **2013**, *23*, 1111–1119.

[172] F. Wei, L. Jian, Y. Zhu, X.-S. Wang, C.-Y. Cao, W.-G. Song, *Sci. China: Chem.* **2017**, 1236–1242.

[173] R. Zangmeister, T. Morris, M. Tarlov, *Langmuir* **2013**, *29*, 8619–8628.

[174] G. Deroubaix, P. Marcus, *Surf. Interface Anal.* **1992**, *18*, 39–46.

[175] J. Ghijsen, L. H. Tjeng, J. van Elp, H. Eskes, J. Westerink, G. A. Sawatzky, M. T. Czyzyk, *Phys. Rev. B* **1988**, *38*, 11322–11330.

[176] H. Li, J. Xi, Y. Zhao, F. Ren, *MRS Adv.* **2019**, *4*, 1–8.

[177] D. Mott, J. Galkowski, L. Wang, J. Luo, C.-J. Zhong, *Langmuir* **2007**, *23*, 5740–5745.

[178] A. Lekawa-Raus, K. Walczak, G. Kozlowski, S. Hopkins, M. Woźniak, B. A. Glowacki, K. Koziol, *Scr. Mater.* **2015**, *106*, 34–37.

[179] X. Yu, H. Fan, Y. Liu, Z. Shi, Z. Jin, *Langmuir* **2014**, *30*, 5497–5505.

[180] M. Jastrzębska, H. Isotalo, J. Paloheimo, H. Stubb, *J. Biomater. Sci. Polym. Ed.* **1995**, *7*, 577–586.

[181] A. Mostert, B. Powell, F. Pratt, G. Hanson, T. Sarna, I. Gentle, P. Meredith, *Proc. Natl. Acad. Sci. U. S. A.* **2012**, *109*, 8943–8947.

[182] A. Jorio, R. Saito, *J. Appl. Phys.* **2021**, *129*, 021102.

[183] M. S. Dresselhaus, A. Jorio, A. G. Souza Filho, R. Saito, *Phil. Trans. R. Soc. A* **2010**, *368*, 5355–5377.

[184] S. N. Bokova, E. D. Obraztsova, V. V. Grebenyukov, K. V. Elumeeva, A. V. Ishchenko, V. L. Kuznetsov, *Phys. Status Solidi B* **2010**, *247*, 2827–2830.

[185] V. L. Kuznetsov, S. N. Bokova-Sirosh, S. I. Moseenkov, A. V. Ishchenko, D. V. Krasnikov, M. A. Kazakova, A. I. Romanenko, E. N. Tkachev, E. D. Obraztsova, *Phys. Status Solidi B* **2014**, *251*, 2444–2450.

[186] J. Zhao, A. Buldum, J. Han, J. Lu, *Nanotechnology* **2002**, *13*, 195–200.

[187] S. C. Lim, J. H. Jang, D. J. Bae, G. H. Han, S. Lee, I.-S. Yeo, Y. H. Lee, *Appl. Phys. Lett.* **2009**, *95*, 264103.

[188] A. Fediai, D. A. Ryndyk, G. Seifert, S. Mothes, M. Claus, M. Schröter, G. Cuniberti, *Nanoscale* **2016**, *8*, 10240–10251.

[189] K. Milowska, M. Ghorbani-Asl, M. Burda, L. Wolanicka, N. Catic, P. Bristowe, K. Koziol, *Nanoscale* **2017**, *9*, 8458–8469.

[190] J. Zou, D. Liu, J. Zhao, L. Hou, T. Liu, X. Zhang, Y. Zhao, Y. T. Zhu, Q. Li, *ACS Appl. Mater. Interfaces* **2018**, *10*, 8197–8204.

[191] J. Shuai, L. Xiong, H. Zecheng, L. Zhu, W. Li, *J. Mater. Eng. Perform.* **2019**, *28*, 4393–4402.

[192] D. McIntyre, R. Hirschman, I. Puchades, B. Landi, *J. Mater. Sci.* **2020**, *55*, 6610–6622.

[193] H. C. de Groh, *MRS Adv.* **2017**, *2*, 71–76.

[194] S. H. Brongersma, E. Kerr, I. Vervoort, A. Saerens, K. Maex, *J. Mater. Res.* **2002**, *17*, 582–589.

[195] X. Zhang, C. Shi, E.-Z. Liu, F. he, L. Ma, Q. Li, J. Li, N. Zhao, C. He, *Compos. Part A-Appl. S.* **2017**, *103*, 178–187.

[196] H. Li, A. Misra, Z. Horita, C. C. Koch, N. A. Mara, P. O. Dickerson, Y. Zhu, *Appl. Phys. Lett.* **2009**, *95*, 071907.

[197] Y.-J. Tan, K. Lim, *Surf. Coat. Technol.* **2003**, *167*, 255–262.

[198] R. M. Sundaram, A. Sekiguchi, M. Sekiya, T. Yamada, K. Hata, *R. Soc. Open Sci.* **2018**, *5*, 180814.

[199] M. Ghorbani-Asl, P. Bristowe, K. Koziol, *Phys. Chem. Chem. Phys.* **2015**, 18273–18277.

[200] J. Kasparian, R. Ackermann, Y.-B. André, G. Méchain, G. Méjean, B. Prade, P. Rohwetter, E. Salmon, K. Stelmaszczyk, J. Yu, A. Mysyrowicz, R. Sauerbrey, L. Woeste, J.-P. Wolf, *J. Eur. Opt. Soc-Rapid* **2008**, *3*.

[201] D. Morgan, C. Hardwick, S. Haigh, A. Meakins, *Aerospace Lab* **2012**, 1–10.

[202] G. Sweers, B. Birch, J. Gokcen, *Aero magazine* **2012**, 19–28.

[203] A.-2. L. Committee, Aircraft Lightning Zone, **2018**.

[204] R. X. K. Gao, H. M. Lee, S. P. Gao in 2017 International Symposium on Electromagnetic Compatibility - EMC EUROPE, **2017**, pp. 1–5.

[205] T. R. Bott, G. F. Hewitt, G. L. Shires, *Process Heat Transfer*, 1st ed., CRC-Press, **1994**.

[206] E. Belenkov, V. Mavrinskii, T. Belenkova, V. Chernov, *J. Exp. Theor. Phys.* **2014**, *120*, 820–830.

[207] J. W. Arblaster, *J. Phase Equilib. Diffus.* **2015**, *36*, 422–444.

[208] M. F. Ashby, *Materials Selection in Mechanical Design, Fourth Edition*, 4th ed., Butterworth-Heinemann, **2010**.

[209] Y. D. Fomin, V. Brazhkin, *Carbon* **2020**, *157*, 767–778.

[210] W. M. Haynes, *CRC Handbook of Chemistry and Physics*, 95th ed., CRC Press, **2014**.

[211] M. Aroyo, *Plat. Surf. Finish.* **1998**, *85*, 69–76.

[212] M. Paunovic, M. Schlesinger, D. D. Snyder in *Modern Electroplating*, John Wiley & Sons, Ltd, **2010**, Chapter 1, pp. 1–32.

[213] M.-S. Hong, Y. Park, T. Kim, K. Kim, J.-G. Kim, *Journal of Materiomics* **2020**, *6*, 158–166.

[214] M. Rabchinskii, A. Dideikin, D. Kirilenko, M. Baidakova, V. Shnitov, F. Roth, S. Koniakhin, N. Besedina, S. Pavlov, R. Kuricyn, N. Lebedeva, P. Brunkov, A. Vul', *Sci. Rep.* **2018**, *8*, 14154.

[215] T. Wirtz, O. De Castro, J.-N. Audinot, P. Philipp, *Annu. Rev. Anal. Chem.* **2019**, *12*, 523–543.

[216] R. Saeed, J. Schlegel, C. Castano Giraldo, R. Sawafta, *Int. J. Eng. Res. Sci. Technol.* **2016**, *5*, 405–412.

[217] M. Heaney in *Electrical measurement, signal processing, and displays*, **2003**, Chapter 7, pp. 1–7.

[218] F. M. Smits, *Bell Syst. Tech. J.* **1958**, *37*, 711–718.

[219] V. Garcia-Vazquez, *Rev. Sci. Instrum.* **2017**, *88*, 114701.

[220] L. J. Van der Pauw in *Semiconductor Devices: Pioneering Papers*, **1991**, pp. 174–182.